



La genèse des gisements de type roll front dans le bassin d'Erlian, Chine

Christophe Bonnelli

► To cite this version:

Christophe Bonnelli. La genèse des gisements de type roll front dans le bassin d'Erlian, Chine. Sciences de la Terre. Université de Lorraine, 2013. Français. NNT : 2013LORR0282 . tel-01750627

HAL Id: tel-01750627

<https://hal.univ-lorraine.fr/tel-01750627v1>

Submitted on 29 Mar 2018

HAL is a multi-disciplinary open access archive for the deposit and dissemination of scientific research documents, whether they are published or not. The documents may come from teaching and research institutions in France or abroad, or from public or private research centers.

L'archive ouverte pluridisciplinaire **HAL**, est destinée au dépôt et à la diffusion de documents scientifiques de niveau recherche, publiés ou non, émanant des établissements d'enseignement et de recherche français ou étrangers, des laboratoires publics ou privés.



AVERTISSEMENT

Ce document est le fruit d'un long travail approuvé par le jury de soutenance et mis à disposition de l'ensemble de la communauté universitaire élargie.

Il est soumis à la propriété intellectuelle de l'auteur. Ceci implique une obligation de citation et de référencement lors de l'utilisation de ce document.

D'autre part, toute contrefaçon, plagiat, reproduction illicite encourt une poursuite pénale.

Contact : ddoc-theses-contact@univ-lorraine.fr

LIENS

Code de la Propriété Intellectuelle. articles L 122. 4

Code de la Propriété Intellectuelle. articles L 335.2- L 335.10

http://www.cfcopies.com/V2/leg/leg_droi.php

<http://www.culture.gouv.fr/culture/infos-pratiques/droits/protection.htm>



UNIVERSITÉ
DE LORRAINE

geo
Ressources



AREVA

Université de Lorraine, GeoRessources-CREGU
UMR 7359, Vandoeuvre-Lès-Nancy, 54506 Nancy, France
Ecole doctorale RP2E (Ressources, Procédés, Produits et Environnement)
Collegium Sciences et Technologies

THESE

Présentée pour l'obtention du titre de
Docteur de l'université de Lorraine (Nancy)
en Géosciences
par
Christophe Bonnetti

Genèse des gisements de type roll front et tabulaire dans le bassin d'Erlian (Chine)

Soutenance publique le 13/12/2013

Membres du jury :

Rapporteurs :	M. Pagel J. Brugger	Professeur, Université Paris-Sud, France Professeur, Université d'Adelaide, Australie
Examinateurs :	M. Jébrak X. Liu	Professeur, Université de Québec à Montréal, Canada Professeur, East China Institute of Technology, Chine
(président)	A. S. André-Mayer	Professeur, Université de Lorraine, France
Directeurs de thèse :	M. Cuney S. Bourlange	Directeur de recherche CNRS-GéoRessources-CREGU Maître de conférences, Université de Lorraine
Invités :	F. Malartre R. Michels A. Benedicto	Maître de conférences, Université de Lorraine Chargé de recherche CNRS, Université de Lorraine Areva Mines, Areva Ressources Canada



UNIVERSITÉ
DE LORRAINE

geo
Ressources



AREVA

Université de Lorraine, GeoRessources-CREGU
UMR 7359, Vandoeuvre-Lès-Nancy, 54506 Nancy, France
Ecole doctorale RP2E (Ressources, Procédés, Produits et Environnement)
Collegium Sciences et Technologies

THESE

Présentée pour l'obtention du titre de
Docteur de l'université de Lorraine (Nancy)
en Géosciences
par
Christophe Bonnetti

Genèse des gisements de type roll front et tabulaire dans le bassin d'Erlian (Chine)

Soutenance publique le 13/12/2013

Membres du jury :

Rapporteurs :	M. Pagel J. Brugger	Professeur, Université Paris-Sud, France Professeur, Université d'Adelaide, Australie
Examinateurs :	M. Jébrak X. Liu	Professeur, Université de Québec à Montréal, Canada Professeur, East China Institute of Technology, Chine
(président)	A. S. André-Mayer	Professeur, Université de Lorraine, France
Directeurs de thèse :	M. Cuney S. Bourlange	Directeur de recherche CNRS-GéoRessources-CREGU Maître de conférences, Université de Lorraine
Invités :	F. Malartre R. Michels A. Benedicto	Maître de conférences, Université de Lorraine Chargé de recherche CNRS, Université de Lorraine Areva Mines, Areva Ressources Canada

REMERCIMENTS

Ce travail de thèse a été financé par AREVA Mines dans le cadre d'une collaboration entre le laboratoire GéoRessources – CREGU de Nancy et l'East China Institute of Technology de Fuzhou en Chine. Je tiens à remercier l'ensemble des personnes qui ont contribué à la réalisation de ce projet.

Tout d'abord, je remercie très sincèrement les membres du jury qui ont accepté d'évaluer mon travail de thèse :

- Mr J. Brugger, pour ses compétences en minéralogie et en géochimie ainsi que sa connaissance des gisements d'uranium d'Australie du Sud qui ont permis de préciser nos études des gisements chinois. Au plaisir de partager une bonne fondue !
- Mr M. Pagel, pour ses connaissances sur la diagenèse des grès et des gisements d'uranium qui ont permis de discuter des modèles métallogéniques proposés.
- Mme A-S. André-Mayer, merci d'avoir présidé ce jury et surtout merci de ta gentillesse et de ton soutien au cours de ces trois années.
- Mr M. Jébrak, pour les discussions scientifiques autour du projet. Après avoir été brièvement ton étudiant à l'UQAM, ce fut un plaisir de te compter parmi les membres de ce jury.
- Mr X. Lui, pour avoir permis que ce projet se déroule dans les meilleures conditions avec nos partenaires et amis chinois.

Je tiens désormais à remercier toutes les personnes qui ont collaboré à ce travail :

(1) Mon encadrement

Un remerciement tout particulier à mon directeur de thèse M. Cuney qui est à l'initiative de ce projet de thèse et qui m'a apporté ses précieux conseils au fil de ces trois ans. Je remercie également les co-encadrants de ce travail, S. Bourlange, F. Malartre et R. Michels. Merci à vous pour votre aide, votre soutien et vos conseils, ce fut un très grand plaisir de collaborer avec vous tous, sur le terrain et à Nancy.

(2) Nos partenaires chinois

Je remercie très fortement X. Liu et toute l'équipe de l'East China Institute of technology de Fuzhou qui nous ont accueillis très chaleureusement et qui ont permis que les missions de terrain se déroulent dans les meilleures conditions. Je remercie tout particulièrement Menhong et Liu qui m'ont accompagné et ont traduit les conversations lors des différentes missions en Chine. J'adresse également mes sincères remerciements aux géologues de la division 208 du CNNC qui ont permis les visites de gisements réalisées lors de la thèse, et ce dans les meilleures conditions.

(3) Les collègues du labo

Je remercie l'ensemble des collègues du laboratoire GéoRessources, du CRPG et du SCMEM de Nancy. Je pense notamment au binôme A. Richard et J. Mercadier, A. Tarantola, M-C. Caumont, P. Lach, L. Truche, O. Vanderhaeghe, V. Huault, C. Carpentier, E. Deloule, O. Rouer, S. Mathieu, C. Demeurie et bien d'autres. Merci pour votre collaboration ! Je tiens également à remercier énormément Askar, frère Toé, Steph, Sandrine et les jeunes pour les bons moments passés. A ce titre, je souhaite faire un gros coup de cœur pour mes amis : le corse, Mr Eglinger, Mat, Roland Salardus ! On se souviendra des parties de belote (et autre...). J'ai ici une pensée toute particulière pour Mr Eglinger qui a été mon compagnon de thèse et avec qui nous avons partagé toutes les étapes de cette grande aventure. La dernière ligne droite restera un grand souvenir ! Enfin, je dis un grand merci à P. Lagrange pour sa gentillesse, son soutien et sa bonne humeur.

(4) Les collègues d'AREVA Mines

Je souhaite tout d'abord remercier J-P. Milesi, J-L. Lescuyer et G. Stein qui ont permis que la thèse puisse voir le jour du côté d'AREVA. Je remercie également tous les collègues d'AREVA, et tout particulièrement A. Benedicto et M. Brouand qui ont collaboré à ce projet, mais également les membres de l'équipe AREVA Mongolie, avec Eric Jacques, Olivier Cardon, Yohann Brault et bien d'autres.

(5) Les collaborations universitaires

J'aimerai remercier M. Poujol de l'université de Rennes pour l'acquisition des données isotopiques Sm/Nd ainsi que T. Allard de l'université Paris 6 pour les mesures des défauts d'irradiation sur argiles.

Enfin je souhaite adresser mes plus vifs remerciements à mes amis ainsi qu'à ma famille qui m'ont soutenu et grâce à qui tout s'est réalisé.

Je tiens à remercier deux personnes en particulier : P-A. Wulser qui m'a soutenu dès l'origine du projet de faire une thèse et qui est toujours resté disponible, et T. Riegler qui représente un des soutiens les plus forts que j'ai reçus au cours de la thèse.

Je remercie bien évidemment mes parents qui au-delà même de la thèse, m'ont toujours et en toute circonstance, apporté leur soutien à tous les niveaux. Ils ont joué un rôle essentiel dans ma réussite !

Encore une fois, merci à tous...

TABLE DES MATIERES

INTRODUCTION GENERALE	19
1. INTRODUCTION ET PROBLEMATIQUE.....	20
2. OBJECTIFS DE LA THESE	24
3. ORGANISATION DU MANUSCRIT	25
PARTIE A : LA MISE EN PLACE DES BASSINS SEDIMENTAIRES.....	27
CHAPITRE 1 : L'EXTENSION CONTINENTALE AU MESOZOÏQUE EN ASIE DE L'EST.....	29
1. LE CADRE GEOLOGIQUE DE L'ASIE DE L'EST	30
2. LE CRATON DE CHINE DU NORD	31
3. LES PREUVES D'UN AMINCISSEMENT LITHOSPHERIQUE	32
3.1. <i>LA GRAVIMETRIE</i>	32
3.2. <i>LA TOMOGRAPHIE SISMIQUE</i>	33
3.3. <i>L'ETUDE DES ENCLAVES DU PALEOZOÏQUE ET DU CENOZOÏQUE</i>	36
3.4. <i>L'AGE DU MANTEAU LITHOSPHERIQUE EN CHINE DU NORD</i>	38
4. LES PREUVES D'UNE EXTENSION CRUSTALE	39
4.1. <i>LES BASSINS SEDIMENTAIRES INTRACONTINENTAUX</i>	39
4.2. <i>LE VOLCANISME</i>	41
4.3. <i>LE PLUTONISME</i>	43
4.4. <i>LES « METAMORPHIC CORE COMPLEX » (MCC) : TEMOINS DE L'EXTENSION CRUSTALE</i>	45
5. LE MODELE GEODYNAMIQUE DE L'EXTENSION MESOZOÏQUE EN ASIE DE L'EST.....	46
5.1. <i>SYNTHESE DES STRUCTURES EXTENSIVES ET DES EVENEMENTS GEOLOGIQUES EN ASIE DE L'EST A LA FIN DU MESOZOÏQUE</i>	46
5.2. <i>MODELE GEODYNAMIQUE : EVOLUTION DE LA MARGE EST-ASIATIQUE A LA FIN DU MESOZOÏQUE</i>	50
CHAPITRE 2: CONTEXTE SEDIMENTAIRE ET EVOLUTION STRATIGRAPHIQUE DES DEPOTS POST-RIFTS DANS LE BASSIN D'ERLIAN..	53
ARTICLE 1: SEDIMENTOLOGY, STRATIGRAPHY AND PALYNOLOGICAL OCCURRENCES OF THE LATE CRETACEOUS ERLIAN FORMATION, ERLIAN BASIN, INNER MONGOLIA, PEOPLE'S REPUBLIC OF CHINA.....	55
1. ABSTRACT	56
2. INTRODUCTION	57
3. GEOLOGICAL AND STRATIGRAPHICAL SETTING	59
3.1. <i>THE ERLIAN BASIN</i>	59
3.2. <i>TECTONO-STRATIGRAPHIC EVOLUTION</i>	60
3.2.1. <i>The pre-rift stage</i>	61
3.2.2. <i>The syn-rift stage</i>	62

3.2.3. <i>The post-rift stage</i>	62
3.3. <i>OVERVIEW OF THE STUDY AREA</i>	63
4. MATERIALS AND METHODS.....	65
5. FACIES MODEL OF THE ERLIAN FORMATION.....	66
5.1. <i>LITHOFACIES AND SEDIMENTARY STRUCTURES</i>	66
5.1.1. <i>Sand</i>	66
5.1.2. <i>Sand, silt and mud</i>	67
5.1.3. <i>Silt and mud</i>	68
5.1.4. <i>Mud</i>	69
5.2. <i>FACIES ARCHITECTURE</i>	71
5.2.1. <i>Channels</i>	71
5.2.2. <i>Crevasse splays</i>	72
5.2.3. <i>Floodplain fines</i>	72
5.3. <i>DEPOSITIONAL ENVIRONMENTS</i>	75
5.3.1. <i>The lower member of the Erlian Formation</i>	75
5.3.2. <i>The upper member of the Erlian Formation</i>	76
6. STRATIGRAPHIC EVOLUTION OF THE ERLIAN FORMATION.....	78
7. PALYNOLOGICAL OCCURRENCES.....	80
7.1. <i>SPORES AND POLLEN ASSEMBLAGES</i>	81
7.1.1. <i>Assemblage 1</i>	81
7.1.2. <i>Assemblage 2</i>	81
7.1.3. <i>Assemblage 3</i>	82
7.1.4. <i>Assemblage 4</i>	83
7.2. <i>BIOSTRATIGRAPHIC INFORMATION</i>	86
8. METALLOGENIC IMPLICATIONS	89
9. CONCLUSIONS.....	90
PARTIE B : LES SOURCES PRIMAIRES DE L'URANIUM AU NORD-EST DE LA CHINE.....	93
CHAPITRE 3 : LE CYCLE DE L'URANIUM DANS LA CROUTE CONTINENTALE..	95
1. CONCENTRATION DE L'URANIUM DANS LA CROUTE CONTINENTALE.....	96
2. CYCLE DE L'URANIUM DE L'ARCHEEN A L'ACTUEL	98
CHAPITRE 4: LES SOURCES PRIMAIRES DE L'URANIUM DANS L'ENVIRONNEMENT DU BASSIN D'ERLIAN	101
ARTICLE 2: INDOSIAN GRANITES AS MAJOR PRIMARY URANIUM SOURCE FOR THE SEDIMENTARY-HOSTED U DEPOSITS OF THE ERLIAN BASIN, NE CHINA.	103
1. ABSTRACT	104
2. INTRODUCTION	105
3. GEOLOGICAL SETTING.....	107
4. MATERIALS AND METHODS.....	111
5. PETROGRAPHY	112

5.1. BIOTITE GRANITES	112
5.2. TWO-MICA GRANITES	115
5.3. VOLCANIC ROCKS	118
6. GEOCHEMISTRY	119
7. GEOCHRONOLOGY	122
7.1. U-Pb ISOTOPIC AGES ON ZIRCON.....	122
7.2. U-Th-Pb CHEMICAL AGES ON MONAZITE	127
7.2.1. In two-mica granite	127
7.2.2. In sandstones of the Erlian Basin.....	129
8. SM-ND ISOTOPES	132
9. URANIUM LEACHING.....	134
10. DISCUSSION.....	137
10.1. HERCYNIAN VS INDOSINIAN GRANITES	137
10.2. URANIUM MASS BALANCE CALCULATION	140
10.3. U ENRICHMENT DURING GEODYNAMIC EVOLUTION IN NORTHEAST CHINA	141
11. CONCLUSIONS.....	144
PARTIE C : GENESE DES MINERALISATIONS URANIFERES DANS LE BASSIN D'ERLIAN.....	151
CHAPITRE 5 : LES GISEMENTS D'URANIUM DE TYPE GRES.....	153
1. GENERALITES SUR LES GISEMENTS DE TYPE GRES	154
2. UNE CLASSIFICATION SOMMAIRE	155
3. GENERALITES SUR LES GISEMENTS DE TYPE ROLL	157
CHAPITRE 6: LES MINERALISATIONS SYN-SEDIMENTAIRES VS DIAGENETIQUE DANS LE BASSIN D'ERLIAN.....	161
ARTICLE 3: THE NUHETING DEPOSIT, ERLIAN BASIN, CHINA: SYNSEDIMENTARY VS DIAGENETIC URANIUM MINERALIZATION.....	163
1. ABSTRACT	164
2. INTRODUCTION	165
3. GEOLOGICAL SETTING.....	166
3.1. THE ERLIAN BASIN.....	166
3.2. THE NUHETING DEPOSIT.....	168
4. MATERIALS AND METHODS	170
5. SEDIMENTOLOGY AND PETROGRAPHY OF THE HOST-ROCK	171
5.1. SEDIMENTOLOGY OF THE ERLIAN FORMATION.....	171
5.2. CHARACTERISTICS OF THE HOST-ROCK	173
5.2.1. Lithofacies	173
5.2.2. Petrography/mineralogy	174
6. CHARACTERIZATION OF THE ORGANIC MATTER.....	177
6.1. PETROGRAPHY.....	177
6.2. TYPOLOGY.....	178

7. URANIUM MINERALIZATION STAGES	180
7.1. DISSEMINATED URANIUM CONCENTRATION.....	180
7.2. URANIUM MINERALS ASSOCIATED WITH PYRITE AND ORGANIC MATTER.....	181
7.2.1. Distribution of the mineralization	182
7.2.2. Pyrite typology and its trace element signature	183
7.2.3. Uranium minerals	186
7.3. POST ORE-STAGE	190
8. DISCUSSION.....	190
8.1. SEDIMENTOLOGY OF THE ERLIAN BASIN	191
8.2. NATURE AND EVOLUTION OF THE ORGANIC MATTER	192
8.3. A METALLOGENIC MODEL FOR THE NUHETING DEPOSIT	193
8.3.1. Synsedimentary uranium concentration	193
8.3.2. Diagenetic uranium mineralization.....	194
8.3.3. Epigenetic cementation	194
9. CONCLUSIONS.....	196
CHAPITRE 7: LES MINERALISATIONS DE TYPE ROLL FRONT DANS LE BASSIN D'ERLIAN	203
ARTICLE 4: THE MULTIPLE ROLES OF SULPHATE-REDUCING BACTERIA AND FE-TI OXIDES IN THE GENESIS OF THE BAYINWULA ROLL FRONT-TYPE URANIUM DEPOSIT, ERLIAN BASIN, NE CHINA.....	205
1. ABSTRACT	206
2. INTRODUCTION.....	207
3. GEOLOGICAL SETTING.....	208
3.1. THE ERLIAN BASIN.....	208
3.2. THE BAYINWULA DEPOSIT	210
4. MATERIALS AND METHODS.....	212
5. SEDIMENTOLOGY OF THE SAIHAN FORMATION	213
6. PRE-ORE URANIUM CONCENTRATION.....	215
6.1. URANIUM CONTENT OF THE HOST SANDSTONE	215
6.2. SANDSTONE PETROGRAPHY AND U-BEARING MINERALS	216
6.3. URANIUM MASS BALANCE CALCULATION	220
7. CHARACTERIZATION OF THE ORGANIC MATTER.....	221
7.1. PETROGRAPHY.....	221
7.2. TYPOLOGY.....	222
8. ORE-STAGE SULPHIDIZATION.....	224
8.1. PETROGRAPHY OF IRON DISULPHIDES	224
8.2. SULFIDE TRACE ELEMENT SIGNATURE.....	226
8.3. SULPHUR ISOTOPES	229
8.4. ORE-STAGE FE-TI OXIDE ALTERATION	230
8.5. U MINERALIZATION	231
9. DISCUSSION.....	234
9.1. SEDIMENTOLOGY OF THE SAIHAN FORMATION.....	234

9.2. THE SOURCE OF URANIUM.....	235
9.3. NATURE AND EVOLUTION OF ORGANIC MATTER.....	236
9.4. SRB AND ORE-STAGE SULPHIDIZATION	236
9.5. URANIUM MINERALIZATION.....	238
9.6. METALLOGENIC MODEL	238
9.6.1. Pre-ore Fe-Ti oxides alteration.....	239
9.6.2. Pre-ore sulphidization.....	239
9.6.3. Ore-stage Fe-Ti oxides alteration and sulphidization.....	239
9.6.4. Ore-stage U mineralization.....	240
10. REGIONAL IMPLICATIONS	242
11. CONCLUSIONS.....	242
CONCLUSIONS GENERALES.....	253
REFERENCES BIBLIOGRAPHIQUES	261

LISTE DE FIGURES

- Figure 1.** Carte des districts uranifères de Chine montrant la localisation des bassins sédimentaires ainsi que les différents gisements et minéralisations connus (modifié d'après Xingzong and Weixun 1990; Cong 2009; Dahlkamp 2009;). J-T= district du Junggar-Tienshan (JB= bassin de Junggar, KD= depression de Kashi, TB= bassin de Tarim, THB= bassin de Turpan-Hami, YB= bassin de Yili): 1= zone U à la marge Sud du bassin de Yili; 2= zone U zone à la marge Nord du bassin de Yili; 3= Bayanghe (volc); 4= Bashidulak (ss); 5= Shihongtan (ss). Y-L= district de Yinshan-Liaohe (CB= bassin de Chelaomiao, EB= bassin d'Erlan, GB= bassin de Gangou, LB= bassin de Liaohe, OB= bassin d'Ordos): 1= Benxi (metasom); 2= Saima (intr. peralksyenite); 3= Qinglong (ss,volc?); 4= Guyuan-Duolun (volc); 5= Nuheting and Subeng (ss); 6= Bayantala; 7= Chelaomiao; 8= Dongsheng (ss). Q-Q= district de Qilian-Qiling: 1= Hongshiquan (intr. alaskite); 2= Jiling (metasom); 3= Lantian (grt. ve); 4= Chenjiazhang/Danfeng (intr. peg); 5= Wudang Huaiyong (ss); 6= Lu Zong; 7= Ruoergai (C-Si-Pel); 8= Ruoergai (C-Si-Pel/Au associé à l'U). W-Y= district du Yunnan Ouest: 1= Gaoligong, Tengchong-Lianghe et Longchuanjiang; 2= Lincang; BangmaiLincang, Mengwang (ss). S-CH= district du Sud de la Chine.DHE= district de Da Hinggan-Ergun (volc). Volc= volcanic-type; ss= sandstone-type; metasom= metasomatite-type; intr. peg= intrusive pegmatite-type; grt. ve= granite vein-type; C-Si-Pel= pelite-type. 21
- Figure 2.** Carte tectonique simplifiée de l'Asie de l'Est. MTL= Median Tectonic Line; MCT= Main Central Trust (Charles, 2010; Enkin et al., 1992). 30
- Figure 3.** Carte simplifiée du craton de Chine du Nord (CCN; Charles, 2010; Faure et al. 2007). 31
- Figure 4.** Carte de l'anomalie de Bouguer de la Chine (Ma, 1989; Charles, 2010). 33
- Figure 5.** Cartes de la profondeur de la transition lithosphère-asthénosphère marquée par la zone de moindre vitesse (ou LVZ : Low Velocity Zone) pour la Chine (a) et le Craton de Chine du Nord (b), issues de An et Shi (2006) et Chen (2010), respectivement. Les traits noirs correspondent aux coupes présentées en Figure 6 (Chen et al., 2009; Chen, 2010). 34
- Figure 6.** Profils topographiques, de l'anomalie gravimétrique de Bouguer et images migrées des ondes S par fonction récepteur (S-RF), (Chen, 2010). Les lignes noires en tiretés représentent la limite lithosphère-asthénosphère et les blanches la discontinuité de Moho. BBB (Bassin de la Baie de Bohai), LU (Luxi Uplift), TM (Taihang Mountains), LM (Lüliang Mountains), S-S RS (Shaanxi-Shanxi Rift System), YCHTRS (Yinchuan-Hetao Rift System), YM (Yan Mountains). 35
- Figure 7.** Carte de répartition des enclaves présentes en Chine de l'Est (Menzies et al., 1993). Les kimberlites du Paléozoïque ainsi que les basaltes du Cénozoïque associés aux enclaves sont également représentés. 36
- Figure 8.** Graphique $^{187}\text{Os}/^{188}\text{Os} = f(\text{Al}_2\text{O}_3 \text{ roche totale})$, (Charles, 2010) pour les péricidotites des enclaves du Craton de Chine du Nord (Gao et al., 2002; Wu et al., 2003), du Craton de Chine du Sud (Zhi et al., 2001), de Corée du Sud (Lee et Walker., 2006) et des kimberlites du Paléozoïque. Les valeurs pour le MSP (manteau supérieur primitif) sont issues de Meisel et al. (2001), et celles pour les péricidotites abyssales de Snow et Reisberg (1995). 38
- Figure 9.** Carte de localisation des bassins d'âge Mésozoïque de Chine du Nord (Meng, 2003). NCMT= North China Mongolia Tract. 39
- Figure 10.** Profil sismique dans un « sous-bassin » du bassin d'Erlan (Dou and Chang, 2003). Les failles normales contrôlant le dépôt des sédiments du Crétacé sont bien visibles, mettant en avant la structure en demi-graben. 41
- Figure 11.** Carte synthétique de répartition des roches volcaniques de la fin du Mésozoïque en Chine de l'Est (Wu et al., 1982; SMJGRT, 1980; Yarmolyuk and Kovalenko, 2001; Meng, 2003). 42
- Figure 12.** Carte synthétique de répartition des granitoïdes de la fin du Mésozoïque en Asie de l'Est (compilée par Charles, 2010 d'après les données de Zorin, 1999; Wang et al., 1998; Chough et al., 2000; Li, 2000; Wu et al., 2000; Choi et al., 2005; Wu et al., 2005a, 2005b; Ishihara, 2007; Wu et al., 2007). 43

- Figure 13.** Carte synthétique de répartition des dômes métamorphiques extensifs en Asie de l'Est. Modifiée par Charles (2010) d'après Lin et Wang (2006) et complétée d'après Daoudene et al. (2009)..... 46
- Figure 14.** Carte de synthèse des principaux marqueurs présumés de l'extension de la fin du Mésozoïque et du Cénozoïque (Charles, 2010). Données des bassins issues de Traynor et Sladen (1995), Allen(1997), Lee (1999), Ren et al. (2002), Meng (2003), Zhang et al. (2003), Dill et al. (2004), Erdenetsogt et al. (2009). Données des roches volcaniques issues de Li (2000), Kirillova (2003), Meng (2003), Lin et Wang (2006), Wang et al. (2006). Données des granitoïdes issues de GSJ (1992), Wang et al. (1998), Zorin (1999), Chough et al. (2000), Li (2000), Wu et al.(2000), Zhou et Li (2000), Choi et al. (2005), Wu et al. (2005a, b), Zhou et al. (2006), Wu et al. (2007), Wong et al. (2009). Abréviations des dômes extensifs : BU = Buteel-Burgutoy (Mazukabzov et al., 2006; Donskaya et al., 2008); ED = Ereendavaa (Daoudene et al., 2009) ; ER = Ertomiao (Darby, 2003) ; GD = Gudaoling (Charles et al., 2010) ; HG = Hongzhen (Luo et al., 1992); KA = Kalaqin (Han et al., 2001) ; LL = Linglong (Charles et al., 2010); LS =Lushan (Lin et al., 2000); LU = Luotian (Eide et al., 1994; Hacker et al., 1998; Faure et al., 1999); SL = Sud Liaodong (Yin et Nie, 1996; Liu et al., 2005; Lin et Wang, 2006; Lin et al., 2008); XI = Xishan (Lin et Wang, 2006); YA =Yagan- OnchHayrhan (Zheng et al., 1991; Webb et al., 1999); YW = Yiwulüshan (Darby et al., 2004; Lin et Wang, 2006); ZA = Zagan (Donskaya et al., 2008). 47
- Figure 15.** Synthèse des événements géologiques en Asie de l'Est à la fin du Mésozoïque (Charles 2010). Les données sur les bassins sont issues de Ren et al. (2002) et Meng (2003). Les références pour les dômes extensifs sont issues de Yin et Nie (1996); Yang et al. (2007a); Lin et al. (2008); Webb et al. (1999); Davis et al. (2002); Darby et al. (2004); Donskaya et al. (2006). Les données sur l'activité volcanique sont issues de la compilation des âges de Zhang et al. (2008a). Les données sur les pics de plutonisme sont issues de Wu et al. (2005a, 2005b, 2007). Les données sur la déformation crustale sont basées sur cette synthèse des événements. Le mouvement des plaques par rapport au nord est représenté par les flèches noires, et les vitesses de déplacement des plaques Pacifique et Izanagi sont estimées d'après Northrup et al. (1995); Maruyama et al. (1997); Bartolini et Larson (2001); Stepashko (2006). Abréviations des massifs : BA = Badaling ; DA = Dahaituo ; GD = Gudaoling ; GJL = Guojialing ; HYG = Haiyang; LAO = Laohushan; LJ = Luanjiahe; LL = Linglong; PRG = Pinkish-reddish granodiorite; WD = Weideshan; XUE = Xuejiashiliang; YMW = Yinmawanshan. 49
- Figure 16.** Modèle géodynamique de l'évolution de la marge Est-asiatique entre la fin du Jurassique et la fin du Crétacé (Charles, 2010)..... 52
- Figure 17.** Structural map of the Erlian Basin showing the distribution of uranium deposits and oil-bearing depressions (modified after CNNC, unpublished data; Dou et al., 2003; Meng et al., 2003; Wei et al., 2005; Dahlkamp, 2009). U= uranium, BB= Bohai Basin, EB= Erlian Basin, EGB= East Gobi Basin, HB=Hailar Basin, OB= Ordos Basin, SB= Songliao Basin, YB= Yingen Basin, LB= Lake Baikal, MOZ= Mongol-Okhotsk Zone. 59
- Figure 18.** Tectono-stratigraphic log of the Erlian Basin (modified after Gou et al., 1986; Cai et al., 1990; Dou, 1997; Graham et al., 2001; Lin et al., 2001; ICS, 2006; Wang et al., 2006; Sha, 2007; Van Itterbeeck et al., 2007; Li et al., 2011; Scott et al., 2012). J.= Jurassic; U1= Unconformity 1; U2= Unconformity 2..... 61
- Figure 19.** A= Geological map of the central-northern part of the Wulanchabu Sub-basin, Erlian Basin (modified after CNNC, unpublished data). U= Uranium. This map shows (i) the location of the A-B cross-section (Fig.) and (ii) the location of the Nuheting area. B= Cross-section of the Erennaoer Sag (modified after Dahlkamp, 2009). K₁ba= Arshan Formation; K₁bt₁1, K₁bt₁2, K₁bt₁3 and K₁bt₂= Tengge'er Formation; K₁bs= Saihan Formation; K₂e₁= lower member of the Erlian Formation; K₂e₂= upper member of the Erlian Formation; E= Eogene. U1= Unconformity 1; U2= Unconformity 2. C= Topographic map of the Nuheting area showing the location of drill holes DH1 to DH7 (modified after CNNC, unpublished data). DH1= Drill hole 1...to DH7= Drill hole 7..... 64
- Figure 20.** Lithofacies observed in the Erlian Formation. A= coarse-grained oxidized orange sandstone with planar lamination; B= secondary oxidized red fine-grained sandstone with remnant of primary reduction; C= very fine-grained reduced grey sandstone; D= finely laminated sand, silt and mud; E= root network and gypsum-bearing black silty mudstone; F= massive dark grey silty mudstone with minor secondary oxidation along silty pathway; G= black mudstone; H= beige calcareous mudstone. 70

- Figure 21.** Summary log of the Erlian Formation correlating facies architecture, depositional environments and sequence stratigraphy. For lithofacies see facies code in table 1. For architectural elements see symbol definition in table 2. The column to the left shows drill cores from DH4 (Drill hole 4) presenting the most complete and representative stratigraphic recovery of the Erlian Formation. Squares A to H refer to lithofacies photographs presented in figure 20. They show the relative position of the different lithofacies within the stratigraphic column of the Erlian Formation. The black arrow on the top left part indicates the drill core reading direction, from the bottom to the top and from right to left. MFS= Maximum Flooding Surface..... 74
- Figure 22.** Architectural model of the Erlian Formation (modified after Miall, 2010). A= depositional environment for the lower member of the Erlian Formation; B= depositional environment for the upper member of the Erlian Formation. For architectural elements see symbol definition in table 2 77
- Figure 23.** Spores and pollen most commonly observed or presenting an accurate stratigraphic value in palynological assemblages belonging to sedimentary units of the Erlian Basin. 85
- Figure 24.** Tectono-stratigraphic log of the Erlian Basin showing the distribution of the palynological occurrences in sedimentary units of the Erlian Basin (modified after Gou et al., 1986; Cai et al., 1990; Dou, 1997; Graham et al., 2001; Lin et al., 2001; ICS, 2006; Wang et al., 2006; Sha, 2007; Van Itterbeeck et al., 2007; Li et al., 2011; Scott et al., 2012). J.= Jurassic; U1= Unconformity 1; U2= Unconformity 2; In the column Sedimentology the main biostratigraphical ages of the Erlian Formation proposed by authors are represented. Ages based on dinosaur fauna: (a)= Brett-Surman (1979); (b)= Rozhdestvensky (1966, 1977); (c)= Weishampel and Horner (1986); and ages based on charophytes and ostracods: (d)= Van Itterbeeck et al. (2005). 88
- Figure 25.** Présentation des concentrations moyennes normalisées au manteau primitif des éléments chimiques dans la croûte continentale en comparaison avec les valeurs pour les MORB* (modifiée d'après Hofmann, 1988). *Les MORB qui dérivent actuellement d'un manteau appauvri sont plus pauvres relativement dans les éléments les plus incompatibles car ils ont déjà été extrait en partie par une fusion antérieur du manteau responsable de l'appauvrissement. 97
- Figure 26.** Cycle de l'uranium dans les différents contextes de gisements en relation avec les principaux processus de fractionnement au cours d'un cycle géologique (Cuney, 2009). Les réservoirs représentés sont le manteau et la croûte continentale. Les types de gisements sont les caractères rouges gras ; les mécanismes métallogéniques sont en caractères noirs gras. KCa = magma Calco-alcalin potassique ; Pak = magma Peralcalin ; Pal = magma Peralumineux. 98
- Figure 27.** Structural map of the Erlian Basin showing the distribution of different types of uranium deposits and oil-bearing depressions (modified after CNNC, unpublished data; Dou et al., 1998; Meng, 2003; Wei et al., 2005; Dahlkamp, 2009; Bonnetti et al., accepted). U= uranium, BB= Bohai Basin, EB= Erlian Basin, EGB= East Gobi Basin, HB=Hailar Basin, OB= Ordos Basin, SB= Songliao Basin, YB= Yingen Basin, LB= Baikal Lake, MOZ= Mongol-Okhotsk Zone..... 108
- Figure 28.** Geological map of the study areas showing the the sample location and indicating ages, U content and Th/U value per sample when it has been analysed (modified after CNNC, unpublished data). A= geological map of the central part of the Wulanchabu Sub-basin; B= geological map of the western part of the Manite Sub-basin..... 110
- Figure 29.** Major and accessory minerals occurring in biotite granite of the basement surrounding the northern part of the Erlian Basin. A= biotite (Bt) and Chlorite (Chl); B= amphibole (Amp); C= Titanite (Ttn); D= Zircon (Zrn) and apatite (Ap); E= metamict U-thorite showing a destruction halo associated with pyrite (Py), REE carbonate and uranium oxide; F= metamict allanite (Aln) associated with REE carbonate; G= metamict allanite showing a destruction halo associated with secondary epidote (Ep), secondary monazite (Mnz) and fe oxide; H= Fe-Ti oxide. 114
- Figure 30.** Major and accessory minerals occurring in two-mica granite of the northern part of the Sunite Horst. A= biotite (Bt) associated with muscovite (Ms); B= monazite (Mnz); C= xenotime (Xtm); D= secondary quartz and muscovite in greisenized part of the two-mica granite. 116
- Figure 31.** Volcanic rocks occurring at the bottom of the Wulanchabu Sub-basin and in part of the Bayinbaolige Horst located at the northern margin of the Manite Sub-basin. Macroscopic and microscopic illustrations are given for each rock-type. A= dacite (E13); B= dacite texture showing quartz, feldspar and epidote

crystals enclosed in microlith; C= trachyte (E06); D= trachyte texture showing finely crystallized quartz and feldspar; E= rhyolite (E05); F= rhyolite texture showing quartz and feldspar crystals enclosed in microlith.	118
Figure 32. Q-P diagram showing the relative proportions of quartz, K-feldspar and plagioclase in the igneous rocks of the Erlian area (modified after Debon and Lefort, 1983, 1988). Q= chemical-mineralogical parameter (in millications) P= chemical-mineralogical parameter (in millications) estimating the relative proportions of K-feldspar (positive) and plagioclase (negative).	121
Figure 33. A-B diagram indicating the peraluminosity (A parameter) and the correlation (B parameter) of igneous rocks occurring in the basement of the Erlian basin (modified after Debon and Lefort, 1983, 1988). A= chemical-mineralogical parameter (in millications) giving the excess of alumina not bound to the feldspars; B= chemical-mineralogical parameter (in millications) used as a differentiation index for igneous rocks.	122
Figure 34. Cathodoluminescence microphotographs of zircon grains analysed for U-Pb isotopic determinations, for each sample. The white circles indicate the spots of the isotopic analyses presented in table 7.....	123
Figure 35. Results of the ion-probe dating of the zircons from biotite granites and volcanic rocks occurring in the northern margins of the Wulanchabu and the Manite sub-basins. The results are represented in concordia and weighted average diagrams. A= E01; B= ZK152; C= E07; D= E08; E= E09; F= E05; G= E14 and H= E11.....	126
Figure 36. U, Th and Pb element mapping realized by EMP and U-Th-Pb isochron age for monazites from the two-mica granite occurring in the northern part of the Sunite Horst. A= U distribution; B= Th distribution; C= Pb distribution; D= Th/Pb vs U/Pb plot (ellipse errors are 2σ).	127
Figure 37. Plots of average weighted ages using individual ages and errors (2σ) for each representative grain of monazite. A= Hercynian monazite; B= Indosinian monazite; C= Yanshanian monazite; D= Cretaceous monazite. Black lines on photographs correspond to EMP profiles of analysis realized on monazite grains.	131
Figure 38. $\epsilon_{Nd(t)}$ evolution diagram for igneous rocks occurring at the northern margins of the Wulanchabu and Manite sub-basins. The depleted mantle (DM) model is from De Paolo (1988).	134
Figure 39. Th vs U diagram showing the magmatic fractionation trend and the trend of U leaching for Hercynian and Indosinian igneous rocks.	135
Figure 40. EMP profile of analysis on U-thorite from preserved Indosinian biotite granite showing U release into the rock due to metamictisation.	136
Figure 41. Evolution of U and Th contents, Th/U ratios and the degree of leaching for major U-bearing minerals according to depth of drill hole ZK.	137
Figure 42. Discrimination diagrams for Hercynian and Indosinian igneous rocks occurring in the basement of the Wulanchabu and Manite sub-basins. A= the Rb-(Yb+Nb) discrimination diagram for Hercynian and Indosinian granites (modified after Pearce et al., 1984) showing the fields of syn-collisional granites (syn-COLG), within-plate granites (WPG), volcanic-arc granites (VAG) and ocean-ridge granites (ORG); B= the Rb-(Yb+Ta) discrimination diagrams for Hercynian and Indosinian granites (modified after Pearce et al., 1984) showing the fields of syn-collisional granites (syn-COLG), within-plate granites (WPG), volcanic-arc granites (VAG) and ocean-ridge granites (ORG); C= the Th/Yb-Ta/Yb discrimination diagram for Hercynian and Indosinian igneous rocks (modified after Pearce, 1982). Vectors indicate the influence of subduction (S), crustal contamination (C), within-plate enrichment (W) and fractional crystallisation (F). Dashed lines separate the boundaries of the tholeiitic (TH), calcalkaline (CA), and high-K calcalkaline (K-CA) field. Active continental margin and oceanic island arc fields modified after Schulz et al. (2004)....	139
Figure 43. Geodynamic evolution model for the eastern part of the CAOB, placing emphasis on the two successive micro-continents accretion during the late Carboniferous-Permian and the early-middle Triassic, and integrating U enrichment through time until the formation of the deposits hosted in the Erlian Basin. A= model cross section of the oceanic subduction and the block accretion during the late Carboniferous-Permian (modified after Lin et al., 2008); B= model cross section of the continental subduction and the block accretion during the early-middle Triassic (modified after Lin et al., 2008); C= Tectonic map of northeast China (modified after Lin et al., 2008); D= Evolution diagram of geological event related to U enrichment through time in northeast China.	143

Figure 44. Coupe schématique montrant la distribution des principaux types de gisement d'uranium encaissés dans les grès ainsi que la distribution des grès réduits et oxydés (modifié d'après Cuney et Kyser, 2008).	156
Figure 45. Coupe schématique d'un gisement de type roll montrant les zonations minéralogiques classiques de ce type de minéralisation (Devoto, 1978).....	159
Figure 46. Coupe schématique du modèle de gisement roll front d'Adams et Smith (1981) impliquant la migration secondaire d'hydrocarbures le long des failles recouvrant les réservoirs gréseux qui encaissent la minéralisation.....	160
Figure 47. Structural map of the Erlian Basin showing the distribution of different types of uranium deposits and oil-bearing depressions (modified after Bonnelli et al., accepted; CNNC, unpublished data; Dahlkamp, 2009; Dou et al., 1998; Meng, 2003; Wei et al., 2005). U= uranium, BB= Bohai Basin, EB= Erlian Basin, EGB= East Gobi Basin, HB= Hailar Basin, OB= Ordos Basin, SB= Songliao Basin, YB= Yingtan Basin, LB= Lake Baikal, MOZ= Mongol-Okhotsk Zone.....	166
Figure 48. A= geological map of the central-northern part of the Wulanchabu Sub-basin, Erlian Basin (after CNNC, unpublished data). Fm= formation; U= uranium. This map shows the location of A-B cross-section (Fig. 48B) and the location of the Nuheting area (Fig. 48C). B= cross-section of the Erennaoer Sag (after Dahlkamp, 2009). K ₁ ba= Arshan Formation; K ₁ bt ₁ , K ₁ bt ₂ , K ₁ bt ₃ and K ₁ bt ₂ = Tengge'er Formation; K ₁ bs= Saihan Formation; K ₂ e ₁ = lower member of the Erlian Formation; K ₂ e ₂ = upper member of the Erlian Formation; E= Eocene. C= topographic map of the Nuheting area showing the location of drill holes DH1 to DH5 (after CNNC, unpublished data).....	169
Figure 49. Sedimentological log of the Erlian Formation correlated to the geochemical profile of DH2 showing the evolution of uranium, organic carbon and total sulfur (modified after Bonnelli et al., accepted). Black squares A and B show the location in the log of the main host-facies presented in figure 50. Dep. Env.= depositional environment; < mbr = lower member; > mbr = upper member.	172
Figure 50. Main lithofacies hosting the uranium mineralization of the Nuheting deposit. A= root network and gypsum-bearing black mudstone of swamp; B= massive dark grey silty mudstone of floodplain pond with secondary oxidation along silt-dominant beds.	173
Figure 51. Main detrital minerals of the host-rock. A= lithic grain; B= plagioclase (Pl); C= chlorite (Chl); D= epidote (Ep); E= monazite (Mnz); F= Fe/Ti oxide; G= zircon (Zrn); H= titanite (Ttn).	175
Figure 52. Structured elements of organic matter occurring in the host-rock of the Nuheting deposit. A= coal fragment; B= megaspore; C= Tasmanaceae-type algae; D= Thrombolite-type microbial structure. Qz= quartz.....	178
Figure 53. HI vs OI diagram showing the typology of organic matter of overbank deposits occurring in the Erlian Formation (modified after Herbin and Deroo, 1979; Demaison et al., 1983).....	180
Figure 54. Characterization of synsedimentary uranium concentration in the host-rock of the Nuheting deposit. A= uranium-rich clayey matrix of silty mudstone, location of EMP data-points; B= uranium-rich clayey matrix; C= UO ₂ nanocrystals within very fine gypsum crystals; D= celestite (Clt).....	181
Figure 55. Diagenetic uranium mineralization distribution in mineralized samples of the Nuheting deposit. A= RX-tomography 3D imagery showing the distribution of high-density minerals; B= uranium mineralization along secondary induced fracture; C= uranium mineralization along pyrite and organic matter-rich level; D= uranium mineralization disseminated in the host-rock. Coff.= coffinite; Py= pyrite; Qz= quartz.	182
Figure 56. Location of ICPMS ablation spots on the different populations of pyrite. A= pyritized organic matter; B= pyrite cement; C= pyrite cement; D, E, F and G= idiomorphic pyrite. Cb= carbonate; Clt= celestite; Coff.= coffinite; Py= pyrite; Qz= quartz.	184
Figure 57. Se, V, Mo diagram permitting the characterization of two populations of pyrite. The Se-rich group represents pyrite cement and idiomorphic pyrite; the Mo-rich group represents pyrite replacing organic matter. Py= pyrite.	186
Figure 58. Uranium mineralization from the Nuheting deposit. A= organic matter fragment replaced by coffinite; B= pyritized organic matter fragment replaced by coffinite; C= coffinite at the edge of the pyrite cement; D= coffinite epigeny of a sub-idiomorphic pyrite crystal; E= coffinite replacing pyritized thrombolite-type microbial structure and botyoidal coffinite deposited at the margin of a quartz grain with evidence of quartz corrosion; F= coffinite replacing pyritized thrombolite-type microbial structure; G=	

- coffinite replacing a pyritized gypsum crystal; H= coffinite replacing a pyritized celestite crystal. OM= organic matter; Coff.= coffinite; Py= pyrite; Qz= quartz; Gp= gypsum; Clt= celestite. 188
- Figure 59.** Late cementation of uranium mineralization in the Nuheting deposit. A= sulfate and carbonate cement; B= cementation of the uranium mineralization. Clt= celestite; Qz= quartz; U= uranium. 190
- Figure 60.** Drill hole cross-section of the Nuheting deposit. The cross-section C-D is located in figure 2C. K₂e₁= lower member of the Erlian Formation; K₂e₂= upper member of the Erlian Formation; s= silt; vgc= very coarse grain. 191
- Figure 61.** Mineral succession diagram of the different stages related to uranium mineralization of the Nuheting deposit. 195
- Figure 62.** Schematic genetic model of the Nuheting deposit representing the synsedimentary uranium concentration during the deposition of sediments belonging to the Erlian Formation and the diagenetic uranium remobilization. 196
- Figure 63.** Structural map of the Erlian Basin showing the distribution of different types of uranium deposits and oil-bearing depressions (modified after CNNC, unpublished data; Dou et al., 1998; Meng, 2003; Wei et al., 2005; Dahlkamp, 2009; Bonnetti et al., accepted). U= uranium, BB= Bohai Basin, EB= Erlian Basin, EGB= East Gobi Basin, HB=Hailar Basin, OB= Ordos Basin, SB= Songliao Basin, YB= Yingen Basin, LB= Baikal Lake, MOZ= Mongol-Okhotsk Zone. 209
- Figure 64.** A= geological map of the western part of the Manite Sub-basin, Erlian Basin (after CNNC, unpublished data). This map shows the location of studied drill-holes (DH) and the position of the cross-section presented in figure 2.B, from DH1 to DH3. B= drill-hole cross-section of the Bayinwula deposit. S=silt; vgc= very coarse grained sand. 211
- Figure 65.** Sedimentological log of the upper member of the Saihan Formation with the location of roll front-type uranium mineralization. This detailed log is located on the inserted global tectonic-stratigraphic log of the Erlian Basin (modified after Gou et al., 1986; Cai et al., 1990; Dou et al., 1998; Graham et al., 2001; Lin et al., 2001; Meng, 2003; ICS, 2006; Sha, 2007). C= coal; M= mud; S= silt; VFS= very fine sand; FS= fine sand; MS= medium sand; CS= coarse sand; VCS= very coarse sand. 214
- Figure 66.** U-bearing minerals occurring in the host sandstone. A= monazite (Mnz); B= zircon Zrc); C= weakly altered Fe-Ti oxide in the reduced sandstone with EMP analysis profile below; D= strongly altered Fe-Ti oxide in the reduced sandstone with EMP analysis profile below. Black circles in C and D correspond to Raman analyses spots. 217
- Figure 67.** EMP analyses realized on Fe-Ti oxides from the reduced host sandstone and the pyrite zone of the Bayinwula deposit. A= FeO vs TiO₂ diagram showing pre-ore Fe-Ti oxides alteration trend; B= UO₂ vs FeO diagram showing pre-ore uranium concentration on Fe-Ti oxides and uranium over concentration related to ore-stage sulphidization. 219
- Figure 68.** Structured elements of organic matter occurring in the host sandstone of the Bayinwula deposit. A= Phytoclast; B= Coal fragment; C= Fine coal debris; D= Tasmacae-type algae. 222
- Figure 69.** HI vs OI diagram showing the typology of organic matter occurring in the host sandstone of the Bayinwula deposit (modified after Herbin and Deroo, 1979; Demaison et al., 1983). 224
- Figure 70.** Ore-stage iron disulphides in epigeny of organic matter fragments and Fe-Ti oxides. A and B= iron disulphide in epigeny of organic matter; C and D= iron disulphide in epigeny of Fe-Ti oxide. FeS₂ (1)= frambooidal population; FeS₂ (2)= collomorph population; FeS₂ (3)= cement to sub-idiomorphic population. E= non-epigenized Fe-Ti oxide; F= Fe-Ti oxide epigenized into FeS₂. Black circles and numbers indicate EMP uranium concentration in wt.% UO₂. 225
- Figure 71.** Representative iron disulphide populations occurring in the host sandstone of the Bayinwula deposit. Black circles indicate the location of ICPMS ablation spots realized for trace element measurement. White circles indicate the location of SIMS spots realized for stable isotopes analysis. A= preore-stage sub-idiomorphic iron FeS₂; B to J= ore-stage FeS₂ populations located in the “wings” of the roll; K and L= ore-stage FeS₂ populations located in the “nose” of the roll. 227
- Figure 72.** As vs Ni diagram showing the trace element concentrations decrease from frambooidal iron disulphides (FeS₂ (1)) to sub-idiomorphic iron disulphides (FeS₂ (3)). FeS₂ (1)= frambooidal; FeS₂ (2)= collomorph; FeS₂ (3)= sub-idiomorphic. 229

- Figure 73.** Sulphur stable isotopes signature of ore-stage iron disulphides. FeS₂ (1) + (2)= frambooidal + collomorph iron disulphide; FeS₂ (3)= sub-idiomorphic iron disulphide..... 230
- Figure 74.** PHREEQC model of ilmenite solubility as a function of pH, under anoxic conditions. Two conditions are selected: (i) H₂S free system, and (ii) in the presence of 10 bar H₂S partial pressure..... 231
- Figure 75.** Uranium mineralization of the Bayinwula deposit. A= ningyoite epigeny of FeS₂ associated with organic matter; B= Ningyoite associated with organic matter; C= ningyoite epigeny of FeS₂ associated with organic matter; D= ningyoite epigeny of frambooidal FeS₂; E and F= coffinite epigeny of sub-idiomorphic FeS₂. 233
- Figure 76.** Metallogenetic model of the Bayinwula roll front deposit. A= drill hole cross-section of the Bayinwula deposit in correlation with geochemical zoning. B= mineral alteration and U remobilization in the oxidized zone; C= uranium mineralization associated with iron disulphide and organic matter in the ore zone; D= ore stage iron disulphides in epigeny of Fe-Ti oxide and organic matter related to BSR occurring in the pyrite zone (or BSR zone); E= Fe-Ti oxides and organic matter in the reduced host sandstone..... 241

LISTE DES TABLES

Table 1. Lithofacies identified within the Erlian Formation (using the classification of Miall, 2010).....	71
Table 2. Architectural elements identified within the Erlian Formation (using the classification of Miall, 2010).	73
Table 3. Composition of the palynological assemblage observed in sedimentary units of the Erlian Basin. Proportion Sub-classes (in %) were determined over the total amount of palynomorphs counted.	84
Table 4. Representative EMP analyses of major and accessory minerals occurring in biotite granites of the basement surrounding the northern part of the Erlian Basin.	115
Table 5. Representative EMP analyses of monazite and xenotime occurring in the two-mica granite located in the northern part of the Sunite Horst.	117
Table 6. Incompatible trace element ratios for igneous rocks occurring in the basement of the Wulanchabu and Manite sub-basins.....	120
Table 7. Analytical results of the U/Pb ion-microprobe determinations on zircons from biotite granites and volcanic rocks occurring in the northern margins of the Wulanchabu and the Manite sub-basins. Lead isotope ratios are corrected for common lead (using ²⁰⁴ Pb count rates) and U/Pb ratios are calculated using the correlation line of the standards.....	125
Table 8. Representative analytical data for monazite from the two-mica granite (E10). Th*= the amount of apparent Th.....	128
Table 9. Representative EMP analyses of monazite grains from sandstones of the Saihan and Erlian formations occurring in the Erlian Basin.....	130
Table 10. Analytical data for monazite grains from sandstones of the Erlian Basin. Th*= the amount of apparent Th.	132
Table 11. Whole rock Nd isotopic data for samples from biotite granite (γ), two-mica granite (γ) and volcanic rocks occurring at the northern margins of the Wulanchabu and Manite sub-basins. $^{143}\text{Nd}/^{144}\text{Nd}_i$ initial and $\varepsilon_{\text{Nd}_{(t)}}$ was calculated using the equation Michard et al., 1985).....	133
Table 12. Representative EMP analysis of monazites occurring in the host-rock of the Nuheting deposit.	176
Table 13. Representative EMP analysis of Fe/Ti oxides occurring in the host-rock of the Nuheting deposit....	177
Table 14. Rock-Eval pyrolysis (REP) results from overbank deposit samples of the Erlian Formation (using REP interpretation methods Espitalie et al., 1985).	181
Table 15. Trace element composition of idiomorphic pyrite and pyrite cement. DH= Drill hole, Loc.= location; Tot.= total.	189
Table 16. Trace elements composition of frambooidal pyrite in epigeny of organic matter. DH= Drill hole, Loc.= location; Tot.= total.	190
Table 17. Representative EMP analyses on uranium minerals from the Nuheting deposit.....	194
Table 18. Representative EMP analyses on Fe-Ti oxide from the Bayinwula deposit.....	225
Table 19. Rock-Eval pyrolysis (REP) results from sandstone of the Saihan Formation hosting the Bayinwula deposit (using REP interpretation methods of Espitalié et al., 1985).	228
Table 20. Representative trace element concentrations of the different populations of iron disulphide occurring in the host sandstone of the Bayinwula deposit.....	233
Table 21. Representative EMP analyses of uranium mineralization from the Bayinwula deposit.....	239

LISTE DES ANNEXES

Appendix 1. Classification diagram for granites from the basement of the Erlian Basin (modified after Cox et al, 1979)	146
Appendix 2. Classification diagram for volcanic rocks from the basement of the Erlian Basin	146
Appendix 3. Major and trace elements whole-rock geochemical data for granites and volcanic rocks from the basement of the Erlian Basin.....	147
Appendix 4. REE whole-rock geochemical data for granites and volcanic rocks from the basement of the Erlian Basin.....	148
Appendix 5. Spider diagrams and REE patterns for granites and volcanic rocks form the basement of the Erlian Basin.....	149
Appendix 6. Q-A diagram showing petrographic composition of sandstones, siltstones and mudstones from the Erlian Formation, in the Nuheting area. This diagram shows a carbonatation trend for part of samples from the Nuheting area	198
Appendix 7. Na+K / Al-(Na+K))/2 / (Mg+Mn+Fe)/3 diagram showing the typology of clay minerals occurring in sandstones, siltstones and mudstones from the Erlian Formation, in the Nuheting area.....	198
Appendix 8. XR spectra showing the clay minerals assemblage from the host-rock of the Nuheting deposit .	199
Appendix 9. Major elements whole-rock geochemical data for drill cores of the Nuheting deposit (in %).	200
Appendix 10. RE elements whole-rock geochemical data for drill cores of the Nuheting deposit (in ppm).	200
Appendix 11. Trace elements whole-rock geochemical data for drill cores of the Nuheting deposit (in ppm). 201	201
Appendix 12 Trace elements whole-rock geochemical data for drill cores of the Nuheting deposit (in ppm). 201	201
Appendix 13. Whole-rock geochemistry of stratigraphic drill-core samples from the Bayinwula area. Major elements (in %), organic carbon (Corg, in %) and total sulphur (Stot, in %).....	244
Appendix 14. Whole-rock geochemistry of drill-core samples from the Bayinwula deposit. Major elements (in %), organic carbon (Corg, in %) and total sulphur (Stot, in %)	245
Appendix 15. Whole-rock geochemistry of stratigraphic drill-core samples from the Bayinwula area. Trace elements (in ppm).....	246
Appendix 16. Whole-rock geochemistry of drill-core samples from the Bayinwula deposit. Trace elements (in ppm).	247
Appendix 17. Q-A diagram showing the relative abundance between quartz, feldspar and clay minerals in sandstone of the Saihan Formation.....	248
Appendix 18. Na+K / Al-(Na+K))/2 / (Mg+Mn+Fe)/3 diagram showing the typology of clay minerals occurring in sandstone of the Saihan Formation.	249
Appendix 19. X-ray diffractograms of sandstone hosting the Bayinwula deposit from the oxidized to the reduced zone.	250
Appendix 20 .A= representative Raman spectra from relatively preserved Fe-Ti oxides. B= Reference spectrum of ilmenite from RRUFF database.	251
Appendix 21. A= representative Raman spectra from altered Fe-Ti oxides. B= Reference spectrum of anatase from RRUFF database. C= reference spectrum of hematite from RRUFF database.....	252

INTRODUCTION GENERALE



1. Introduction et problématique

L’Asie centrale constitue un vaste domaine continental issu de l’acréation successive de blocs continentaux de l’Archéen jusqu’à l’actuel. La ceinture orogénique centre asiatique (COCA) d’âge Paléozoïque, qui s’étend du Kazakhstan à l’océan Pacifique, représente un socle sur lequel reposent de nombreux bassins sédimentaires, pour la plupart de type intracontinentaux, et dont les sédiments généralement continentaux sont riches en matière organique. Le nombre important de gisements d’uranium découvert dans les bassins mésozoïques de cette région (Transbaïkalie, Kazakhstan, Ouzbékistan, Mongolie, Chine du Nord), suggère des processus génétiques qui se sont développés à l’échelle de la province orogénique qui représente également une province métallogénique. Par comparaison avec les autres provinces métallogéniques uranifères majeures du monde (Canada, Australie, Afrique) qui sont en relation avec des socles archéens à protérozoïques, il est possible à partir de l’exemple choisi pour cette étude, le bassin d’Erlian, d’aborder les conditions de genèse d’une province uranifère très jeune.

Ainsi, il convient de s’interroger sur la provenance ultime de cet uranium, de même que sur les processus géologiques et les conditions physico-chimiques impliqués dans sa concentration sous forme de gisements. La grande majorité de ces gisements sont encaissés dans des réservoirs gréseux perméables et réduits, et présente des morphologies de type « roll front » ou tabulaire. Plusieurs modèles métallogéniques ont été proposés pour ces gisements, certains font état de relations avec la matière organique continentale, d’autres proposent la migration secondaire d’hydrocarbures pour expliquer la réduction de l’uranium, et enfin certains modèles impliquent des processus biogéniques. Cependant, les sources primaires de ces minéralisations ne sont que peu décrites et l’évolution tectono-sédimentaire de ces bassins mésozoïques, à l’origine de la formation des réservoirs perméables encaissant la minéralisation uranifère, reste à préciser.

Le Nord de la Chine constitue la partie Sud-Est de la province métallogénique d’Asie centrale et contient deux des cinq districts uranifères identifiés sur le territoire chinois (**Figure 1**): le district du Junggar-Tienshan situé au Nord-Ouest et le district du Yinshan-Liaohe situé au Nord-Est de la Chine.

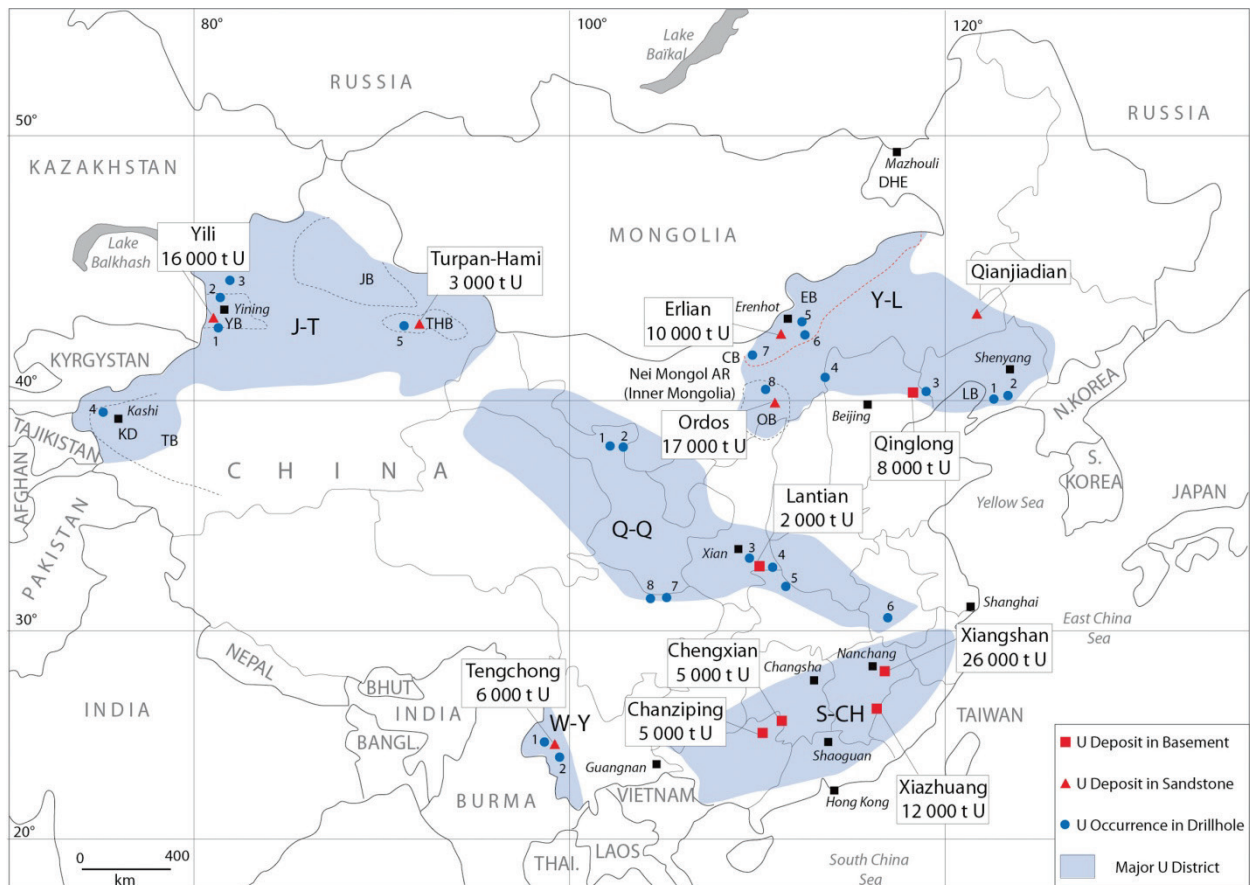


Figure 1. Carte des districts uranifères de Chine montrant la localisation des bassins sédimentaires ainsi que les différents gisements et minéralisations connus (modifié d'après Xingzong and Weixun 1990; Cong 2009; Dahlkamp 2009;). J-T= district du Junggar-Tienshan (JB= bassin de Junggar, KD= depression de Kashi, TB= bassin de Tarim, THB= bassin de Turpan-Hami, YB= bassin de Yili): 1= zone U à la marge Sud du bassin de Yili; 2= zone U zone à la marge Nord du bassin de Yili; 3= Bayanghe (volc); 4= Bashidulak (ss); 5= Shihongtan (ss). Y-L= district de Yinshan-Liaohe (CB= bassin de Chelaomiao, EB= bassin d'Erlian, GB= bassin de Gangou, LB= bassin de Liaohe, OB= bassin d'Ordos): 1= Benxi (metasom); 2= Saima (intr. peralksyenite); 3= Qinglong (ss,volc?); 4= Guyuan-Duolun (volc); 5= Nuheting and Subeng (ss); 6= Bayantala; 7= Chelaomiao; 8= Dongsheng (ss). Q-Q= district de Qilian-Qiling: 1= Hongshiquan (intr. alaskite); 2= Jiling (metasom); 3= Lantian (grt. ve); 4= Chenjiazhang/Danfeng (intr. peg); 5= Wudang Huaiyong (ss); 6= Lu Zong; 7= Ruoguai (C-Si-Pel); 8= Ruoguai (C-Si-Pel/Au associé à l'U). W-Y= district du Yunnan Ouest: 1= Gaoligong, Tengchong-Lianghe et Longchuanjiang; 2= Lincang; BangmaiLincang, Mengwang (ss). S-CH= district du Sud de la Chine.DHE= district de Da Hinggan-Ergun (volc). Volc= volcanic-type; ss= sandstone-type; metasom="metasomatite-type"; intr. peg= intrusive pegmatite-type; grt. ve= granite vein-type; C-Si-Pel= pelite-type.

De nombreux gisements d'uranium de type grès sont encaissés dans les bassins d'âge Mésozoïque du Nord de la Chine: les gisements de Wuyier, Wuyiyi, Wuyisan et Shihongtan dans le bassin de Yilli (Min et al., 2005a; 2005b); les gisements de la zone de Dongsheng dans le bassin d'Ordos (Cai et al., 2007a; 2007b); les gisements de Saihangobi et Bayinwula dans le bassin d'Erlian (Bo et Kuan , 2006; Nie et al., 2007; Fan et al., 2008; Zhang et al., 2008; 2010) et enfin quelques minéralisations encaissées dans le bassin du Kailu, dans la partie Ouest du bassin de Songliao (Cai et Li, 2008). Ce type de gisement uranifère correspond actuellement aux ressources d'uranium les plus économiques grâce à la possibilité d'utiliser des techniques d'extraction *in situ* (ISR) peu coûteuses. Par conséquent, la compréhension des processus de genèse de ces minéralisations constitue à la fois un défit scientifique et économique.

En l'état actuel des connaissances sur ces gisements, de nombreuses interrogations subsistent quant aux conditions physico-chimiques liées à leur minéralisation. Deux modèles ont été proposés pour les gisements de type « roll front » (Reynolds et al., 1982): (i) le modèle chimique et (ii) le modèle biogénique.

- (i) Dans le cas d'un modèle chimique classique (Devoto, 1978), les eaux météoriques oxydantes s'infiltrent dans les réservoirs gréseux réduits du bassin, l'uranium est lessivé et transporté sous forme U (VI), puis déposé de manière incrémentale au front d'oxydo-réduction. La précipitation de l'uranium se fait ici grâce à des processus chimiques, en relation avec la matière organique détritique contenue dans les grès ou en réaction avec des minéraux sulfurés comme la pyrite.
- (ii) Dans le cas d'un modèle biogénique (Jensen, 1958; Lizitsyn et Kuznetsova, 1967; Belyi et al., 1972; Rackley, 1972), les bactéries sulfato-réductrices sont responsables de la formation des sulfures de fer ainsi que de la production de H₂S qui peut être impliqué dans la réduction de l'uranium. Dans certains cas, la précipitation de l'uranium peut être co-génétique de la sulfato-réduction bactérienne (Cai et al., 2007a).
- (iii) Un troisième modèle a été proposé par Adams et Smith (1981), avec la migration secondaire d'hydrocarbures dans les réservoirs gréseux comme agent réducteur pour la minéralisation uranifère.

L'étude géologique du bassin d'Erlian et des minéralisations uranifères qui y sont associées permet ainsi d'aborder différentes problématiques relatives à la genèse des gisements de type « roll front » :

- (i) Le socle sur lequel reposent les bassins sédimentaires d'âge Mésozoïque encaissant la plupart des gisements d'uranium de la province centre asiatique s'est formé principalement au Paléozoïque, au cours de l'accrétion du craton sibérien et du craton de Chine du Nord ainsi que de plusieurs autres microcontinents. Plusieurs orogenèses se sont également succédées (indosinienne et yanshanienne) avant l'épisode d'extension continentale de la fin du Mésozoïque qui est à l'origine de l'ouverture des bassins. L'ensemble de ces épisodes géodynamiques ont été associés à du magmatisme dont les roches plutoniques et volcaniques sont relativement bien représentées dans la CACO. Cependant, ces roches sont-elles toutes enrichies en uranium ? Le cadre géodynamique de chacun de ces épisodes permet-il d'expliquer cet enrichissement ?
- (ii) La majorité des bassins sédimentaires du Nord de Chine encaissant les minéralisations uranifères se sont développés en domaine intracontinental. Les gisements de type « roll front » sont hébergés dans les réservoirs gréseux perméables de ces bassins. Les conditions tectono-sédimentaires contrôlant le développement de ces bassins permettent-elles d'expliquer la genèse de ces réservoirs gréseux confinés ? L'évolution stratigraphique de ces bassins montre-t-elle des points communs ?
- (iii) Les sédiments de ces bassins contiennent de la matière organique en relative abondance. Cette matière organique est elle uniquement d'origine détritique ? Quelle est l'importance des pré-concentrations syn-sédimentaires associées à la matière organique ou en adsorption sur les minéraux argileux ?
- (iv) Les minéralisations de type « roll front » encaissées dans ces bassins correspondent à l'aboutissement des processus de concentration de l'uranium depuis sa source primaire. Ces gisements se trouvent dans des réservoirs gréseux réduits, riches en matière organique et en pyrite. Les conditions de dépôt de la minéralisation sont-elles essentiellement chimiques ou biogéniques ? De plus, ces bassins sont également connus pour leurs ressources pétrolières. Des migrations d'hydrocarbures se sont-elles produites et si oui, jouent-elles un rôle dans la précipitation de l'uranium ? Enfin, ces gisements sont-ils tous de même type et présentent-ils des modes de genèse comparables ?

2. Objectifs de la thèse

L'intérêt scientifique de cette étude est de traiter l'ensemble du cycle de l'uranium à l'échelle du bassin d'Erlian, depuis sa source primaire dans les roches magmatiques du socle jusqu'à son dépôt sous forme de gisements de type « roll front ».

Afin de réaliser ces travaux, une approche multi-disciplinaire combinant modèle de faciès sédimentaires, pétrographie, minéralogie, géochimie élémentaire, géochronologie et géochimie isotopique a été menée. Plus spécifiquement, cette approche fut appliquée pour:

- (i) Caractériser les sources primaires de l'uranium présent dans le bassin d'Erlian par l'étude des granites et des roches volcaniques qui se sont mises en place depuis le Paléozoïque jusqu'à l'ouverture du bassin. Identifier les contextes géodynamiques respectifs afin de discuter des processus d'enrichissement en uranium.
- (ii) Préciser la dynamique sédimentaire du bassin d'Erlian et en particulier son rôle dans la genèse des réservoirs gréseux perméables permettant de générer les pièges pour les minéralisations uranifères.
- (iii) Identifier et caractériser d'éventuelles pré-concentrations syn-sédimentaires associées à la matière organique et/ou en adsorption sur les minéraux argileux des faciès sédimentaires fins.
- (iv) Déterminer les conditions physico-chimiques du dépôt de l'uranium par une étude détaillée des minéralisations du bassin. Caractériser le rôle de la matière organique. Comparer et discuter le modèle observé dans le bassin d'Erlian aux autres gisements de la province.

Cette thèse s'inscrit dans les programmes de recherche du laboratoire GeoRessources sur la genèse des ressources minérales, ainsi que dans le cadre de la thématique R&D d'Areva « Signature des périodes fertiles pour l'uranium » et d'une collaboration étroite entre les équipes de recherche du laboratoire GeoRessources (Nancy), de l'East China Institute of Technology, et des équipes d'exploration du China National Nuclear Corporation (CNNC).

3. Organisation du manuscrit

L'essentiel de ce travail de réflexion porte sur la zone Nord du bassin d'Erlan, plus particulièrement dans les sous-bassins de Wulanchabu et de Manite. Ce manuscrit de thèse est organisé en trois grandes parties, comprenant chacune différents chapitres.

La première partie (partie A) du manuscrit porte sur la mise en place des bassins sédimentaires au Mésozoïque qui encaissent les minéralisations uranifères. Cette partie couple deux chapitres (chapitres 1 & 2). Le chapitre 1 présente (i) les différents objets géologiques qui témoignent de l'extension continentale au Mésozoïque, en Asie de l'Est et (ii) le modèle géodynamique de cette extension. Le chapitre 2 est un article accepté pour publication dans le journal *Cretaceous Research*. Il présente le modèle de faciès sédimentaire de la formation d'Erlan ainsi que son calage biostratigraphique et permet de discuter de l'évolution stratigraphique des sédiments post-rifts et son rôle dans la formation des réservoirs perméables qui constituent les pièges pour la minéralisation.

La seconde partie (partie B) de ce manuscrit s'intéresse plus particulièrement aux sources primaires de l'uranium dans l'environnement du bassin d'Erlan. Cette partie s'articule également en deux chapitres (chapitres 3 & 4). Le chapitre 3 présente les concentrations en uranium dans la croûte continentale ainsi que les processus liés à son enrichissement. Le chapitre 4 correspond à un article en préparation, à soumettre dans le journal *Ore Geology Reviews*. Dans ce chapitre, une étude minéralogique détaillée intégrant les données géochimiques, isotopiques et géochronologique a permis de caractériser les sources primaires de l'uranium dans le socle environnant le bassin d'Erlan et de discuter du ou des contextes géodynamiques correspondant à la mise en place de ces roches fertiles en U.

La troisième partie (partie C) est consacrée à la genèse des minéralisations d'uranium dans le bassin d'Erlan. Cette partie s'articule en trois chapitres (chapitres 5, 6 & 7). Le chapitre 5 présente les différents types de gisements d'uranium encaissés dans les grès des bassins sédimentaires. Le chapitre 6 correspond à un article à soumettre dans le journal *Ore Geology Reviews*. Essentiellement basé sur une étude minéralogique détaillée associée à l'analyse des éléments traces, ce chapitre met en évidence des pré-concentrations syn-sédimentaires en uranium et présente leur évolution au cours de la diagenèse. Enfin, le chapitre 7 est un article à soumettre dans le journal *Chemical Geology*. Il présente les données minéralogiques, géochimiques et isotopiques du gisement de roll front étudié qui permettent de proposer un modèle génétique.

Enfin la partie discussion-conclusion intègre les résultats obtenus et présentés sous forme de publications dans chacune des trois parties. Cette dernière partie permet également de proposer des perspectives sur les travaux restants encore à réaliser pour une meilleure compréhension de ces systèmes minéralisés.

Toutes les références bibliographiques citées dans les différents chapitres sont regroupées à la fin du manuscrit afin de faciliter leur accès.

PARTIE A :

**LA MISE EN PLACE DES BASSINS
SEDIMENTAIRES**

CHAPITRE 1 :

L'EXTENSION CONTINENTALE AU MESOZOÏQUE

EN ASIE DE L'EST



1. Le cadre géologique de l'Asie de l'Est

L'Asie constitue un des plus vastes domaines continental, issu de l'accrétion successive de blocs continentaux de l'Archéen jusqu'à l'actuel. La Chine constitue la partie sud-est de ce vaste domaine continental à l'histoire géologique complexe (**Figure 2**). Les limites entre ces blocs continentaux datés de l'Archéen au Paléoprotérozoïque correspondent à des orogènes du Phanérozoïque dont la chaîne de collision de l'Himalaya, encore active aujourd'hui (Charles, 2010).

L'Asie du sud-est s'étend entre la Mongolie et le Japon au Nord en passant par la Chine du Nord et les deux Corée, et la Chine du Sud à l'île de Taïwan au Sud (**Figure 2**). Cette immense zone géographique est bordée à l'Est par l'Océan Pacifique. Elle est le résultat de l'accrétion de blocs continentaux (e.g. Bloc Chine du Nord, Bloc Chine du Sud) le long d'orogenèses (ex. Qinling-Dabie). Elle se caractérise par une histoire géologique complexe alternant entre phases orogéniques et « calmes » tectoniques (Kusky et al., 2007).

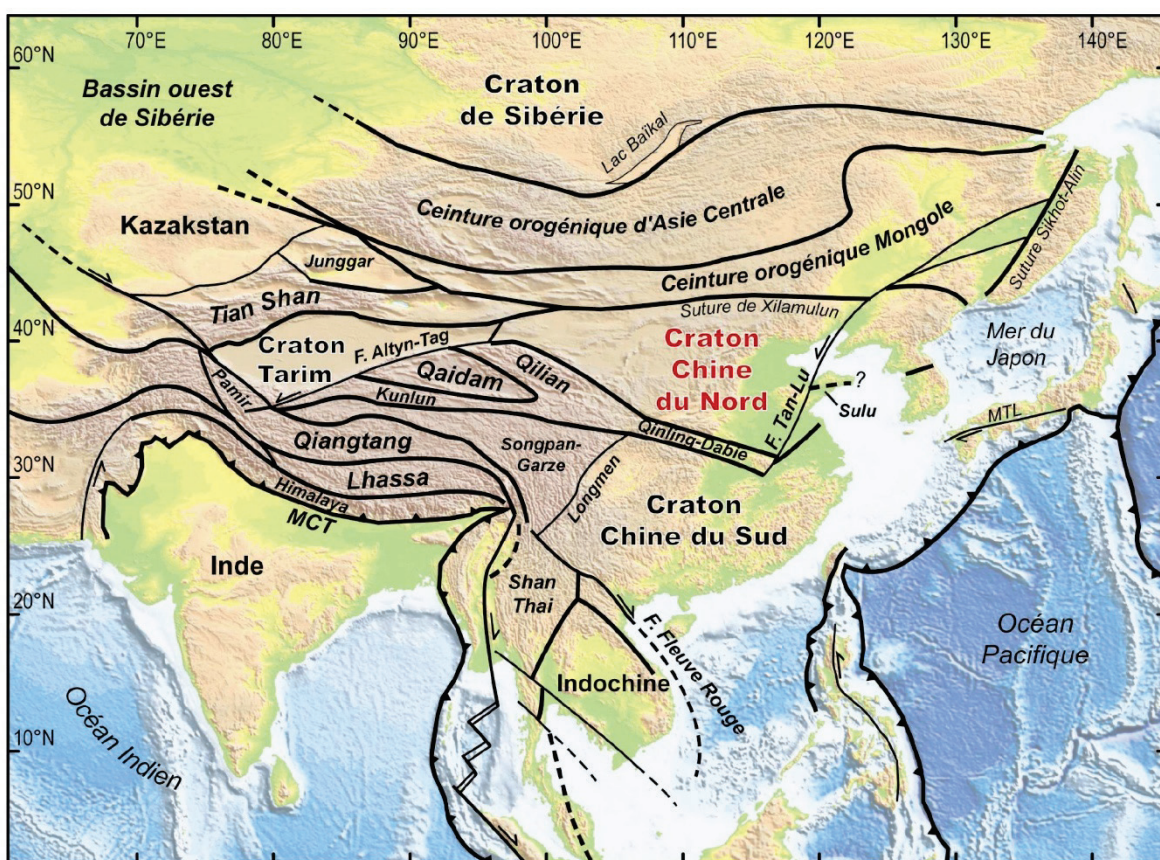


Figure 2. Carte tectonique simplifiée de l'Asie de l'Est. MTL= Median Tectonic Line; MCT= Main Central Trust (Charles, 2010; Enkin et al., 1992).

2. Le craton de Chine du Nord

Le Craton de Chine du Nord (CCN; ou craton Sino-Coréen) s'étend sur une superficie d'environ 1,7 million de kilomètres carrés entre le NE de la Chine, la Mongolie Intérieure et la Mer Jaune (**Figure 3**; Bai, 1996; Bai et Dai, 1996, 1998). Ce craton est délimité au Sud-Ouest par l'orogenèse de Chine Centrale (incluant le Qinling-Dabie et le Sulu), et par les ceintures orogéniques du nord Hebei et Mongole au Nord (constituant la partie chinoise de la ceinture orogénique d'Asie Centrale) comme illustré dans la figure (Charles, 2010).

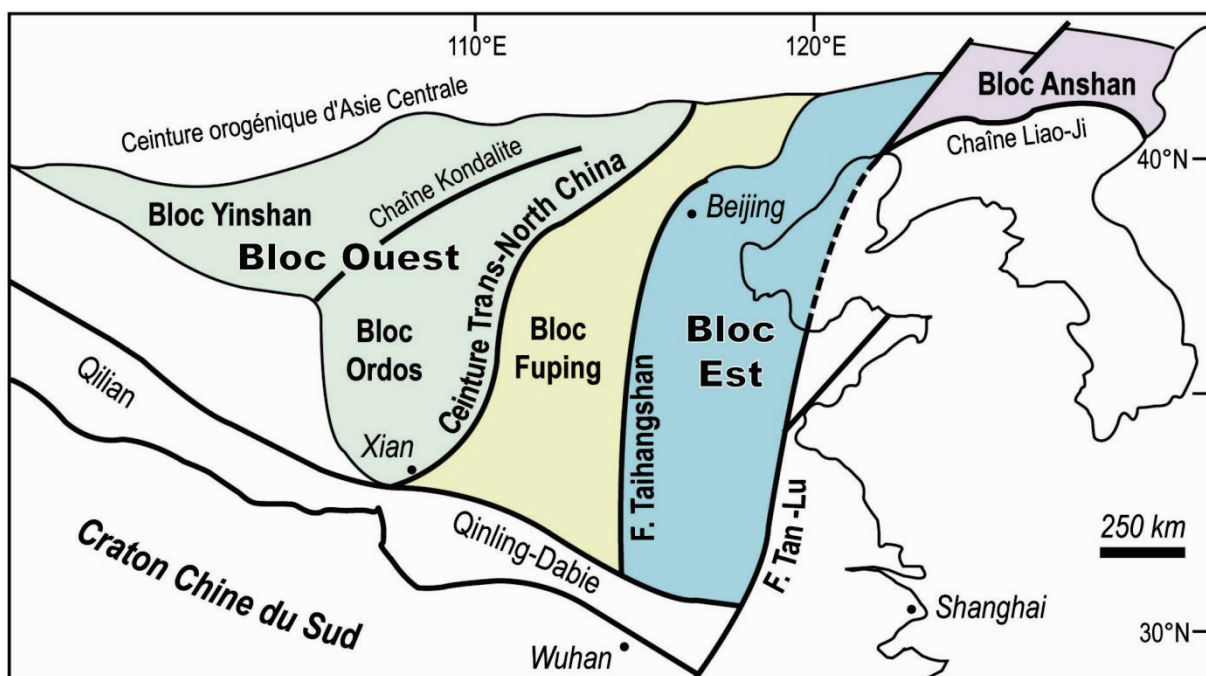


Figure 3. Carte simplifiée du craton de Chine du Nord (CCN; Charles, 2010; Faure et al. 2007).

La limite ouest du craton est représentée par les ceintures du Qilian et de l'Ouest Ordos marquant la transition entre le CCN et le craton du Tarim (**Figure 2**; **Figure 3**; Charles, 2010). Concernant la limite sud-est du CCN, les relations avec le Craton de Chine du Sud et certaines parties de la Péninsule coréenne sont toujours discutées (Oh et Kusky, 2007).

Le CCN résulte de l'amalgamation de micro-blocs constitués de roches d'âges supérieurs à 2,5 Ga (Jahn et al., 1987; Jahn et Ernst, 1990; Liu et al., 1992; Wu et al., 1992, Liu et al., 2004a; Zheng et al., 2004). L'âge de formation du craton est discuté par les auteurs: certains présentent un âge égal ou antérieur à 2,5 Ga, alors que d'autres considèrent une accrétion au Paléoprotérozoïque (1,8 Ga; Kusky et al., 2007; Trap, 2007). Le craton peut être subdivisé en

trois blocs principaux : (i) le Bloc Ouest, (ii) le Bloc de Fuping et (iii) le Bloc Est, séparés par deux chaînes : la ceinture Trans-North China à l'Ouest et la chaîne Taihangshan à l'Est (**Figure 3**; Zhao et al., 1998, 1999; Faure et al., 2007 ; Trap et al., 2008).

Le Bloc Ouest est la partie stable du craton avec une importante racine mantellique, un faible flux de chaleur et n'a subi que peu de déformation interne depuis le Précambrien (Yuan, 1996; Zhai et Liu, 2003). A contrario, le Bloc Est est très atypique pour un craton, et montre de nombreux séismes, un fort flux de chaleur, une lithosphère amincie et l'absence d'une racine mantellique épaisse.

3. Les preuves d'un amincissement lithosphérique

La compréhension de la géométrie globale et de la nature des terrains situés sous le craton ne peut se faire que grâce à des méthodes indirectes telles que la gravimétrie, la sismologie ou encore la géochimie des enclaves.

3.1. La gravimétrie

La carte de l'anomalie de Bouguer à l'échelle de la Chine permet de mettre en évidence les zones d'épaississement ou d'amincissement crustal (**Figure 4**). A l'Est de la Chine, un linéament orienté NNE (LGNS : linéament gravimétrique Nord-Sud), long d'environ 3500 km et large d'une centaine de kilomètres est marqué par une forte diminution de l'anomalie de Bouguer, passant de -100 mGal à l'Ouest, à moins de -40 mGal à l'Est (Fig. 4; Ma, 1989). Ce fort gradient gravimétrique recouvrant toutes les discontinuités de la Chine de l'Est (bordures des cratons, les ceintures orogéniques du Dabie et du Yanshan) et séparant deux régions très différentes d'un point de vue topographique (**Figure 4**), tectonique et sismique (Ye et al., 1987; Ma, 1989; Griffin et al., 1999; Menzies et Xu, 1998; Niu, 2005; Menzies et al., 2007; Xu, 2007; Chen, 2010) témoigne d'un fort amincissement crustal. En effet, à l'Est du LGNS (au sein du Craton de Chine du Nord) l'épaisseur de la croûte est faible (< 35 km en moyenne ; Ma, 1989; Li et Mooney, 1998) et l'anomalie de Bouguer est faiblement négative voire positive (**Figure 4**) indiquant l'existence d'une lithosphère amincie (<80-100km) sous cette région (Ma, 1989; Chen et al., 1991).

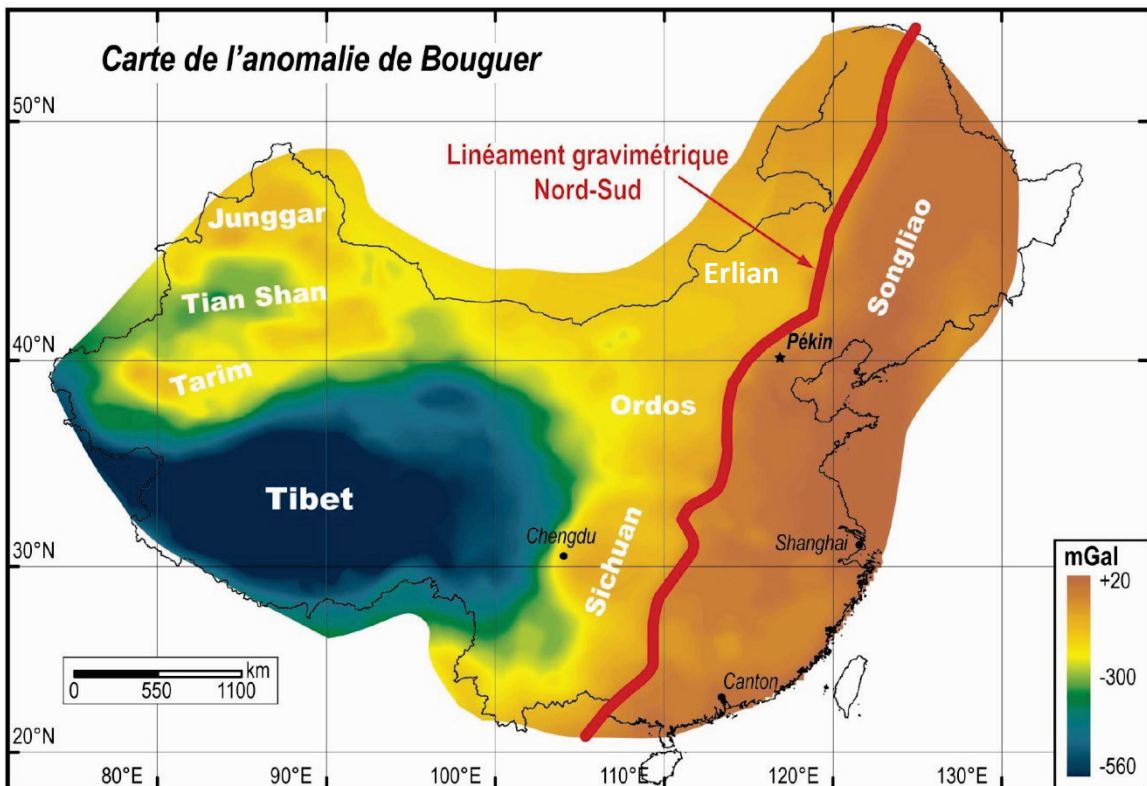


Figure 4. Carte de l'anomalie de Bouguer de la Chine (Ma, 1989; Charles, 2010).

3.2. La tomographie sismique

Pour la Chine, les données tomographiques ont permis de mettre en évidence de fortes anomalies à l'Est du Craton de Chine du Nord où les ondes sismiques sont ralenties à faible profondeur démontrant la présence d'une lithosphère amincie sous la partie Est du craton (Chen et al., 1991; Liu, 1992). Cet amincissement lithosphérique est particulièrement visible sur la carte de la profondeur de la zone de transition entre la lithosphère et l'asthénosphère (LVZ) de Chine (**Figure 5**; An et Shi, 2006). En effet, la lithosphère épaisse de plus de 200 km au niveau de la chaîne de l'Himalaya passe à moins de 80 km dans la partie orientale du CCN (**Figure 5A**). De plus, les études tomographiques plus récentes menées à l'échelle du CCN (Chen et al., 2008, 2009; Chen, 2009; Chen, 2010) montrent une diminution importante de l'épaisseur lithosphérique, passant de 140 km sous la région du Yanshan (au nord de Pékin), à 60 km sous la Baie de Bohai (**Figure 5B**). Selon des profils orientés E-W à NW-SE réalisés par Chen (2010), il apparaît que les zones d'amincissement lithosphérique visibles sur les images migrées des ondes S par fonction récepteur (S-RF), correspondent aux zones de plus basse altitude ainsi qu'aux zones d'anomalie gravimétrique de Bouguer faiblement négatives voire positives (**Figure 6**).

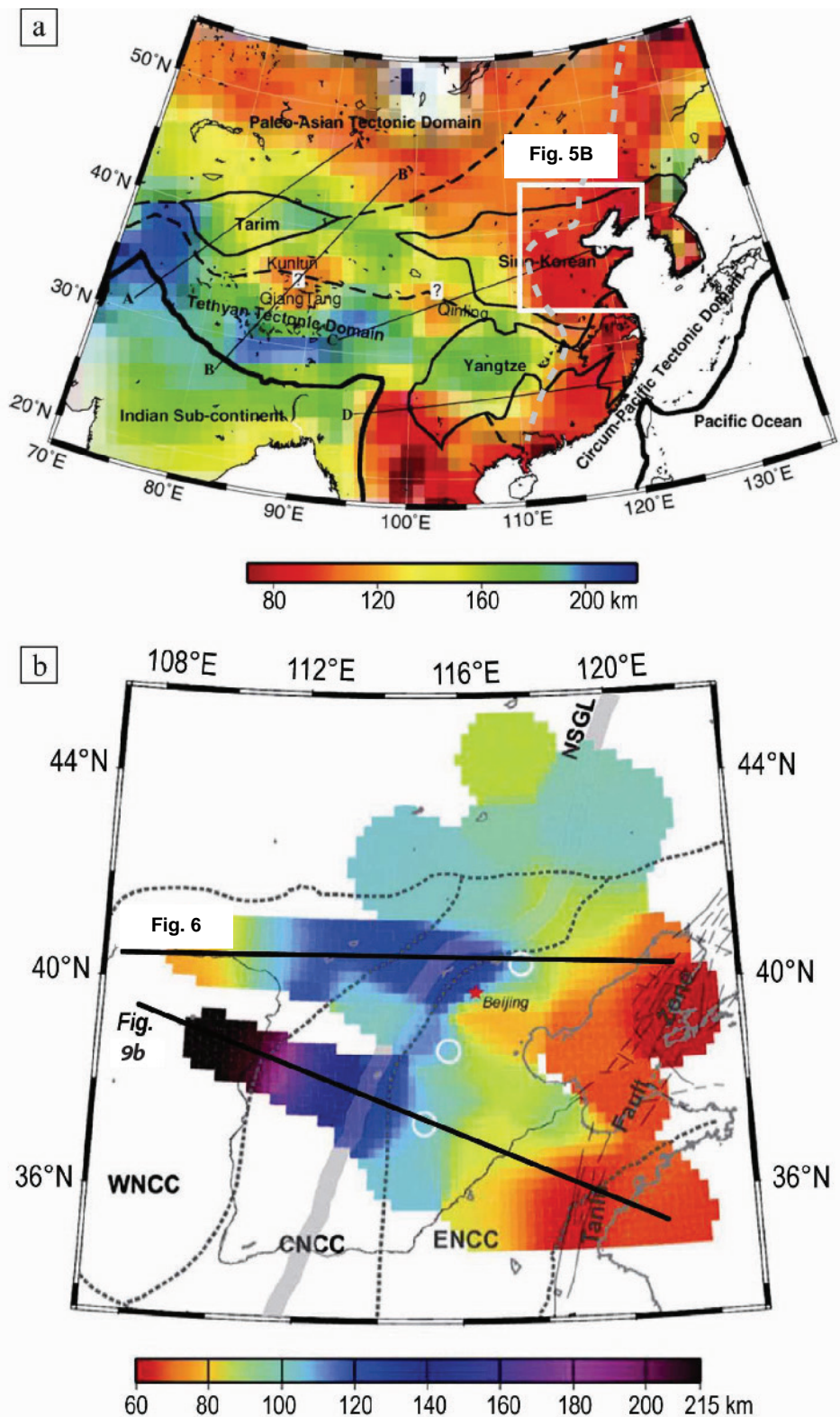


Figure 5. Cartes de la profondeur de la transition lithosphère-asthénosphère marquée par la zone de moindre vitesse (ou LVZ : Low Velocity Zone) pour la Chine (a) et le Craton de Chine du Nord (b), issues de An et Shi (2006) et Chen (2010), respectivement. Les traits noirs correspondent aux coupes présentées en Figure 6 (Chen et al., 2009; Chen, 2010).

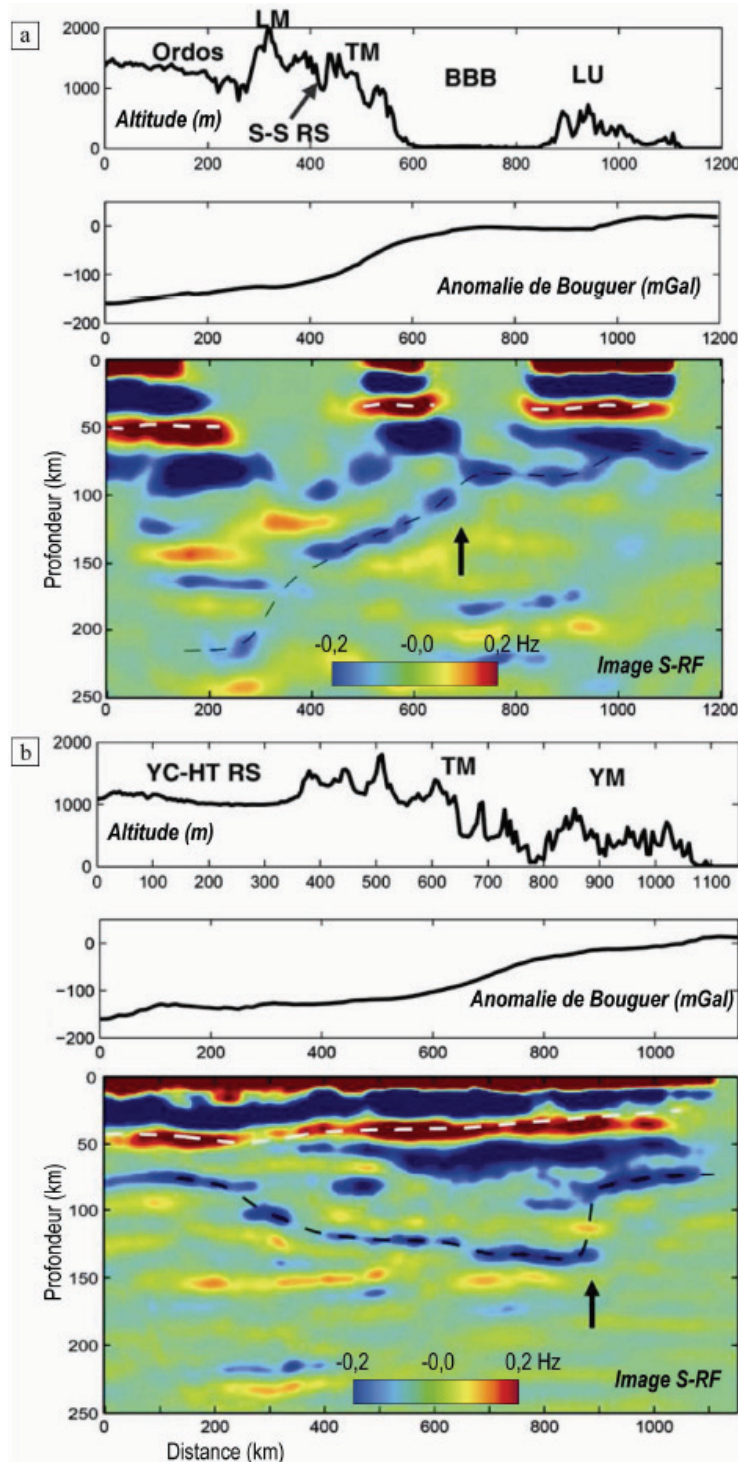


Figure 6. Profils topographiques, de l'anomalie gravimétrique de Bouguer et images migrées des ondes S par fonction récepteur (S-RF), (Chen, 2010). Les lignes noires en tirets représentent la limite lithosphère-asthénosphère et les blanches la discontinuité de Moho. BBB (Bassin de la Baie de Bohai), LU (Luxi Uplift), TM (Taihang Mountains), LM (Lüliang Mountains), S-S RS (Shaanxi-Shanxi Rift System), YCHTRS (Yinchuan-Hetao Rift System), YM (Yan Mountains).

3.3. L'étude des enclaves du Paléozoïque et du Cénozoïque

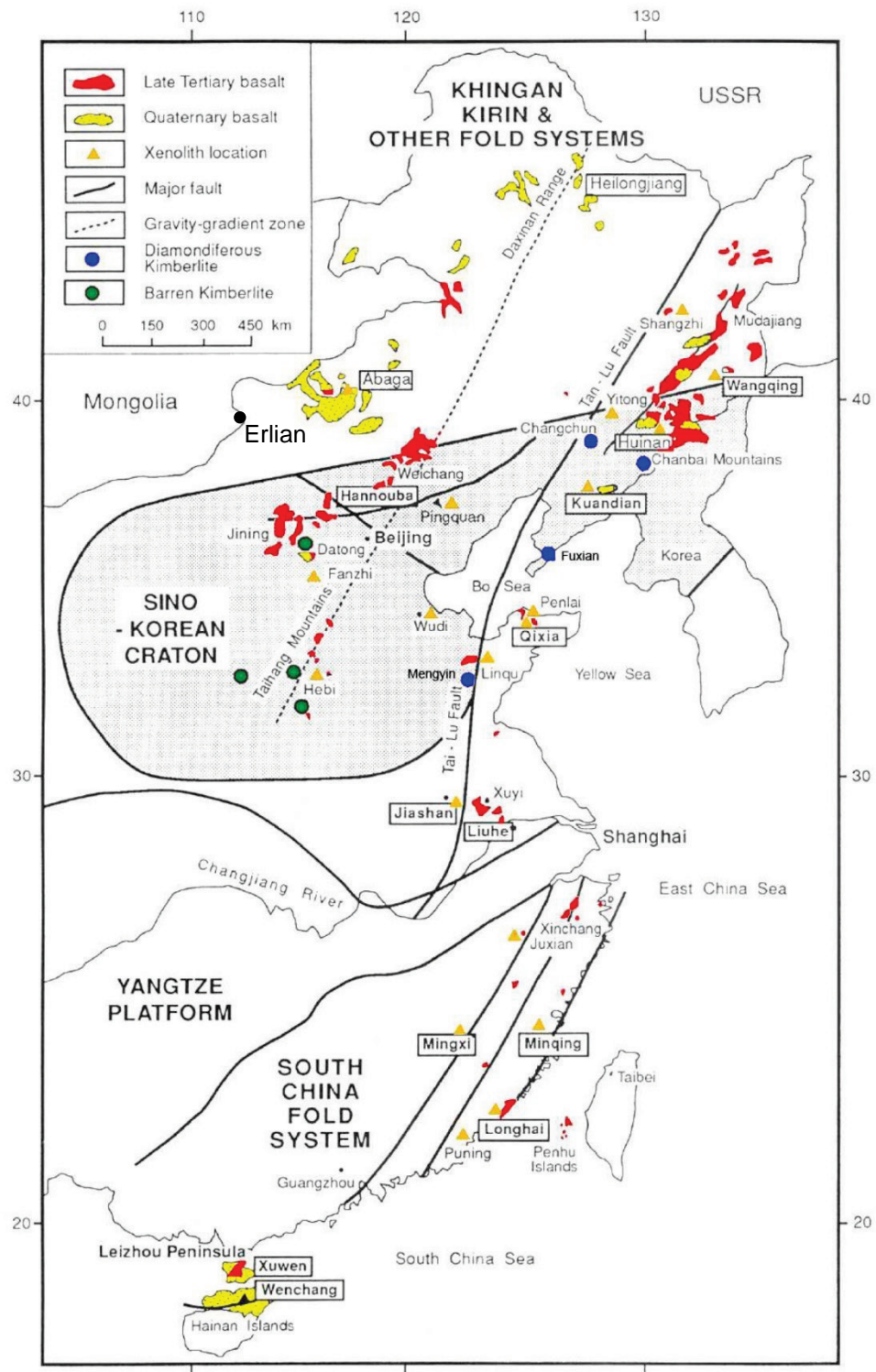


Figure 7. Carte de répartition des enclaves présentes en Chine de l'Est (Menzies et al., 1993). Les kimberlites du Paléozoïque ainsi que les basaltes du Cénozoïque associés aux enclaves sont également représentés.

Les kimberlites de l'Ordovicien ont permis d'amener vers des niveaux plus superficiels des enclaves (Lu et al., 1991; Zhang et al., 1991; Chi et al., 1992). Ces roches (He, 1987; Zhang et al., 1989) sont constituées essentiellement par des périclites à grenat (>80 km, 3 GPa) contenant des diamants (150-200 km, 5-6 GPa).

L'étude des éléments en traces dans les grenats, (Griffin et al., 1992, 1998, 1999) montre que le « géotherme grenat » pour la lithosphère sous cette région correspond à un flux de chaleur de surface d'environ $36-40 \text{ mW.m}^{-2}$ (Fig.). A cela s'ajoute la caractérisation des conditions P-T, pour la partie la plus profonde de la lithosphère (180-200 km), grâce aux inclusions dans les diamants donnant une gamme de températures d'environ 1100°C pour des pressions égales à 4-6 GPa (**Figure 7**; Zhao, 1998; Menzies et Xu, 1998). Et les périclites des enclaves ordoviennes sont présentes dans le champ des périclites caractéristiques des cratons, avec des olivines fortement magnésiennes (**Figure 7**; Boyd, 1987; Xu, 2001). En résumé, à l'Ordovicien, le CCN était composé d'une croûte et d'un manteau d'âge Archéen à Protérozoïque, avec une épaisseur lithosphérique d'environ 180-200 km et un faible flux de chaleur en surface (40mW.m^{-2}).

Au Cénozoïque, l'activité magmatique est notamment caractérisée par la mise en place de basaltes qui ont ramené en surface des enclaves de roches mantelliques (**Figure 7**). Ces enclaves sont constituées de périclites à spinelle (essentiellement, <80 km) et grenat (plutôt rares), et caractérisées par l'absence de diamants (Menzies et al., 2007). Xu et al. (1998) ont montré dans la région de Nushan (au SE du CCN), qu'au Cénozoïque la lithosphère était constituée d'une croûte épaisse de 30 km, d'un manteau composé de périclites à spinelle (de 30 à 50 km de profondeur) et de périclites à grenat stables vers 100 km de profondeur, c'est à-dire à la base de la lithosphère. A partir de la différenciation des périclites proposée par Boyd (1987), les périclites à spinelle incluses dans les basaltes du Cénozoïque correspondent au champ caractérisant les périclites « océaniques, orogéniques, ophiolitiques » (**Figure 7**; Xu et al., 1998; Fan et al., 2000; Rudnick et al., 2004).

Menzies et al. (1993) ont proposé qu'au Cénozoïque, l'épaisseur de la lithosphère continentale sous le CCN était de 75 à 80 km. L'étude des enclaves du Craton de Chine du Nord met donc en évidence un amincissement lithosphérique majeur (>120 km) entre le Paléozoïque (épaisseur lithosphérique $\approx 200-180\text{km}$) et le Cénozoïque (épaisseur lithosphérique $\approx 75-80 \text{ km}$).

3.4. L'âge du manteau lithosphérique en Chine du Nord

Les études géochronologiques utilisant la méthode U/Pb sur zircon ont confirmé l'âge ancien de la croûte continentale du CCN. Deux groupes d'âges pour la croûte continentale, le premier à 2,5-2,9 Ga, le second à 3,2-3,6 Ga ont été identifiés par Wu et al., (1992). Plus récemment, Zheng et al. (2004) ont montré la présence de reliques de croûte ancienne (~3,6 Ga) au sein d'une croûte plus jeune, reflétant une réactivation possible de la croûte. La plupart des auteurs s'accordent à considérer qu'une part importante (80%) de la croûte continentale du CCN est âgée de la fin de l'Archéen (entre 2,8 et 2,5 Ga), le reste étant constitué des bassins sédimentaires du Mésozoïque, du Tertiaire et des roches magmatiques du Mésozoïque (Charles, 2010).

Le manteau lithosphérique du CCN a pu être daté en plusieurs endroits grâce à l'étude du système isotopique Re-Os des périclites contenues dans les enclaves du Paléozoïque et du Cénozoïque (Gao et al., 2002 ; Wu et al., 2003). Selon les auteurs, quelques rares parties du manteau lithosphérique sont datées de l'Archéen (2,6-2,5 Ga, site de Fuxian), ce qui est comparable aux âges de la croûte continentale décrits précédemment. La **figure 8** montre que les rapports isotopiques $^{187}\text{Os}/^{188}\text{Os}$ d'une grande majorité des périclites étudiées correspondent à des modèles d'âges (T_{RD}) plus récents que les âges obtenus pour la croûte continentale du CCN.

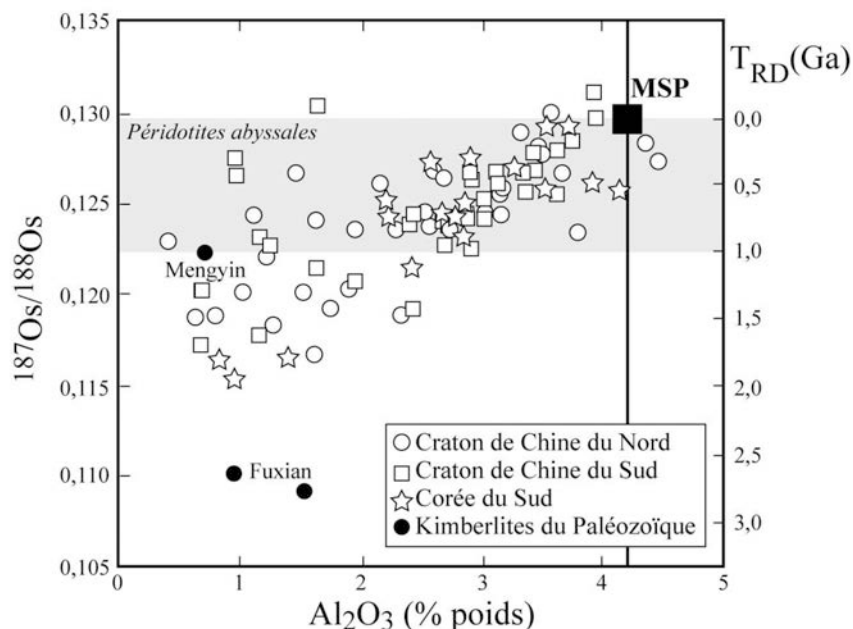


Figure 8. Graphique $^{187}\text{Os}/^{188}\text{Os} = f(\text{Al}_2\text{O}_3 \text{ roche totale})$, (Charles, 2010) pour les périclites des enclaves du Craton de Chine du Nord (Gao et al., 2002; Wu et al., 2003), du Craton de Chine du Sud (Zhi et al., 2001), de Corée du Sud (Lee et Walker., 2006) et des kimberlites du Paléozoïque. Les valeurs pour le MSP (manteau

supérieur primitif) sont issues de Meisel et al. (2001), et celles pour les péridotites abyssales de Snow et Reisberg (1995).

Gao et al. (2002) et Wu et al. (2003) interprètent ces différences d'âges entre le manteau lithosphérique et la croûte continentale sus-jacente comme le fait d'un rajeunissement de la racine mantellique du craton. En effet, le manteau lithosphérique ancien serait remplacé par du matériel juvénil au cours du Protérozoïque et du Phanérozoïque (Gao et al., 2002; Wu et al., 2003). Basé sur des évidences géologiques (ex. bassins, magmatisme), Gao et al. (2002) proposent que le remplacement lithosphérique dans l'est du Craton de Chine du Nord se soit produit au cours du Jurassique et du Crétacé.

4. Les preuves d'une extension crustale

4.1. Les bassins sédimentaires intracontinentaux

Des centaines de bassins se sont développés en Asie de l'Est et plus particulièrement en Chine du Nord. Les principaux bassins extensifs de Chine du Nord sont les bassins de Songliao (260 000 km²), Hailar, Erlian, Est Gobi, Yingen et Sanjing (**Figure 9**) et ont fait l'objet de nombreuses études (ex. Ru et Pigott, 1986; Liu, 1986; Ma et Wu, 1987; Gilder et al., 1961; Tian et al., 1992).

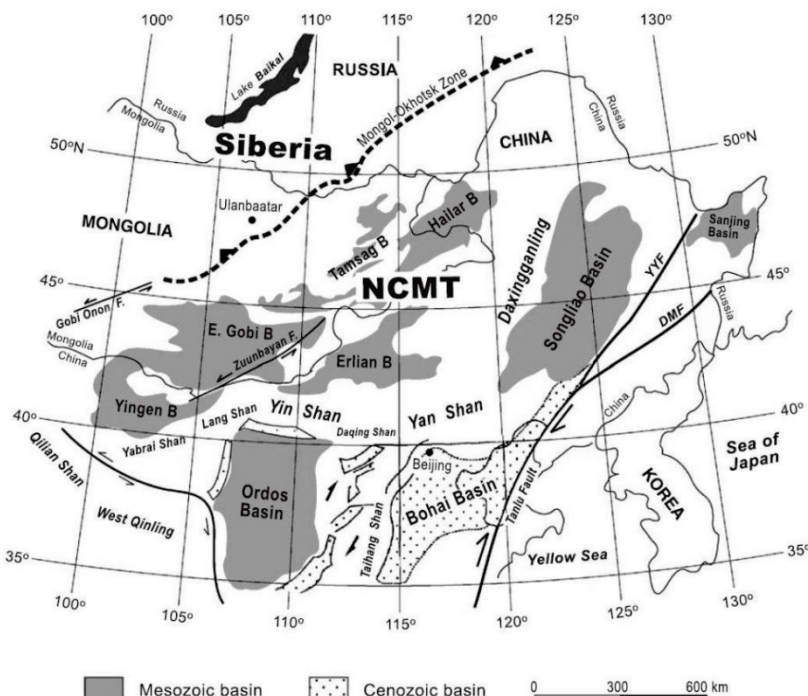


Figure 9. Carte de localisation des bassins d'âge Mésozoïque de Chine du Nord (Meng, 2003). NCMT= North China Mongolia Tract.

La datation des coulées de lave intercalées dans les bassins et la stratigraphie ont permis de déterminer le début d'ouverture des bassins comme prenant place au Jurassique supérieur. Ainsi, l'ouverture du bassin de l'Est Gobi se produit à 155 ± 1 Ma, d'après les datations $^{40}\text{Ar}/^{39}\text{Ar}$ sur les laves interstratifiées (Graham et al., 2001). Un âge sensiblement identique (156-145 Ma) a été déterminé pour la série volcano-sédimentaire de Qingganling à la base de la série du bassin d'Erlian, grâce aux datations $^{40}\text{Ar}/^{39}\text{Ar}$ et K/Ar (Chen et Chen, 1997) et aux fossiles typiques de cette période (Wang et al., 1995a, 1995b).

Le bassin d'Erlian (**Figure 9**) commence à s'ouvrir à la fin du Jurassique-début du Crétacé (Chen and Chen, 1997; Graham et al., 2001; Wang et al., 2006). En ce qui concerne le bassin de Songliao, au Nord-Est de la Chine, le volcanisme précoce dans le bassin est daté à 147-157 Ma par les méthodes K/Ar et $^{40}\text{Ar}/^{39}\text{Ar}$ (Wang et al., 2002, 2006). Par conséquent, l'ouverture des bassins en Chine du Nord semble débuter de manière synchrone vers 155 Ma (Meng, 2003).

A partir des données de sondages pétroliers, une corrélation des séquences sédimentaires entre tous les bassins a été établie, montrant une cyclicité dans la sédimentation, alternant entre des dépôts conglomératiques fluviatiles et d'argiles lacustres, typique d'un environnement continental. A cela s'ajoute un volcanisme plus ou moins important, en intercalation dans les couches sédimentaires (ex. Wang et al., 2002, 2006; Pei et al., 2008; Zhang et al., 2010a, 2010b).

Ces grands bassins sont en réalité constitués de nombreux « sous-bassins » de taille plus modeste (~30- ~3500 km²), et étroit d'un point de vue cartographique. En coupe, ces nombreux petits bassins (~300) montrent généralement une géométrie en demi-graben bordés principalement par des failles normales fragiles listriques (**Figure 10**).

Les discordances au sein des bassins ainsi que la géométrie des failles impliqueraient plusieurs phases de rifting (Meng, 2003). La structure en « Basin & Range » a été invoquée (Ren et al., 2002) faisant état de la disposition parallèle des reliefs par rapport aux bassins, et induisant de ce fait une extension lithosphérique (~100 km horizontalement). La subsidence des bassins s'accélère au début du Crétacé pour continuer jusqu'à ~100 Ma.

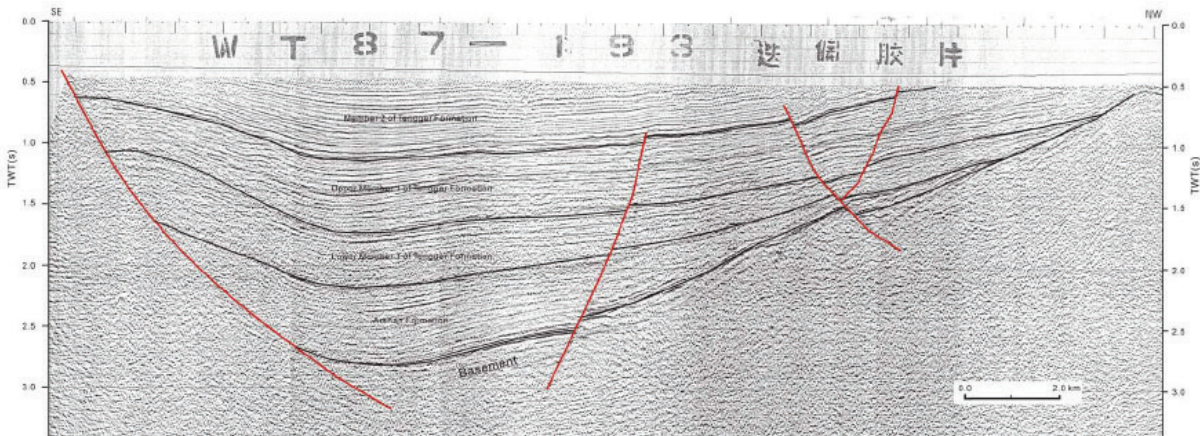


Figure 10. Profil sismique dans un « sous-bassin » du bassin d’Erlian (Dou and Chang, 2003). Les failles normales contrôlant le dépôt des sédiments du Crétacé sont bien visibles, mettant en avant la structure en demi-graben.

4.2. Le volcanisme

Le volcanisme de la fin du Mésozoïque couvre une surface importante en Chine du Nord et dans ses régions voisines (Sud de la Mongolie, Péninsule Coréenne, Japon). Le volcanisme en Chine du Nord est particulièrement développé dans la région du Daxingganling (au nord-est de Pékin; **Figure 11**) sur une surface d’environ 100 000 km² (BGMRNM, 1991) pour une épaisseur de 4 à 5 km (Wang et al., 2006). Ces roches volcaniques sont aussi présentes sous la forme de dépôts volcano-sédimentaires, à la base des bassins intracontinentaux évoqués précédemment. Elles sont principalement composées de basaltes, basaltes alcalins, andésites, trachyandésites, trachytes ou rhyolites. Malgré les différences lithologiques retrouvées, les nombreuses études géochimiques mettent en évidence une source commune : soit (i) une source issue du manteau lithosphérique faiblement appauvri ou bien (ii) une source issue du manteau appauvri avec une contamination crustale (Fan et al., 2003; Zhang et al., 2007; Zhang et al., 2010a).

La compilation des âges K/Ar et Ar/Ar faite par Lin et al. (1998) donnant un âge moyen de 155 Ma montre que l’activité volcanique en Chine du Nord débuterait à la fin du Jurassique. Ceci est corroboré par (i) de récentes datations ⁴⁰Ar/³⁹Ar montrant une activité volcanique s’initiant vers 163 Ma et se poursuivant jusqu’à la fin du Crétacé inférieur (113 Ma; Wang et al., 2006), et (ii) par des datations U/Pb sur zircon faites plus récemment (Ying et al., 2010b).

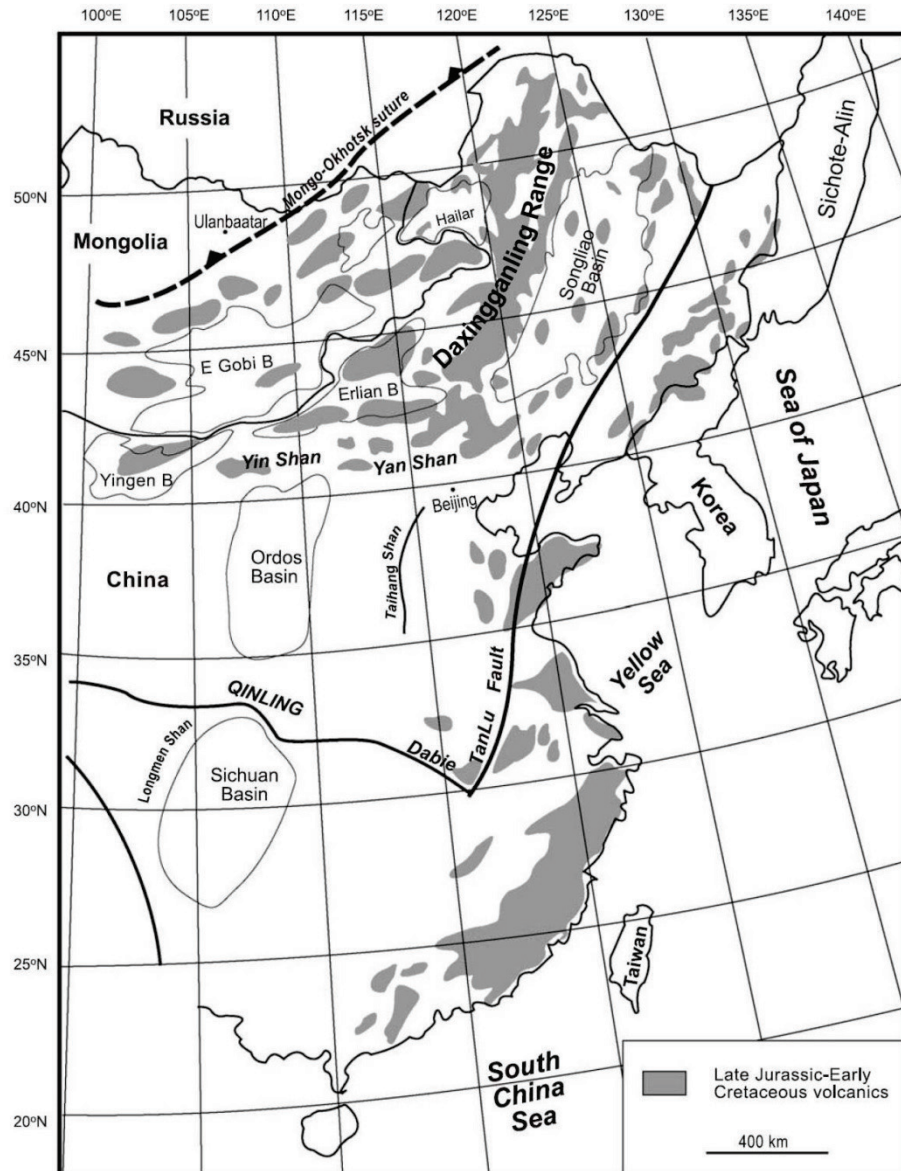


Figure 11. Carte synthétique de répartition des roches volcaniques de la fin du Mésozoïque en Chine de l'Est (Wu et al., 1982; SMJGRT, 1980; Yarmolyuk and Kovalenko, 2001; Meng, 2003).

Wang et al. (2006) ont proposé une migration spatiale et temporelle du volcanisme de l'Ouest vers l'Est, entre la suture de Mongol-Okhotsk et la paléo-subduction Pacifique (~160-140 Ma pour la Mongolie ; ~120-130 Ma par la région du Daxingganling, le bassin de Songliao et le Liaoning ; ~100 Ma pour la Péninsule coréenne et ~80 Ma pour le Japon). Le pic du volcanisme se situe entre 120-130 Ma (Wang et al., 2006) au nord-est de la Chine, ce qui correspond au pic de plutonisme mis en évidence par Wu et al. (2005a). Il est à noter que l'origine du volcanisme en Chine du Nord, bien qu'encore discutée par les auteurs, est intimement liée au moteur de l'extension Mésozoïque.

4.3. Le platonisme

Le volcanisme est accompagné par un important platonisme, très présent en Chine du Nord et ses régions avoisinantes. La carte de la **figure 12** montre une répartition importante des massifs granitiques en Chine du Sud, en Chine du Nord et dans la Péninsule coréenne, ainsi qu'au Japon (Zorin, 1999; Wang et al., 1998; Chough et al., 2000; Li, 2000; Wu et al., 2000; Choi et al., 2005; Wu et al., 2005a, 2005b; Ishihara, 2007; Wu et al., 2007). En Chine du Nord, les régions présentant le plus grand nombre de massifs granitiques sont le Jiaodong, le Liaodong et la chaîne du Yanshan (Wang et al., 1998; Wu et al., 2005a, 2005b; Chen et al., 2007).

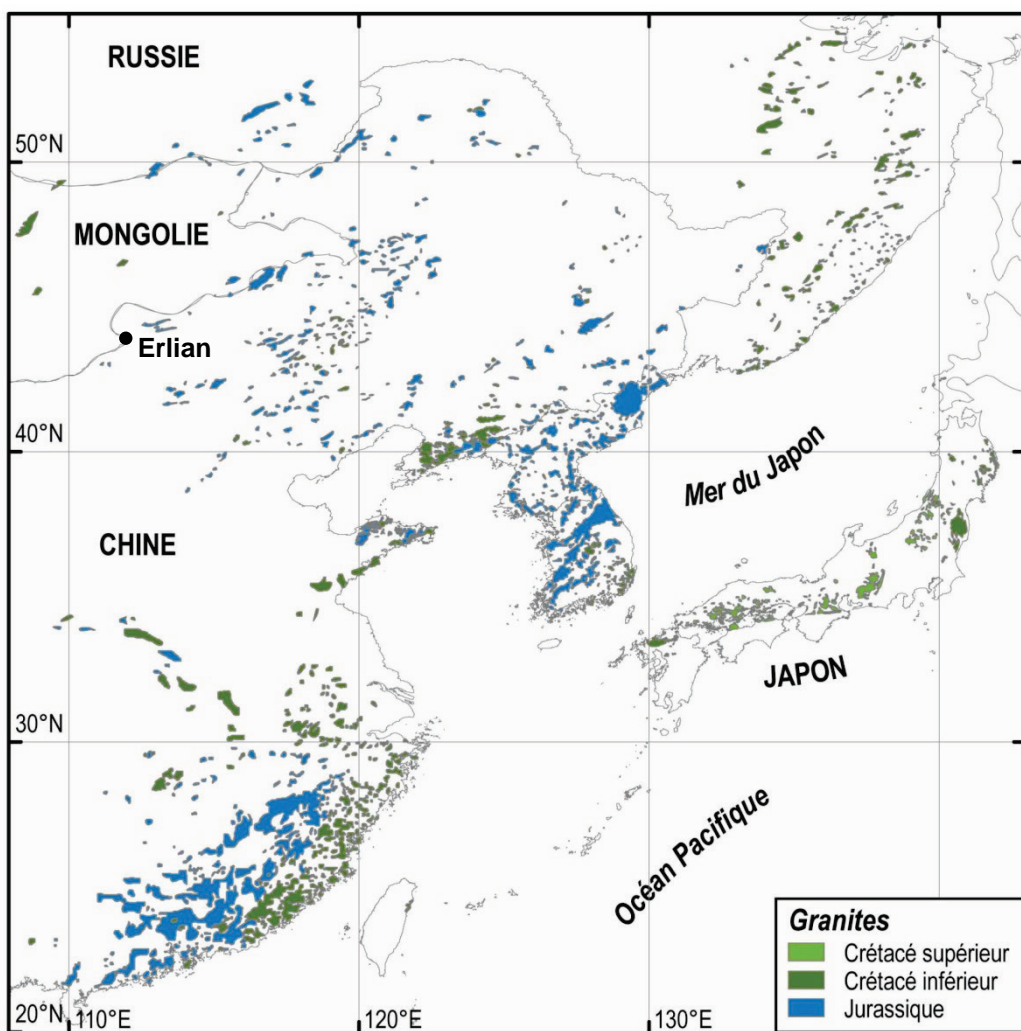


Figure 12. Carte synthétique de répartition des granitoïdes de la fin du Mésozoïque en Asie de l'Est (compilée par Charles, 2010 d'après les données de Zorin, 1999; Wang et al., 1998; Chough et al., 2000; Li, 2000; Wu et al., 2000; Choi et al., 2005; Wu et al., 2005a, 2005b; Ishihara, 2007; Wu et al., 2007).

Les massifs granitiques sont pour la plupart constitués de roches monzonitiques à quartz (65%), de monzogabbros et de monzodiorites (15%), de granitoïdes (10%) et de syénites (10%). Les minéraux principaux sont le plagioclase, l'amphibole (hornblende), le pyroxène, le quartz et le feldspath potassique (Charles, 2010). La magnétite, la titanite, le zircon, l'apatite constituent les minéraux accessoires. Les diagrammes de Harker des éléments majeurs et traces (CaO, TiO₂, MgO en % poids ; V, Co, Sr en ppm) présentés par Chen et al. (2007), montrent une décroissance linéaire en fonction de la silice (SiO₂), privilégiant un modèle de mélange de magmas felsique et mafique pour la formation des roches granitiques.

Les granitoïdes et leurs enclaves sont caractérisés par un fort appauvrissement en éléments de terres rares lourdes et un enrichissement significatif en éléments de terres rares légères, suggérant à nouveau la coexistence de deux types de magma. D'autres études géochimiques et pétrographiques menées sur les granitoïdes du Jurassique et du Crétacé (Wu et al., 2000; Wu et al., 2002; Wu et al., 2005b) ont démontré l'existence notable de granites de type A (anorogénique) et de type I (source ignée basique à intermédiaire) selon la nomenclature de Chappell et White (1974).

Les granitoïdes sont essentiellement peralcalins, alcalins à calcoalcalins témoignant d'une forte fusion des matériaux mantelliques et crustaux. Les auteurs considèrent l'existence d'une lithosphère anormalement chaude ayant permis la formation d'un grand volume de roches plutoniques en Chine de l'Est.

Différentes études géochronologiques (e.g. Miao et al., 1998 ; Wang et al., 1998; Wu et al., 2000; Davis et al., 2001; Wu et al., 2002; Guo et al., 2004; Wu et al., 2005a, 2005b; Su et al., 2007; Yang et al., 2007a, 2007b; Wu et al., 2007) ont montré l'existence de deux phases majeures de plutonisme en Chine du Nord et plus largement en Asie de l'Est lors de cette phase d'extension: (i) au Jurassique (~190-150 Ma; Yanshanien) et (ii) au Crétacé inférieur (~135-100 Ma). Basé sur la compilation des datations disponibles dans la littérature pour les granites en Chine de l'Est, Wu et al. (2005a) ont démontré l'existence d'un pic de plutonisme entre 120-130 Ma. De plus, la période d'activité plutonique semble durer plus longtemps au Jurassique (45 Ma) qu'au Crétacé (10 Ma).

Afin d'expliquer la source mixte des roches granitiques présentes en grand volume en Chine du Nord et en Chine de l'Est, il apparaît nécessaire de considérer un fort flux thermique dans la région à la fin du Mésozoïque permettant de ce fait la fusion partielle de la croûte et du manteau lithosphérique.

4.4. Les « metamorphic core complex » (MCC) : témoins de l'extension crustale

Certains granites sont déformés ductilement sur leur bordure par des zones de cisaillement ductile à mouvement normal et montrant des linéations d'étirement orientées NW-SE (Charle, 2010). Ces directions sont parallèles à la direction d'extension reconnue pour le développement des failles normales fragiles en bordure des bassins intracontinentaux. Le plutonisme peut être également associé au développement des dômes métamorphiques extensifs reconnus en Chine de l'Est (e.g. Davis et al., 1996; Darby et al., 2004; Lin et Wang, 2006; Lin et al., 2008). Les datations de la déformation ductile (mylonite) ont été effectuées pour différents MCC répartis à travers toute la Chine de l'Est et ses régions voisines (**Figure 13**): 122-116 Ma pour le MCC du Sud Liaodong (Yin et Nie, 1996; Yang et al., 2007a; Lin et al., 2008), 126 Ma pour le MCC de Yagan-Onch Hayrhan (Webb et al., 1999), 120 Ma selon Davis et al. (2002) pour le MCC de Hohhot, 126-116 Ma pour le MCC du Yiwulüshan, Darby et al. (2004), 127-112 pour le MCC de Zagan et 122 Ma pour celui de Buteel-Burgutoy (Donskaya et al., 2008). Les MCC étant le résultat d'une très forte extension de la croûte continentale (Davis et Coney, 1979; Brun et Van Den Driessche, 1994; Tirel et al., 2008), leur présence en Chine du Nord et plus largement en Chine de l'Est marque l'existence d'une extension crustale importante dans cette région au début du Crétacé (~130- 110 Ma).

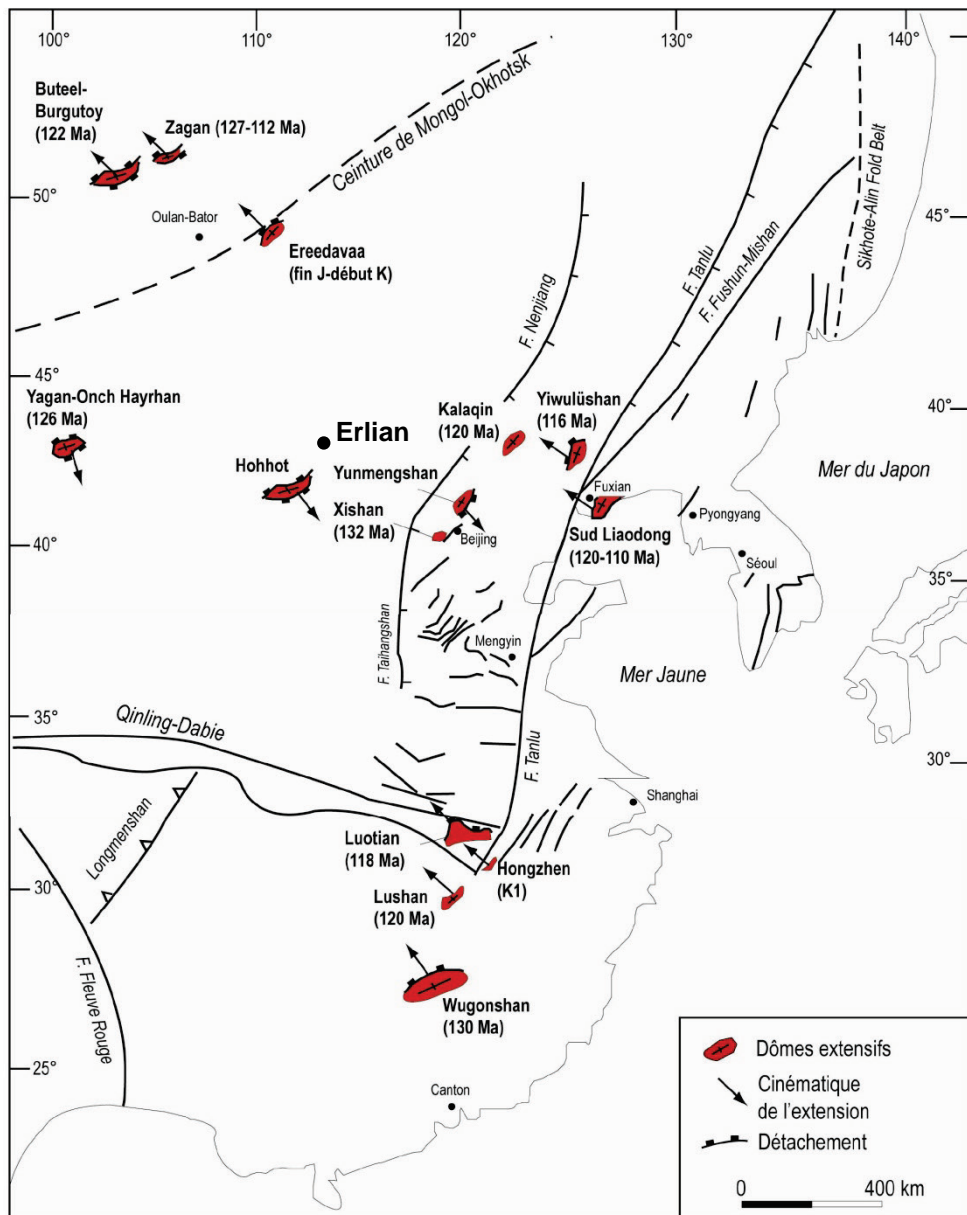


Figure 13. Carte synthétique de répartition des dômes métamorphiques extensifs en Asie de l'Est. Modifiée par Charles (2010) d'après Lin et Wang (2006) et complétée d'après Daoudene et al. (2009).

5. Le modèle géodynamique de l'extension Mésozoïque en Asie de l'Est

5.1. Synthèse des structures extensives et des événements géologiques en Asie de l'Est à la fin du Mésozoïque

En Asie de l'Est, l'étendue géographique des marqueurs d'une extension crustale du Mésozoïque-Cénozoïque va bien au-delà des anciennes zones orogéniques (e.g. Qinlingb Dabie, suture de Xing-Meng ou Solonker). De plus, l'orientation globale NNE-SSW à NE-SW des structures et notamment des bassins et des massifs de roches volcaniques, montre une

forte obliquité par rapport aux orientations E-W à WNW-ESE des anciens orogènes et de leurs sutures (**Figure 14**).

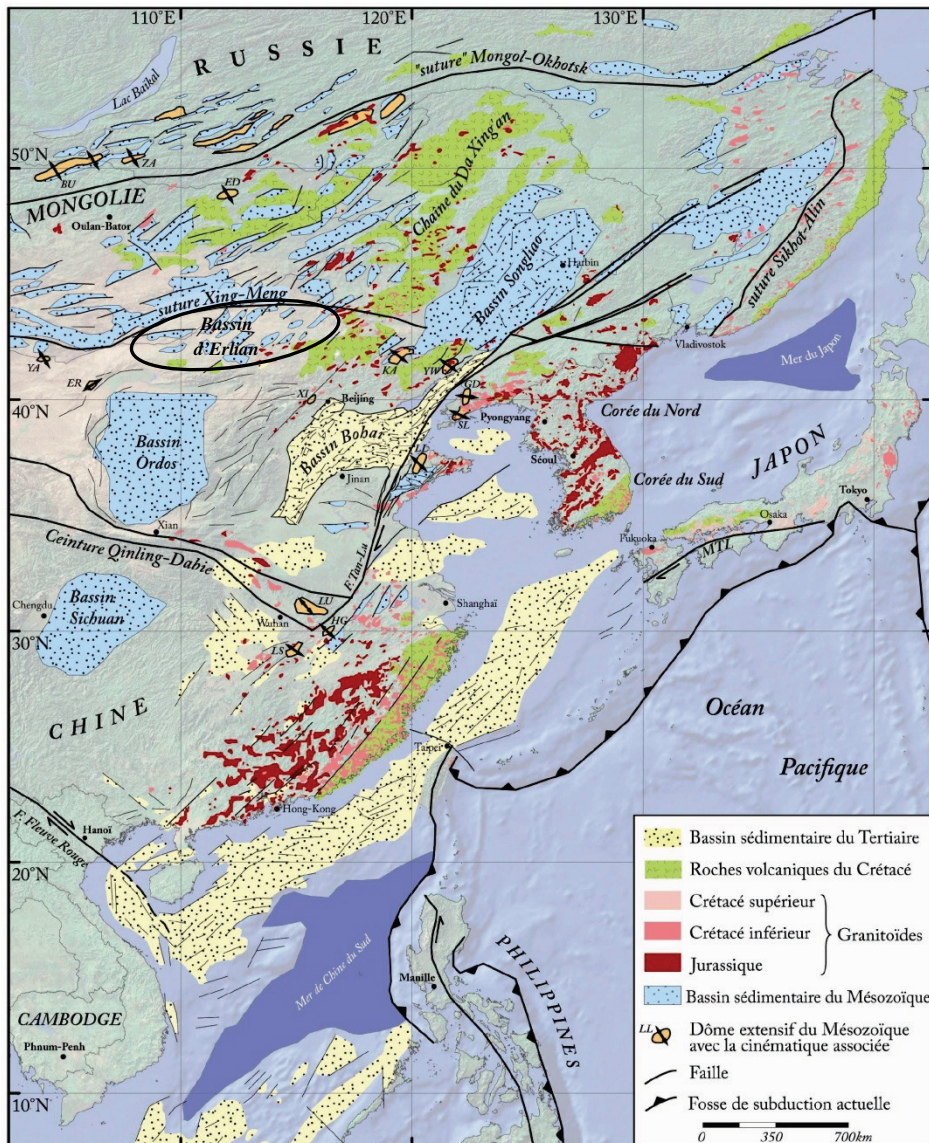


Figure 14. Carte de synthèse des principaux marqueurs présumés de l'extension de la fin du Mésozoïque et du Cénozoïque (Charles, 2010). Données des bassins issues de Traynor et Sladen (1995), Allen(1997), Lee (1999), Ren et al. (2002), Meng (2003), Zhang et al. (2003), Dill et al. (2004), Erdenetsogt et al. (2009). Données des roches volcaniques issues de Li (2000), Kirillova (2003), Meng (2003), Lin et Wang (2006), Wang et al. (2006). Données des granitoïdes issues de GSJ (1992), Wang et al. (1998), Zorin (1999), Chough et al. (2000), Li (2000), Wu et al.(2000), Zhou et Li (2000), Choi et al. (2005), Wu et al. (2005a, b), Zhou et al. (2006), Wu et al. (2007), Wong et al. (2009). Abréviations des dômes extensifs : BU = Buteel-Burgutoy (Mazukabzov et al., 2006; Donskaya et al., 2008); ED = Ereendavaa (Daoudene et al., 2009) ; ER = Ertomiao (Darby, 2003) ; GD = Gudaoling (Charles et al., 2010) ; HG = Hongzhen (Luo et al., 1992); KA = Kalaqin (Han et al., 2001) ; LL = Linglong (Charles et al., 2010); LS = Lushan (Lin et al., 2000); LU = Luotian (Eide et al., 1994; Hacker et al., 1998; Faure et al., 1999); SL = Sud Liaodong (Yin et Nie, 1996; Liu et al., 2005; Lin et Wang, 2006; Lin et al., 2008); XI = Xishan (Lin et Wang, 2006); YA = Yagan-OnchHayrhan (Zheng et al., 1991; Webb et al., 1999); YW = Yiwulishan (Darby et al., 2004; Lin et Wang, 2006); ZA = Zagan (Donskaya et al., 2008).

Les roches volcaniques affleurent principalement au niveau de la Chaîne du Daxingganling au Nord-Est de la Chine, mais sont aussi présentes le long des côtes orientales russes, dans le bassin du Gyeongsang en Corée du Sud et sont largement représentées le long des côtes Sud-Est chinoises (**Figure 15**; Charles, 2010).

Les roches plutoniques (granitoïdes) dont la mise en place a été datée au Mésozoïque sont largement répandues à l'échelle de toute l'Asie de l'Est (**Figure 15**). Deux grandes périodes de production de magma et de leur mise en place en profondeur ont été définies : (i) au Jurassique et (ii) au Crétacé. Le plutonisme du Jurassique est plus réparti dans le temps mais fût moins intense qu'au Crétacé qui a atteint son paroxysme entre 130 et 120 Ma (Wu et al., 2005a, 2005b).

Wu et al. (2005a, 2005b) proposent que cette importante activité magmatique soit liée à la subduction de la paléo-plaque Pacifique associée à une délamination lithosphérique amenant à l'amincissement de la lithosphère sous le CCN. En Chine du Sud, une migration de l'Ouest vers l'Est, similaire à celle décrite pour les roches volcaniques a aussi été identifiée par Li (2000), Zhou et Li (2000) et Wong et al. (2009) pour le plutonisme. Les auteurs relient cette migration au retrait du panneau plongeant de l'ancienne plaque Pacifique (ou Izanagi) durant la fin du Mésozoïque.

L'Asie de l'Est comporte également de nombreux bassins sédimentaires qui se sont développés dès le Jurassique Supérieur (~155 Ma) jusqu'au Cénozoïque (**Figure 15**) et structurés en demi-grabens (Ren et al., 2002 ; Meng, 2003). Le remplissage sédimentaire dans un contexte extensif prend place dans une période comprise en moyenne entre 140 et 120 Ma. La subsidence thermique prend ensuite le relais sur la subsidence tectonique.

La forte activité magmatique présente dans toute l'Asie de l'Est à la fin du Mésozoïque, couplée à l'amincissement lithosphérique amenant à une remontée des isothermes ont permis l'apport d'un flux thermique suffisant pour permettre le développement de structures particulières comme des dômes extensifs séparant ainsi des radeaux de croûte dans lesquels se mettent en place des plutons qui sont peu ou pas déformés (Charles, 2010). Pour conclure, la répartition géographique et temporelle des structures géologiques décrites ci-dessus sont liées au même contexte extensif prenant place dès la fin du Mésozoïque dans toute l'Asie de l'Est (e.g. Mongolie, Chine du Nord, Chine du Sud, Corée, sud Sibérie).

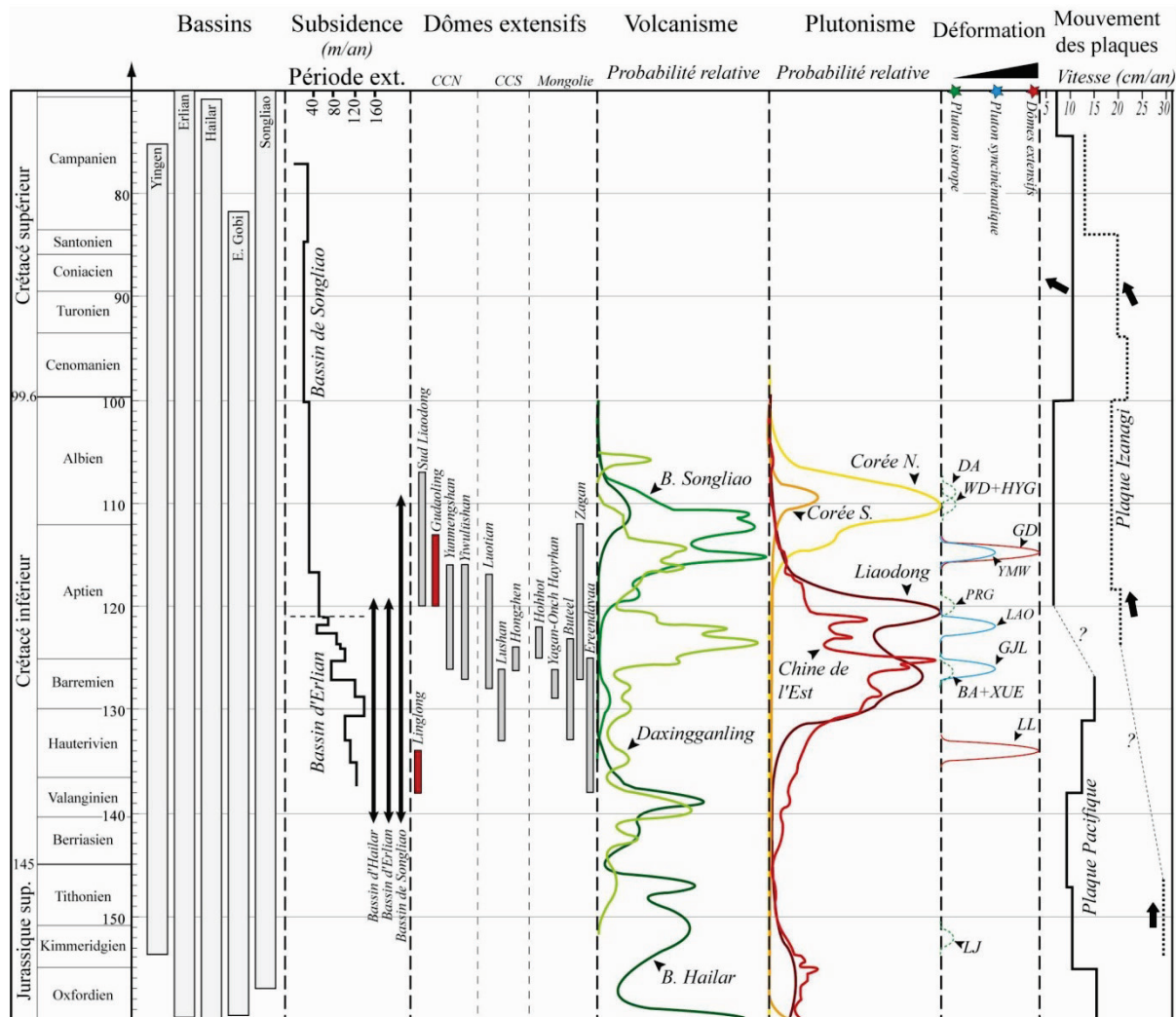


Figure 17. Synthèse des événements géologiques en Asie de l'Est à la fin du Mésozoïque (Charles 2010). Les données sur les bassins sont issues de Ren et al. (2002) et Meng (2003). Les références pour les dômes extensifs sont issues de Yin et Nie (1996); Yang et al. (2007a); Lin et al. (2008); Webb et al. (1999); Davis et al. (2002); Darby et al. (2004); Donskaya et al. (2006). Les données sur l'activité volcanique sont issues de la compilation des âges de Zhang et al. (2008a). Les données sur les pics de plutonisme sont issues de Wu et al. (2005a, 2005b, 2007). Les données sur la déformation crustale sont basées sur cette synthèse des événements. Le mouvement des plaques par rapport au nord est représenté par les flèches noires, et les vitesses de déplacement des plaques Pacifique et Izanagi sont estimées d'après Northrup et al. (1995); Maruyama et al. (1997); Bartolini et Larson (2001); Stepashko (2006). Abréviations des massifs : BA = Badaling ; DA = Dahaituo ; GD = Gudaoling ; GJL = Guojialing ; HYG = Haiyang; LAO = Laohushan; LJ = Luanjiahe; LL = Linglong; PRG = Pinkish-reddish granodiorite; WD = Weideshan; XUE = Xuejiashiliang; YMW = Yinmawanshan.

5.2. Modèle géodynamique : évolution de la marge Est-asiatique à la fin du Mésozoïque

En intégrant les données de surface (objets crustaux : données thermobarométriques sur enclaves, structures, nature du magmatisme, dynamique des bassins...) et de profondeur (gravimétrie, tomographie, directions des anisotropies sismiques), ainsi que la paléogéographie, Charles (2010) a proposé un modèle géodynamique pour expliquer le moteur de l'extension continentale en Asie de l'Est de la fin du Mésozoïque (**Figure 16**). Les coupes correspondent à un transect globalement orienté NW-SE, passant par le Japon, la Corée, la région de Pékin et la Mongolie.

➤ Avant le Jurassique Supérieur (< 160-150 Ma)

La lithosphère continentale est épaisse d'environ 200 km, le flux de chaleur est relativement faible (50 mW.m⁻²; Fu et al., 2005), ce qui est caractéristique d'un environnement cratonique (Charles, 2010), ici celui de Chine du Nord. Le long de la marge Est-asiatique, c'est la plaque Izanagi qui subducte vers l'Ouest avec une direction principale de déplacement vers le NNW (Maruyama et al., 1997). Le craton de Chine du Nord est encadré d'anciennes sutures, traces d'anciens océans, dont les subductions ont toujours été en direction du craton (e.g. Solonker, Qinling-Dabie). Il est possible que certains des panneaux plongeants ayant subductés soient stagnants au niveau de la zone de transition entre les manteaux supérieur et inférieur (Charles, 2010). Ces panneaux se déshydrateraient favorisant (i) une diminution de la viscosité du manteau supérieur asthénosphérique, (ii) une baisse de la température de fusion du manteau et (iii) une activité magmatique (Kusky et al., 2007). L'Asie de l'Est apparaît comme la région du globe où la longueur de panneaux subductés soit la plus importante (18000 km depuis les 150 derniers millions d'années; Kusky et al., 2007).

➤ Entre le Jurassique Supérieur et le Crétacé Inférieur (140-100 Ma)

Le changement des propriétés thermiques et chimiques induit par l'hydratation forte du manteau supérieur conduirait à un amincissement de la racine lithosphérique du craton de Chine du Nord (Charles, 2010). Le retrait du panneau plongeant Izanagi le long de la marge Est-asiatique pourrait être le moteur de l'extension dans le manteau supérieur lithosphérique et dans la croûte (**Figure 16B**; Charles, 2010). Le fort flux thermique issu de la déshydratation des panneaux anciens et de celui d'Izanagi associé au retrait de ce dernier favoriserait l'érosion thermo-mécanique de la lithosphère et le développement de structures

extensives telles que les dômes extensifs dans un contexte de croûte non épaisse (Charles, 2010).

Le manteau supérieur devient progressivement ductile et moins résistant que la croûte, au sein de laquelle se localise toute la déformation. On passe alors d'un modèle « Jelly sandwich » à un modèle « Crème brûlée » (Charles, 2010). La croûte se scinde en boudins séparés par des dômes extensifs. Les dômes extensifs sont exhumés dès 140-130 Ma jusqu'à 110 Ma, marquant le paroxysme de l'extension dans la croûte (Charles, 2010).

La déformation au sein des boudins de croûte est modérée à nulle comme montré par (i) les plutons granitiques (cisaillés ou isotropes) issus de l'importante activité magmatique (dont le pic est daté à 120-130 Ma; Wu et al., 2005a) liée au flux de chaleur important, ainsi qu'au (ii) développement des bassins sédimentaires intracontinentaux avec une forte subsidence tectonique (e.g. Songliao; Ren et al., 2002; **Figure 16B**). Le retrait du panneau plongeant s'exprime en surface par la migration temporelle et spatiale du volcanisme comme montré par Wang et al., (2006). L'étirement dans le manteau, identifiable grâce aux anisotropies sismiques, est vraisemblablement synchrone de celui dans la croûte et pourrait atteindre un maximum entre 140 et 110 Ma (Charles, 2010). Cette période correspond aussi à un ralentissement de la vitesse de subduction de la plaque Izanagi, ce qui favoriserait le retrait du panneau plongeant (Schellart, 2005). De plus, le rajeunissement du manteau lithosphérique mis en évidence par l'étude du système isotopique Re-Os des périclases est probablement synchrone de cette période (Gao et al., 2002). Le Jurassique Supérieur-Crétacé Inférieur est la période la plus favorable pour l'extension et l'amincissement de la lithosphère continentale en Asie de l'Est.

➤ Le Crétacé supérieur (100-65 Ma)

Le panneau Izanagi atteint la zone de transition entre les manteaux supérieur et inférieur. Ainsi, le panneau devient stagnant sous le Craton de Chine du Nord, et son retrait devient moins important (Charles, 2010; **Figure 16C**). La déshydratation du panneau permet la formation de granites du Crétacé supérieur. Le flux de chaleur diminue probablement lié à l'effet de masque du panneau stagnant qui induirait un amincissement lithosphérique moins important comparé au Jurassique Supérieur-Crétacé Inférieur (Charles, 2010). Les conditions thermiques et rhéologiques ne permettent sans doute plus le développement de dômes extensifs. Les sédiments déposés dans les bassins sont liés à la subsidence thermique et non à

une subsidence tectonique (Ren et al., 2002). Le Crétacé Supérieur semble donc être une période de calme tectonique concernant l'extension continentale dans la région.

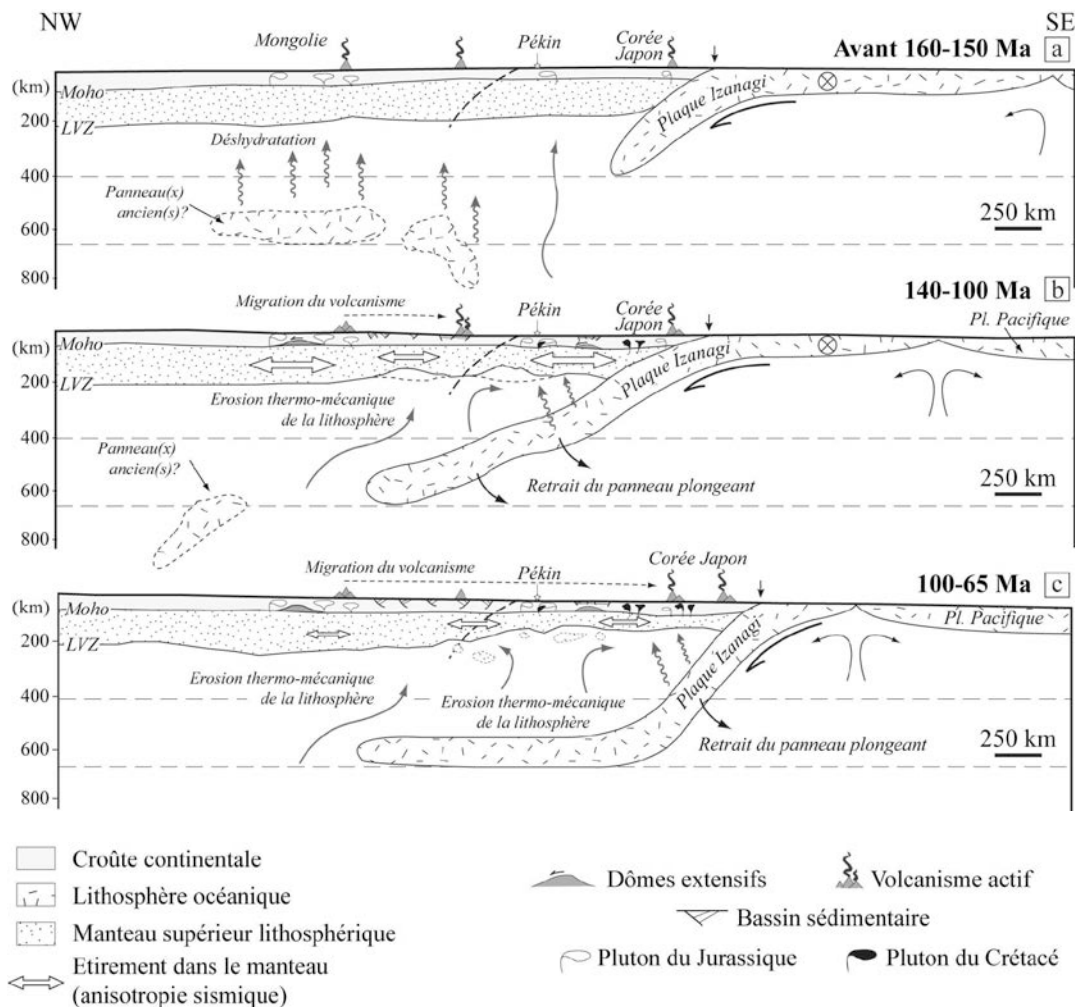


Figure 18. Modèle géodynamique de l'évolution de la marge Est-asiatique entre la fin du Jurassique et la fin du Crétacé (Charles, 2010).

CHAPITRE 2:

CONTEXTE SEDIMENTAIRE ET EVOLUTION

STRATIGRAPHIQUE DES DEPOTS POST-RIFTS DANS LE

BASSIN D'ERLIAN.



Article1: Sedimentology, stratigraphy and palynological occurrences of the late Cretaceous Erlian Formation, Erlian Basin, Inner Mongolia, People's Republic of China.

Christophe Bonnetti^a, Fabrice Malartre^a, Vincent Huault^a, Michel Cuney^a, Sylvain Bourlange^a, Xiaodong Liu^b, Yunbiao Peng^c

^aUniversité de Lorraine, GeoRessources-CNRS-CREGU,
BP239, F54506 Vandoeuvre-les-Nancy, France

^bEast China Institute of technology, 56 Xuefu Road , Linchan, 344000 Fuzhou, Jiangxi, China

^cGeological Team No.208, BOG, CNNC, Baotou, Inner Mongolia, China

Accepted manuscript for publication in Cretaceous Research Journal

1. Abstract

The Erlian Basin is one of the non-marine Cretaceous basins of north-east China that developed during the late Mesozoic continental extension in eastern Asia. This basin experienced two major tectonic events: (i) a syn-rift stage that was dominated by a fluvial-lacustrine depositional environment and (ii) a post-rift stage that was dominated by a fluvial environment. A new sedimentological study performed on Erlian Formation drill cores has led to the determination of an architectural model and to the subsequent characterisation of the stratigraphic evolution of this sedimentary unit during the late Cretaceous. The palynological occurrences that were identified in samples provided a possible stratigraphical age for the Erlian Formation.

Sediments of the Erlian Formation occur at the top of the Cretaceous stratigraphic column of the Erlian Basin and were deposited during the post-rift stage. Facies architecture and the ideal succession of facies that were identified for this formation exhibit two different members, both dominated by a fluvial depositional environment: (i) the lower member, which is dominated by channels of a braided river system and (ii) the upper member, which is dominated by overbank deposits. The lower member expresses a tectonically induced uplift as indicated by channels clustering under negative accommodation, whereas a period of stratigraphic base-level rise that is associated with an increase of accommodation is identified in the upper member. Therefore the Erlian Formation highlights an alternation of short uplifts that were dominated by braided fluvial channel deposits with periods of stratigraphic base-level rise that were dominated by overbank deposits. This sedimentological architecture has significant metallogenetic implications for the origin of confined permeable sandstone layers, which represent adequate host-rocks for roll front-type uranium deposits.

The palynological assemblages identified from the study of five samples belonging to different sedimentary units of the Erlian Basin indicated a Jurassic-Cretaceous age for the Tengge'er Formation and an Aptian-Albian age for the Saihan Formation (occurrence of *Asteropollis*). The next assemblage (*Exesipollenites-Ulmipollenites/Ulmoideipites-Buttinia-Momipites*) recognized in two samples of the Erlian Formation has revealed a post-late Campanian age therefore more likely indicating a late Cretaceous age of deposition for the sediments of the Erlian Formation.

Keywords: Late Cretaceous, Erlian Basin, Erlian Formation, Sedimentology, Stratigraphy, Palynology.

2. Introduction

In north-eastern China, Cretaceous to Tertiary sediments are widely distributed in several fault-controlled sedimentary basins (Sha, 2007), especially in the Heilongjiang, Jilin and Liaoning provinces and in eastern Inner Mongolia. Mesozoic sedimentary basins of north-east China are highly prospective mainly because of their coal-bearing Cretaceous deposits (e.g., the Jixi, Boli, Shuangyashan, Hegang and Fuxin coal basins; RTMCFEH, 1986), oil and gas fields (e.g., in the Daqing and Liaohe oil and gas fields; Ye et al., 1990) and sandstone-hosted uranium deposits (e.g., in the Erlian and Ordos basins; Cai et al., 2007; Dahlkamp, 2009). Energy resources such as uranium deposits are mainly hosted in post-rift sediments that were deposited in a fluvial environment (e.g., the Nuheting and the Subeng uranium deposits hosted in the Erlian Formation of the Erlian Basin, Dahlkamp, 2009; the Qianjiadian uranium deposit hosted in the Yaojia Formation of the Kailu Basin, Cai and Li, 2008). Cretaceous sediments also delivered a lot of amazing paleontological data. For instance, the Yixian Formation of Aptian age is famous for the well-preserved Jehol biota with detailed soft-tissue preservation of the organisms such as plants, freshwater molluscs, early birds, theropod dinosaurs and primitive mammals (e.g., Gu et al., 1976, 1997; SIGMR, 1980; Yu et al., 1987; Chen and Jin, 1999; Sun et al., 2001; Ji et al., 2004;). The Jehol biota and other localities indicate that placental and marsupial mammal dichotomy appeared near the end of the early Cretaceous (Zhou et al., 2003). Among land plants, the most important event was the appearance of flowering plants (e.g. *Archaeofructus*, Sun et al., 2002; Taylor et al., 2009), or Angiosperms, which probably originated in the early Cretaceous (or in late Jurassic) and then rapidly diversified in the late Cretaceous to become the dominant land plants of the Cenozoic (Skelton, 2006). Therefore, the understanding of both the development of these basins and the geological processes leading to the genesis of oil and gas, coal and uranium deposits appears to be a key for exploration and discovery of energy resources. Cretaceous strata of Mesozoic sedimentary basins in north-east China has been the focus of much research since the 1920s (e.g., Granger and Berkey, 1922; Grabau, 1923; Wang, 1929). All of these basins (Sha, 2007; Carroll et al., 2010) mainly developed from the late Jurassic to the early Cretaceous during a major NW-SE continental extension (Charles, 2013). Authors considered the deposition of late Cretaceous sediments (Ren et al., 2002; Meng et al., 2003; Charles, 2013) as part of a post-rift stage likely corresponding to the closure of these basins. However, whereas early Cretaceous sedimentary units are mostly well defined in most of the basins in north-east China (e.g., the Bayanhua Group in the Erlian Basin, Song et al., 1986; Lin et al., 2001), the

stratigraphic scheme of late Cretaceous sediments remains doubtful. Indeed, except for the Songliao Basin where the late Cretaceous sediments have continuously been deposited (Sha, 2007; Li et al., 2011; Wan et al., 2012), late Cretaceous sediments are absent or only partially occur in many other basins because of either a lack of deposition or erosion (Sha, 2007). Therefore, in some basins, such as the Erlian Basin, both the characterisation of the stratigraphic evolution and the determination of accurate biostratigraphic ages of late Cretaceous sediments is of a great interest to better characterise the sedimentological expression of the post-rift stage, part of the tectono-sedimentary evolution of these basins. In the Erlian Basin, sedimentary facies and the depositional environment of the Erlian Formation were characterised from outcrop observations by Currie and Eberth (1993) and Van Itterbeeck et al. (2005). However, no continuous succession of facies along the stratigraphic column of this formation was suitable on outcrops. Therefore no accurate architectural model with stratigraphic evolution has been proposed previously in the literature. A late Cretaceous age was proposed for the Erlian Formation (Rozhdestvensky, 1966, 1977; Brett-Surman, 1979; Gou et al., 1986; Weishample and Horner, 1986; Cai et al., 1990; Jerzykiewicz and Russel, 1991; Currie and Eberth, 1993; Ma, 1994; Van Itterbeeck et al., 2005). Nevertheless, there is a significant distinction according to the species used for dating this formation. Indeed all age determinations that were based on the dinosaur fauna (Rozhdestvensky, 1966, 1977; Brett-Surman, 1979; Weishample and Horner, 1986) indicated a Cenomanian to Santonian age whereas Van Itterbeeck et al. (2005) used charophytes and ostracods to prove a correlation with the Nemget Formation which is considered Campanian-Maastrichtian in age. Only Van Itterbeeck et al. (2007) have presented a description of spores and pollen (i.e., palynology is the most accurate biostratigraphic tool in fluvial palaeoenvironment) and also proposed a late Cretaceous age for the Erlian Formation.

The following study of the Erlian Formation results from a collaborative work between the GéoRessources Laboratory of Lorraine University (France), the East China Institute of Technology (ECIT) and the Chinese National Nuclear Corporation (CNNC). In 2011, a field trip was conducted in the Erlian Basin to (i) characterise the facies architecture of the Erlian Formation occurring in the Erennaoer Sag in the Wulanchabu Sub-basin and (ii) collect drill-core samples from the Nuheting uranium deposit. The main purpose of this paper is to propose an architectural model of the sedimentary facies belonging to the Erlian Formation and to characterise its stratigraphic evolution. Some samples from the Erlian Formation were selected and analysed to identify pollen and spore occurrences.

3. Geological and stratigraphical setting

3.1. The Erlian Basin

The Erlian Basin (or Eren Basin) is located in north-east China (**Figure 17**), Inner Mongolia, near the border of China and Mongolia. This basin occurs in the Northern China – Mongolia Tract (NCMT), to the south of the Mongol-Okhotsk Zone separating the Sino-Korean Craton to the south from the Siberian Craton to the north (Meng et al., 2003). It is an intracontinental basin formed during the Mesozoic continental extension of eastern Asia (Charles, 2013) and framed by the Songliao Basin to the east, the Hailar Basin to the north, the east Gobi Basin to the west and the Ordos Basin to the south-west (Meng et al., 2003).

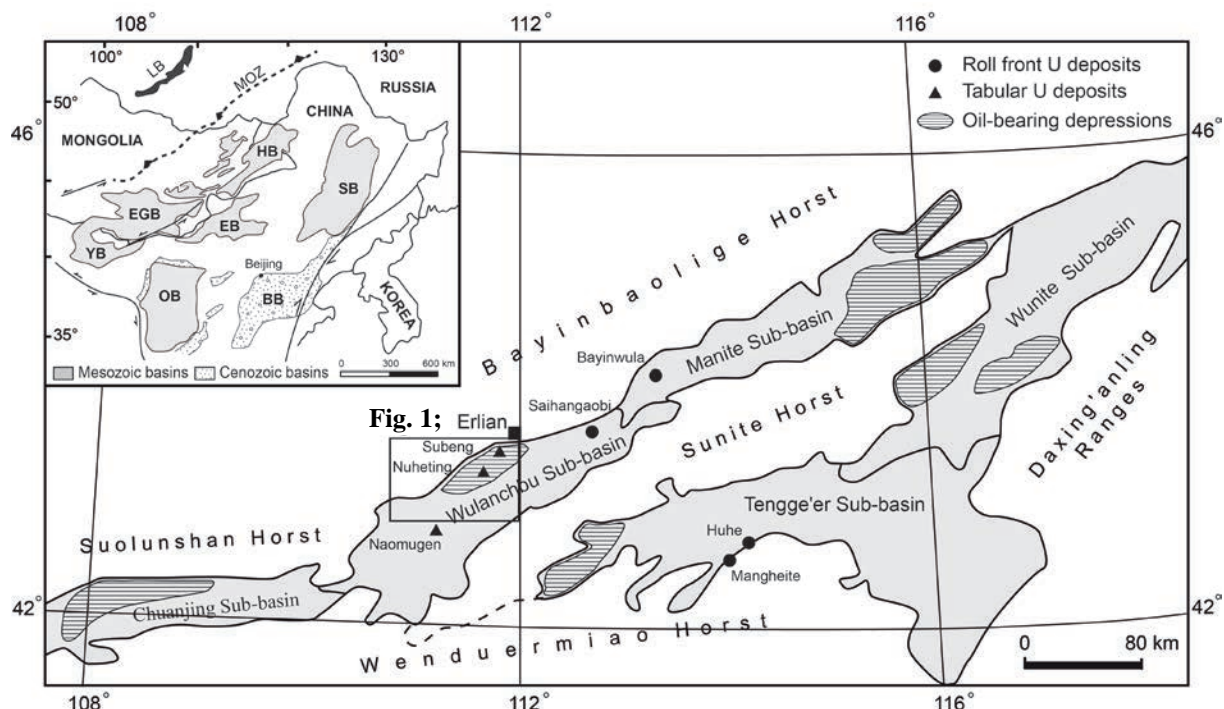


Figure 19. Structural map of the Erlian Basin showing the distribution of uranium deposits and oil-bearing depressions (modified after CNNC, unpublished data; Dou et al., 2003; Meng et al., 2003; Wei et al., 2005; Dahlkamp, 2009). U= uranium, BB= Bohai Basin, EB= Erlian Basin, EGB= East Gobi Basin, HB=Hailar Basin, OB= Ordos Basin, SB= Songliao Basin, YB= Yingde Basin, LB= Lake Baikal, MOZ= Mongol-Okhotsk Zone.

The Erlian Basin lies on a folded and metamorphosed basement corresponding to the southern margin of the Xing'an or Xing Meng Mongolian Orogenic Belt (Lin et al., 2001; Dou and Chang, 2003). The Xing'an Mongolian Orogenic Belt represents the eastern part of the Central Asia Orogenic Belt that was accreted during the Palaeozoic (Zhou et al., 2010). This basement mainly composed of both Palaeozoic and early Mesozoic intermediate to felsic granitic plutons (Wu et al., 2005a, 2005b, 2005c), mafic to felsic volcanic rocks (Chen and

Chen, 1997; Ying et al., 2010) and Proterozoic to Palaeozoic sedimentary or metasedimentary units (Wu et al., 2005b; Zhou et al., 2010). From north to south there is a parallel alternation of horsts and half-grabens that could be related to a “Basin and Range” structural pattern (Wernicke et al., 1988; Ren et al., 1998). The Erlian Basin is divided in approximately 52 half-graben-shaped depressions (Dou and Chang, 2003; Meng et al., 2003) that are controlled by a normal-fault system.

The Erlian Basin is approximately 800 km long and 50-200 km wide, oriented ENE-WSW, and corresponding to a surface area of approximately 130 000 km² (Dou and Chang, 2003; **Figure 18**). It comprises five major sub-basins: the Chuanjing Sub-basin to the west, the Wulanchabu Sub-basin in the central-west, the Manite Sub-basin in the central-north, the Tengge'er Sub-basin in the south-east and the Wunate Sub-basin to the north-east. These sub-basins are framed by a series of horsts or ranges oriented ENE-WSW: the Daxing'anling Ranges to the east, the Bayinbaolige Horst to the north and the Suolunchan Horst further to the west, and finally the Wendurmiao Horst to the south. The Sunite Horst occupies the central part of the Erlian Basin and divides it into two different main parts, north and south (Dou and Chang, 2003).

3.2. Tectono-stratigraphic evolution

The main stage of the Erlian Basin infilling occurred in the early Cretaceous, during the rifting phase (Lin et al., 2001; Meng et al., 2003). The entirety of the depositional systems occurring in the basin corresponds to an intracontinental environment and the sediments are alluvial, fluvial and fluvial-lacustrine (Lin et al., 2001). The accommodation in the basin is controlled by the combination of several factors such as tectonic subsidence, lake-level variations, sedimentation rate and climatic changes (Lin et al., 2001). The Erlian Basin developed in three main tectonic stages that are bounded by two major unconformities (Graham et al., 2001) and associated with different stratigraphic units, various depositional systems and lithologies (Lin et al., 2001; Sha, 2007; **Figure 1:**).

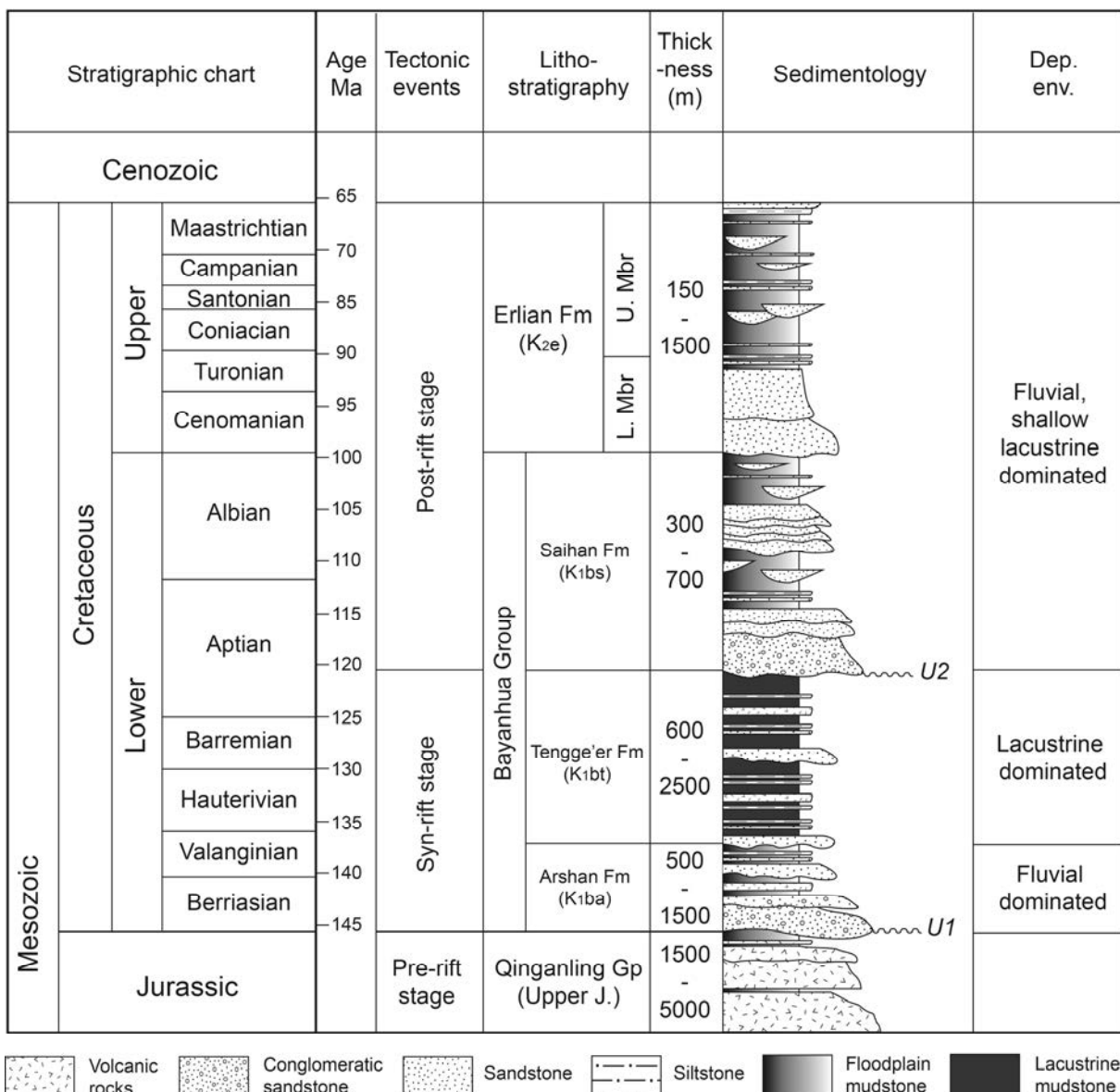


Figure 1: Tectono-stratigraphic log of the Erlian Basin (modified after Gou et al., 1986; Cai et al., 1990; Dou, 1997; Graham et al., 2001; Lin et al., 2001; ICS, 2006; Wang et al., 2006; Sha, 2007; Van Itterbeeck et al., 2007; Li et al., 2011; Scott et al., 2012). J.= Jurassic; U1= Unconformity 1; U2= Unconformity 2.

3.2.1. The pre-rift stage

This stage is mainly characterised by late Jurassic to very early Cretaceous volcanic rocks of the Qinganling Group (156.0 – 142.6 Ma; Chen and Chen, 1997; Graham et al., 2001; Wang et al., 2006) and corresponds to the initiation of the rifting stage. A major unconformity at the bottom of the basin (Graham et al., 2001; Lin et al., 2001; U1 in **Figure 1**) shows the transition from the pre-rift to the syn-rift stage. Erosion of the top part of volcanic rocks from the Qinganling Group by the alluvial and fluvial sedimentary system of the Arshan Formation is at the origin of the unconformity.

3.2.2. *The syn-rift stage*

This stage corresponds to early Cretaceous stratigraphic units represented by sedimentary formations belonging to the Bayanhua Group (Gou et al., 1986; Cai et al., 1990; Sha, 2007): the Arshan (or Alashan) Formation (K_{1ba}) that is dominated by alluvial, fluvial and shallow lacustrine environments and the Tengge'er Formation (K_{1bt}) that is dominated by a deep to semi-deep lacustrine environment. This stage is characterised by a strong tectonic subsidence in which listric normal faults have controlled the development of half-grabens occurring in the Erlian Basin (Meng et al., 2003). The syn-rift sediments are relatively thick (Dou and Chang, 2003) and contain abundant volcanic intercalations (Shuvalov, 2000).

3.2.3. *The post-rift stage*

Post-rift sediments in the Erlian Basin are characterised by the early Cretaceous Saihan or Saihantala Formation (K_{1bs}) and the late Cretaceous Erlian (Erendabusu or Irendabasu) Formation (K_{2e}), both dominated by fluvial and shallow lacustrine environments (Currie and Eberth, 1993; Lin et al., 2001; Van Itterbeeck et al., 2005). The post-rift late Cretaceous strata are relatively thin (Dou and Chang, 2003) and devoid of volcanic rocks (Shuvalov, 2000). The post-rift stage began at the end of the early Cretaceous (Dou, 1997; Lin et al., 2001), precisely during the Aptian, when the thermal subsidence replaced the tectonic subsidence (Ren et al., 2002; Charles, 2013). Then, the Erlian Basin was in a regime of relative uplift resulting from a weak NW-SE compression (Wei et al., 2005) caused by the subduction of the Pacific plate towards the Eurasian continent. The transition between the syn-rift and the post-rift stages in the basin is shown by a major unconformity (Graham et al., 2001; Lin et al., 2001; Nie, 2008; U2 in **Figure 1:**) separating the sediments of the Tengge'er Formation from those of the Saihan Formation. Indeed, the evolution of the tectonic regime and consequently the variations of the sedimentary system are shown by a transition from a deep-lacustrine dominated depositional environment during the syn-rift stage to a fluvial-shallow lacustrine dominated environment during the post-rift stage. Moreover a tectonically induced uplift is evidenced in a seismic profile presented in Nie (2008) by an angular unconformity between top sediments of the Tengge'er Formation which have been tilted and basal channels of the Saihan Formation which are in erosional contact with those sediments. This is why the second unconformity has been placed at this boundary and not between the Saihan and Erlian formations even though the Erlian Formation is the first unit to extend over the rift shoulder.

3.3. Overview of the study area

The selected area for this study (**Figure 3;**) is in the central-north of the Wulanchabu Sub-basin, a well preserved part of the Erlian Basin. Here, the sediments of the Erlian Formation occur in the Erennaoer Sag and host the Nuheting and the Subeng uranium deposits (Dahlkamp, 2009). The study was performed around the Nuheting deposit which is 40 km to the south-west of Erlian City. The Erlian Formation defined by Granger and Berkey (1922) and formally described by Berkey and Morris (1927), and Zhang (2009) crops out to the west of the Nuheting deposit. However, good exposures are extremely rare and limited to undulating low-relief ridges, denuded (treeless, grassy) and rounded hills (typical “steppe” landscape and associated geomorphology) and small valley cuttings of a few recent ephemeral rivers.

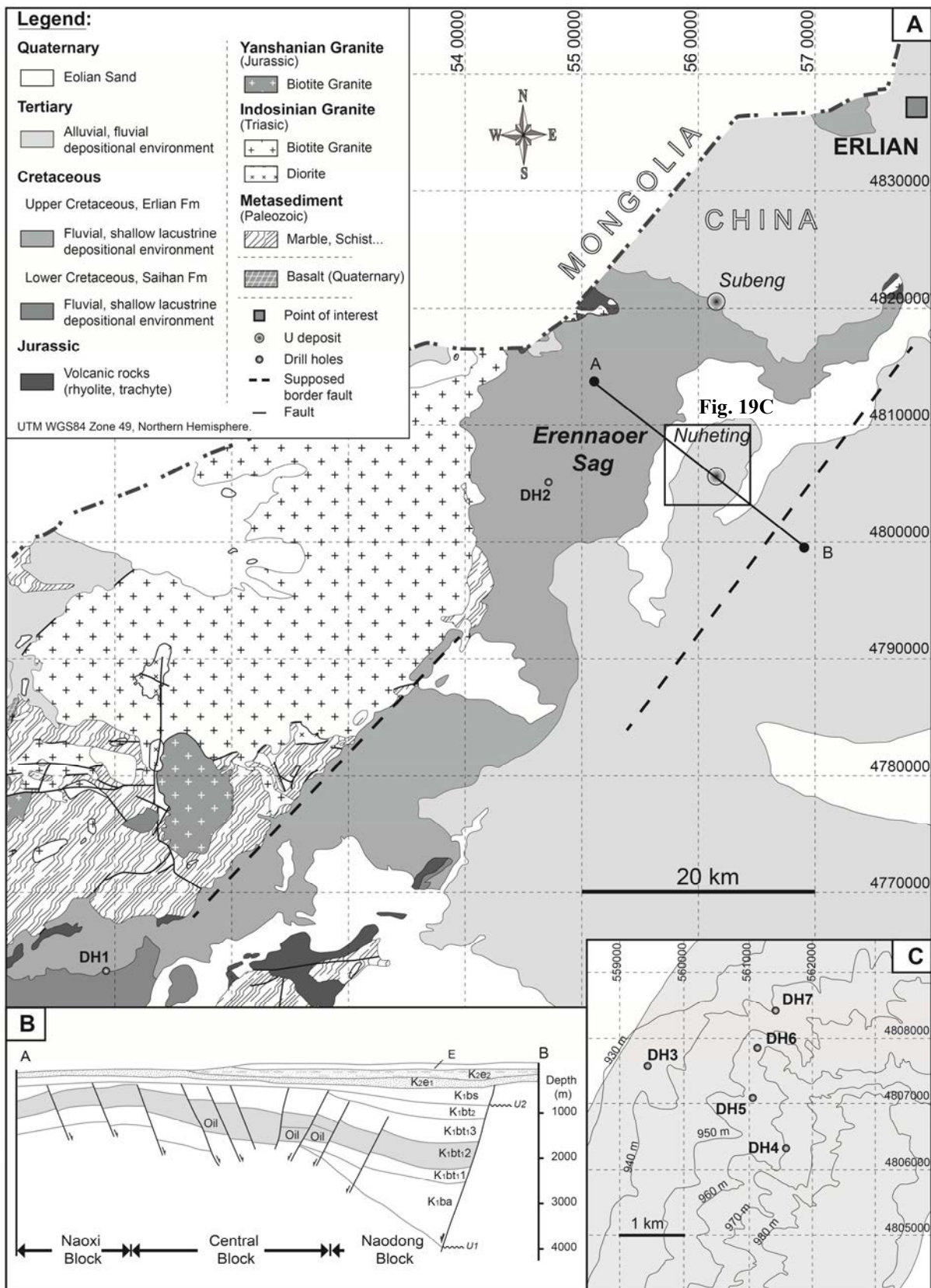


Figure 3; . A= Geological map of the central-northern part of the Wulanchabu Sub-basin, Erlian Basin (modified after CNNC, unpublished data). U= Uranium. This map shows (i) the location of the A-B cross-section; and (ii) the location of the Nuheting area (Figs. 19B, C). B= Cross-section of the Erennaoer Sag (modified after Dahlkamp, 2009). K₁ba= Arshan Formation; K₁bt₁1, K₁bt₁2, K₁bt₁3 and K₁bt₂= Tengge'er Formation; K₁bs=

Saihan Formation; K₂e₁= lower member of the Erlian Formation; K₂e₂= upper member of the Erlian Formation; E= Eogene. U1= Unconformity 1; U2= Unconformity 2. C= Topographic map of the Nuheting area showing the location of drill holes DH1 to DH7 (modified after CNNC, unpublished data). DH1= Drill hole 1...to DH7= Drill hole 7.

4. Materials and methods

The complete study of both facies model and palynological occurrences of the Erlian Formation presented in this paper was drill-core samples from seven drill holes (DH) and on collected during a field trip that was conducted in 2011. Regarding the very poor outcrops of the Erlian Formation in the study area, it was very beneficial to obtain access to cores recovered during drilling in connection with uranium exploration to recover the most continuous stratigraphic record of this sedimentary unit. However, the drilling characteristics (e.g., low drill core recovery in some studied drill holes or mud injection) and the low quality of drill core preservation of some sections have limited certain observations (e.g., hidden or destroyed sedimentary structures).

DH3 to DH7 located around the Nuheting deposit were logged to build the facies model of the Erlian Formation. Lithofacies were characterised and architectural elements were identified by facies association, using the formal method of field architectural element analysis (see Miall, 1996). This field work led to the characterisation of the main depositional environments of the Erlian Formation.

The aim of the palynological investigations in the Erlian Formation was mainly to test the abilities of palynology to improve the stratigraphic framework in such non-marine deposits. Therefore, the focus has been on diagnostic palynomorphs that are able to support accurate biostratigraphic age determination.

Five samples have been processed for the palynological study. They were collected in fine-grained facies such as floodplain fines rich in organic matter that contain the best conditions for pollen preservation. These samples come from DH1, DH2, DH4 and DH5 (**Figure 3;**). DH1 is located in the south-western part of the study area and penetrates both the Tengge'er Formation (in the lower part) and the Saihan Formation (in the upper part). Two drill-core samples were collected to characterise pollen assemblages of these two sedimentary units. DH2 is located to the West of the Nuheting deposit and penetrates both the Saihan Formation (in the lower part) and the Erlian Formation (in the upper part). One sample has been collected in DH2. Finally DH4 and DH5 are located in the Nuheting area and penetrate the sediments of the Erlian Formation. One sample was collected in each of these drill holes to

characterise the pollen assemblage of the Erlian Formation. Sample preparation was conducted at the EPOC laboratory at Bordeaux University (France). Samples were subjected to a successive standard hydrochloric and hydrofluoric acid digestion. They all proved to be palynologically productive and yielded organic residue. The quality of preservation is variable but globally remains quite good. The pollen characterisation and the pollen counting were conducted at the G²oRessources laboratory at Lorraine University (France). Three slides were mounted for each sample. To ensure a good statistical value, the aim of the analysis was to identify, when possible, at least 100 palynomorphs on each slide.

5. Facies model of the Erlian Formation

To build the facies model of the Erlian Formation, the different lithofacies were first determined (**Figure 42, Table 1**) while logging drill cores from the Nuheting deposit. The lithofacies presented in **Figure 42** correspond to a compilation of the most representative facies that were observed in the different studied drill holes. Then, major architectural elements resulting from facies associations (**Table 4**), such as large channels and floodplain fines of this sedimentary unit, were identified. The facies architecture and the evolution of the ideal succession of facies during the deposition of sediments belonging to the Erlian Formation led to the characterisation of the main depositional environments. In the Erennaor Sag, the Erlian Formation is approximately 50 m thick and can be subdivided into two members (**Figure 43**): (i) a lower member that is dominated by multi-story coalescing of erosional channel fill units and (ii) an upper member in which overbank sediments accumulated.

5.1. Lithofacies and sedimentary structures

All recognized facies on drill cores belong to siliciclastic rocks. They range in grain size from coarse-grained to fine-grained sediments (**Figure 22, Table 1**). As a preamble to describe and interpret the fine-grained facies, we note that there is no evidence of bioturbation. However, this apparent lack of biological animal activity may be because of both the restricted investigated volume of sediments from cores and the low quality of core preservation. These lithofacies were described using the classification of Miall (2010).

5.1.1. Sand

Sand facies are poorly sorted, with locally very few gravels, and with major sub-angular to sub-rounded grains (**Figure 22A**). The presence of quartz and some feldspar indicates a sub-arkose composition. Moreover, this lithofacies presents peculiar 10 cm to 2 m thick secondary oxidized red (**Figure 22B**), orange or yellow (**Figure 22A**) layers, because of the presence of either haematite or limonite. Some problems occurred with apparently massive sandstones, because sedimentary structures may be often hidden. Internal-bed sedimentary structures are scarce and poorly preserved in that type of relatively coarse-grained facies. When developed, some slightly curved or planar lamination (foresets) may be observed with no evidence of clear grain size sorting. These laminations can be related to solitary or stacked trough crossbeds (St) or planar crossbeds (Sp). **Figure 22A** shows a large scale planar lamination partially cut by the drill-core. The lamination belongs to large tractive bedforms such as transverse dunes. The other type of cross-lamination (poorly preserved) may correspond to linguoid dunes. The sedimentary structures that are associated with this lithofacies show variability in detailed internal geometry and represent a deposition under velocity variations (but both at lower flow regime) during the transport and the deposition of the sedimentary sandy volumes.

Concerning the lithology, another sand facies (Sr) is coarse to very fine grained, with major sub-angular to sub-rounded grains of quartz and some rare feldspar (quartz-arenite composition), mostly well sorted, and much more cohesive (**Figure 22C**) than sand St or Sp. It occurs as 10 cm to 3 m thick reduced grey or partially oxidised orange layers with some ripple cross-lamination (CNNC observation), indicating a lower flow regime. Very fine (< 1 mm) phytoclasts or coal debris are disseminated within the sand.

5.1.2. Sand, silt and mud

This facies comprises an alternation of sand, silt and mud (Fl), is fine laminated (mm to cm thick, **Figure 22D**) and with very small-scale cross-stratification. The clear lamination is because of the repetitive grain size variation. It consists of even, thinly (but apparently not rhythmically) interstratified and graded mudstone, siltstone and very fine-grained sandstone (triplet lamination). Large phytoclasts, often associated with pyrite, were observed parallel to the lamination plane. Individual laminations are separated one from another by sharp contacts caused by abrupt changes in grain size. Within very fine-grained sand packages, the lamination is horizontal or wavy. Very fine sands present geometrical structure variations that are associated with a continuous or discontinuous lamination. They locally show slightly

erosive, scoured bases that cut into underlying deposits. Sometimes, they can be lenticular and display a small-scale mounded shape. Silt and mud are more likely to be continuous and represent very weak currents to suspension-dominated hydrodynamic conditions. This fine lamination is sometimes destroyed most likely by the flowage of soft mud (micro-slides) that induced soft-sediment deformation structures (**Figure 22D**, lower part of the core). This type of structures has registered the events and the rheological conditions occurring in the environment between each depositional stage. Indeed, the deformed layers are covered by non-deformed ones. Small-scale cross strata are formed by oscillation processes marking the ultimate stage of the waning flood. The horizontal bedding was formed by settling of suspension clouds under low-energy conditions as a result of turbulence decrease with receding water. This alternating facies resulted from bed loads (very fine-grained sand) and suspended loads (silt and mud) over the floodplain during overbank flood.

5.1.3. Silt and mud

This facies (Fsm) presents 10 cm to 2 m thick light to dark grey or black layers with massive organisation and a large amount of disseminated pyrite and coal debris (**Figure 22E, F**). No obvious lamination and primary sedimentary structures are visible. This structureless facies, which reflects an original lack of depositional layering, may be related to a very homogeneous steady depositional process. The main noticeable criteria of this facies compared to the previous one is that it is devoid of sand, except for some disseminated and rare floating coarse grains. The amount of carbonaceous remains and associated pyrite suggest a swamp depositional environment (used here as a poorly drained distal floodplain), where reduced conditions are at least semi-permanent. The primary framboidal shape of part of the pyrite that was observed reflects a bacterial origin (living under anoxic water conditions, *sensu* Diessel, 1992) and therefore provides the evidence of a reduced state of the depositional environment. This facies may sometimes have a superimposed orange network (**Figure 22E**). This centimetre-scale 3D-geometry corresponds to primary voids that are subsequently filled with ferruginised silts. Moreover, there is no clear leached horizon development. The branching pattern that is associated with thickness variations (cm to mm) may be interpreted as roots. According to Reinhardt and Sigleo (1988) and Retallack (1997), it corresponds to a very weakly developed stage of palaeosols within a fresh-water peatland. This facies may also show intrasediment evaporite growth. The habitus of the evaporites is not concretions or glaebules but occur here as millimetre to centimetre, well-developed crystals that can be

isolated in the sediment (**Figure 22E**) or form aggregates. Two main forms can be recognised: elongate, acicular, needle gypsum, and classic arrow-head gypsum. The occurrence of evaporites appears to be facies-controlled as none of them were observed in other facies. Moreover, there is no true evaporite layer. Therefore, this observation indicates a primary crystallization, within the depositional environment is partly induced by chemical or biochemical processes. Indeed, the organic sulphur is mineralised more or less quickly in pyrite by numerous micro-organisms especially in anaerobic to dysoxic conditions. Next, FeS₂ was oxidised in an aerobic environment to provide sulphates under the effect of chimiolithotrophic bacteria, such as *Thiobacillus* (Rackley, 1972; Casagrande, 1987; Mustin et al., 1993; Canfield and Farquhar, 2012).

5.1.4. Mud

This facies (Fm) consists of a massive, non stratified, isotropic, brown, grey, black (**Figure 22G**) or beige (**Figure 22H**) mud. It corresponds to the most distal floodplain facies that were encountered in the Erlian Formation which were deposited in floodplain ponds (may be ephemeral). Locally, carbonates were found in beige mud by hydrochloric acid test on cores. Therefore, we may have at least seasonal standing waters where subordinate chemical carbonate sedimentation can occur and mix with clay minerals. It would be a little surprising to produce and preserve carbonates in such acidic, organic-rich environments. Maybe this peculiar facies could have developed in a relatively protected area with very low input of organic matter. The occurrence of different types of authigenic carbonate minerals (such as siderite, dolomite, ankerite and calcite) has been reported in such peat-rich depositional environment (Treese and Wilkinson, 1982; Bustin et al., 1989; Brown and Cohen, 1995; Cabrera et al., 2002).

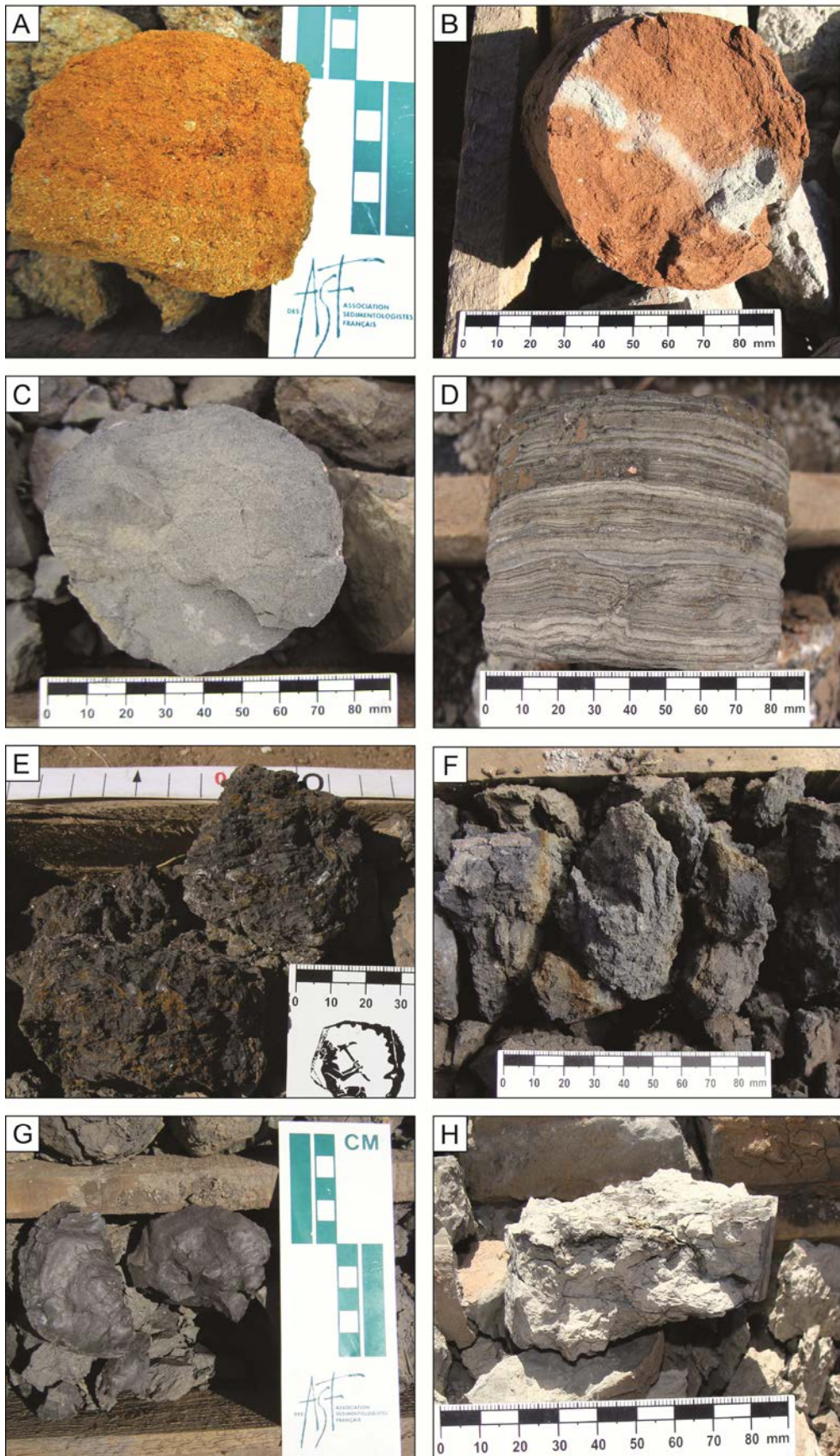


Figure 22. Lithofacies observed in the Erlian Formation. A= coarse-grained oxidized orange sandstone with planar lamination; B= secondary oxidized red fine-grained sandstone with remnant of primary reduction;

C= very fine-grained reduced grey sandstone; D= finely laminated sand, silt and mud; E= root network and gypsum-bearing black silty mudstone; F= massive dark grey silty mudstone with minor secondary oxidation along silty pathway; G= black mudstone; H= beige calcareous mudstone.

Table 1. Lithofacies identified within the Erlian Formation (using the classification of Miall, 2010).

Facies code	Lithofacies	Sedimentary structures	Interpretation
St	sand, fine to v. coarse, with floating gravels	curved laminations (foresets): solitary or stacked trough crossbeds	large tractive bedforms: may correspond to sinuous-crested and linguoid (3-D) structures
Sp	sand, fine to v. coarse, with floating gravels	planar laminations (foresets): solitary or stacked planar crossbeds	large tractive bedforms: may correspond to transverse and linguoid (2-D) structures
Sr	sand, v. fine to coarse	ripple crosslamination	bedforms deposited in a lower flow regime
Fl	sand, silt, mud	Horizontal lamination, massive	overbank, waning flood or pond deposits
Fsm	silt, mud (organic matter-rich)	massive	back-swamp deposits
Fm	mud	massive	pond deposits

5.2. Facies architecture

The major key classification (Miall, 2010) criteria are the grain size distribution and trends, and the internal architecture. The facies architecture of the Erlian Formation is characterised by the succession and the geometry of architectural elements such as channels, crevasse splays and floodplain fines (**Figure 23; Table 2**). These architectural elements are described using the classification of Miall (2010).

5.2.1. Channels

Channels (CH) present a facies association of sand with either trough crossbeds (St) or planar crossbeds (Sp) and sand with small ripple cross-lamination (Sr) in the case of a lower flow regime. Here, the lithofacies show a gradational upward-fining succession. The scale and the shape of these sand bodies are highly variable and can occur as fingers, lenses or sheets with concave-up erosional bases. Fining-up successions are common and well developed if coarse-

grained sands appear at the frequently erosive beds. As previously mentioned, trough cross bedding is a characteristic for the appearance of massive sandstones. Often there are a few preserved laminations (i.e., no clearly visible sedimentary structures). As the major part of the sandstone appears to be structureless, low inclined discrete surfaces may represent accreting sandy forms (downstream bars?). The transport and deposition of the sandy bed load is important and the channel would be filled by multiple, stacked, and multi-scale bar-form structures. During variations of flow velocity, modifications of the structures are registered. In particular, small scours can cut into sandy bars, and erosion may form reactivation surfaces. The sands appear homogenous and present few preserved muds until the top of the section. Amalgamation surfaces are sometimes recognisable. The individual channels are stacked to form multi-story channel belts. The thickness of (CH) elements ranges from 5 to 10 metres. The lateral extent of single channels cannot be precisely determined.

5.2.2. Crevasse splays

Crevasse splays (CS) show a facies combination of medium to fine-grained sand (St or Sr), silt and mud (Fl). In core sections, this association is recognised by the most representative facies: thinly bedded (millimetre-scale) nature of the sandstone units, which show sharp bases and silt-mud alternate laminations. It often occurs with floating very coarse grains to small gravels. The tabular sandstones record the delivery of sands as sheet-like crevasse splays spreading out over low relief floodplains away from the margins of the main channels. Usually crevasse splays can occur as lens of 0.1-6 m thick and their lateral extension may reach up to 10 by 10 km, but cannot be precisely determined here.

5.2.3. Floodplain fines

Floodplain fines (FF) are composed of lithofacies Fl, Fsm and Fm that may build lateral sheets of many kilometres and up to tens of metres thick. They correspond to deposits of overbank sheet flow, floodplain ponds and swamps. The floodplain fines consist of finely laminated clay, and silty clays, and massive mudstones. They mark the more distal setting in the Erlian Formation depositional environment.

The ideal facies succession (**Figure 23**) of the Erlian Formation corresponds to a 5-10 m thick gradational sequence that is both fining-upward and thinning-upward. Regarding the facies

architecture of the formation, this ideal succession of facies characterises the transition from channels to overbank.

Table 4. Architectural elements identified within the Erlian Formation (using the classification of Miall, 2010).

Symbol	Element	Principal facies assemblage	Geometry and interpretation
FF	Floodplain fines	Fl, Fsm, Fm	Sheet, may be many km in lateral dimensions, up to 10s of m thick. Deposits of overbank sheet flow, floodplain ponds and swamps.
CS	Crevasse splay	St, Sr, Fl	Lens (0.1-5 m thick); delta-like propagation into the floodplain from the margins of main channels.
CH	Channels	St, Sp, Sr	Finger, lens or sheet with concave-up erosional base; scale and shape are highly variable; the individual channels are stacked to form multi-story channel belts.

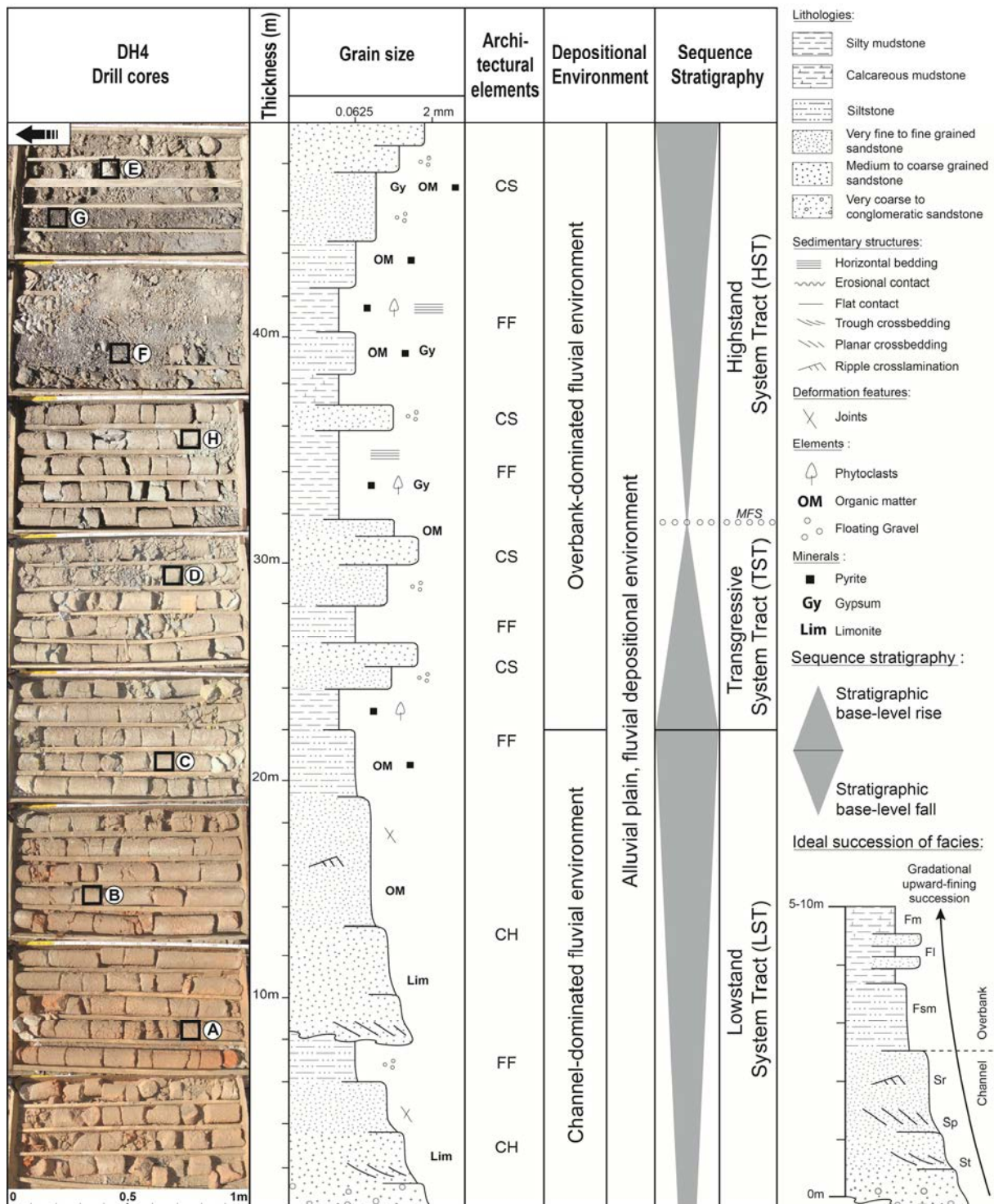


Figure 23. Summary log of the Erlian Formation correlating facies architecture, depositional environments and sequence stratigraphy. For lithofacies see facies code in table 1. For architectural elements see symbol definition in table 2. The column to the left shows drill cores from DH4 (Drill hole 4) presenting the most complete and representative stratigraphic recovery of the Erlian Formation. Squares A to H refer to lithofacies photographs presented in figure 20. They show the relative position of the different lithofacies within the stratigraphic column of the Erlian Formation. The black arrow on the top left part indicates the drill core reading direction, from the bottom to the top and from right to left. MFS= Maximum Flooding Surface.

5.3. Depositional environments

In the lower part of the Erlian Formation, channels display a homogenous, largely mud-free fill. The lower part is dominated by a high ratio of load (mainly sands) to discharge with much suspension bypassing and/or a high ratio of fine-grained facies erosion. Multiple erosive lags, elementary sedimentary structures that are organised as single metre-scale fining-upward units, suggest a flow velocity and flow turbulence that is consistent with channelised deposition. As a consequence, there is restricted floodplain with only few thin, very discontinuous silty clay caps of sandy channels. In the upper part of the sedimentary Erlian system, there is an extensive deposition of overbank dominated facies. Floodplains overlie fine-grained fill with a few channel sands, and swamps with the deposition and preservation of organic matter (peat) are common.

Overall, the facies architecture and the succession of facies of the Erlian Formation characterise an alluvial plain depositional environment which is consistent with the works presented in Currie and Eberth (1993) and in Van Itterbeeck et al. (2005). The new facies architecture based on drill core material that is presented in this paper indicate two different members (**Figure 23; Figure 24**): (i) the lower member, belonging to a braided channel-dominated fluvial environment (multiple channel filling and then abandonment) and (ii) the upper member, corresponding to an overbank dominated fluvial environment (overbank flow of bed load sandy deposits within fine-grained, low-energy sediments).

5.3.1. The lower member of the Erlian Formation

The lower member (~20 m) of the Erlian Formation shows facies that can be interpreted as a channel dominated fluvial environment. It presents sandy braided channels with minor preserved floodplain deposits (**Figure 23; Figure 24**). Internally, these channels are constructed of planar cross-bed sets. Smaller 3-D dunes building trough cross-bed sets may be in deeper channels. Extensive sheets of in-channel, lower flow-regime dunes may occur with deposits typically dominated by either lithofacies Sp or St, but those do not occur together because they represent dune types formed under different hydraulic conditions. The lithofacies Sr usually follow the deposition of lithofacies Sp and St within a lower-flow regime of in-channel sand fill. This member is secondary oxidised indicating that oxygenated fluids have flowed through. The fluvial style corresponds to a shallow, perennial, sand-bed braided river such as most of the Platte River of Colorado and Nebraska (Miall, 2010). This type of braided river is characterised by the presence of large, flat-topped 3-D dunes fields,

which are active during high water stages (Miall, 1996). These rivers were braided only during low discharge stages, when the tops of the dunes were exposed. At times of high discharge, they occurred as single, very broad, shallow channels occupying almost the full width of the floodplain. Therefore, fine-grained floodplain deposits constitute a minor part of the lithofacies assemblage (Miall, 1996).

5.3.2. The upper member of the Erlian Formation

The upper member (~ 30 m) of the Erlian Formation is a succession of facies that may be interpreted as an overbank dominated fluvial environment. It shows minor channel occurrence, more likely anastomosed or abandoned channels, and major well-preserved storage of floodplain fines (**Figure 23**; **Figure 24**). Within the floodplain deposits it is possible to distinguish crevasse splays spreading from the crevasse channel into the floodplain, swamp and shallow lake or floodplain pond. Anastomosed channels correspond to a system of interconnected channels flowing through large swamp areas, such as observed in the Magdalena River in Columbia or parts of the Columbia River in British Columbia (Miall, 2010). They are relatively stable in position, isolated and bounded by floodplain deposits. These are normally fine grained and their evolution takes the form of crevasse channels. Channel bodies are typically straight to sinuous ribbon sandstone (Miall, 1996) and show minor lateral migration. Floodplain deposits are characterised by swamp or shallow lacustrine silts and muds which may contain pond deposits, coals, calcretes, or evaporites depending on the climate. Crevasse splay deposits are also very common.

These types of depositional environments that are dominated by floodplain deposits are highly favourable for preserving detrital organic matter, such as phytoclasts, coal debris or pollen because of their suboxic to anoxic characteristics.

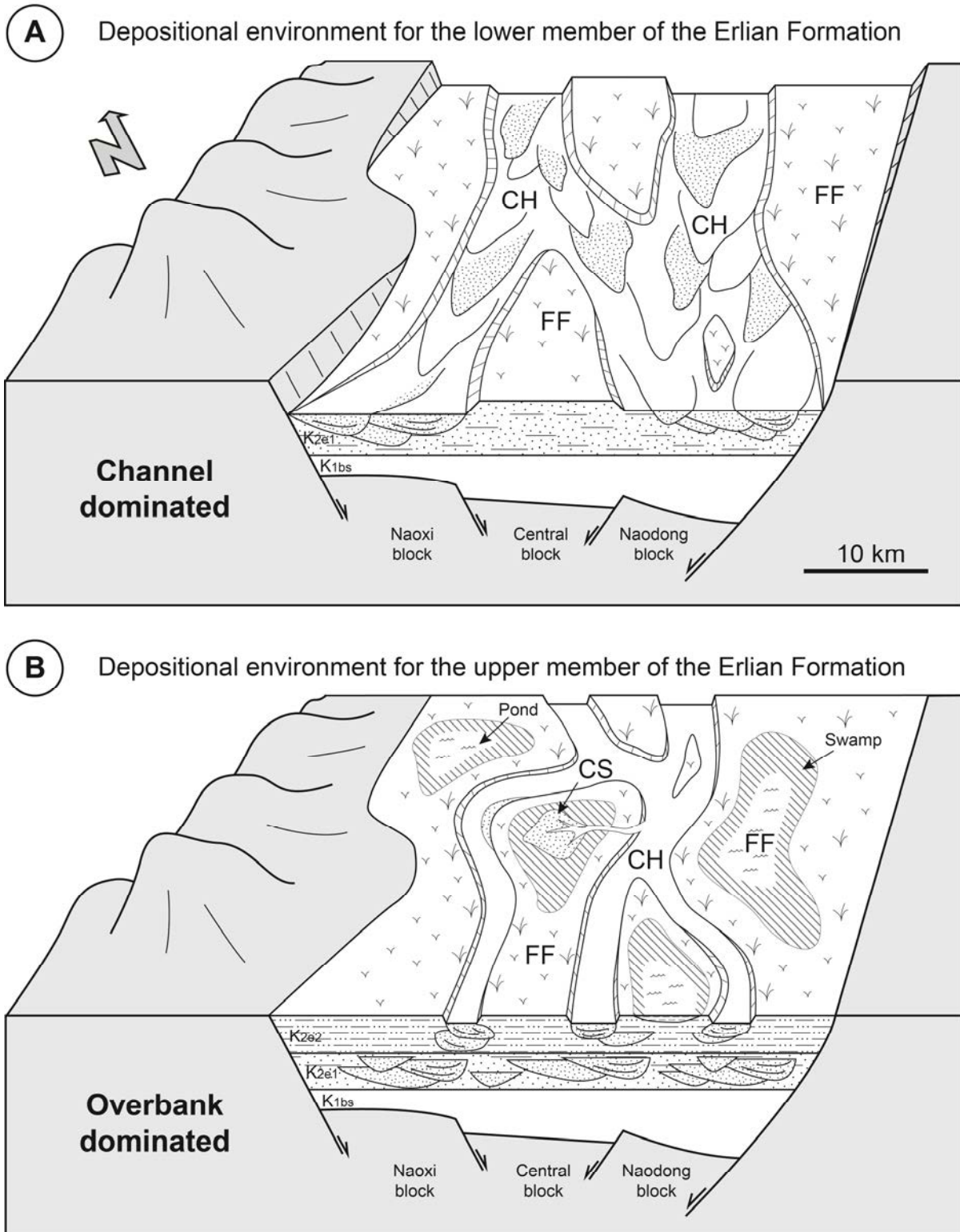


Figure 24. Architectural model of the Erlian Formation (modified after Miall, 2010). A= depositional environment for the lower member of the Erlian Formation; B= depositional environment for the upper member of the Erlian Formation. For architectural elements see symbol definition in table 2.

6. Stratigraphic evolution of the Erlian Formation

The main problem encountered when providing a complete reconstruction of the depositional environment belonging to the Erlian Formation is the scarcity of good natural outcrops. Nevertheless, Currie and Eberth (1993) and Van Itterbeeck et al. (2005) previously proposed a general model of a braided river valley to explain lateral and vertical changes within the Erlian Formation.

As stated by Miall (1996), braided rivers tend to occupy most of their alluvial valley, leaving little spatial development for floodplains. Thus, in classical model of braided rivers, fine-grained floodplain deposits constitute a minor part of the lithofacies assemblage. The most important autocyclic process is the change of channel location. Channels may change in location, shape and thickness by gradual lateral movement, or they may change entirely in position to another part of the floodplain by episodic shifting (Miall, 1996). The avulsive shifting of braided channels is an integral part of the braiding process. Within braided fluvial systems, the lateral extent of floodplain fines is unlikely to be greater than a few hundred meters (Miall, 1996).

As stated previously (see Materials and methods), five drill cores (DH1 to DH5) were studied in order to log the succession of facies. All logs display identical vertical evolution and have been divided into two members. All cores are at least few hundred meters to a kilometre away from the others (**Figure 19**) and belong to an area of approximately 10 km². Therefore, the lateral extent of these two members and their vertical thickness (20 to 30 m for the lower member and more than 30 m for the upper member) may support an allocyclic fluvial evolution of preserved lithofacies within each member rather than a simple shift from major braided channels to fine-grained floodplain deposits because of avulsion. Consequently, the vertical succession of facies within the Erlian Formation does not purely reflect a local evolution under autogenic processes but rather register basin-scale stratigraphic trends. Although, fluvial deposits are difficult to interpret because of the frequency of lateral facies changes and the lack of (i) individual beds distinctiveness, (ii) laterally extensive marker-beds (palaeosol, coal, etc.), and (iii) a continuous stratigraphic record.

Therefore, the evolution between the two members of the Erlian Formation can be interpreted in terms of relative base-level changes. As stated in several studies (Schumm, 1977, 2006; Shanley and McCabe, 1994; Miall, 1996; Ethridge et al., 1998; Marriott, 1999; Posamentier and Allen, 1999; Schumm et al., 2000), the processes of fluvial changes (regarding aggradation or incision) occur in order to allow the rivers to adjust to equilibrium profile

variations. The response of fluvial systems to base level changes may be assessed in relation to sea-level connected sedimentary systems that register normal versus forced regressions and transgressions. However, here, there is no evidence of a connection with the sea. The sediments of the Erlian Formation were deposited within an intracontinental basin (Meng et al., 2003; Charles, 2013), and thus are beyond the reach of any marine influence similar to many other North China basins. Nevertheless, the fluvial facies evolution of cores belonging to the Erlian Formation is clear enough to propose a sequence scheme, even if this interpretation should be made with caution (complex interrelationships between base level changes, climate, and sediment-supply are difficult to separate). Subsidence is the critical factor that controls sedimentation and the resulting facies and strata architecture of the Erlian Formation.

The lower member first recorded a situation of negative accommodation. The fluvial system responded by downcutting earlier deposits (Saihan Formation -K₁bs- where present or lower units) which are characterised by stacked high-energy channel facies that are associated with the low preservation of fine-grained facies. They mark the loss of accommodation space and are good candidate to call the sequence boundary. Therefore, stacked upward fining successions with no or few preserved fine-grained facies (**Figure 21**) may be attributed to the lowstand system tract (LST). This major phase of channel clustering can be explained by tectonically induced uplift, which is consistent with a post-rift event. This geological setting is characterised by the relay from tectonic subsidence occurring during the early Cretaceous to thermal subsidence (Ren et al., 2002; Meng et al., 2003; Charles, 2013) which becomes dominant during the late early Cretaceous with the deposition of the Saihan Formation (Dou, 1997; Lin et al., 2001) and allows much less accommodation for sediments. Moreover, Wei et al. (2005) indicate that the Erlian Basin was in a relative uplift regime during this period, resulting from weak NW-SE compression caused by the subduction of the Pacific plate towards the Eurasian continent. The transition between the syn-rift and the post-rift stages in the basin is shown by a major unconformity (Graham et al., 2001; Lin et al., 2001; Nie, 2008; **Figure 18**) separating the lacustrine sediments of the Tengge'er Formation from the basal fluvial channels of the Saihan Formation, although the syn-rift sediments mainly accumulated in depocentres of half-grabens, whereas post-rift sediments were not only restricted to half-grabens and recovered a much larger surface of the basin.

Next, a stratigraphic trend inversion can be identified with the beginning of the upper member of the Erlian Formation when fine-grained facies were continuously more and well preserved. The general trend that is observed is an increase in overbank-generated facies (mainly

registered by the preservation of crevasse splays). Thus, this member recorded an increase of accommodation at the onset of a period of stratigraphic base-level rise. We place the maximum fluvial flooding surface (MFS) at the sedimentary level where mudstones dominate the stratigraphic record (**Figure 21**). The very poorly amalgamated channels that contrast with the great development of aggrading floodplain fines (in which crevasse splays may also occur) may characterise a highstand system tract (HST, **Figure 21**). Therefore, this observation indicates that the post-rift stage during which sediments of the Erlian Formation were deposited is not only dominated by an uplift regime but more likely correspond to an alternation of short uplifts that enhanced base-level fall with induced fluvial channel deposits, with periods of stratigraphic base-level rise dominated by overbank deposits. A similar tectono-stratigraphic evolution has been proposed for the East Gobi Basin in Johnson (2004), in which syn-rift deposits are unconformably overlain by post-rift sediments that were deposited in a fluvial environment (Davidson, 2005). Moreover mudstone and sandstone layers of a fluvial system have been described in late Cretaceous strata of neighbouring basins in north-east China (Sha, 2007), such as the Kailu Basin in the western part of the Songliao Basin (e.g., fluvial deposits of the late Cretaceous Yaojia Formation; Cai and Li, 2008). Therefore, the sedimentological architecture of post-rift sediments occurring in intracontinental basins in north-east China and south-east Mongolia may show a similar tectono-stratigraphic evolution during the post-rift stage in this part of the Asian continent.

7. Palynological occurrences

In this part will be presented the different spores and pollen assemblages identified over the five samples processed for the palynological study. As previously exposed, samples were collected in DH1, DH2, DH4 and DH5 and belong to different sedimentary units of the Erlian Basin. Sample DH1-2400 belongs to the Tengge'er Formation, samples DH1-205 and DH2-1015 to the Saihan Formation and samples DH4-507 and DH5-480 to the Erlian Formation. The aim of this palynological study was to assess the possibility of pollen and spores occurring in the Erlian Formation to provide biostratigraphic information that can lead to an age determination. Therefore this preliminary study focused on diagnostic palynomorphs. In order to precise this biostratigraphical inquiry, some samples of underlying formations were studied.

Over the three slides per sample which have been studied, a total amount of 292 to 635 palynomorphs have been counted for each sample. Some of the samples contain Paleozoic

spores (e.g., *Densosporites*) indicating minor reworking. The most common taxa (**Table 3**) are *Exesipollenites* (**Figure 23**) and gymnosperm pollen with bisaccate morphology or monosulcate forms. The stratigraphic value of these common forms is quite low and for some of them (e.g., the commonly found *Ephedripites*; **Figure 23**), unknown. Fortunately, some gymnosperm and angiosperm pollen of major stratigraphic interest were also present on the slides. Some of the palynomorphs mentioned hereafter as “indeterminate forms” could also be of great interest, but they require specific analyses which do not fit the framework of this preliminary study. Moreover, it is not clearly established whether the quality of preservation of these palynomorphs would allow reliable determinations or not. A major part of these indeterminate forms belongs to triporate and tricolpate forms. Some of them have most likely not been described and therefore could be of great stratigraphic interest.

7.1. Spores and pollen assemblages

7.1.1. Assemblage 1

This assemblage presents an association dominated by smooth forms (*Taxodiaceaeapollenites*; more than 50 % of the total) also including bisaccates and Cheirolepidiacean pollen (about 20% each) and some (< 2%) monosulcate and trilete forms (mainly *Cyathidites* and *Callialasporites* in a minor proportion). This assemblage does not display any deciding factor allowing a precise age assignment. Less common forms such as monosulcate and trilete forms lend weight to the hypothesis of a datation between Jurassic and Cretaceous. However it was recognized in sample DH1-2400 (**Figure 24**) collected in lacustrine mudstone of the Tengge'er Formation which was deposited during the early Cretaceous (Cai et al., 1990; Lin et al. 2001; Sha, 2007; Song et al., 1986). Therefore this assemblage may be representative of this sedimentary unit.

7.1.2. Assemblage 2

This is an assemblage widely dominated by smooth forms of small size (*Exesipollenites*, 32% of the total spores and pollen) and with more than 10% of *Cicatricosisporites* (**Figure 23**). Among the forms representing between 5 and 10% of the palynological assemblages, smooth forms (*Taxodiaceaeapollenites*), trilete spores (*Cyathidites*), bisaccate grains and some *Cerebropollenites* were observed. Some palynomorphs represent less than 5% of the total. They are all of poor or unknown stratigraphic interest: monosulcate pollen grains, representatives of *Ephedripites*, *Triplanosporites* genera and 2-3 % of reworked forms

(*Densosporites*). From assemblage 1 to assemblage 2, we can notice the presence of *Cicatricosisporites*, in association with *Ephedripites* and the predominance of *Exesipollenites*. It can be compared with pollen assemblage frequently described in early Cretaceous of Asia (Nichols, 2003). Moreover, this assemblage was described in sample DH2-1015 collected in floodplain silty mudstones of the Saihan Formation, which is dated of Aptian-Albian age by authors (Cai et al., 1990; Fan et al., 2008; Nie et al., 2007; Sha, 2007; Song et al., 1986). Therefore assemblage 2 is consistent with the age of the Saihan Formation (**Figure 24**). Indeed younger pollen indicator like *Asteropollis asteroides*, frequently found in uppermost early Cretaceous units (Nichols, 2003; Nichols et al., 2006), does not occur in this assemblage.

7.1.3. Assemblage 3

This assemblage displays numerous similarities with assemblage 2, notably the abundance of *Exesipollenites*. However, bisaccate forms are more common (about 20%) and smooth forms (*Taxodiaceaepollenites*) are just below 20%. Palynomorphs representing 5 to 29% of the whole assemblage, mainly consist of trilete (*Cyathidites*) and monosulcate forms. This category also contains a taxon of major stratigraphic interest (a bit more than 5%): *Asteropollis asteroides*. *Cicatricosisporites* (**Figure 23**), albeit always present, is less abundant and therefore belongs to the category of taxa below 5%, along with taxa like *Triplanosporites*, *Callialasporites*, *Ischyosporites* and Cheirolepidiacean pollen occur. Reworked *Densosporites* are abundant (more than 4%). This assemblage is typical of DH1-205 sample (**Figure 24**) collected in the Saihan Formation. The main difference of this assemblage with the former one, in addition with the lower frequency of *Exesipollenites*, is the conclusive presence of *Asteropollis asteroides* (**Figure 24**). This form attributed to the first Angiosperms was first described at the Lower-Upper Cretaceous boundary in North America (Nichols, 2003), but since it has been described in other part of the world (Hedlund and Norris, 1968), including Asia, where the oldest records of *Asteropollis asteroides* were described by Vakhrameev (1991) from the Hauterivian-Barremian Andakhuduk Formation in Mongolia. Therefore this early occurrence of angiosperm palynomorphs in lower Cretaceous of north-east Asia could highlight this region of the world as the place where flowering plants appeared. Everywhere else in the world, it is frequently found in association with Albian macrofossils (Nichols et al., 2006).

7.1.4. Assemblage 4

This assemblage shows similarities with the former one (abundance of *Exesipollenites* and common occurrence of monosulcate pollen) in association with palynomorphs of low stratigraphic value (bisaccates, monosulcate and smooth forms, *Cyathidites* and Cheirolepidiacean pollen). But it is noticed for pollen occurrence of great stratigraphic value like *Ulmipollenites* (**Figure 23**) and *Ulmoideipites* and, more seldom, poorly preserved palynomorphs possibly belonging to *Buttinia* and *Momipites* (**Figure 23**). Due to the poor quality of preservation of some palynomorphs, the percentage of indeterminate forms reaches a value of 12% in these samples. *Ulmipollenites* and *Ulmoideipites* are known to appear at the end of Campanian (Li et al., 2011; Scott et al., 2012). These diagnostic pollen grains are well represented in DH5-480 (**Figure 24**), but more sparsely in DH4-507 (only 2 occurrences), both collected in floodplain silty mudstones of the Erlian Formation. The other diagnostic palynomorphs mentioned in **table 3** (*Cranwellia*, *Buttinia*, *Momipites*) are very poorly represented in the assemblages (and sometimes poorly preserved), but their occurrence in association with *Ulmipollenites* and *Ulmoideipites* would allow a discussion in favour of a late Cretaceous age (Van Itterbeeck et al., 2007; Li et al., 2011).

Table 3. Composition of the palynological assemblage observed in sedimentary units of the Erlian Basin. Proportion Sub-classes (in %) were determined over the total amount of palynomorphs counted.

	< 5%	5-29%	30-49%	> 50%	Assemblage 1	Assemblage 2	Assemblage 3	Assemblage 4
Spores								
<i>Cicatricosporites</i> sp.	○				○	○ ○ ○	○ ○ ○	
<i>Cyathidites</i> sp.	○				○ ○ ○ ○ ○	○ ○ ○ ○ ○	○ ○ ○ ○ ○	
<i>Ischyosporites</i> sp.					○	○ ○ ○ ○ ○	○ ○ ○ ○ ○	
<i>Leptolepidites</i> sp.					○	○ ○ ○ ○ ○	○ ○ ○ ○ ○	
<i>Triplanosporites</i> sp.					○	○ ○ ○ ○ ○	○ ○ ○ ○ ○	
Gymnosperms								
<i>Bisaccate forms</i>	○ ○				○ ○ ○ ○ ○	○ ○ ○ ○ ○	○ ○ ○ ○ ○	
<i>Callialasporites</i> sp.	○ ○				○ ○ ○ ○ ○	○ ○ ○ ○ ○	○ ○ ○ ○ ○	
<i>Cerebropollenites</i> sp.	○ ○ ○ ○ ○				○ ○ ○ ○ ○	○ ○ ○ ○ ○	○ ○ ○ ○ ○	
<i>Cheirolepidiacean forms</i>	○ ○ ○ ○ ○				○ ○ ○ ○ ○	○ ○ ○ ○ ○	○ ○ ○ ○ ○	
<i>Ephedripites</i> sp.					○ ○ ○ ○ ○	○ ○ ○ ○ ○	○ ○ ○ ○ ○	
<i>Exesipollenites</i> sp.					○ ○ ○ ○ ○	○ ○ ○ ○ ○	○ ○ ○ ○ ○	
<i>Monosulcate forms</i>	○ ○ ○ ○ ○				○ ○ ○ ○ ○	○ ○ ○ ○ ○	○ ○ ○ ○ ○	
<i>Taxodiaceaepollenites</i> sp.	●				○ ○ ○ ○ ○	○ ○ ○ ○ ○	○ ○ ○ ○ ○	
Angiosperms								
<i>Aquilapollenites</i> sp.							○	
<i>Asteropollis asterooides</i>							○	
Hedlund and Norris, 1968							○	
<i>Buttinia</i> sp.(?)							○ ○ ○ ○ ○	
<i>Cranwellia</i> sp.							○ ○ ○ ○ ○	
<i>Momipites</i> sp.(?)							○ ○ ○ ○ ○	
<i>Normapolles</i> sp.							○ ○ ○ ○ ○	
<i>Sabalpollenites</i> sp.							○ ○ ○ ○ ○	
<i>Ticolpate forms</i>							○ ○ ○ ○ ○	
<i>Triporate forms</i>							○ ○ ○ ○ ○	
<i>Ulmoideipites</i> sp.							○ ○ ○ ○ ○	
<i>Ulmipollenites</i> sp.							○ ○ ○ ○ ○	
<i>Indeterminate forms</i>							○ ○ ○ ○ ○	
<i>Reworked forms</i>		○			○	○ ○ ○ ○ ○	○ ○ ○ ○ ○	

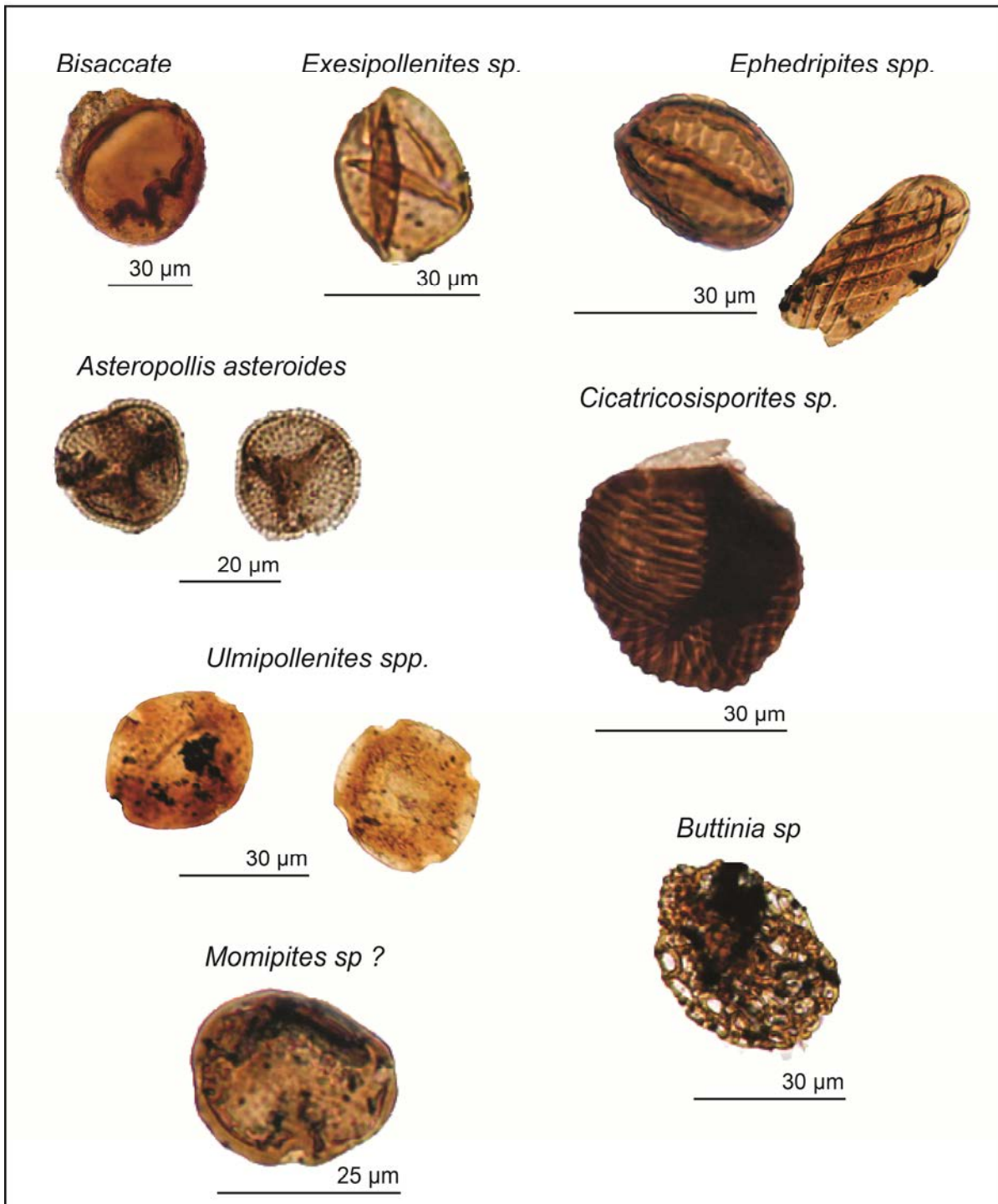


Figure 23. Spores and pollen most commonly observed or presenting an accurate stratigraphic value in palynological assemblages belonging to sedimentary units of the Erlian Basin.

The limited number of samples used for this study prevents the recognition of any continuous trends in the evolution of palynological assemblages, but it allows the characterisation of a spore and pollen assemblage for the Erlian Formation (**Table 3**). This assemblage shows an abundance of *Exesipollenites* and common occurrences of monosulcate pollen in association

with palynomorphs of low stratigraphic value (bisaccates, monosulcate and smooth forms, *Cyathidites* and Cheirolepidiacean pollen). However, it is notable for the pollen occurrence of great stratigraphic value, such as *Ulmipollenites* (**Figure 23**) and *Ulmoideipites* which are known to appear at the end of the Campanian (Li et al., 2011; Scott et al., 2012). These diagnostic pollen grains are well represented in DH3-480, but more sparsely in DH2-507 (only 2 occurrences). The other diagnostic palynomorphs mentioned in **table 3** (*Cranwellia* and possibly *Buttinia* and *Momipites*; **Figure 23**) are very poorly represented in the assemblage (and sometimes poorly preserved), but their occurrence in association with *Ulmipollenites* and *Ulmoideipites* would allow a discussion in favour of a late Cretaceous age (Van Itterbeeck et al., 2007; Li et al., 2011). Because of the poor quality of preservation of some palynomorphs, the percentage of indeterminate forms reaches a value of 12% in these samples.

7.2. Biostratigraphic information

The Erlian Basin and more likely the Erlian Formation have yielded a wide range of well-preserved fossils of great paleobiological and evolutionary interests: (i) the namely feathered dinosaurs (*Sinosauropelta*, *Protarcheopteryx*, *Caudipteryx*, *Gigantoraptor*; Xu et al., 2007), (ii) the reportedly one of the oldest occurrence of flowering plants (*Archaeofructus*) belonging to the basal angiosperm group, and interpreted as herbaceous aquatic plants. However publications concerning the Cretaceous of Mongolia and northern China including description of palynological assemblages remain quite rare (Cai et al., 1990; Fan et al., 2008; Hicks et al., 1999; Ichinnorov 2003a, 2003b; Nichols et al., 2001; Song et al., 1986), especially for late Cretaceous sedimentary units. Fortunately, palynomorphs of the Erlian Formation were at least once described by Van Itterbeeck et al. (2007) and scientific literature is also available on the relatively nearby basins of northern China (Li et al., 2011; Nichols et al., 2006; Scott et al., 2012).

Spores and pollen occurrences identified in samples of underlying sedimentary units of the Erlian Formation such as the Tengge'er and the Saihan formations respectively led to the characterization of assemblages 1 and 2-3. Because of a poor diagnostic palynomorphs occurrence a Jurassic-Cretaceous age is proposed for the assemblage 1. Nevertheless this assemblage has been characterized in lacustrine mudstone of the Tengge'er Formation which was deposited during the early Cretaceous (Cai et al., 1990; Lin et al. 2001; Sha, 2007; Song et al., 1986; **Figure 24**). Therefore this assemblage may be representative of this sedimentary

unit. Assemblages 2 and 3 belonging to the Saihan Formation are characteristic of early Cretaceous pollen assemblages described in Asia (Nichols, 2003). Moreover the occurrence of the early angiosperm *Asteropollis asteroides* in assemblage 3 which is frequently observed in association with Albian macrofossils (Nichols et al., 2006) is consistent with the Aptian-Albian age of the Saihan Formation (Cai et al., 1990; Fan et al., 2008; Nie et al., 2007; Sha, 2007; Song et al., 1986; **Figure 24**). Therefore palynological occurrences identified in both sedimentary units the Tengge'er and the Saihan formations are in accordance with their respective ages previously proposed by authors.

Palynological occurrences (assemblage 4) that were observed in samples of the Erlian Formation were compared with spores and pollen assemblages that were characterised by Li et al. (2011) and Scott et al. (2012) for the late Cretaceous to early Palaeocene Sifangtai and Mingshui formations of the Songliao Basin. The identical palynomorphs such as *Ulmipollenites* or *Ulmoideipites*, *Cranwellia*, *Buttinia* and *Momipites* were identified. Moreover, most of the palynomorphs occurring in samples of the Erlian Formation are similar to the ones described in Van Itterbeeck et al. (2007), especially *Ulmoideipites*, which is a key-pollen of the assemblage because it is known to appear at the end of the Campanian (Li et al., 2011; Scott et al., 2012). According to studies on vertebrates from the Erlian Formation (Rozhdestvensky, 1966, 1977; Brett-Surman, 1979; Gou et al., 1986; Weishample and Horner, 1986; Cai et al., 1990; Jerzykiewicz and Russel, 1991; Currie and Eberth, 1993; Ma, 1994; Van Itterbeeck et al., 2005), we stated an important distinction in the introduction between ages based on the dinosaur fauna dated from Cenomanian to Santonian and age determination using charophytes and ostracods (Van Itterbeeck et al., 2005), indicating a Campanian-Maastrichtian age. According to spores and pollen occurrences presented in this paper, we propose a post-late Campanian age which is consistent with ages proposed in Van Itterbeeck (2005, 2007), indicating a latest Cretaceous age of deposition for the sediments of the Erlian Formation.

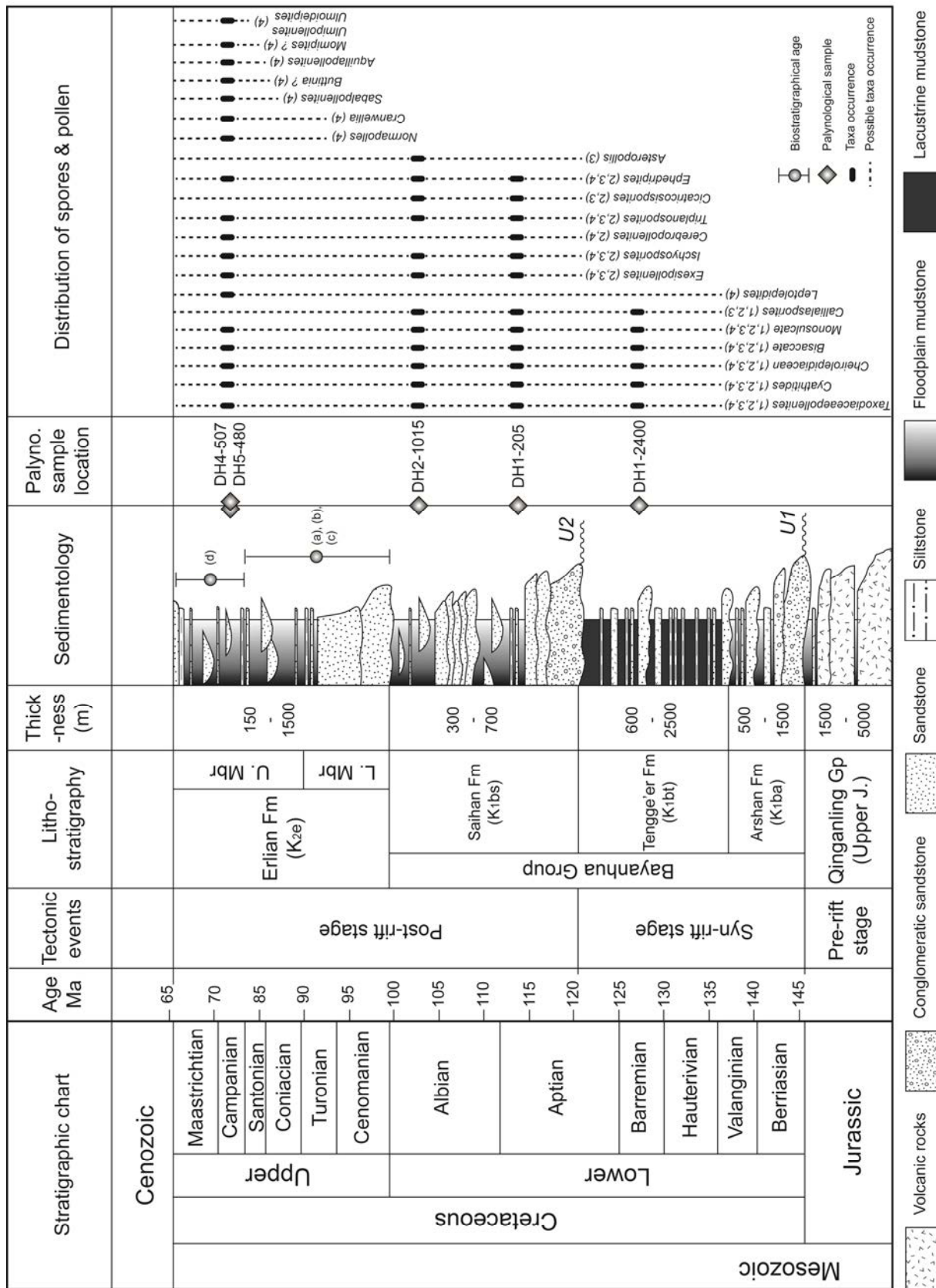


Figure 24. Tectono-stratigraphic log of the Erlian Basin showing the distribution of the palynological occurrences in sedimentary units of the Erlian Basin (modified after Gou et al., 1986; Cai et al., 1990; Dou, 1997; Graham et al., 2001; Lin et al., 2001; ICS, 2006; Wang et al., 2006; Sha, 2007; Van Itterbeeck et al., 2007;

Li et al., 2011; Scott et al., 2012). J.= Jurassic; U1= Unconformity 1; U2= Unconformity 2; In the column Sedimentology the main biostratigraphical ages of the Erlian Formation proposed by authors are represented. Ages based on dinosaur fauna: (a)= Brett-Surman (1979); (b)= Rozhdestvensky (1966, 1977); (c)= Weishample and Horner (1986); and ages based on charophytes and ostracods: (d)= Van Itterbeeck et al. (2005).

8. Metallogenetic implications

The partitioning of sandstone dominated versus mudstone dominated stratigraphic record resulting from the tectono-sedimentary evolution that occurred during the post-rift stage in the Erlian Basin is at the origin of confined permeable sandstone layers. This sedimentological architecture related to a braided fluvial environment has significant metallogenetic implications because these confined permeable sandstones represent good reservoirs (or host-rocks) for roll front-type uranium deposits (e.g., sandstone layers of the Saihan Formation hosting the Bayinwula and the Saihangobi deposits; Nie et al., 2007; Fan et al., 2008; Nie, 2008). Additionally, the mudstone layers play several roles in the genesis of energy resources: (i) they constitute good aquitars (or non permeable to semi-permeable barriers) to confine the circulation of oxygenated groundwater responsible for epigenetic roll front uranium mineralisation in permeable sandstones (Devoto, 1978); and (ii) they indicate swamps and floodplain ponds which are highly favourable to preserve organic matter (Diessel, 1992), the development of coal deposits (Nie, 2008) and syn-sedimentary uranium mineralisation (e.g., the Nuheting and Subeng deposits in the Erlian Formation; Dahlkamp, 2009). Therefore, the tectono-stratigraphic evolution of the Erlian Formation revealed by the present study is of great interest to understand the genesis of energy resources as the upper member of the Erlian Formation hosts several syn-sedimentary uranium deposits (Dahlkamp, 2009) and its lower member that is dominated by sand facies may represent prospective host-rock for roll front-type uranium mineralisation. Moreover, a similar geological setting for post-rift sediments has been at least identified in the East Gobi Basin by Johnson (2004) which indicates a favourable potential to discover new energy resources in the region.

9. Conclusions

The Erlian Basin is an intracontinental Cretaceous basin of north-east China with no marine influence. This basin developed from the late Jurassic to the upper Cretaceous and was controlled by two major tectonic events during sedimentation: (i) a syn-rift stage that was dominated by a fluvial-lacustrine depositional environment and (ii) a post-rift stage that was dominated by a fluvial environment. The sediments of the Erlian Formation occur at the top of the Cretaceous system of the basin and was deposited during the post-rift stage. The facies architecture and the ideal sedimentological succession of facies identified for this formation indicated two different members that were both dominated by a fluvial depositional environment: (i) the lower member, which is mostly channel dominated, and (ii) the upper member, which is mainly overbank dominated. The lower member registered tectonically induced uplift and ensuing stratigraphic base-level fall that was highlighted by a major phase of braided channels clustering under negative accommodation. The upper member indicates a period of stratigraphic base-level rise that is associated with an increase of accommodation and the deposition of fine-grained facies. Therefore, the Erlian Formation highlights an alternation of short uplifts that were dominated by braided fluvial channel deposits with periods of stratigraphic base-level rise that were dominated by overbank deposits. The architectural setting developed during the post-rift stage of the Erlian Basin presents significant metallogenic implications with the formation of confined permeable sandstones which represent favourable host-rocks for the genesis of roll front-type uranium mineralisation.

The palynological assemblages recognised from the study of five samples belonging to different sedimentary units of the Erlian Basin evidence a Jurassic-Cretaceous age for the Tengge'er Formation (assemblage 1) and an Aptian-Albian age for the Saihan Formation (assemblages 2 and 3). Then assemblage 4 reveals a post-late Campanian age therefore more likely indicating a latest Cretaceous age of deposition for the sediments of the Erlian Formation.

Acknowledgements

Financial support for this study was provided by AREVA Mines, the East China Institute of Technology in Fuzhou, Jiangxi and the Geological Team N°208, BOG, CNNC in Baotou, Inner Mongolia. The authors acknowledge colleagues from the East China Institute of Technology for the presentations and scientific discussions that have been organised about the geology of the Erlian Basin, as well as people from the Geological Team N°208 for field support and the access to drill cores. The authors also acknowledge Menhong from the Geological team N°208 for translation during the field trip, Li Guanglai from the East China Institute of Technology who brought to our attention several important papers on the stratigraphy of China and Antonio Benedicto and other geologists from AREVA Mines for the discussion of the tectono-sedimentary evolution of eastern Asia. Finally, the authors would like to thank both reviewers of this paper David Batten (University of Manchester) and Jimmy Van Itterbeeck (Shell International), for improving the paper.

PARTIE B :

LES SOURCES PRIMAIRES DE L'URANIUM AU

NORD-EST DE LA CHINE

CHAPITRE 3 :

LE CYCLE DE L'URANIUM DANS LA CROUTE CONTINENTALE



1. Concentration de l'uranium dans la croûte continentale

En normalisant les éléments traces au manteau primitif, et en les classant du plus incompatible au moins incompatible (dans les conditions de la fusion partielle du manteau), les continents montrent un net enrichissement en éléments incompatibles et une décroissance non-linéaire vers les moins incompatibles et même vers les éléments compatibles, à partir de l'Al (**Figure 25**; Hofmann, 1988). L'élément chimique uranium se classe dans la famille des éléments dits incompatibles (ou hygromagmatophile) du fait de sa faible affinité avec les réseaux cristallins des silicates. Cette faible affinité est due à sa forte valence de charge combinée à un rayon ionique élevé. Il fait parti du groupe *High Field Strength Elements* (HFSE) au même titre que le thorium (Rollinson, 1983). Les éléments hygromagmatophiles ont un coefficient de partage *KD* minéral-liquide silicaté inférieur à 1 et de ce fait sont préférentiellement concentrés dans les liquides silicatés lors des processus de fusion partielle ou lors de la cristallisation des magmas. Ainsi, la croûte continentale se trouve enrichie en élément incompatible dont l'uranium, extrait du manteau par fusion partielle (Hofmann, 1988 ; Shaw and Sturchio, 1992). En termes de concentration par rapport au manteau primitif = 21 ppb dont l'uranium est extrait, la croûte continentale inférieure (1 à 1.4 ppm cad enrichissement par un facteur 47 à 66) montre un enrichissement alors que la croûte continentale supérieure présente un plus fort enrichissement. La croûte océanique (composition basique) est légèrement plus différenciée que le manteau (composition ultrabasaltique) car elle résulte de la fusion partielle de celui-ci. La subduction de la croûte océanique et des sédiments permet de recycler l'uranium et d'autres éléments incompatibles d'origine continentale dans le manteau, par rapport au thorium et donc ce processus entraîne une diminution continue du rapport Th/U, généralement déterminé à partir du rapport $^{232}\text{Th}/^{238}\text{U}$ (kappa).

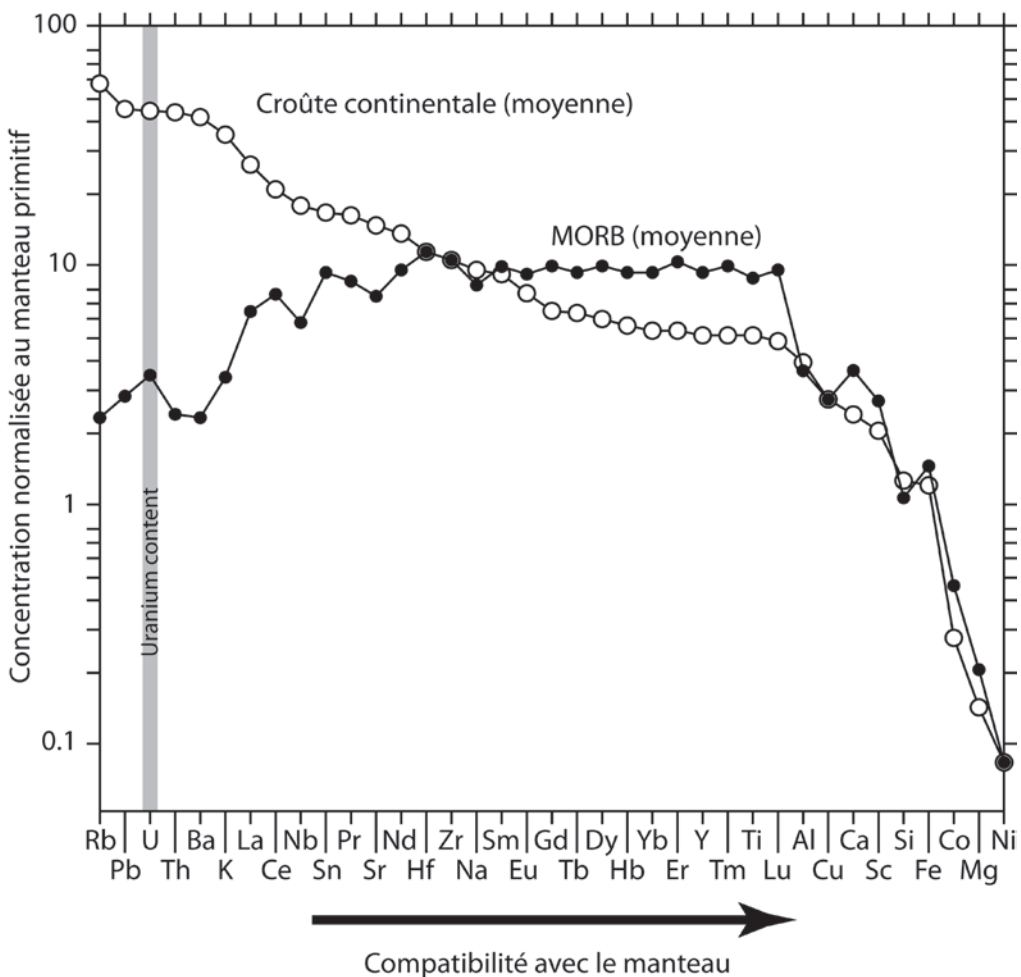


Figure 27. Présentation des concentrations moyennes normalisées au manteau primitif des éléments chimiques dans la croûte continentale en comparaison avec les valeurs pour les MORB* (modifiée d'après Hofmann, 1988). *Les MORB qui dérivent actuellement d'un manteau appauvri sont plus pauvres relativement dans les éléments les plus incompatibles car ils ont déjà été extrait en partie par une fusion antérieure du manteau responsable de l'appauvrissement.

Les propriétés chimiques (valence et rayon ionique élevés) font que cet élément sera préférentiellement incorporé dans les minéraux lourds tels que le zircon, la monazite, l'uraninite, thorianite/thorite, Zr, ETR, Th ayant des valences et rayon ioniques voisins (Cuney and Friedrich, 1987). Cet élément présente également l'intérêt d'être radioactif ce qui lui confère, outre le fait qu'il génère de la chaleur dans la croûte continentale, toutes les propriétés d'un géochronomètre permettant de dater les processus géologiques. En conclusion, c'est donc grâce à ces nombreuses propriétés physiques et chimiques que l'uranium peut-être considéré comme un traceur géochimique de la différentiation, de la croissance, de l'évolution et de la remobilisation de la croûte continentale au cours des temps géologiques (**Figure 26**). En effet, cet élément est aussi bien mobilisé durant des processus

géologiques profonds (magmatisme, métamorphisme et interactions fluide-roche) que de processus de surface (altération, érosion, transport et dépôt).

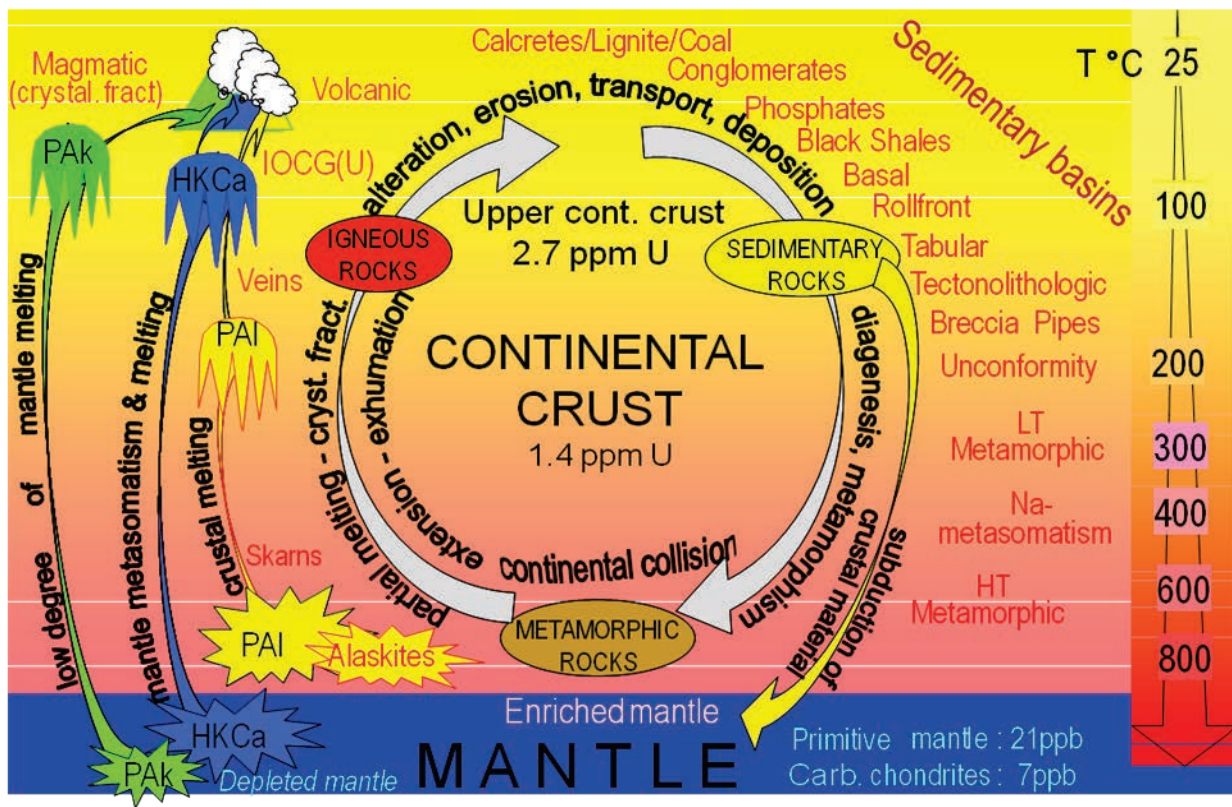


Figure 28. Cycle de l'uranium dans les différents contextes de gisements en relation avec les principaux processus de fractionnement au cours d'un cycle géologique (Cuney, 2009). Les réservoirs représentés sont le manteau et la croûte continentale. Les types de gisements sont les caractères rouges gras ; les mécanismes métallurgiques sont en caractères noirs gras. KCa = magma Calco-alcalin potassique ; Pak = magma Peralcalin ; Pal = magma Peralumineux.

2. Cycle de l'uranium de l'Archéen à l'actuel

La typologie des gisements d'uranium est également un marqueur des processus impliqués dans la formation des premiers continents et, en subséquent, de leur évolution (Cuney, 2010). Cuney (2010) propose quatre périodes d'évolution majeure pour les concentrations d'uranium à travers les temps géologiques.

La première période s'étale depuis les premiers stades d'accrétion terrestre jusqu'à 3.2 Ga. Cette période est caractérisée par la formation de la première croûte continentale principalement composée de basaltes et de séries TTG avec une concentration très faible en uranium (quelques ppm au maximum). L'uranium est principalement porté par des phases réfractaires et aucune concentration économique n'est connue, même dans les séries les plus différencierées. La seconde période est marquée par l'apparition de granites enrichis en uranium

datés dès 3.1 Ga. Ces granitoïdes riches en éléments incompatibles, et en particulier en uranium et thorium, sont associés à une période de forte croissance crustale s'étalant de 3.2 à 2.2 Ga. L'uranium est essentiellement fractionné par des processus magmatiques donnant lieu à la production de magmas fortement potassique permettant de concentrer et précipiter l'uranium sous forme d'uraninite (UO_2). Pour exemple, ces granites ultra-potassiques, avec des affinités calco-alcalines, sont décrits dans le craton du Kaapval-Kalahari en Afrique du Sud (Robb et al., 1990). L'érosion de ces granites pré-concentrés en uranium conduit à la formation des premières concentrations uranifères dans les bassins sédimentaires clastiques sous forme de conglomérats à galets de quartz à or-uranium du Witwatersrand, la première concentration économique sur terre, en Afrique du Sud dont les dépôts les plus anciens du Dominion Reef sont datés à environ à 3.08 Ga (Robb and Meyer, 1990). Les uraninites dans ce type de gisement sont d'origine détritique mais aussi remobilisées localement dans des plans de cisaillement. Les accumulations détritiques ne sont possibles qu'en l'absence d'oxygène car l'uraninite est très facilement soluble en conditions oxydantes.

La seconde période, allant de l'Archéen au Paléoprotérozoïque supérieur, est marquée également par l'apparition de deux grands types de granites porteurs d'uranium : (i) les granites métalumineux fortement fractionnés et enrichis en potassium, ainsi que les pegmatites associées à ces processus (auxquels appartiennent probablement les premiers granite CAK à 3.1 Ga) et (ii) les leucogranites peralumineux fortement différenciés résultant de la fusion partielle des métasédiments (Cuney and Friedrich, 1987 ; Cuney, 2009). Les granites métalumineux sont connus dans la plupart des cratons archéens tel que le craton du Yilgarn (Champion and Smithies, 2007) et le socle de East Alligator River Uranium district en Australie, la Province du Supérieur au Canada, le craton Amazonien au Brésil (Tallarico et al., 2005), les cratons de Dharwar (Jayayanda et al., 1995) et Singhbum en Inde (Sarangi and Singh, 2006) ou encore au sein du bouclier Baltique. Ces granites métalumineux où des uraninites ont été décrites sont datés entre 3.1 et 2.5 Ga. Les granites peralumineux, capable également de cristalliser de l'uraninite, commencent à apparaître vers 2.7 Ga (Cuney, 2009). Ces granites sont généralement enrichis en uranium, mais appauvris en éléments incompatibles tels que le thorium, en raison de la faible solubilité des minéraux accessoires porteurs de ces éléments (Cuney and Friedrich, 1987). Pendant cette période, les degrés les plus élevés de fractionnement magmatique sont atteints. Tel est l'exemple des pegmatites peralumineuses à ETR de Tanco dans le Manitoba, qui ont réussi à cristalliser une uraninite pauvre en Th-ETR (Duhamel et al., 2009). Il est intéressant de souligner que le

fractionnement des magmas très peralumineux offre l’unique mécanisme capable de produire un enrichissement en uranium par rapport au thorium en conditions réductrices.

La troisième période s’étale de 2.2 à 0.4 Ga et est marquée par le phénomène d’oxyatmoverversion ou *Great Oxidation Event* (GOE) à environ 2.3 Ga (Holland, 2002 ; Farquhar and Wing, 2003; Bekker et al., 2004). Cet événement marque une augmentation spectaculaire de la fugacité en oxygène de l’atmosphère et donc un changement irréversible dans les modes de transfert et de dépôt de l’uranium. Ainsi, l’uranium mis alors en contact avec les eaux superficielles oxydantes, passe en solution sous forme de complexes de carbonates d’uranyle (sous la valence U6+). L’uranium facilement lessivable provient des accumulations de type paléo-placers formées avant 2.3 Ga et soumises aux circulations de fluides météoriques. Les autres sources d’uranium possibles sont les uraninites provenant des granites très fractionnés, les silicates d’uranium métamictes, les oxydes présents dans les roches plutoniques ou sédimentaires ou encore les verres volcaniques facilement altérables (Cuney, 2009). A la même période, d’énormes quantités de matières organiques ont été accumulées dans les sédiments de plateau et les milieux des mers épicontinentales. Pour exemple, des concentrations uranifères élevées sont décrites dans les séries de schistes noirs dans le bassin de Franceville au Gabon (Mossman et al., 1998). Cette période marque donc l’apparition de concentrations uranifères hydrothermales et l’incorporation de cet élément dans les séries sédimentaires de plateforme continentale. Ces formations seront par la suite remobilisées durant des phases orogéniques plus tardives. La fusion partielle de ces séries métasédimentaires pré-enrichies en uranium permettra la genèse de pegmatites enrichies en uraninite le long de ces ceintures orogéniques d’âge Protérozoïque. Ces minéralisations sont décrites comme des sources potentielles pour la genèse des gisements de type discordance (*unconformity-related deposits*) ou encore de type métasomatique (*sodic metasomatic deposits*). Les cratons archéens et protérozoïques seront remobilisés au cours d’événements orogéniques successifs durant le Méso et Néoprotérozoïque (Cuney, 2009).

Enfin, la dernière période d’évolution majeure pour les concentrations uranifères proposée par Cuney (2009) s’étend depuis l’Ordovicien, environ 0.45 Ga, jusqu’à l’actuel. La métallogénie est soumise alors à l’apparition des plantes vasculaires qui a pour conséquence de créer d’épaisses séquences sédimentaires silicoclastiques réduites continentales dans lesquelles l’uranium peut être piégé. Ces pièges peuvent fournir des concentrations actuellement économique tel que les bassins intracontinentaux Mésozoïque à Cénozoïque au Niger (Pagel et al., 2005) ou encore en Asie Centrale (Munara, 2012).

CHAPITRE 4:

LES SOURCES PRIMAIRES DE L'URANIUM DANS L'ENVIRONNEMENT DU BASSIN D'ERLIAN



Article 2: Indosinian granites as major primary uranium source for the sedimentary-hosted U deposits of the Erlian Basin, NE China.

Christophe Bonnelli^a, Michel Cuney^a, Sylvain Bourlange^a, Etienne Deloule^b, Marc Poujol^c,
Xiaodong Liu^d, Yunbiao Peng^e

^aUniversité de Lorraine, GeoRessources-CNRS-CREGU, BP239, F54506 Vandoeuvre-lès-Nancy, France.

^bCNRS-CRPG, UMR 7358, F-54506 Vandoeuvre-lès Nancy, France.

^cUniversité de Rennes 1, Géosciences Rennes - UMR CNRS 6118, OSUR, 35042 Rennes Cedex, France.

^dEast China Institute of technology, 56 Xuefu Road , Linchan, 344000 Fuzhou, Jiangxi, China

^eGeological Team No.208, BOG, CNNC, Baotou, Inner Mongolia, China

Paper to be submitted in Ore Geology Reviews

1. Abstract

Hercynian and Indosinian granites are widespread in northeast China and widely represented in the Central Asia Orogenic Baelt (CAOB) which corresponds to the basement of the Erlian Basin. The present study aims to (i) characterise the possible role of these granites as major primary uranium sources for sedimentary-hosted U mineralisation and (ii) determine the different stages of U enrichment through the regional geodynamic evolution. Outcrop and drill-core samples of both Hercynian and Indosinian igneous rocks from the basement occurring at the northern margin of the Erlian Basin have been investigated with emphasis on detailed mineralogical study, whole-rock geochemical data, geochronological constraint and Sm-Nd isotopes.

Elevated values of $^{143}\text{Nd}/^{144}\text{Nd}_\text{i}$ indicated that all igneous rocks analysed were derived from an enriched mantle (EM) and negative $\epsilon\text{Nd}_{(t)}$ ranging from -2.0 to 2.4 evidenced a mixing between the mantle and crustal material for Indosinian granites. Hercynian granites correspond to a calcalkaline magmatic series derived from a slightly contaminated mantle and were emplaced during the late Carboniferous-Permian oceanic subduction as indicated by a volcanic arc geochemical signature. Indosinian granites correspond to a high-K calcalkaline series and were emplaced during a continental subduction at the early-middle Triassic. Crustal material was subducted which has resulted of a high degree of contamination in the mantle associated with enrichment in K and incompatible elements such as Th and U. Therefore, Indosinian granites evidenced highly fractionated magmas expressed by the crystallization of U-rich biotite granites and two-mica granites. In biotite granites, the major U-bearing minerals are U-thorite and allanite and show texture of metamictisation indicating that a large part of their U content has been released and is available for leaching. Mass balance calculation showed that indosinian granites may liberate $\sim 15000\text{t U.km}^3$ and thus correspond to a major primary source of uranium for U mineralisation hosted in the Erlian Basin. Moreover, $\epsilon\text{Nd}_{(t)}$ model ages would likely indicate a Neoproterozoic U extraction from the mantle, corresponding to a giant syn-rift magmatic event in eastern Asia, responsible for the breakup of Rodinia. Therefore, this would highlight genetic conditions of a young uraniferous province in central Asia.

Keywords: Erlian Basin, Indosinian granites, Uranium source

2. Introduction

Eastern Asia represents a large continental domain resulting from the successive accretion of continental blocks from the Archaean to the present time. Archaean to Palaeo-proterozoic continental blocks are bounded by different orogenies developed during the Phanerozoic and contributing to their accretion. This large continental domain extends from southern Siberia to Japan via China and the Korean Peninsula. Eastern China is mainly composed of both continental blocks the South China Block (SCB) and the North China Block (NCB). The NCB resulted from the accretion of several older (> 2.5 Ga) micro-blocks (Jahn et al., 1987; Jahn and Ernst, 1990; Liu et al., 1992; Wu et al., 1992; Liu et al., 2004; Zheng et al., 2004) and may have been accreted during either the Archaean or during the Palaeoproterozoic (e.g. 1.8 Ga; Kusky et al., 2007; Trap, 2007). The western part of the craton is relatively stable and presents a well-developed mantle root, a low heat flow and does not show major internal deformations since the Precambrian (Yuan, 1996; Zhai and Liu, 2003; Charles et al., 2013). However, the eastern part of the NCB shows a significant seismic activity, a strong heat flow, a thinned lithosphere and devoid of a thick mantle root. The NCB's lithospheric mantle was dated in different places by Re-Os isotopy on peridotite xenoliths hosted in Palaeozoic and Cenozoic rocks (Gao et al., 2002; Wu et al., 2003). Except for some rare parts, most of the ¹⁸⁷Os/¹⁸⁸Os model ages determined on peridotites indicates that the lithospheric mantle is younger than ages obtained for the continental crust of the NCB. Gao et al. (2002) and Wu et al. (2003) have proposed previously that the old lithospheric mantle would have been replaced by juvenile material during the Proterozoic and the Phanerozoic. It is now widely accepted that eastern Asia was built up during Palaeozoic times by successive subductions and collisions of intraoceanic arcs and continental micro-blocks around the Siberian craton (Lin et al., 2008). Therefore, several orogenies associated with magmatic events have succeeded before the major continental extension that occurred during the late Mesozoic (Charles et al., 2013) in eastern Asia. Along the northern margin of the NCB, the Hercynian Central Asia Orogenic Belt (CAOB), extending from Kazakhstan to the Pacific Ocean corresponds to the area where the NCB and several microcontinents of Mongolia were successively welded to Siberia. In northern China, especially in Inner Mongolia, the CAOB is represented by a 300-km-wide NW-SE-trending belt that separates Mongolian arcs developed along the southern margin of Siberia with microcontinents and magmatic arcs belonging to the NCB (Xiao et al., 2003; Li, 2006). During the late Palaeozoic (Carboniferous-Permian), the Baolidao magmatic arc and the Erdaojing accretionary complex were formed in response to a north-directed

subduction (Xiao et al., 2003; Lin et al., 2008; Fig. 17). Then, these magmatic arcs and microcontinents were completely accreted to Siberia and the NCB during a continental subduction at the Indosinian (early-middle Triassic) which is highlighted by a suture zone along the NCB's northern margin (Lepvrier and Maluski, 2008; Lin et al., 2008). From the late Triassic to the late Jurassic-early Cretaceous (190-150 Ma; Miao et al., 1998; Wang et al., 1998; Wu et al., 2000; Wu et al., 2002; Guo et al., 200; Wu et al., 2005a, 2005b; Su et al., 2007), transtensional episodes alternating with transpressional tectonics during the Yanshanian orogeny are responsible for the widely-represented Jurassic magmatic event in northern China (Faure et al., 2012; Charles et al., 2013). Then, the Yanshanian orogeny was followed by a major stage of continental extension related to the palaeo Pacific plate subduction (Charles et al., 2013), from the late Jurassic to the late Cretaceous, during which developed the intracontinental Erlian Basin (Sha, 2007; Meng, 2003; Charles et al., 2013). Therefore, sediments of the Erlian Basin: (i) lie on a basement mainly composed of Hercynian, Indosinian and Yanshanian magmatic rocks belonging to the CAOB and (ii) may be derived from these basement rocks. Central Asia represents one of the largest uraniferous provinces in the world, with uranium ore deposits located from the Transbaikal area in Russia, in southern Kazakhstan, in Uzbekistan, in Mongolia and in northern China. In comparison with other world class provinces (Canada, Australia and Africa), which are associated with Archaean to Palaeoproterozoic basements, the present study area provides an opportunity to investigate genetic conditions of uranium deposits generated within a younger uraniferous province. Most of the deposits discovered in this region are of sandstone-hosted tabular or roll-front type (e.g., in the Erlian and Ordos basins, Cai et al., 2007; Dahlkamp, 2009; OECD-NEA/IAEA, 2010) which currently represents one of the most economic uranium resources with respect to using in situ recovery (ISR) for their extraction. Nie (2008) and Dahlkamp (2009) have reported U-rich biotite granites (U mean from 4 to 13 ppm and Th/U ratios from 5.6 to 11.1) occurring in the basement surrounding the Erlian Basin. However, these granites have not been studied in details to characterize petrographically and geochemically their uranium concentration and no geochronological constraint was proposed to link this uranium enrichment to a particular geodynamic context or to one of the orogenies previously mentioned.

The purpose of this paper is to characterize the possible primary uranium source-rocks occurring in the basement of the Erlian Basin that are responsible for the sedimentary-hosted

mineralisation. In this paper, mineralogical, geochemical, geochronological and Sm-Nd isotopic data are presented. The study focusses on Hercynian and Indosinian magmatic rocks.

3. Geological setting

The Erlian Basin (or Eren Basin) is located in northeast China (**Figure 27**), Inner Mongolia, close to the border between China and Mongolia. It is an intracontinental basin, formed during the Mesozoic continental extension of eastern Asia (Ren et al., 2002; Charles et al., 2013), and covers an area of approximately 130 000 km² (Dou and Chang, 2003; Wei et al., 2005). This basin developed during three main tectono-stratigraphic stages: (i) a pre-rift stage mainly characterised by the emission of late Jurassic to early Cretaceous volcanic rocks of the Qinganling Group (156.0 – 142.6 Ma; Cheng and Cheng, 1997; Graham et al., 2001; Wang et al., 2006), which corresponds to the initiation of the rifting; (ii) a syn-rift stage characterised by the deposition of early Cretaceous sedimentary units (Gou et al., 1986; Cai et al., 1990; Sha, 2007): the Arshan Formation dominated by alluvial, fluvial and shallow lacustrine environments and the Tengge'er Formation dominated by deep to semi-deep lacustrine environment; and (iii) a post-rift stage characterised by a switch from tectonic to thermal subsidence and the deposition of the early Cretaceous Saihan Formation and the late Cretaceous Erlian Formation, both dominated by fluvial and shallow lacustrine environments (Currie and Eberth, 1993; Lin et al., 2001; Van Itterbeeck et al., 2005, 2007; Bonnelli et al., accepted). The Erlian Basin is composed of five major sub-basins as following (**Figure 27**): the Chuanjing Sub-basin to the West, the Wulanchabu Sub-basin in the central-west part, the Manite Sub-basin in the central-north, the Tengge'er Sub-basin in the southeastern part and the Wunite Sub-basin to the northeast (Dou et al., 1998; Dou and Chang, 2003; Wei et al., 2005). These sub-basins are framed by a series of horsts or ranges oriented ENE-WSW: the Daxing'anling Ranges to the East, the Bayinbaolige Horst to the North and the Suolunchan Horst more to the West, and finally the Wendurmiao Horst to the South. The Sunite Horst occupies the central part of the Erlian Basin and divides it in two different main parts (Dou et al., 1998; Wei et al., 2005), north and south.

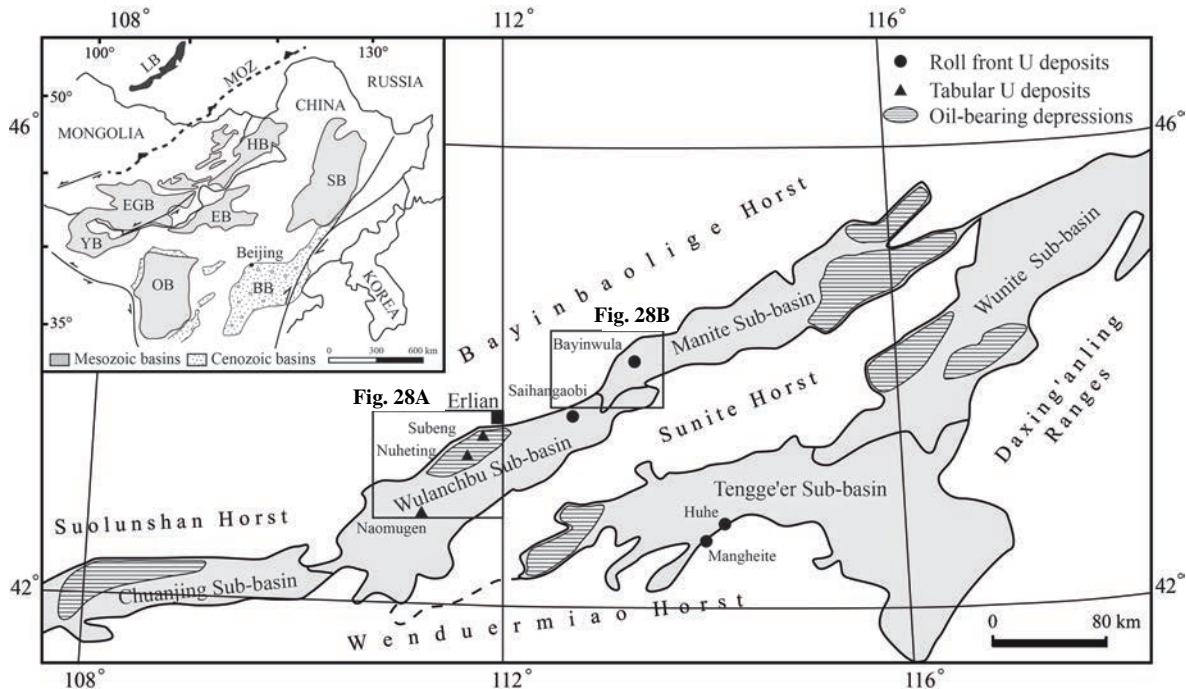


Figure 29. Structural map of the Erlian Basin showing the distribution of different types of uranium deposits and oil-bearing depressions (modified after CNNC, unpublished data; Dou et al., 1998; Meng, 2003; Wei et al., 2005; Dahlkamp, 2009; Bonnelli et al., accepted). U= uranium, BB= Bohai Basin, EB= Erlian Basin, EGB= East Gobi Basin, HB= Hailar Basin, OB= Ordos Basin, SB= Songliao Basin, YB= Yingen Basin, LB= Baikal Lake, MOZ= Mongol-Okhotsk Zone.

The Basin lies on a folded and metamorphised basement corresponding to the southern margin of the Xing'an or Xing Meng Mongolian Orogenic Belt (Lin et al., 2001; Dou and Chang, 2003; Wei et al., 2005) which represents the eastern part of the CAOB that was accreted during the Palaeozoic (Ge et al., 2007; Ying et al., 2010a, 2010b; Zhou et al., 2010). This basement was formed during successive orogenies that have succeeded in northern China from the late Palaeozoic to the late Jurassic-early Cretaceous, the Hercynian, the Indosinian and the Yanshanian orogenies (Su et al., 2007; Lepvrier and Maluski, 2008; Lin et al., 2008; Faure et al., 2012). It is mainly composed of: (i) Palaeozoic to early Mesozoic intermediate to felsic granitic plutons (Miao et al., 1998; Wang et al., 1998; Wu et al., 2000, 2002, 2005a, 2005b, 2007; Davis et al., 2001; Guo et al., 2004; Ge et al., 2007; Su et al., 2007; Yang et al., 2007; Zhou et al., 2010), (ii) mafic to felsic volcanic rocks (Ge et al., 2007; Zhou et al., 2010) and (iii) Palaeozoic sedimentary or metasedimentary units (Wu et al., 2005b; Zhou et al., 2010). From North to South there is a parallel alternation of horsts and half-grabens which could be related to a “Basin and Range” structural pattern (Meng et al., 2003; Ren et al., 1998; Wernicke et al., 1988). Regarding its geometry, the Erlian Basin was divided in about

52 half-graben-shaped depressions (Dou and Chang, 2003; Meng et al., 2003) controlled by a normal-fault system.

The selected areas for this study (**Figure 28**) correspond to the central part of the Wulanchabu Sub-basin (**Figure 28A**) and the western part of the Manite Sub-basin (**Figure 28B**). Both areas were selected because basement rocks are well outcropping and because they are surrounding parts of the basin that host uranium deposits (e.g. the Nuheting deposit, Dalhkamp, 2009; the Bayinwula deposit, Fan et al., 2008; **Figure 28**). The study was carried out in the Bayinbaolige Horst and in the northern part of the Sunite Horst.



Figure 2: . Geological map of the study areas showing the the sample location and indicating ages, U content and Th/U value per sample when it has been analysed (modified after CNNC, unpublished data). A= geological map of the central part of the Wulanchabu Sub-basin; B= geological map of the western part of the Manite Sub-basin.

4. Materials and methods

A total of twenty-five samples (**Figure 28**), including fifteen samples of granite, six samples of volcanic rocks and 4 samples of sandstone from the Saihan and the Erlian formations, were collected from outcrops. Seven of the fifteen granite samples correspond to drill cores that were collected in the drill hole ZK (**Figure 28**). Basement rocks were sampled at the western margin of the Wulanchabu Sub-basin (**Figure 28**) and at both margins of the Sunite Sub-basin, north and south. Whole-rock geochemical analyses were realised by ICP-AES for major elements and ICP-MS for trace elements at the SARM-CRPG in Nancy, France. The mineralogical study was carried out in the GéoRessources laboratory (France) using optical microscope and at the microanalytical facility of the Lorraine University (SCMEM, Nancy, France) using: (i) a JEOL J7600F scanning electron microscope (SEM) and (ii) a CAMECA SX100 electron microprobe (EMP). The U and Pb isotope analyses realized on zircons were performed using the CAMECA IMS 1270 ion microprobe facility, at CRPG, Nancy. The analysed masses were: 203.5 (background noise, measured for 4s), ZrO₄ (2s), ²⁰⁴Pb (10s), ²⁰⁶Pb (4s), ²⁰⁷Pb (40s), ²⁰⁸Pb (10s), ²³⁸U (2s), ²³⁸U¹⁶O (2sec) and ²³⁸U¹⁶O₂ (2s). Each analysis consisted of 16 iterative cycles over each mass. The mass resolution was about 5 000, which is sufficient to separate the molecular interferences. It is important to note that the quantity of analysed material was very small, which constitutes one limitation of this method: the analytical uncertainty will be greater with younger samples. The age calculations were based on the isotopic ratios corrected for background noise and common lead (using ²⁰⁴Pb). The U and Pb abundances are calculated on the basis of the ZrO₄ and UO₂ correlation for the standard, and the isotope ratio ²³⁸U/²⁰⁶Pb (Compston et al., 1984). The ²⁰⁷Pb/²⁰⁶Pb ratio was directly derived from each spot analysis. The standard used for determination of the correlation line, following Compston et al. (1984), was the 91500 zircon dated at 1 064 Ma (Wiedenbeck et al., 1995). U-Th-Pb chemical dating on monazites was performed at SCMEM, in Nancy, using a CAMECA SX100 electron microprobe equipped with five wavelength-dispersive spectrometers using an acceleration voltage of 20 kV and a beam current of 100 nA. Counting times (peak + background) were 30 s for Th, 30 s for U and 80 s for Pb. The detailed analytical method and the age calculation procedure are presented in Cocherie and Albarède (2001). Sm–Nd isotopic values were determined on crushed wholerock samples by isotope dilution. All analyses were carried out at the Geosciences Rennes Laboratory at the University of Rennes 1. Samples were spiked with a ¹⁵⁰Nd–¹⁴⁹Sm mixed solution and dissolved in HF-HNO₃. REE elements were separated using BioRad AG 50W×8 H⁺ 200–400

mesh cationic resin. Sm and Nd were separated and collected by passing the solution through a further set of ion exchange columns loaded with Ln spec Eichrom resin. Sm and Nd were loaded with HNO₃ reagent on to double Re filaments and analysed in a Finnigan MAT262 multicollector mass spectrometer in static mode. In each analytical session, the unknowns were analysed together with the Ames nNd-1 Nd standard, which during the course of this study yielded an average of 0.511964 (standard deviation = 7.23×10⁻⁶). All analyses of the unknowns were adjusted to a nominal ¹⁴³Nd/¹⁴⁴Nd value of 0.511850 for the La Jolla standard. Mass fractionation was monitored and corrected using the value ¹⁴⁶Nd/¹⁴⁴Nd= 0.7219. Procedural blanks analysed during the period of these analyses were ~190 pg and are considered to be negligible compared to the total quantity of Nd in the samples.

5. Petrography

5.1. Biotite granites

Biotite granites are well-represented in the Bayinbaolige Horts (Samples E01-E05 and E07-E09, **Figure 28**), at the northern margins of the Wulanchabu and Manite sub-basins. These granites are strongly weathered on outcrops. Drill core observations on drill hole ZK showed that the weathering could affect vertically several tens of meters of the granites. Nevertheless, non-weathered sections of these granites can be observed in the deeper parts of the drill hole ZK. Biotite granites present granular to microgranular texture. Granites from the northern margin of the Wulanchabu Sub-basin may show a ductile deformation characterised by grain boundary migrations (GBM) of quartz crystals mainly developed in shear zone (**Figure 29**), whereas those occurring at the northern margin of the Manite Sub-basin are weakly deformed. However, they all present a late fracturation that may play a significant role in the weathering process (**Figure 29**).

The main mineral assemblage of biotite granites is quartz, K-feldspar, plagioclase, biotite and amphibole (**Figure 29**). EMP analyses on amphibole characterise a dominantly calcic-amphibole (10-12 wt.% CaO; **Table 4**) which is of hornblende type. Accessory mineral assemblage (**Figure 29**) is titanite, zircon, U-thorite, allanite, Fe-Ti and Ti oxide and apatite. Zircon may have a low to moderate U content (0.21 wt.% UO₂ in Zrn1, **Table 4**). U-thorite presents a mineralogical composition broadly ranging from 55.74 to 71.73 wt.% ThO₂, 17.81-18.32 wt.% SiO₂ and less than 1 wt.% UO₂ up to 13.25 wt.% UO₂ (**Table 4**) depending of its degree of alteration and metamictisation. In the weathered part of the biotite granites, Urano-thorite tends to present a composition close to the thorite end member with an extremely low

or no uranium content (**Table 4**). Allanite shows a chemical composition of 27-31 wt.% SiO₂, 12-14 wt.% Al₂O₃, 10-12 wt.% CaO, 8-14 wt.% FeO and 6-12 wt.% Ce₂O₃, 1-8 wt.% La₂O₃, 2-3 wt.% Nd₂O₃ and 1-2 wt.% ThO₂ (**Table 4**). Allanite may also contain a significant U concentration (up to 0.38 wt.% UO₂ in Aln1, **Table 4**). Fe-Ti oxides with 49.41 wt.% TiO₂, 35.14 wt.% FeO, 13.04 wt.% MnO present a nearly stoichiometric ilmenite composition and do not contain uranium detectable by the EMP. Altered Fe-Ti oxides with 70.33 wt.% TiO₂, 15.33 wt.% FeO and 0.11 wt.% MnO are characterised by a strong depletion of their Fe and Mn content. They may contain significant uranium concentration (0.09 wt.% UO₂, Ilm1 in **Table 4**). Alteration minerals are chlorite, epidote, REE carbonate, monazite, Fe oxide and pyrite. They occur in fractures or in the destruction halos of metamict U-bearing accessory minerals. Chlorite widely occurs in alteration of biotite (**Figure 29**). The major U-bearing accessory minerals such as Urano-thorite and allanite both present a destruction halo due to alpha radiation. In the destruction halo of allanite a rare earth element (REE) carbonate of bastnäsite type and secondary epidote are newly formed (**Figure 29**). It may also be associated with secondary monazite devoid of Th. In the destruction halo of uranothorite pyrite, uranium oxide, REE carbonate and galena have been identified (**Figure 29**). In the weathered part of biotite granites, the destruction halo of the two major U-bearing accessory minerals, U-thorite and allanite, is associated with Fe oxide. The uranium content of both minerals has been strongly leached out, with U content generally below the detection limit of the EMP (**Table 4**). In the non-weathered part of the biotite granites (at several tens of meters of depth) the U-bearing accessory minerals are metamict and their U content has been partly to totally released in the rock but not leached out of the rock whereas in the weathered part their U content has been leached by oxidizing fluid.

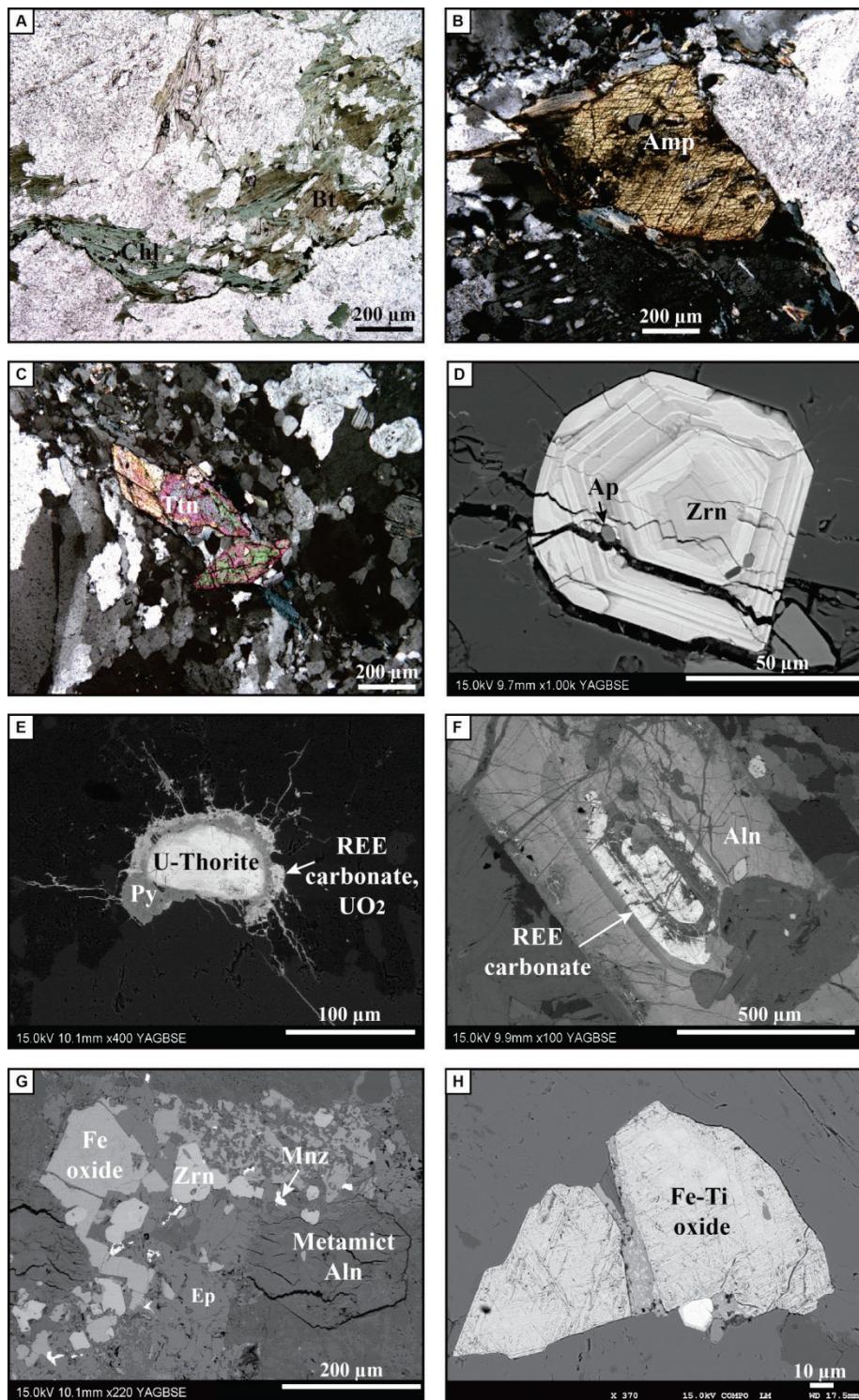


Figure 4; Major and accessory minerals occurring in biotite granite of the basement surrounding the northern part of the Erlian Basin. A= biotite (Bt) and Chlorite (Chl); B= amphibole (Amp); C= Titanite (Ttn); D= Zircon (Zrn) and apatite (Ap); E= metamict U-thorite showing a destruction halo associated with pyrite (Py), REE carbonate and uranium oxide; F= metamict allanite (Aln) associated with REE carbonate; G= metamict allanite showing a destruction halo associated with secondary epidote (Ep), secondary monazite (Mnz) and fe oxide; H= Fe-Ti oxide.

Table 6. Representative EMP analyses of major and accessory minerals occurring in biotite granites of the basement surrounding the northern part of the Erlian Basin.

Location		Bayinbaolige and Sunite horsts														
Lithology		Biotite granite														
Mineral	Amp	Ttn		Aln		U-Th		Th		Zrn		Ox. Fe-Ti				
Sample	ZK152	Zk137	E08	ZK1165	Zk137	Zk152	Zk923	Zk137	Zk258	E03	E09			E01		
Analysis n°	Amp1	Amp2	Ttn1	Ttn2	Aln1	Aln2	U-th1	U-th2	Th1	Th2	Zrn1	Zrn2			Ox1	Ox2
Oxides (wt.%)																
SiO ₂	39.97	41.88	29.29	28.96	27.28	30.70	18.32	17.81	10.67	8.89	30.87	31.30	SiO ₂	1.47	0.02	
TiO ₂	0.48	0.60	36.25	35.53	2.10	1.46	0.00	0.00	0.12	0.02	0.00	0.01	TiO ₂	70.33	49.41	
Al ₂ O ₃	9.85	9.24	1.39	1.68	12.81	13.51	0.02	0.03	0.17	0.19	0.00	0.00	Al ₂ O ₃	1.05	0.01	
FeO	24.45	21.20	1.54	1.83	8.24	14.04	0.20	0.24	0.96	1.01	0.96	0.33	FeO	15.43	35.14	
MgO	6.53	9.15	0.01	0.01	0.41	2.09	0.02	0.08	0.08	0.04	0.01	0.00	MnO	0.11	13.04	
CaO	10.71	11.29	26.93	26.53	10.11	10.91	0.00	2.59	3.63	3.86	0.03	0.10	MgO	0.10	0.01	
Na ₂ O	1.39	0.59	0.00	0.05	0.39	0.08	0.03	0.10	0.00	0.00	0.00	0.00	Cr ₂ O ₃	0.04	0.01	
K ₂ O	1.66	1.15	0.00	0.02	0.05	0.02	0.04	0.08	0.04	0.02	0.00	0.00	V ₂ O ₃	2.64	1.72	
F	0.43	1.42	0.65	1.03	1.16	0.24	0.00	1.14	1.17	1.81	0.15	0.34	CoO	0.00	0.02	
P ₂ O ₅	0.04	0.10	0.39	0.39	0.11	0.20	0.16	0.07	1.83	2.03	0.40	0.53	UO ₂	0.09	0.01	
V ₂ O ₃	0.04	0.05	0.00	0.00	0.08	0.00	0.04	0.00	4.91	5.07	0.00	0.00	Total	91.26	99.39	
ZrO ₂	0.00	0.00	0.04	0.00	1.16	0.00	0.00	0.00	3.72	3.55	65.16	67.35				
Y ₂ O ₃	0.00	0.00	0.49	0.30	0.17	0.00	0.22	0.09	2.19	2.68	0.00	0.00				
La ₂ O ₃	0.00	0.01	0.00	0.10	1.77	7.63	0.00	0.00	0.16	0.31	0.00	0.00				
Ce ₂ O ₃	0.00	0.00	0.50	0.96	6.03	11.71	0.00	0.00	0.11	0.34	0.00	0.00				
Nd ₂ O ₃	0.00	0.10	0.58	0.32	2.84	2.38	0.00	0.08	0.43	0.67	0.06	0.00				
PbO	0.02	0.00	0.00	0.00	0.06	0.04	1.02	0.41	0.11	0.19	0.00	0.00				
ThO ₂	0.00	0.00	0.00	0.06	1.34	0.79	70.73	55.74	63.54	63.56	0.05	0.15				
UO ₂	0.00	0.00	0.00	0.04	0.38	0.00	2.07	13.25	0.00	0.00	0.21	0.00				
Total	95.58	96.79	98.05	97.79	76.48	95.82	92.88	91.72	93.83	91.02	97.90	100.12				
Oxygens	23	23	5	5	12.5	12.5	4	4	4	4	4	4	3	3		
Cations																
Si	6.461	6.591	0.991	0.989	3.152	3.005	1.034	1.009	0.581	0.521	0.971	0.964	Si	0.034	0.001	
Al	1.539	1.409	0.055	0.068	1.744	1.559	0.001	0.002	0.011	0.013	0.000	0.000	Ti	1.238	0.947	
Al	0.337	0.305											Al	0.029	0.000	
Ti	0.058	0.071	0.923	0.913	0.182	0.108	0.000	0.000	0.005	0.001	0.000	0.000	Fe	0.302	0.749	
Fe	3.305	2.790	0.044	0.052	0.796	1.149	0.009	0.011	0.044	0.049	0.025	0.008	Mn	0.002	0.281	
Mg	1.574	2.147	0.001	0.000	0.071	0.305	0.002	0.007	0.006	0.003	0.000	0.000	Mg	0.003	0.000	
Ca	1.855	1.903	0.976	0.971	1.251	1.144	0.000	0.157	0.212	0.242	0.001	0.003	Cr	0.001	0.000	
Na	0.436	0.180	0.000	0.003	0.087	0.015	0.003	0.011	0.000	0.000	0.000	0.000	V	0.041	0.029	
K	0.342	0.231	0.000	0.001	0.008	0.002	0.003	0.006	0.003	0.001	0.000	0.000	Co	0.000	0.000	
P	0.005	0.013	0.011	0.011	0.011	0.017	0.008	0.003	0.084	0.101	0.011	0.014	U	0.000	0.000	
V	0.004	0.005	0.000	0.000	0.006	0.000	0.001	0.000	0.177	0.196	0.000	0.000				
Zr	0.000	0.000	0.001	0.000	0.065	0.000	0.000	0.000	0.099	0.010	0.999	1.011				
Y	0.000	0.000	0.009	0.005	0.010	0.000	0.007	0.003	0.063	0.084	0.000	0.000				
La	0.000	0.001	0.000	0.001	0.075	0.275	0.000	0.000	0.003	0.007	0.000	0.000				
Ce	0.000	0.000	0.006	0.012	0.255	0.420	0.000	0.000	0.002	0.007	0.000	0.000				
Nd	0.000	0.006	0.007	0.004	0.117	0.083	0.000	0.002	0.008	0.014	0.001	0.000				
Pb	0.000	0.000	0.000	0.000	0.002	0.001	0.015	0.006	0.002	0.003	0.000	0.000				
Th	0.000	0.000	0.000	0.000	0.035	0.018	0.908	0.719	0.787	0.847	0.000	0.001				
U	0.000	0.000	0.000	0.009	0.000	0.025	0.161	0.000	0.000	0.000	0.001	0.000				

5.2. Two-mica granites

Sample E10 is a two-mica granite (**Figure 28**) located in the northern part of the Sunite Horst. This two-mica granite presents a granular texture (**Figure 30**) and is weakly deformed. The main mineral assemblage is quartz, K-feldspar (major), plagioclase (very minor), biotite and muscovite (**Figure 30**). The accessory mineral assemblage (**Figure 30**) corresponds to monazite, xenotime, zircon and apatite. Monazite presents a composition of ~28 wt.% P₂O₅, 25-30 wt.% Ce₂O₃, 12-14 wt.% La₂O₃, 10-12 wt.% Nd₂O₃ and 6-12 wt.% ThO₂ (**Table 5**). U contents never exceed a few thousands of ppm. Xenotime shows a chemical composition of

~35 wt.% P₂O₅, ~44 wt.% Y₂O₃, 2-5 WT.% Gd₂O₃, ~5 wt.% Dy₂O₃, 3-5 wt.% Er₂O₃, ~3 wt.% Yb₂O₃, and 1-2 wt.% of ThO₂ and UO₂ (**Table 5**). Alteration minerals are chlorite, epidote, secondary quartz and muscovite (**Figure 30**). Chlorite is often observed in alteration of biotite. The granite has been greisenized (**Figure 30**). Secondary quartz and muscovite have been observed related to hydrothermal alteration of K-feldspar. No evidence of alteration of U-bearing minerals such as monazite and xenotime has been observed.

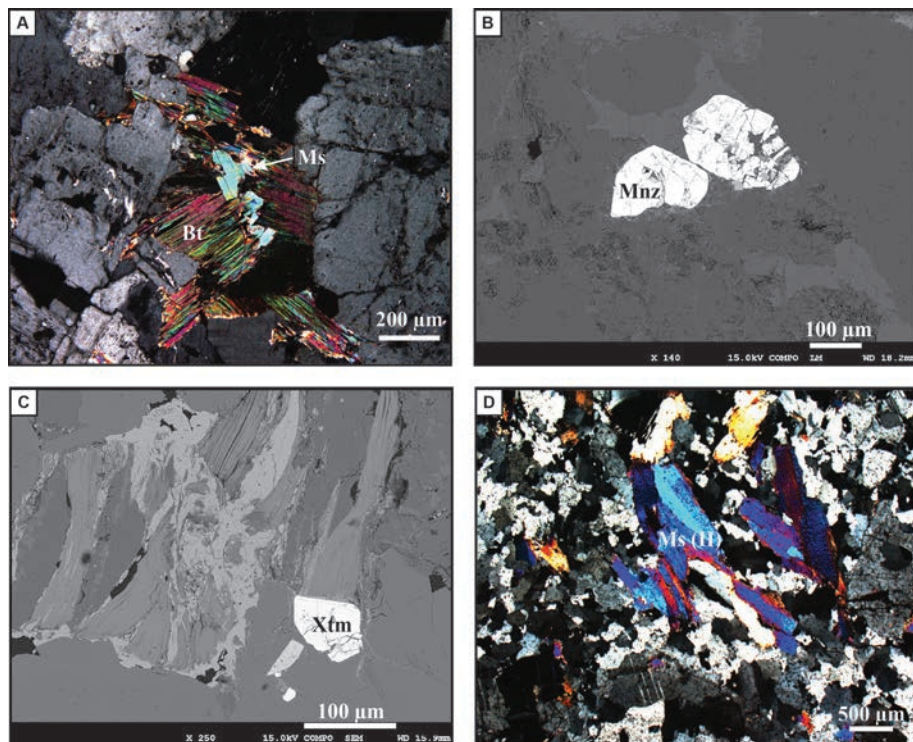


Figure 32. Major and accessory minerals occurring in two-mica granite of the northern part of the Sunite Horst. A= biotite (Bt) associated with muscovite (Ms); B= monazite (Mnz); C= xenotime (Xtm); D= secondary quartz and muscovite in greisenized part of the two-mica granite.

Table 7. Representative EMP analyses of monazite and xenotime occurring in the two-mica granite located in the northern part of the Sunite Horst.

Sunite Horst				
Lithology	2-mica granite			
Mineral	Monazite		Xenotime	
Sample	E10			
Analysis n°	Mnz1	Mnz2	Xnt1	Xnt2
Oxides (wt.%)				
P ₂ O ₅	28.10	28.71	35.07	34.76
SiO ₂	1.76	1.20	0.42	0.70
CaO	0.63	0.65	0.00	0.09
Y ₂ O ₃	2.03	1.94	44.43	44.60
La ₂ O ₃	12.50	13.77	0.00	0.00
Ce ₂ O ₃	26.71	28.64	0.14	0.00
Nd ₂ O ₃	11.05	11.29	0.33	0.35
Sm ₂ O ₃	1.95	2.14	0.81	0.10
Gd ₂ O ₃	1.59	1.62	4.44	3.63
Dy ₂ O ₃	0.60	0.55	5.40	5.01
Er ₂ O ₃	0.00	0.00	3.42	4.36
Yb ₂ O ₃	0.00	0.23	3.03	3.24
PbO	0.16	0.10	0.36	0.44
ThO ₂	10.55	7.40	1.30	1.19
UO ₂	0.00	0.00	1.67	1.96
Total	97.63	98.24	100.82	100.43
Oxygens	4	4	4	4
Cations				
P	0.960	0.970	0.978	0.973
Si	0.070	0.050	0.014	0.023
ΣT-site	1.030	1.020	0.992	0.996
Ca	0.030	0.030	0.000	0.003
Y	0.040	0.040	0.779	0.785
La	0.190	0.200	0.000	0.000
Ce	0.390	0.420	0.002	0.000
Nd	0.160	0.160	0.004	0.004
Sm	0.030	0.030	0.009	0.001
Gd	0.020	0.020	0.048	0.040
Dy	-	-	0.057	0.053
Er	-	-	0.035	0.045
Yb	-	-	0.030	0.033
Pb	0.002	0.001	0.003	0.004
Th	0.100	0.070	0.010	0.009
U	0.000	0.000	0.012	0.014
Σa-site	0.950	0.970	0.989	0.991
% Huttonite	0.0708	0.0479	-	-
% Brabantite	0.0578	0.0578	-	-
% Monazite	0.8293	0.8752	-	-

5.3. Volcanic rocks

Volcanic rocks were observed at the bottom of the Wulanchabu Sub-basin (samples E05 and E06, **Figure 28**) and in samples E11-E14 at the northern margin of the Manite Sub-basin. Whole-rock geochemical data (**Appendix 2**; **Appendix 3**) indicate three different types for these volcanic rocks (**Figure 31**), all of acidic composition: (i) dacite, (ii) trachyte and (iii) rhyolite.

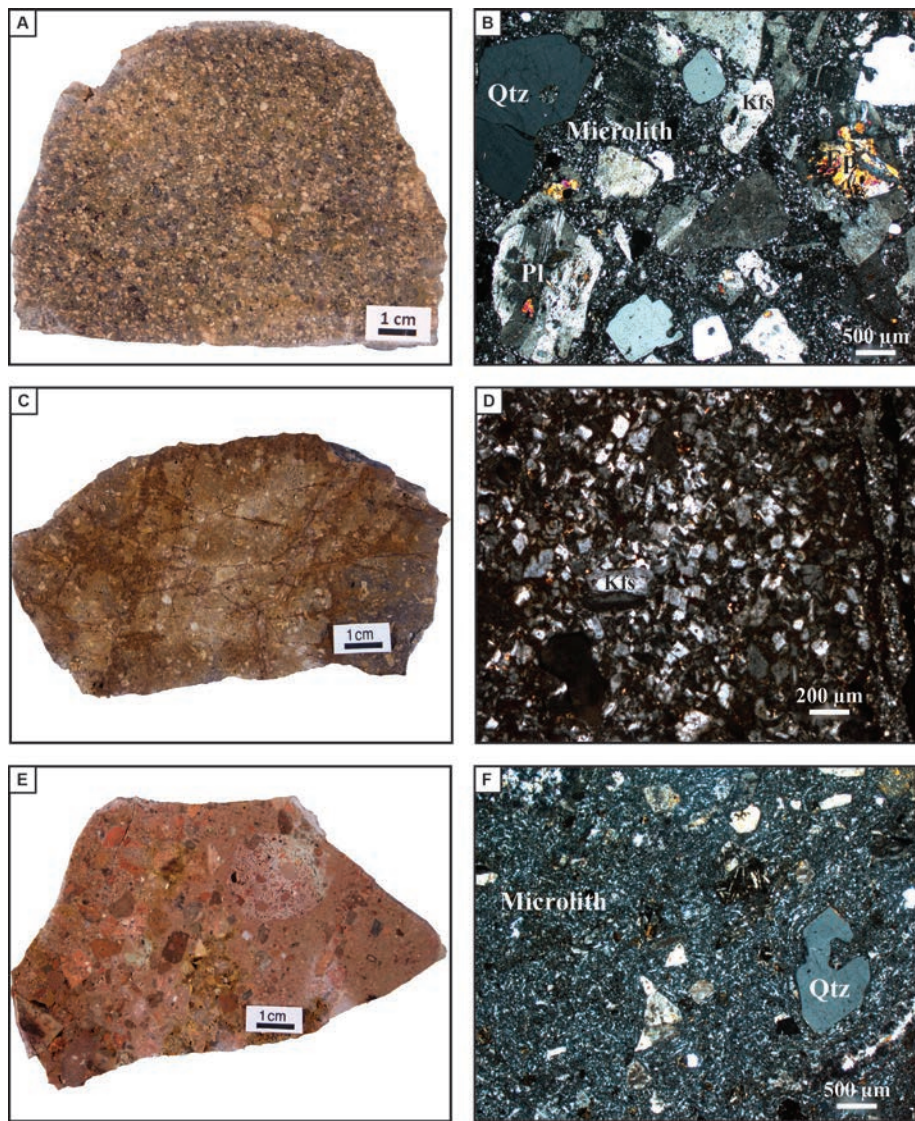


Figure 33. Volcanic rocks occurring at the bottom of the Wulanchabu Sub-basin and in part of the Bayinbaolige Horst located at the northern margin of the Manite Sub-basin. Macroscopic and microscopic illustrations are given for each rock-type. A= dacite (E13); B= dacite texture showing quartz, feldspar and epidote crystals enclosed in microlith; C= trachyte (E06); D= trachyte texture showing finely crystallized quartz and feldspar; E= rhyolite (E05); F= rhyolite texture showing quartz and feldspar crystals enclosed in microlith.

Dacite (sample E13) presents a trachytic texture with quartz, K-feldspar, plagioclase and epidote phenocrysts enclosed in microlith (**Figure 31**). Trachyte (sample E06) shows a trachytic to microgranular texture with quartz, K-feldspar and rare plagioclase phenocrysts in a finely crystalized matrix (**Figure 31**). The proportion of matrix is very low. Rhyolites (samples E05, E11, E12 and E14; **Appendix 2**) show a trachytic texture with quartz and dominantly K-feldspar phenocrysts enclosed in fine grained matrix. Accessory minerals that were observed in trachyte and rhyolite are monazite, xenotime and zircon.

6. Geochemistry

Whole-rock geochemical content of SiO₂ *versus* Na₂O + K₂O characterise the plutonic rocks as alkali granite and granite (**Appendix 1**; **Appendix 3**) indicating a highly felsic rocks. Only sample E08 has a granodiorite composition. Incompatible trace element ratios presented in **table 6** are elevated to very elevated and characterise highly fractionated magma compared to reference ratios presented in Saunders et al. (1988) and Weaver (1991). Moreover, in spider diagrams these granites are characterised by well-pronounced but variable Ba, U and Th positive anomalies (**Appendix 5**) and by REE pattern enriched in light REE compared to heavy REE.

Table 8. Incompatible trace element ratios for igneous rocks occurring in the basement of the Wulanchabu and Manite sub-basins.

Sample n°	Zr/Nb	La/Nb	Ba/Nb	Ba/Th	Rb/Nb	K/Nb	Th/Nb	Th/La	Ba/La
ZK-25.8m	9.1	2.97	20.1	4	14.1	2467	4.69	1.58	6.7
ZK-60.5m	17.3	4.47	10.4	5	2.3	505	2.02	0.45	2.3
ZK-92.3m	10.1	1.44	7.4	1	24.2	4526	6.48	4.49	5.1
ZK-116.5m	11.1	2.68	40.0	19	14.0	2726	2.10	0.78	14.9
ZK-137.0m	9.4	2.09	30.2	20	11.2	2142	1.48	0.71	14.5
ZK-152.0m	36.2	10.25	312.5	133	23.5	7822	2.34	0.23	30.5
ZK-176.5m	23.3	4.11	104.9	45	21.3	4090	2.29	0.56	25.5
E01	8.2	1.60	49.3	24	34.9	5528	2.01	1.26	30.8
E02	6.2	1.52	16.0	5	27.6	2935	2.99	1.97	10.5
E03	11.3	2.32	50.8	19	32.1	5127	2.66	1.15	21.9
E04	43.0	5.65	70.0	18	37.2	7941	3.70	0.66	12.4
E05	10.7	1.13	6.5	15	7.4	1426	0.41	0.36	5.7
E06	17.4	1.79	26.1	85	3.2	1332	0.30	0.17	14.6
E07	34.4	1.36	5.7	8	7.6	2227	0.70	0.52	4.2
E08	47.3	6.09	236.6	250	8.3	4718	0.95	0.16	38.8
E09	36.5	2.99	168.8	232	11.8	5183	0.73	0.24	56.4
E10	12.5	3.06	17.0	5	42.3	6903	3.11	1.02	5.5
E11	25.6	2.04	47.0	41	13.3	3982	1.15	0.56	23.0
E12	32.2	4.26	128.5	89	15.6	4370	1.43	0.34	30.1
E13	34.8	4.06	151.4	103	15.8	5322	1.46	0.36	37.3
E14	18.5	1.77	18.4	18	8.5	2719	0.97	0.55	10.4

The Q-P diagram presented in figure 54 allows estimating the relative proportions of quartz (Q parameter in millications), K-feldspar (positive P value in millications) and plagioclase (negative P value in millications) in the sampled igneous rocks. All the samples including biotite granites, two-mica granite and volcanic rocks show moderately negative to slightly positive P values ($-200 < P < 100$) indicating a major proportion of K-feldspar relatively to plagioclase and elevated to very elevated quartz proportion ($120 < Q < 300$). Two magmatic series can be distinguished (**Figure 32**): (i) samples E08, E09, E12, E13 and ZK1765 belong to a calcalkaline association and (ii) the rest of the samples may correspond to a highly potassic calcalkaline association. Even though weathering associated with a loss of Ca and Na may have slightly increased the P and Q values. Samples belonging to the highly potassic calcalkaline association seem to be more differentiated to the ones belonging to the calcalkaline association. Samples E10 and E05 are characterised by positive P values and very elevated Q values (> 250) indicating greisenization.

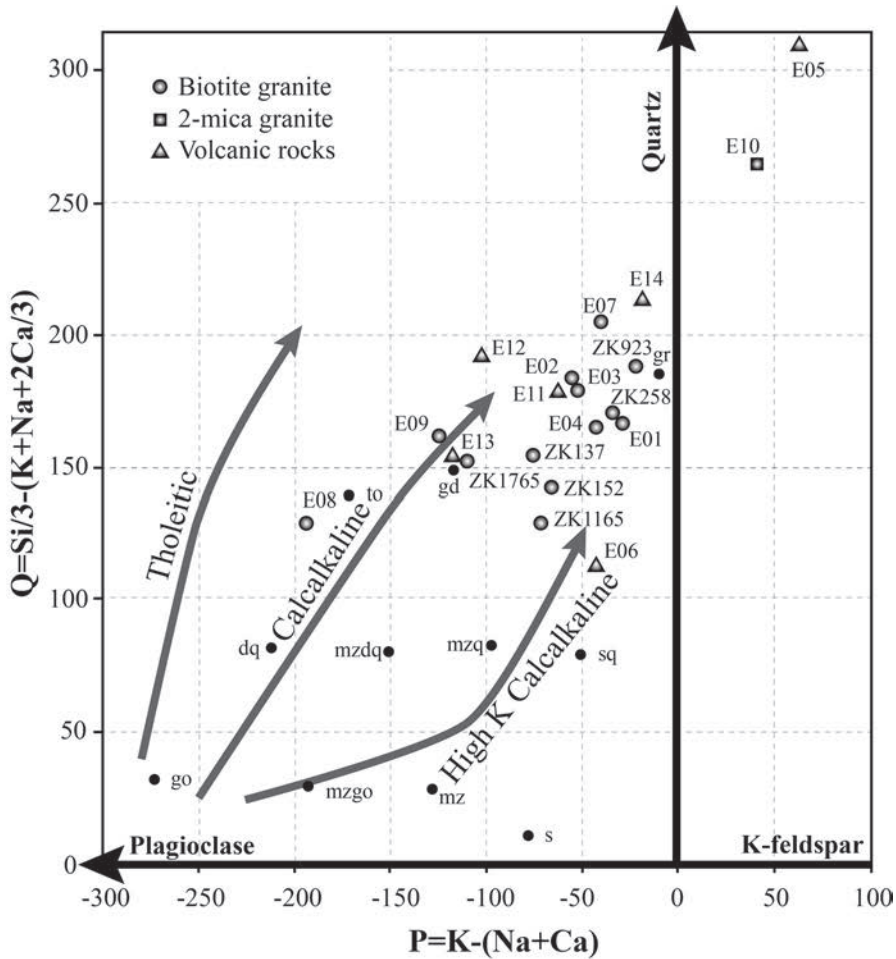


Figure 34. Q-P diagram showing the relative proportions of quartz, K-feldspar and plagioclase in the igneous rocks of the Erlian area (modified after Debon and Lefort, 1983, 1988). Q= chemical-mineralogical parameter (in millications) P= chemical-mineralogical parameter (in millications) estimating the relative proportions of K-feldspar (positive) and plagioclase (negative).

The A-B diagram presented in **figure 33** gives the excess of alumina not bound to the feldspars (A parameter in millications) as associated with a differentiation index (B parameter in millications) and define a metaluminous domain (mainly mantle derived material) versus peraluminous domain (continental crust domain). The samples are slightly metaluminous to significantly peraluminous ($-20 < A < 60$) and most of them are leucocratic ($0 < B < 100$). The A parameter is slightly shifted to higher values in the peraluminous domain due to a loss of Ca and Na. To summarize, biotite granites correspond to low to high-K calcalkaline metaluminous magmatic associations trend are likely derived. The two-mica granite (sample E10) is only slightly peraluminous ($A = 23$) and very felsic ($B < 20$).

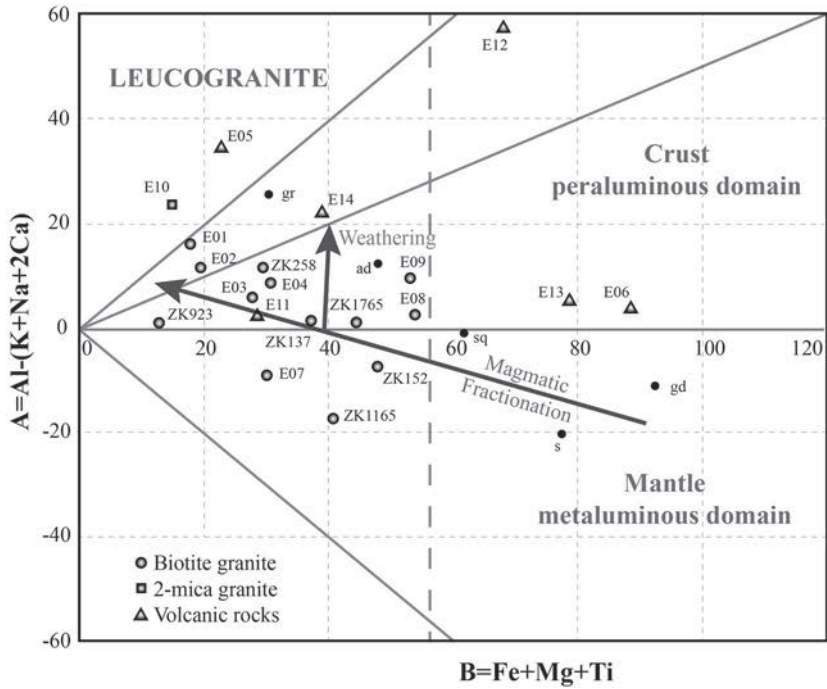


Figure 35. A-B diagram indicating the peraluminosity (A parameter) and the correlation (B parameter) of igneous rocks occurring in the basement of the Erlian basin (modified after Debon and Lefort, 1983, 1988). A= chemical-mineralogical parameter (in millications) giving the excess of alumina not bound to the feldspars; B= chemical-mineralogical parameter (in millications) used as a differentiation index for igneous rocks.

7. Geochronology

Bitotite granites and volcanic rocks occurring in the basement surrounding the northern margins of the Wulanchabu and the Manite sub-basins were dated by U-Pb isotopes on zircon. The two-mica granite occurring in the northern part of the Sunite Horst (E10) has been dated using the U-Th-Pb chemical method on monazite. Similarly, U-Th-Pb chemical ages were determined on detrital monazites occurring in sandstones of the Saihan and the Erlian formations of the Erlian basin.

7.1. U-Pb isotopic ages on zircon

Thirty-five zircon grains (**Figure 34**) from biotite granites and volcanic rocks were analysed with the IMS 1270 ion microprobe. Zircon cores and zones with clear magmatic growth zoning were analysed.

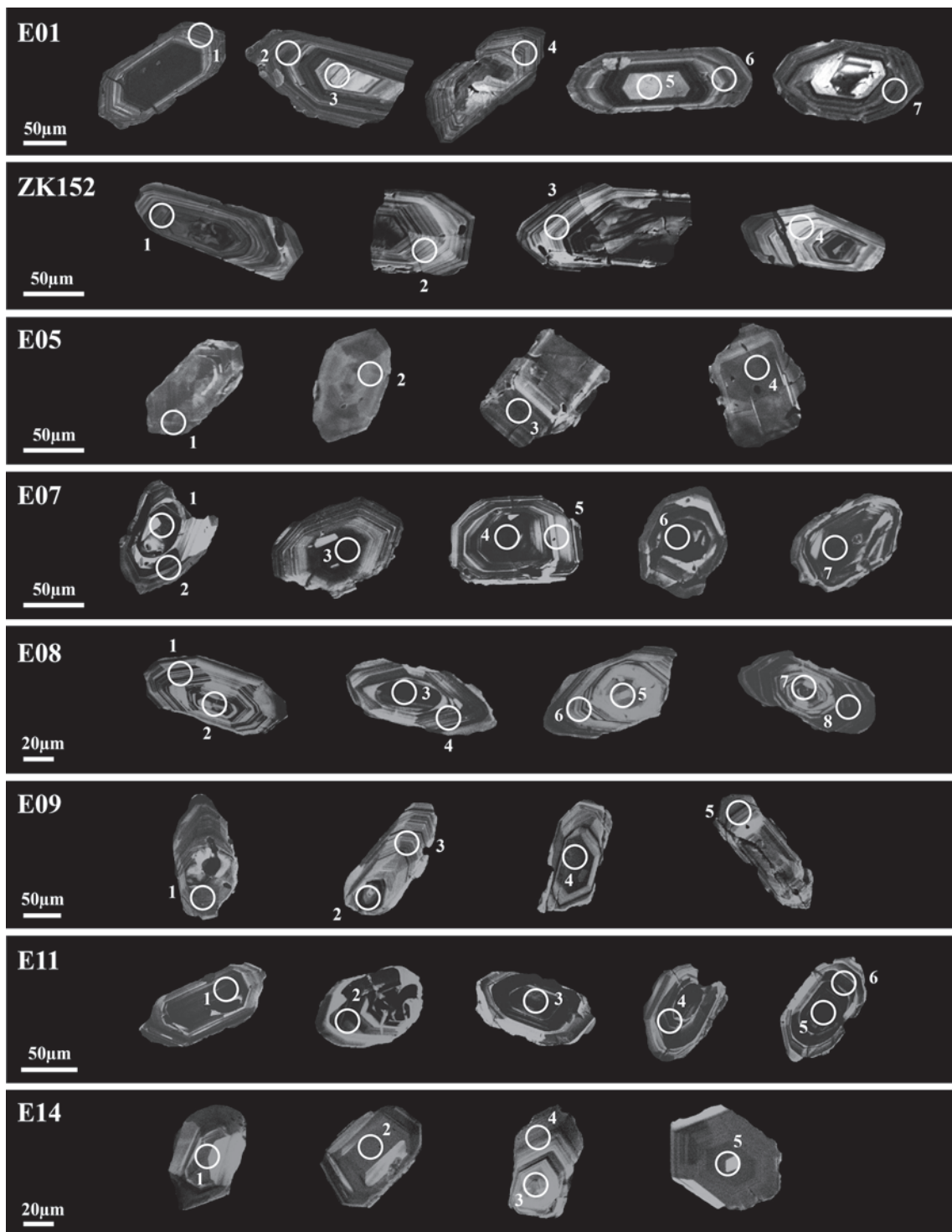


Figure 36. Cathodoluminescence microphotographs of zircon grains analysed for U-Pb isotopic determinations, for each sample. The white circles indicate the spots of the isotopic analyses presented in table 7.

All the results are reported in **Table 7** and in figure 57. The thirty-five analytical points give concordant ages and have been represented in Concordia diagrams (**Figure 35**). Because of the higher quantity of ²⁰⁶Pb than of ²⁰⁷Pb, ²⁰⁶Pb/²³⁸U ratios (and the corresponding ages) have smaller error than ²⁰⁷Pb/²³⁵U ratios (**Table 7**). For this reason only the ²⁰⁶Pb/²³⁸U ages will be discussed in this paper. The ²⁰⁶Pb/²³⁸U age dispersion is similar to the individual errors which are typically ranging from ± 1.3 to ± 6.8 Ma. This indicates a good reproducibility of the analyses. Biotite granites show two different ages (**Table 7, Figure 35**): (i) samples E01 and ZK152 from the northern margin of the Wulanchabu Sub-basin were dated respectively 236.8 ± 5.8 Ma and 233.0 ± 12.0 Ma; (ii) samples E07, E08 and E09 from the northern margin of the Manite Sub-basin are dated respectively at 291.3 ± 3.8 Ma, 304.3 ± 3.8 Ma and 312.4 ± 4.8 Ma. Therefore, the biotite granites studied were not intruded at the same time. The biotite granites were emplaced during the late Carboniferous-early Permian to early-middle Triassic. Similarly, volcanic lavas were erupted at different times. E05 sampled at the base of the basin is dated at 146 ± 0 Ma whereas E11 and E14 sampled in the basement, north of the Erlian Basin, were dated respectively at 296.1 ± 3.7 Ma and 306.0 ± 18 Ma. Therefore, the first population of volcanic rocks were emplaced during the late Carboniferous-early Permian and thus may be synchronous the biotite granite intrusions. The second population was emplaced during the late Jurassic.

Table 9. Analytical results of the U/Pb ion-microprobe determinations on zircons from biotite granites and volcanic rocks occurring in the northern margins of the Wulanchabu and the Manite sub-basins. Lead isotope ratios are corrected for common lead (using ^{204}Pb count rates) and U/Pb ratios are calculated using the correlation line of the standards.

Grain spot	Pb (ppm)	U (ppm)	Th (ppm)	Th/U	^{206}Pbc (%)	$^{204}\text{Pb}/^{206}\text{Pb}$	Radiogenic ratios						Ages in Ma						
							$^{206}\text{Pb}/^{238}\text{U}$	±	$^{207}\text{Pb}/^{235}\text{U}$	±	$^{207}\text{Pb}/^{206}\text{Pb}$	±	Correl. Err.	$^{206}\text{Pb}/^{238}\text{U}$	±	$^{207}\text{Pb}/^{235}\text{U}$	±	$^{207}\text{Pb}/^{206}\text{Pb}$	±
<i>E01</i>																			
1	35.7	1139.6	725.8	0.64	9.0	0.0062	0.155	0.030	0.154	0.007	0.054	0.054	0.19	230.9	2.4	242.5	11.9	356	118
2	15.5	565.3	643.1	1.14	9.8	0.0068	0.221	0.033	0.190	0.010	0.051	0.071	0.18	202.3	2.5	204.9	13.2	235	155
3	30.3	1076.3	763.3	0.71	10.3	0.0072	0.158	0.040	0.177	0.008	0.054	0.082	0.13	207.5	2.2	219.5	16.2	350	175
4	17.5	543.1	348.6	0.64	5.1	0.0032	0.194	0.152	0.178	0.028	0.051	0.293	0.10	237.1	6.8	237.8	60.6	245	564
5	17.1	532.8	348.3	0.65	3.8	0.0023	0.190	0.028	0.177	0.010	0.051	0.079	0.16	235.7	2.9	234.6	16.6	224	173
6	40.1	1276.6	544.6	0.43	6.5	0.0042	0.124	0.067	0.179	0.011	0.053	0.079	0.16	231.2	3.0	238.6	16.8	312	170
7	37.6	1180.2	474.9	0.40	4.8	0.0030	0.123	0.019	0.176	0.004	0.052	0.027	0.29	234.6	1.9	239.3	5.9	286	60
<i>ZK152</i>																			
1	17.1	562.3	398.1	0.71	1.1	0.0006	0.222	0.016	0.159	0.005	0.052	0.034	0.24	223.6	1.9	227.1	7.1	263	76
2	5.8	179.9	143.8	0.80	1.7	0.0010	0.237	0.027	0.173	0.010	0.051	0.068	0.18	238.5	2.9	238.3	14.6	236	150
3	13.3	417.1	273.0	0.65	3.3	0.0020	0.221	0.032	0.159	0.009	0.052	0.071	0.16	235.0	2.7	238.9	15.1	277	154
4	8.9	268.1	182.3	0.68	2.5	0.0015	0.209	0.023	0.179	0.007	0.050	0.049	0.20	243.6	2.4	237.2	10.5	175	111
<i>E05</i>																			
1	19.1	562.3	398.1	0.71	16.8	0.0134	0.195	0.115	0.096	0.017	0.053	0.233	0.11	133.6	3.4	143.7	30.9	313	457
2	16.3	179.9	143.8	0.80	1.8	0.0010	0.257	0.012	0.106	0.007	0.049	0.037	0.25	143.9	1.4	142.7	5.1	124	85
3	15.7	417.1	273.0	0.65	2.1	0.0012	0.138	0.033	0.110	0.024	0.051	0.067	0.15	140.7	1.4	145.6	9.1	225	147
4	14.1	268.1	182.3	0.68	1.1	0.0006	0.167	0.018	0.108	0.006	0.050	0.036	0.25	145.3	1.3	147.6	5.0	186	81
<i>E07</i>																			
1	7.0	180.3	281.4	1.56	1.7	0.0010	0.508	0.016	0.128	0.007	0.050	0.069	0.11	285.2	2.1	276.0	16.7	199	153
2	7.8	196.4	283.3	1.44	1.4	0.0008	0.462	0.021	0.133	0.010	0.052	0.070	0.15	289.8	3.0	290.2	17.7	294	153
3	15.2	379.6	584.4	1.54	3.8	0.0023	0.502	0.018	0.137	0.010	0.054	0.067	0.15	294.1	2.9	303.8	17.7	379	144
4	5.5	138.8	168.6	1.21	9.8	0.0068	0.434	0.042	0.132	0.018	0.056	0.135	0.14	290.9	5.3	307.8	35.5	438	275
5	1.9	49.4	42.5	0.86	3.5	0.0021	0.273	0.029	0.130	0.013	0.051	0.080	0.16	283.5	3.6	277.6	19.4	228	174
6	15.4	392.0	663.0	1.69	5.0	0.0031	0.576	0.014	0.132	0.008	0.046	0.081	0.10	289.0	2.3	259.5	18.4	0	184
7	8.0	206.0	394.0	1.91	1.5	0.0008	0.621	0.013	0.128	0.006	0.049	0.073	0.09	285.0	1.8	270.0	17.3	142	163
<i>E08</i>																			
1	6.0	145.6	108.0	0.74	1.5	0.0009	0.250	0.022	0.133	0.009	0.053	0.069	0.14	302.0	2.9	304.6	18.3	325	150
2	8.8	209.5	144.0	0.69	1.1	0.0006	0.216	0.021	0.124	0.009	0.049	0.069	0.14	306.4	3.0	290.6	17.5	165	154
3	25.5	610.5	495.2	0.81	0.4	0.0002	0.258	0.018	0.132	0.008	0.052	0.064	0.13	305.6	2.5	305.6	16.9	305	140
4	5.5	135.1	126.2	0.93	2.5	0.0015	0.292	0.026	0.126	0.013	0.046	0.093	0.14	300.3	3.8	265.9	21.7	0	184
5	3.8	89.9	50.9	0.57	3.2	0.0019	0.173	0.056	0.139	0.011	0.047	0.085	0.14	308.4	3.6	281.1	21.0	60	192
6	5.2	124.5	108.0	0.87	2.1	0.0012	0.274	0.032	0.139	0.010	0.048	0.084	0.12	304.6	3.1	282.4	20.8	103	188
7	10.9	263.1	452.9	1.72	0.9	0.0005	0.563	0.015	0.131	0.009	0.052	0.066	0.15	303.2	2.9	302.1	17.2	293	144
8	13.1	317.2	323.9	1.02	1.0	0.0006	0.327	0.016	0.107	0.010	0.050	0.070	0.14	301.6	3.0	291.6	17.9	213	155
<i>E09</i>																			
1	6.3	145.6	57.8	0.40	1.5	0.0008	0.131	0.041	0.150	0.010	0.055	0.066	0.16	314.8	3.2	327.5	18.6	418	141
2	7.9	183.5	131.8	0.72	1.4	0.0008	0.233	0.034	0.147	0.010	0.053	0.067	0.15	314.5	3.2	315.3	18.2	321	145
3	9.7	227.0	115.9	0.51	1.0	0.0006	0.163	0.029	0.144	0.006	0.053	0.067	0.11	311.4	2.2	311.7	17.8	314	145
4	8.4	195.4	104.3	0.53	1.5	0.0008	0.171	0.033	0.146	0.008	0.052	0.071	0.12	314.8	2.5	311.7	19.0	289	154
5	9.2	218.5	112.4	0.51	1.3	0.0008	0.159	0.030	0.144	0.012	0.051	0.073	0.17	308.8	3.7	302.0	19.1	250	160
<i>E11</i>																			
1	6.2	149.6	250.6	1.68	2.3	0.0013	0.530	0.014	0.148	0.008	0.045	0.079	0.11	306.0	2.6	266.4	18.5	0	114
2	7.5	185.8	201.9	1.09	1.8	0.0010	0.339	0.021	0.144	0.011	0.051	0.071	0.15	297.5	3.2	289.1	18.0	222	157
3	14.1	340.9	392.2	1.15	1.3	0.0007	0.368	0.016	0.145	0.008	0.052	0.068	0.13	302.1	2.6	298.6	17.6	272	149
4	7.0	172.6	195.3	1.13	1.6	0.0009	0.357	0.018	0.142	0.012	0.051	0.072	0.17	299.2	3.6	291.7	18.3	232	158
5	21.5	526.0	630.0	1.20	0.7	0.0004	0.378	0.014	0.150	0.006	0.050	0.068	0.10	299.3	2.0	286.9	16.8	188	150
6	6.7	167.0	156.1	0.93	1.5	0.0009	0.298	0.025	0.134	0.012	0.052	0.070	0.17	294.7	3.5	294.5	18.1	292	153
<i>E14</i>																			
1	6.4	156.5	114.2	0.92	4.7	0.0028	0.279	0.024	0.140	0.009	0.041	0.097	0.10	301.3	2.8	327.5	18.6	418	141
2	9.2	222.3	226.0	1.02	1.2	0.0007	0.312	0.017	0.146	0.009	0.049	0.069	0.14	304.4	3.0	315.3	18.2	321	145
3	11.8	290.9	308.0	1.06	1.1	0.0006	0.330	0.015	0.144	0.007	0.050	0.069	0.11	298.3	2.3	311.7	17.8	314	145
4	7.7	184.9	211.8	1.15	1.0	0.0006	0.366	0.018	0.143	0.008	0.053	0.064	0.13	303.5	2.5	311.7	19.0	28	

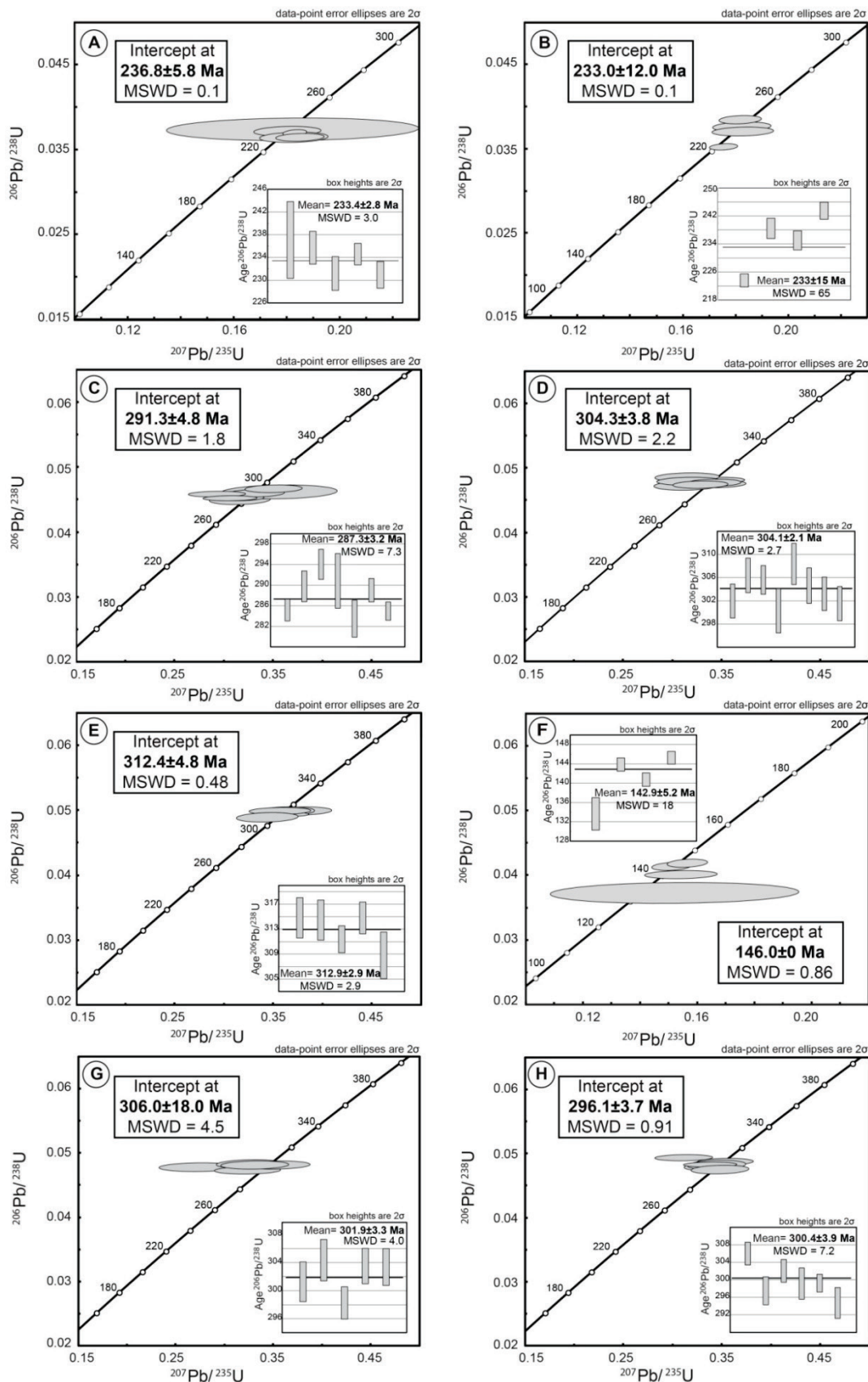


Figure 37. Results of the ion-probe dating of the zircons from biotite granites and volcanic rocks occurring in the northern margins of the Wulanchabu and the Manite sub-basins. The results are represented in concordia and weighted average diagrams. A= E01; B= ZK152; C= E07; D= E08; E= E09; F= E05; G= E14 and H= E11.

7.2. U-Th-Pb chemical ages on monazite

7.2.1. In two-mica granite

Twelve monazites from the two-mica granite (E10) were analysed with the EMP (176 determinations). Representative analytical results are reported in **Table 8**. Monazites show a pronounced magmatic zoning highlighted by the distribution of U, Th and Pb contents (**Figure 36A, B, C**).

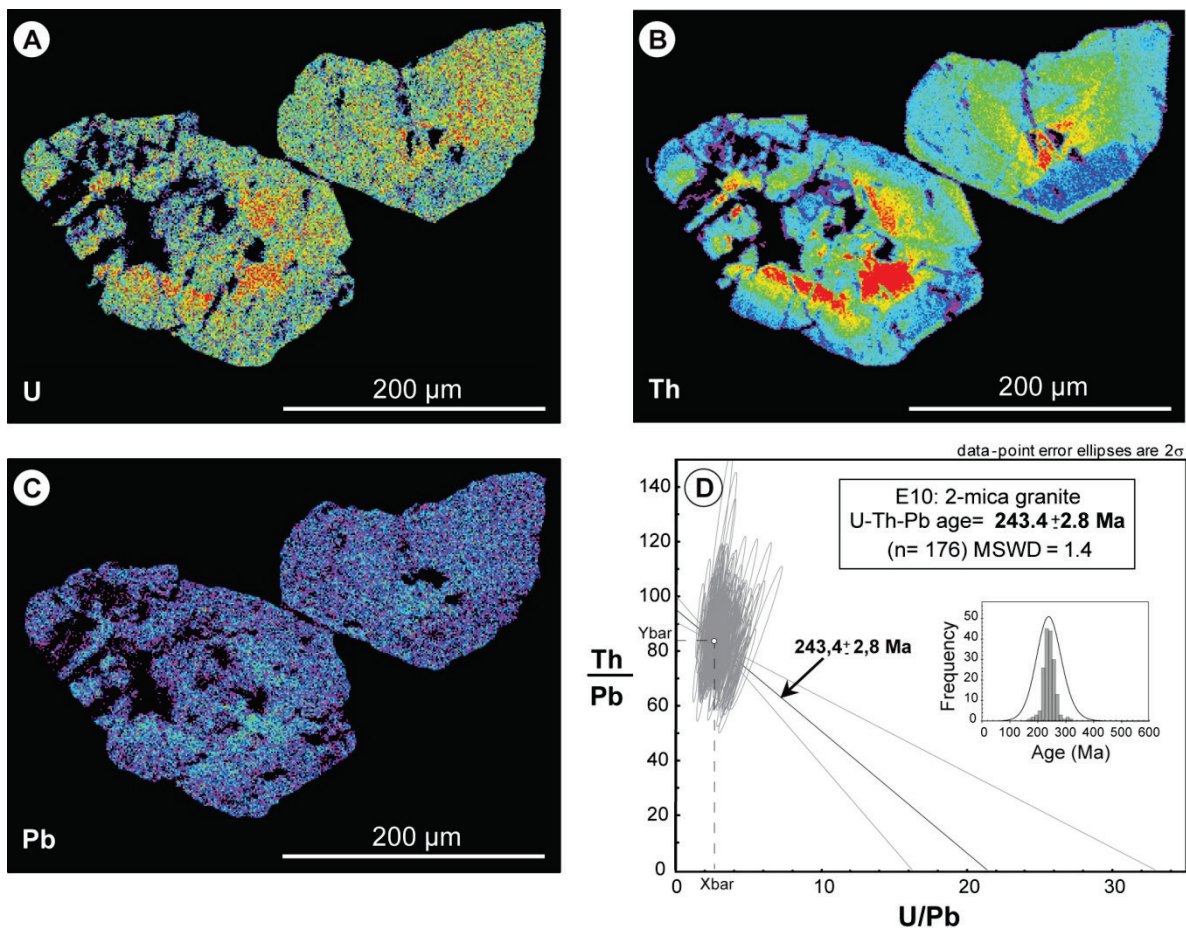


Figure 38. U, Th and Pb element mapping realized by EMP and U-Th-Pb isochron age for monazites from the two-mica granite occurring in the northern part of the Sunite Horst. A= U distribution; B= Th distribution; C= Pb distribution; D= Th/Pb vs U/Pb plot (ellipse errors are 2σ).

Monazite grains yield a chemical U-Th-Pb age at 243.4 ± 2.8 Ma. The age is calculated at the weighted mean point ($X_{\bar{b}ar}$, $Y_{\bar{b}ar}$) of the best-fit line (**Figure 36D**), and error is calculated on the hyperbolas, close to the weighted mean point, where the dimension is the narrowest.

The best regression line (heavy line, **Figure 36**) has a slope indicating the theoretical isochron age. The error envelope (fine lines) corresponds to the two symmetrical hyperbolas. The intercept of the regression line with the U/Pb and Th/Pb axes gives the U-Pb and Th-Pb ages ($324.8 + 61.5 - 111.7$ and $234.4 + 12.7 - 11.5$ Ma, respectively). Note that these ages are calculated on the regression line where the error is the largest. In addition, the distribution of the ages obtained on all analyses give a cumulated frequency histogram with regular Gaussian shape (**Figure 36**).

Table 8. Representative analytical data for monazite from the two-mica granite (E10). Th*= the amount of apparent Th.

REF	Age Ma	Error Ma	U ppm	Error %	Th ppm	Error %	Pb ppm	Error %	Th* ppm	Error %	U/ Pb	Error %	Th/Pb	Error %	Correct. error	Th/U
G1	247	33	3200	4.69	110900	2.00	1338	11.21	121247	2.23	2.392	12.16	82.915	11.39	0.908	34.66
G1	227	32	2900	5.17	113600	2.00	1245	12.05	122963	2.24	2.330	13.12	91.279	12.22	0.907	39.17
G1	240	32	3000	5.00	115700	2.00	1343	11.17	125395	2.23	2.235	12.24	86.181	11.35	0.898	38.57
G1	256	32	3500	4.29	115400	2.00	1446	10.38	126725	2.20	2.421	11.23	79.832	10.57	0.908	32.97
G2	268	49	3000	5.00	68900	2.00	939	15.98	78615	2.37	3.197	16.75	73.414	16.11	0.947	22.97
G2	222	40	2900	5.17	86200	2.00	945	15.88	95559	2.31	3.070	16.70	91.262	16.01	0.943	29.72
G3	243	44	2300	6.52	80100	2.00	950	15.80	87535	2.38	2.422	17.09	84.356	15.92	0.917	34.83
G3	249	41	2700	5.56	86000	2.00	1051	14.28	94731	2.33	2.570	15.32	81.862	14.42	0.923	31.85
G3	247	41	2700	5.56	86500	2.00	1048	14.32	95230	2.33	2.577	15.36	82.574	14.46	0.923	32.04
G3	224	41	2200	6.82	87500	2.00	944	15.90	94601	2.36	2.332	17.30	92.737	16.02	0.912	39.77
G4	225	45	2500	6.00	76000	2.00	844	17.78	84071	2.38	2.964	18.77	90.097	17.89	0.942	30.40
G5	225	44	2200	6.82	79000	2.00	863	17.39	86102	2.40	2.550	18.68	91.585	17.50	0.925	35.91
G6	233	34	2000	7.50	112600	2.00	1235	12.15	119060	2.30	1.620	14.28	91.211	12.31	0.840	56.30
G7	248	41	2800	5.36	86300	2.00	1056	14.21	95355	2.32	2.653	15.19	81.757	14.35	0.927	30.82
G8	259	57	3100	4.84	55800	2.00	759	19.77	65832	2.43	4.087	20.36	73.559	19.87	0.966	18.00
G9	259	43	2600	5.77	81800	2.00	1042	14.40	90214	2.35	2.496	15.51	78.539	14.54	0.919	31.46
G10	218	60	3300	4.55	50500	2.00	594	25.24	61148	2.44	5.552	25.64	84.962	25.32	0.981	15.30
G10	248	45	3400	4.41	73700	2.00	936	16.03	84694	2.31	3.634	16.63	78.781	16.16	0.957	21.68
G11	232	52	2900	5.17	63000	2.00	748	20.07	72366	2.41	3.879	20.72	84.276	20.17	0.964	21.72
G11	230	51	2900	5.17	63900	2.00	750	20.01	73265	2.41	3.869	20.67	85.251	20.11	0.963	22.03
G11	221	50	2700	5.56	66700	2.00	744	20.17	75414	2.41	3.631	20.92	89.707	20.27	0.959	24.70
G11	244	49	3300	4.55	66800	2.00	843	17.80	77468	2.35	3.917	18.37	79.285	17.92	0.963	20.24
G11	246	49	3000	5.00	67700	2.00	849	17.68	77400	2.38	3.535	18.37	79.783	17.79	0.956	22.57
G11	232	47	3000	5.00	71400	2.00	840	17.87	81090	2.36	3.573	18.55	85.049	17.98	0.957	23.80
G11	236	48	2800	5.36	70800	2.00	840	17.87	79846	2.38	3.335	18.65	84.334	17.98	0.952	25.29
G11	240	40	2700	5.56	88700	2.00	1041	14.42	97426	2.32	2.595	15.45	85.246	14.55	0.924	32.85
G12	255	48	4100	3.66	66500	2.00	906	16.55	79765	2.28	4.523	16.95	73.365	16.67	0.969	16.22
G12	241	46	3900	3.85	71400	2.00	903	16.60	84005	2.28	4.317	17.04	79.034	16.72	0.967	18.31
G12	243	42	3500	4.29	80900	2.00	999	15.01	92214	2.28	3.502	15.61	80.949	15.14	0.953	23.11
G12	232	40	3700	4.05	84700	2.00	997	15.04	96650	2.25	3.710	15.58	84.921	15.17	0.957	22.89
G12	248	39	3700	4.05	87400	2.00	1097	13.67	99364	2.25	3.372	14.26	79.643	13.81	0.949	23.62
G12	219	38	3500	4.29	91200	2.00	998	15.02	102493	2.25	3.506	15.62	91.346	15.16	0.953	26.06

7.2.2. In sandstones of the Erlian Basin

Eight monazite grains from sandstones of the Saihan and Erlian formations belonging to post-rift sediments of the Erlian Basin were analysed with EMP. Most monazite grains found in sandstones have a small size (often < 10 µm). Only the grains with a minimum size of 50 µm, presenting the most homogeneous surface, were selected for dating. The chemical composition of monazites (**Table 9**) shows 25-30 wt.% P₂O₅, 26-31 wt.% Ce₂O₃, 12-16 wt.% La₂O₃, 9-12 wt.% Nd₂O₃, ~3 wt.% Pr₂O₃ and 1-2 wt.% Sm₂O₃. Most monazites have Th content ranging from 8 to 10 wt.% ThO₂ and U content from 0.2 to 0.6 wt.% UO₂ (**Table 9**). A minor amount of monazite grains presents lower Th and U contents with respectively 3-5 wt.% ThO₂ and < 0.1 wt.% UO₂.

U-Th-Pb chemical ages for the height monazite grains from Erlian Basin sandstones were calculated. Regarding the small number of analyses for each monazite grains for EMP dating, the average weighted method was preferred. Therefore, the average weighted age was calculated for each grain using individual ages and errors (2σ) of each point of analysis. Plots of average weighted ages and analytical results are respectively presented in **Figure 37** and **Table 10**. Four different ages can be identified and a representative grain for each population is presented in **Figure 37**: (i) two monazite grains give Hercynian age including one age at 322.2±8.8 Ma (Carboniferous, **Figure 37A**); (ii) three monazite grains give Indosinian age with an average weighted age at 238.0±39.0 Ma (lower to middle Triassic, **Figure 37B**); (iii) two grains give a Yanshanian age with an average weighted age at 160.3±7.6 Ma (Jurassic, **Figure 37C**) and (iv) one grain gives a lower Cretaceous age (103.6±6.3 Ma, **Figure 37D**). These four age populations can be correlated with the igneous rocks ages of the basement that were the sources of the sediments deposited in the Erlian Basin.

Table 9. Representative EMP analyses of monazite grains from sandstones of the Saihan and Erlian formations occurring in the Erlian Basin.

Unit	Sandstones of Saihan and Erlian formations							
	Monazite							
Mineral	Cretaceous		Yanshanian		Indosinian		Hercynian	
	Ages	G1-1	G1-2	G1	G2	G1	G2	G1
Analysis n°								G2
Oxides (wt.%)								
P ₂ O ₅	27.76	28.37	28.39	30.38	25.33	26.92	28.36	28.15
SiO ₂	2.06	1.89	1.02	0.86	3.01	1.46	1.83	1.88
CaO	0.47	0.50	1.66	1.58	0.73	0.72	0.50	0.53
Y ₂ O ₃	2.05	2.10	1.94	2.09	0.32	0.35	2.72	2.70
La ₂ O ₃	15.05	14.92	12.98	12.81	14.87	15.53	12.05	12.14
Ce ₂ O ₃	29.53	29.54	26.81	26.40	29.95	31.06	26.58	26.47
Pr ₂ O ₃	3.26	3.06	3.04	3.19	3.30	3.53	3.37	3.37
Nd ₂ O ₃	9.28	9.32	10.29	10.47	10.90	11.26	11.63	11.57
Sm ₂ O ₃	1.38	1.31	1.79	1.78	1.44	1.50	1.76	1.98
Gd ₂ O ₃	0.85	0.8	1.35	1.24	0.71	0.73	0.16	1.70
PbO	0.10	0.11	0.10	0.10	0.05	0.03	0.50	0.16
ThO ₂	8.58	8.28	9.25	9.44	3.26	3.52	8.73	9.08
UO ₂	0.26	0.24	0.55	0.50	0.06	0.08	0.36	0.38
Total	100.64	100.43	99.17	100.85	93.93	96.69	100.03	100.13
Oxygens	4	4	4	4	4	4	4	4
Cations								
P ⁵⁺	0.930	0.940	0.960	0.990	0.900	0.940	0.940	0.940
Si ⁴⁺	0.080	0.070	0.040	0.030	0.130	0.060	0.070	0.070
ΣT-site	1.010	1.010	1.000	1.020	1.030	1.000	1.020	1.010
Ca ²⁺	0.020	0.020	0.070	0.060	0.030	0.030	0.020	0.020
Y ³⁺	0.040	0.040	0.040	0.040	0.050	0.050	0.050	0.050
La ³⁺	0.220	0.220	0.190	0.180	0.230	0.240	0.170	0.180
Ce ³⁺	0.430	0.420	0.390	0.370	0.460	0.470	0.380	0.380
Pr ³⁺	0.050	0.040	0.040	0.040	0.050	0.050	0.050	0.050
Nd ³⁺	0.130	0.130	0.150	0.140	0.160	0.170	0.160	0.160
Sm ³⁺	0.020	0.020	0.020	0.020	0.020	0.020	0.030	0.030
Gd ³⁺	0.010	0.010	0.020	0.020	0.010	0.010	0.020	0.020
Pb ²⁺	0.001	0.001	0.001	0.001	0.001	0.000	0.002	0.002
Th ⁴⁺	0.080	0.070	0.080	0.080	0.030	0.030	0.080	0.080
U ⁴⁺	0.000	0.000	0.000	0.000	0.000	0.000	0.000	0.000
Σa-site	1.000	0.980	1.010	0.970	1.000	1.030	0.980	0.980
% Huttonite	0.0812	0.0740	0.0406	0.0330	0.1259	0.0600	0.0719	0.0740
% Brabantite	0.0464	0.0485	0.1533	0.1403	0.0677	0.0655	0.0518	0.0548
% Monazite	0.8951	0.8847	0.8541	0.8210	0.9391	0.9596	0.8751	0.8747

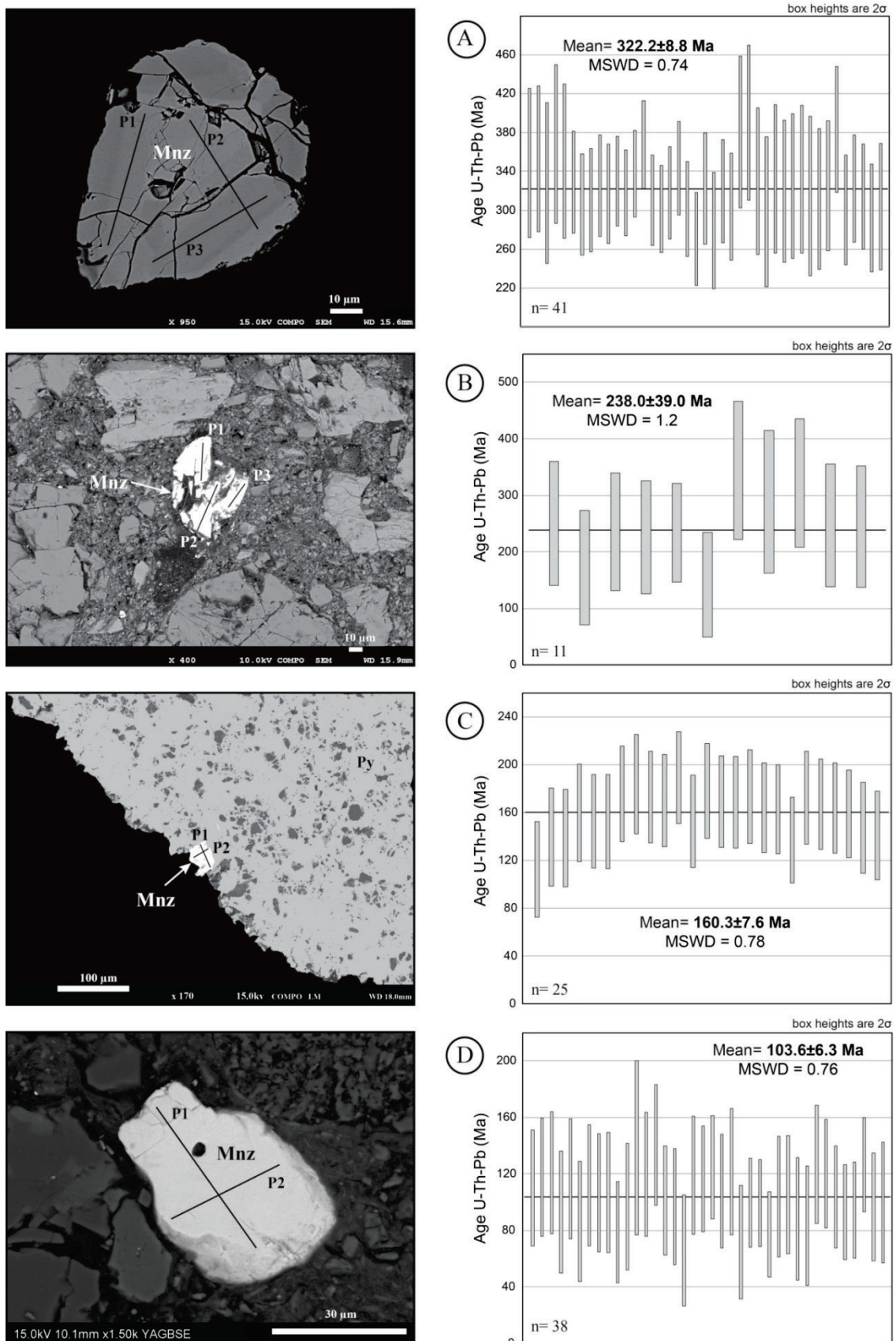


Figure 37. Plots of average weighted ages using individual ages and errors (2σ) for each representative grain of monazite. A= Hercynian monazite; B= Indosinian monazite; C= Yanshanian monazite; D= Cretaceous monazite. Black lines on photographs correspond to EMP profiles of analysis realized on monazite grains.

Table 10. Analytical data for monazite grains from sandstones of the Erlian Basin. Th*= the amount of apparent Th.

REF	Age Ma	Error Ma	U ppm	Error %	Th ppm	Error %	Pb ppm	Error %	Th* ppm	Error %	U/Pb	Error %	Th/Pb	Error %	Correct. error	Th/U
Cretaceous																
G1	110	41	1400	10.71	83200	2.00	430	34.84	87682	2.45	3.252	36.45	193.267	34.90	0.954	59.42
G1	93	43	1000	15.00	79400	2.00	342	43.92	82597	2.50	2.928	46.41	232.486	43.97	0.945	79.40
G1	107	43	1500	10.00	79600	2.00	401	37.37	84400	2.46	3.737	38.68	198.303	37.42	0.965	53.06
G1	101	39	3200	4.69	82700	2.00	418	35.85	92937	2.30	7.647	36.15	197.631	35.90	0.990	25.84
G1	117	37	3700	4.05	85000	2.00	502	29.86	96849	2.25	7.365	30.13	169.185	29.92	0.989	22.97
G1	100	31	7700	2.00	90100	2.00	508	29.50	114729	2.00	15.145	29.57	177.213	29.57	0.995	11.70
G1	106	42	2100	7.14	78900	2.00	401	37.37	85620	2.40	5.232	38.05	196.559	37.42	0.981	37.57
G1	94	34	6800	2.21	83600	2.00	442	33.97	105342	2.04	15.401	34.04	189.343	34.03	0.996	12.29
Yanshanian																
G1	140	41	3000	5.00	79300	2.00	553	27.15	88924	2.32	5.429	27.60	143.514	27.22	0.981	26.43
G1	170	38	4400	3.41	83000	2.00	736	20.39	97146	2.21	8.982	20.68	112.847	20.49	0.982	18.86
G1	153	39	4100	3.66	82400	2.00	651	23.06	95565	2.23	6.302	23.35	126.661	23.14	0.984	20.09
G1	164	38	4100	3.66	85500	2.00	719	20.85	98676	2.22	5.699	21.17	118.839	20.94	0.980	20.85
G1	159	37	4100	3.66	88700	2.00	720	20.82	101871	2.21	5.691	21.14	123.115	20.92	0.980	21.63
G2	187	57	1900	7.89	57900	2.00	534	28.10	64016	2.56	3.559	29.19	108.467	28.17	0.960	30.47
G2	184	87	1100	13.64	37900	2.00	340	44.14	41440	2.99	3.237	46.20	111.530	44.19	0.954	34.45
G2	172	52	1800	8.33	65200	2.00	544	27.58	70988	2.52	3.310	28.81	119.890	27.65	0.955	36.22
Indosinian																
G1	247	49	3300	4.55	67500	2.00	860	17.45	78170	2.35	3.839	18.03	78.527	17.56	0.961	20.45
G1	231	46	3500	4.29	72000	2.00	856	17.53	83303	2.31	4.091	18.05	84.155	17.65	0.965	20.57
G2	236	104	500	30.00	33400	2.00	369	40.66	35015	3.29	1.355	50.53	90.538	40.71	0.804	66.80
G2	227	100	600	25.00	34500	2.00	368	40.77	36437	3.22	1.631	47.83	93.774	40.82	0.851	57.50
G2	234	87	800	18.75	39300	2.00	438	34.26	41884	3.03	1.827	39.06	89.764	34.32	0.876	49.12
G3	236	39	2200	6.82	93300	2.00	1057	14.20	100408	2.34	2.082	15.75	88.305	14.34	0.893	42.40
G3	244	44	1300	11.54	84500	2.00	967	15.52	88703	2.45	1.345	19.34	87.420	15.65	0.796	65.00
Hercynian																
G1	340	38	1800	8.33	106000	2.00	1701	8.82	111861	2.33	1.058	12.13	62.327	9.04	0.709	58.88
G1	348	37	2600	5.77	108300	2.00	1817	8.25	116771	2.27	1.431	10.07	59.589	8.49	0.797	41.65
G1	374	36	2500	6.00	112700	2.00	2021	7.42	120862	2.27	1.237	9.54	55.752	7.69	0.751	45.08
G1	352	44	1700	8.82	87900	2.00	1470	10.21	93440	2.40	1.157	13.49	59.812	10.40	0.742	51.70
G2	329	52	3100	4.84	65300	2.00	1108	13.53	75386	2.38	2.797	14.37	58.912	13.68	0.932	21.06
G2	326	52	2900	5.17	66000	2.00	1096	13.68	75433	2.40	2.645	14.63	60.198	13.83	0.926	22.75
G2	318	51	2900	5.17	67700	2.00	1093	13.72	77127	2.39	2.652	14.66	61.918	13.86	0.926	23.34
G2	302	49	3700	4.05	68000	2.00	1077	13.92	80013	2.31	3.434	14.50	63.119	14.07	0.950	18.37

8. Sm-Nd isotopes

Eleven samples of both Hercynian and Indosinian biotite granites, two-mica Indosinian granite, Hercynian and Jurassic volcanic rocks from the basement of the Erlian Basin yield very low $^{143}\text{Nd}/^{144}\text{Nd}_\text{i}$ ratios (from 0.512241 to 0.512523) which indicates that these igneous rocks are more likely derived from an enriched mantle (EM) than a depleted mantle (DM; Rollinson, 1993). $\epsilon\text{Nd}_{\text{t}}$ values broadly range from -2.0 to 5.2 (**Table 11; Figure 38**). Two distinct $\epsilon\text{Nd}_{\text{t}}$ signatures can be characterised (**Figure 38**): (i) $\epsilon\text{Nd}_{\text{t}}$ shows positive values at ~5.2 for Hercynian biotite granites and volcanic rocks analysed which characterises a mantle source (i.e. $\epsilon\text{Nd}_{\text{t}} > 1$; De Paolo, 1988); (ii) $\epsilon\text{Nd}_{\text{t}}$ shows negative values for Indosinian biotite granites (from -2.0 to -0.1; Table 7) and a positive value (2.4) for the two-mica granite. $\epsilon\text{Nd}_{\text{t}}$ negative values would indicate a crustal source (i.e. $\epsilon\text{Nd}_{\text{t}} < 1$; De Paolo, 1988), however $\epsilon\text{Nd}_{\text{t}}$ values for Indosinian granites range from -2.0 to 2.4 and are distributed around 0.

Therefore, these results tend to characterise a mixing between a mantle and a crustal magmatic source. Two populations of model ages from both Hercynian and Indosinian igneous rocks were determined (**Table 11; Figure 38**): (i) Hercynian biotite granites and volcanic rocks yield T_{DM} model ages ranging from 485 to 726 Ma (mean= 612 Ma) and (ii) Indosinian granites yield T_{DM} model ages ranging from 703 to 893 Ma (mean= 812 Ma). Nevertheless, as $^{143}\text{Nd}/^{144}\text{Nd}_i$ ratios highlight an EM source and not a DM source, model ages calculated for the extraction of uranium from the mantle will only indicate maximum ages for its extraction. Therefore, U extraction from the mantle is younger than 726 Ma for Hercynian granites and younger than 893 Ma for Indosinian granites.

Table 11. Whole rock Nd isotopic data for samples from biotite granite (γ), two-mica granite (γ) and volcanic rocks occurring at the northern margins of the Wulanchabu and Manite sub-basins. $^{143}\text{Nd}/^{144}\text{Nd}_i$ initial and $\varepsilon\text{Nd}_{(t)}$ was calculated using the equation Michard et al., 1985).

Samples	Facies	Age	Sm (ppm)	Nd (ppm)	$^{147}\text{Sm}/^{144}\text{Nd}$	$^{143}\text{Nd}/^{144}\text{Nd}$	Error (x10 ⁻⁶)	$^{143}\text{Nd}/^{144}\text{Nd}_i$	$\varepsilon\text{Nd}_{(t)}$	T_{DM}
ZK258	Biotite γ		4.6	29.7	0.094142	0.512383	5	0.512241	-2.0	872
ZK137	Biotite γ		4.1	24.3	0.102934	0.512425	5	0.512270	-1.4	882
ZK152	Biotite γ	233	3.3	25.6	0.077377	0.512448	5	0.512332	-0.2	703
ZK1765	Biotite γ		3.3	20.3	0.099082	0.512486	6	0.512326	-0.1	780
E02	Biotite γ		2.1	12.3	0.103638	0.512421	6	0.512265	-1.5	893
E04	Biotite γ		5.9	27.4	0.129951	0.512676	5	0.512421	3.3	726
E05	Rhyolite	146	4.3	22.8	0.113638	0.512597	6	0.512486	0.8	728
E07	Biotite γ	291	5.5	23.4	0.141605	0.512802	4	0.512523	5.3	593
E08	Biotite γ	304	2.1	14.3	0.090673	0.512697	6	0.512519	5.2	485
E10	2-mica γ	243	3.5	16.7	0.127057	0.512650	6	0.512451	2.4	745
E14	Rhyolite	306	8.2	32.6	0.151106	0.512814	6	0.512518	5.2	645

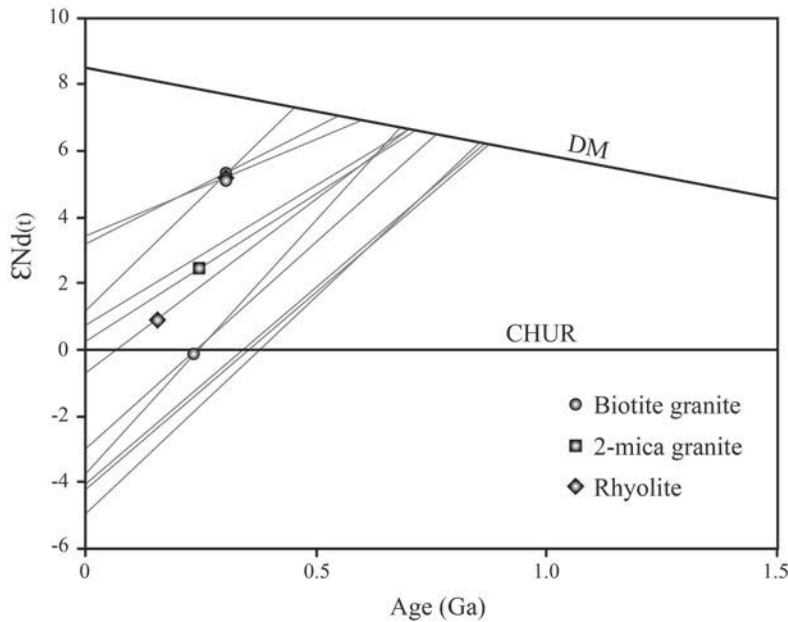


Figure 38. $\varepsilon_{\text{Nd}}(t)$ evolution diagram for igneous rocks occurring at the northern margins of the Wulanchabu and Manite sub-basins. The depleted mantle (DM) model is from De Paolo (1988).

9. Uranium leaching

Hercynian granites have a low Th and U contents respectively ranging from 2.81 to 11.11 ppm and from 0.72 to 2.45 ppm. Their Th/U ratio is ranging from 1.27 to 4.51 (**Figure 39**) which correspond to similar values as the mean crust (i.e. mean crust Th/U=4; Cuney and Kyser, 2008) and indicate that a very minor part of their uranium content has been leached. Indosinian granites show high Th (11.25 to 84.77) and U (1.99 to 21.34) content. Their Th/U is ranging from 2.12 to 19.36. Elevated ratios (> 4 , **Figure 39**) indicate that a significant part of the U content from Indosinian granites has been leached out (Cuney and Friedrich, 1987).

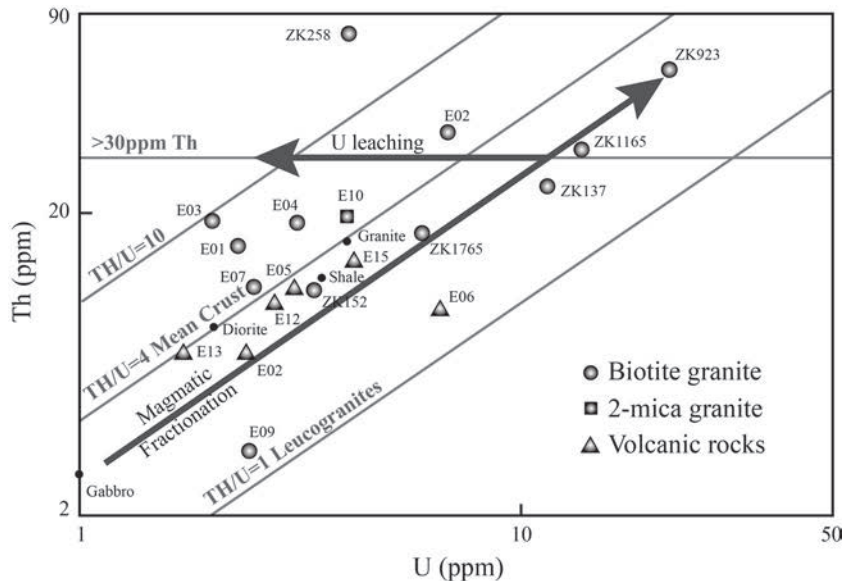


Figure 39. Th vs U diagram showing the magmatic fractionation trend and the trend of U leaching for Hercynian and Indosinian igneous rocks.

As U content of samples collected on outcrops is low due to weathering, observations were focused on U-bearing minerals occurring in non weathered samples from drill hole ZK to highlight the processes involved in U release. EMP analytical profile on a U-thorite section (**Figure 40**) shows a typical evolution of U contents related to metamictisation of the crystal structure. The core of the mineral section is still relatively rich in uranium (> 1 wt.% U; but a fresh uranothorite may have up to 30 wt.% UO₂ when in equilibrium with uraninite; Cuney and Friedrich, 1987) but the external envelope of the section has uranium contents below the detection limit of the EMP. The U-thorite presents a destruction halo associated with pyrite, REE carbonate and uranium oxide. Therefore, U content of the mineral has been released into surrounding fractures and is available for leaching.

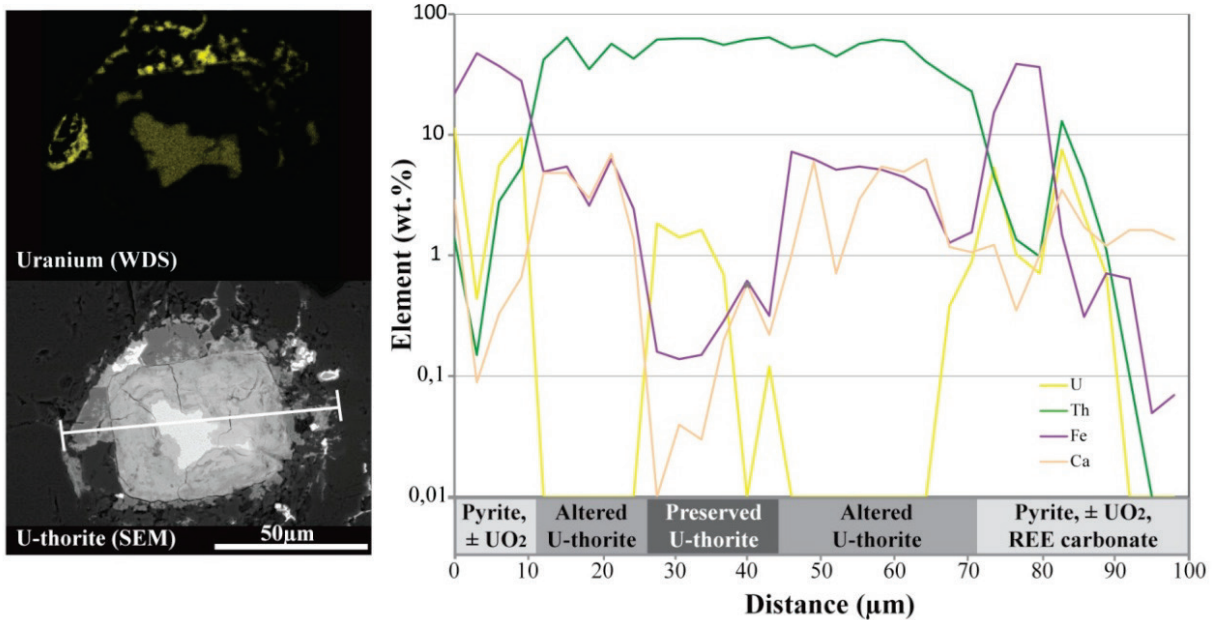


Figure 40. EMP profile of analysis on U-thorite from preserved Indosinian biotite granite showing U release into the rock due to metamictisation.

Evolution of Th and U contents and Th/U ratios from U-rich Indosinian biotite granite observed in drill cores is presented in **figure 41**. In the non-weathered part of the granite (82-180m), U and Th contents are elevated (up to 21.34 ppm U in sample ZK923), Th/U is < 4 and both major U-bearing minerals U-thorite and allanite, are metamict and uranium has been partly to totally released into the rock. In the weathered part of the granite (0-82m), U content decreases down to 3 or 4 ppm U whereas Th content is still very elevated, Th/U strongly increases (up to 19.36 for sample ZK258), allanite and U-thorite are strongly altered, and uranium has been totally leached out from the mineral structure of the U-Th-rich accessory minerals and from the rock (**Figure 41**). Therefore, Indosinian biotite granites may be considered as major source for uranium as they present a high degree of U leaching in their weathered part.

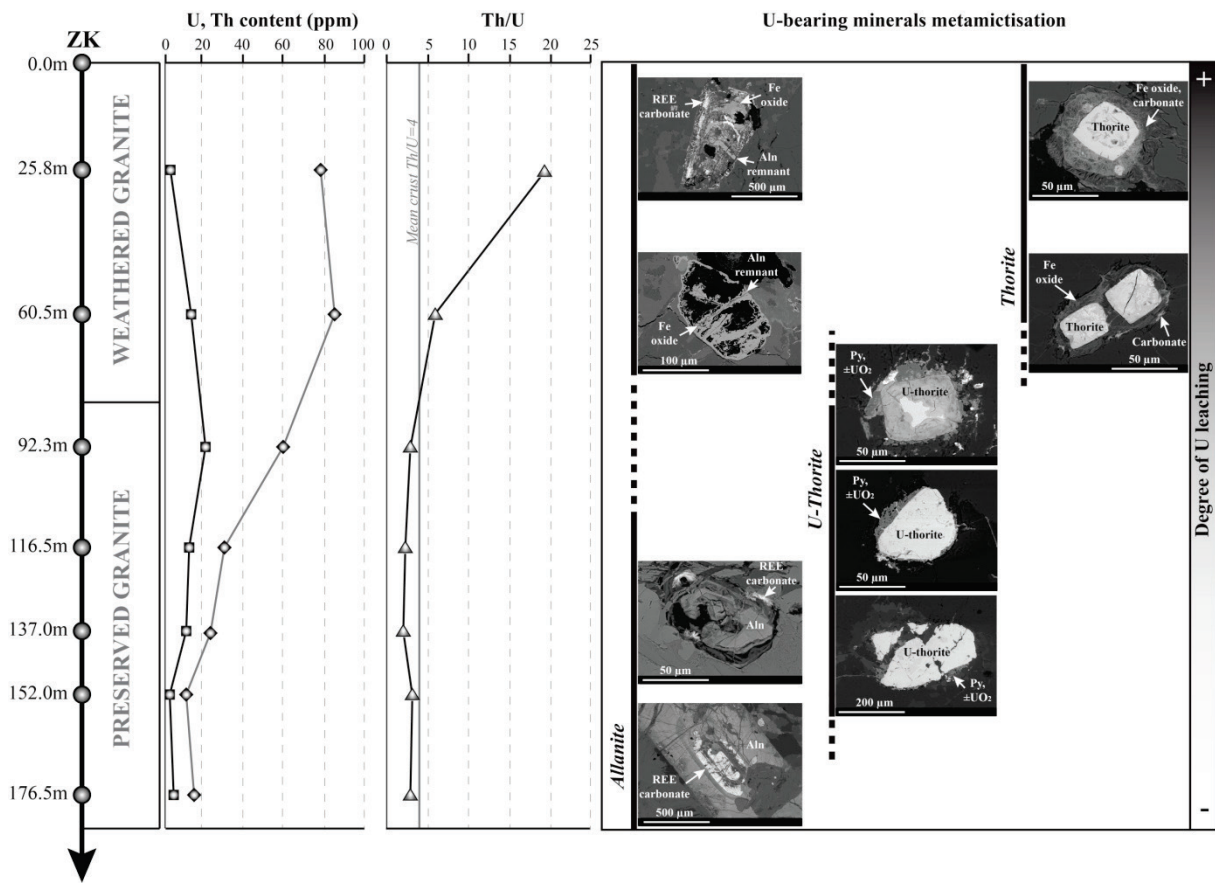


Figure 41. Evolution of U and Th contents, Th/U ratios and the degree of leaching for major U-bearing minerals according to depth of drill hole ZK.

10. Discussion

10.1. Hercynian vs Indosinian granites

Both Hercynian and Indosinian igneous rocks from the basement of the Wulanchabu and Manite sub-basins show a high degree of magmatic fractionation as indicated by their high Si and K contents, elevated incompatible trace element ratios, enrichment in Ba, Th and U, fractionated REE spectra characterised by light REE enrichment, their high quartz and K-feldspar contents and low mafic mineral content. However, significant differences can be stated. Hercynian granites correspond to a low-medium calcalkaline magmatic association whereas Indosinian granites belong to a high-K calcalkaline association. This is also evidenced by their accessory mineral assemblage. Indosinian granites contain U-thorite, allanite, titanite, zircon and apatite reflecting much higher Th and U contents than Hercynian granites which do not contain U-thorite.

Hercynian and indosinian granites are both derived from metaluminous magmas and have a major contribution from the mantle. Slight peraluminous signature may be derived from either highly fractionated magma or enriched mantle source. $^{143}\text{Nd}/^{144}\text{Nd}_i$ ratios evidenced that they were both derived ultimately from an enriched mantle. Moreover, negative $\varepsilon\text{Nd}_{(t)}$ highlights a crustal contamination for the magmatic source of Indosinian granites which is consistent with their higher enrichment in incompatible elements and especially in U. Rb vs Y+Nb and Rb vs Yb+Ta diagrams (Rollinson, 1993) presented in **figure 42** indicates that Hercynian granites belong to volcanic arc granites whereas the Indosinians likely correspond to syn-collisional granites. Additionally, the Th/Yb vs Ta/Yb diagram (**Figure 42**) confirms that Hercynian granites belong to a calcalkaline association and Indosinian's to a high-K calcalkaline association and that they are both derived from an enriched mantle. Hercynian granites have probably played a minor role as a source of uranium for mineralisation hosted in sediments of the Erlian Basin as metamict allanite has been observed, but their low U content and Th/U ratios do not evidence a major remobilization. However, Indosinian granites may correspond to a major source of uranium according to their high U content (up to 21.34 ppm) and their high Th/U ratios (up to 19.36) indicating a major uranium leaching in the weathered part of these granites. Indeed, major U-bearing minerals such as U-thorite and allanite are metamict. In the preserved part of granites, their U content has been released into the rock and uranium is available. In the weathered part, a large part of the uranium that was released has been leached out. Therefore, Indosinian granites may have largely contributed in the uranium mineralisation hosted in the Erlian Basin.

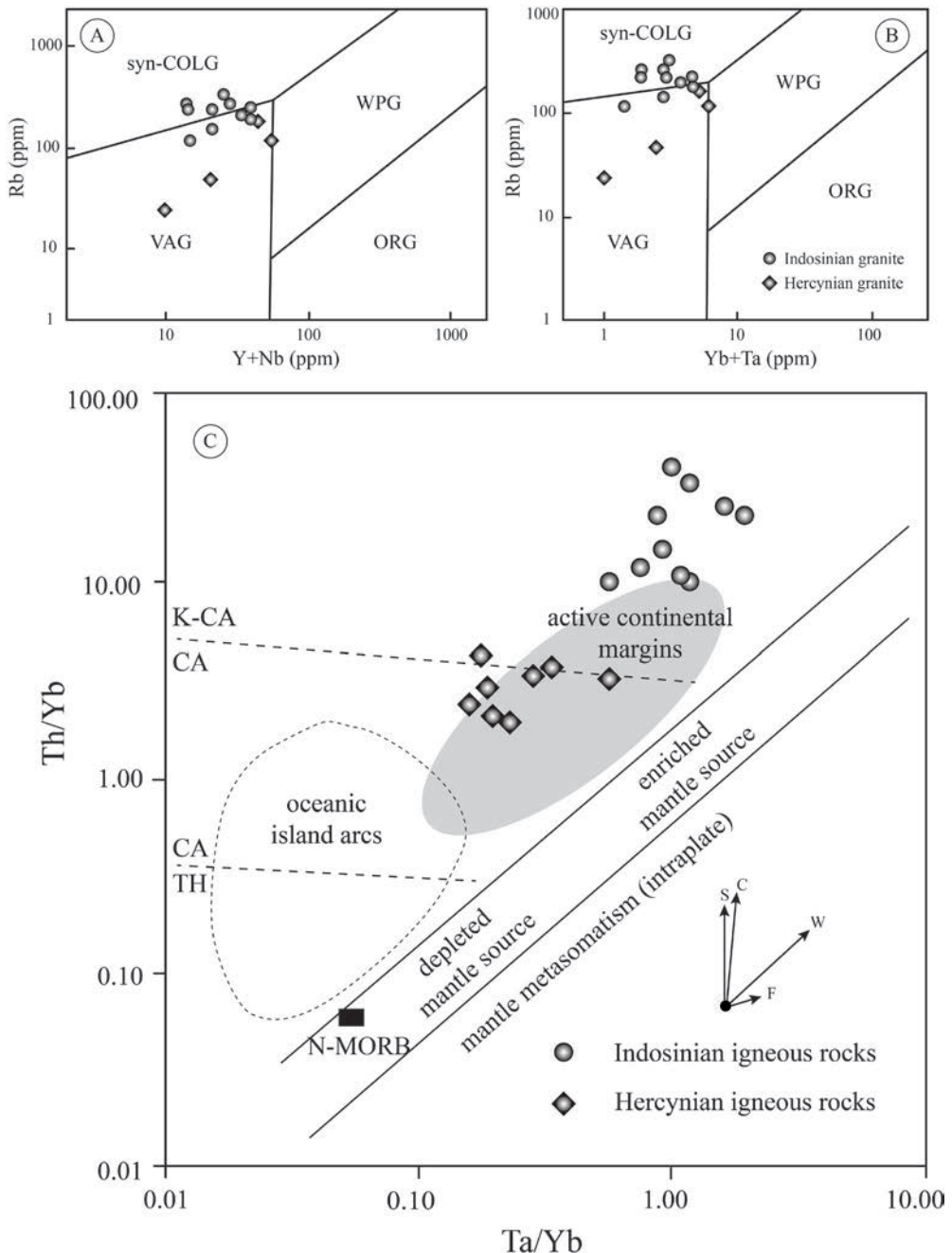


Figure 42. Discrimination diagrams for Hercynian and Indosinian igneous rocks occurring in the basement of the Wulanchabu and Manite sub-basins. A= the Rb-(Yb+Nb) discrimination diagram for Hercynian and Indosinian granites (modified after Pearce et al., 1984) showing the fields of syn-collisional granites (syn-COLG), within-plate granites (WPG), volcanic-arc granites (VAG) and ocean-ridge granites (ORG); B= the Rb-(Yb+Ta) discrimination diagrams for Hercynian and Indosinian granites (modified after Pearce et al., 1984) showing the fields of syn-collisional granites (syn-COLG), within-plate granites (WPG), volcanic-arc granites (VAG) and ocean-ridge granites (ORG); C= the Th/Yb-Ta/Yb discrimination diagram for Hercynian and Indosinian igneous rocks (modified after Pearce, 1982). Vectors indicate the influence of subduction (S), crustal contamination (C), within-plate enrichment (W) and fractional crystallisation (F). Dashed lines separate the boundaries of the tholeiitic (TH), calcalkaline (CA), and high-K calcalkaline (K-CA) field. Active continental margin and oceanic island arc fields modified after Schulz et al. (2004).

10.2. Uranium mass balance calculation

Mass balance calculation was realized on drill-core samples from Indosinian biotite granites and between preserved and weathered parts. EMP analyses on U-thorite (> 100 data-points), allanite (> 200 data-analyses) and zircon (25 data-analyses) were acquired. It shows that zircon are negligible hosts for uranium as it accounts for less than ~1 ppm of the whole-rock uranium content, and it does not show texture of metamictisation and thus correspond to a refractory mineral. U-thorite and allanite correspond to the major uranium bearing minerals. Assuming that all La content of the granite (31.36 ppm) was initially contained in allanite (6.42 wt.% La), the average amount of allanite in the whole rock is 201 ppm. The average Th and U contents in allanite from the non-weathered part of the granite being respectively 2.51 wt.% Th and 0.09 wt.% U, the Th and U amounts contained in allanite in whole rock are respectively 5.0 ppm Th and 0.2 ppm U. Assuming that all Th content of the granite (43.5 ppm) is contained in both minerals allanite and U-thorite, it means that Th content in U-thorite represents 38.5 ppm of the whole rock. The average Th content in U-thorite from the non-weathered part of the granite being 53 wt.% Th, the average amount of U-thorite in the whole rock is 20 ppm. Thus, the U content in U-thorite being 1 wt.% U, the U amount contained in U-thorite in whole rock is 0.2 ppm. The average U content in the preserved part of the granite being 11.2 ppm, this means that the major part (> 95 %) of the non refractory uranium has been released from accessory U-bearing minerals and is available for leaching. If we take as reference the U content in the most preserved U-thorite analysed (11.68 wt.% U), which is still under the possible U content in U-thorite (i.e. up to 28 wt.% U, Cuney and Friedrich, 1987), the U content in U-thorite in whole rock is 2.3 ppm and if we take the stoichiometric U content, it would represent 5.6 ppm of the whole rock. Therefore, eventhough most of the uranium contained in the granite is hosted in accessory minerals, part of it may have been hosted in either in the silica fraction or in uraninite. However, this last U mineral has not been observed. In the weathered part of the granite, the average Th content is 37.2 ppm and the average Th/U ratio is 10.2. Considering a Th/U= 4 in the mean crust (Cuney and Kyser, 2008), the initial U content in this part of the granite should have been at least of 9.3 ppm. The remaining average U content being 3.7 ppm, ~60% of the whole rock U content has been leached out of the granite. Therefore, considering a loss of 5.6 ppm of the whole rock U content, this granite may have liberated ~15000t U/km³.

10.3. U enrichment during geodynamic evolution in northeast China

First of all, $^{143}\text{Nd}/^{144}\text{Nd}_i$ ratios indicate that both Hercynian and Indosinian granites were derived from an enriched mantle. Therefore, $\varepsilon\text{Nd}_{(t)}$ calculated for the depleted mantle yielded model ages correspond to a maximum age for uranium extraction from the mantle (< 893 Ma; **Figure 43**). Consequently, it is now possible to consider this part of the Central Asia Uraniferous Province (CAUP) as a very young metallogenic province compared to other major provinces in the world as Canada, Australia and Africa that are all associated with an Archaean to Palaeoproterozoic basement. Li et al. (2003) proposed a mantle super-plume model to explain the Rodinia breakup which was expressed by a major syn-rift magmatism in south China. Two major phases of widespread magmatism is proposed at 830-795 Ma and at 780-745 Ma (Li et al., 2003). Therefore, during the Neoproterozoic a large amount of crust was created. This giant magmatic event corresponds to the first uranium extraction from the mantle in this area. The CAOB was formed during the Palaeozoic by successive subductions and continental block accretions to the NCB and the Siberian craton. During the late Carboniferous-Permian, the Baolidao magmatic arc was formed in response to a north-trending oceanic subduction (Lin et al., 2008). This timing correspond to U-Pb ages determined on Hercynian granites and volcanic rocks presented in this paper. Therefore, Hercynian igneous rocks occurring in the basement of the Wulanchabu and Manite sub-basins were likely emplaced within this subduction setting as they are characterised by a calc-alkaline series (**Figure 42** and **Figure 43**). During the subduction, the oceanic slab material is recycled in the mantle by dehydration and/or partial melting. Sediments may also be introduced in the mantle explaining the enrichment in incompatible elements such as uranium. During the early-middle Triassic, a continental subduction occurred at the south-eastern margin of the CAOB (Lin et al., 2008) in response to the Indosinian orogeny occurring in Southeast Asia (Lepvrier and Maluski, 2008). Micro-continental blocks are accreted to Siberia and the NCB. In response to the northward tectonic stress from the Indosinian orogeny, some continental blocks may enter in subduction as it was the case under the Xilinhot block (Lin et al., 2008; **Figure 43**). During the continental subduction, part of the continental crust was introduced directly in the mantle and recycled by dehydration and/or partial melting. Therefore, the mantle was highly contaminated and enriched in elements such K, Th and U which may explain the high-K calc-alkaline series and the high degree of U enrichment in Indosinian granites emplaced in northeast China. Then, Yanshanian granites set up during the Jurassic related to transtensional tectonics preceding the major stage of continental extension that

occurred during the Cretaceous in eastern Asia (Charles et al., 2013). The sandstones hosting the U mineralisation deposited during the post-rift stage of the Erlian Basin correspond to the Saihan and Erlian Formation (Fan et al., 2008; Bonnetti et al., accepted). These sedimentary units may contain significant syn-sedimentary U concentration (**Figure 43**) not only as background concentrations within the reduced sandstone but also as syn-sedimentary uranium accumulations reworked during the diagenesis, forming deposits such as the Nuheting and other deposits hosted in the Erlian Formation (Dahlkamp, 2009). As this formation is largely derived from the erosion of Hercynian and Indosinian granites and other igneous rocks as indicated by U-Th-Pb ages on detrital monazites, the uranium of the Erlian Formation also should derive from these granites. Finally, these synsedimentary uranium pre-concentrations are reworked during the Cenozoic (44±5 Ma; Nie, 2008) to form epigenetic roll front deposits.

To summarize, from the uranium extraction from the mantle likely occurring during a syn-rift Neoproterozoic event to the genesis of economic U deposits in the Erlian Basin, the emplacement of a U-rich magmatic rocks in the basement and pre-concentrations of uranium in sedimentary units were needed. During the geodynamic evolution of northeast China, Indosinian granites correspond to U-rich igneous rocks and have evidenced a major role as primary source for the mineralisation hosted in the Erlian Basin.

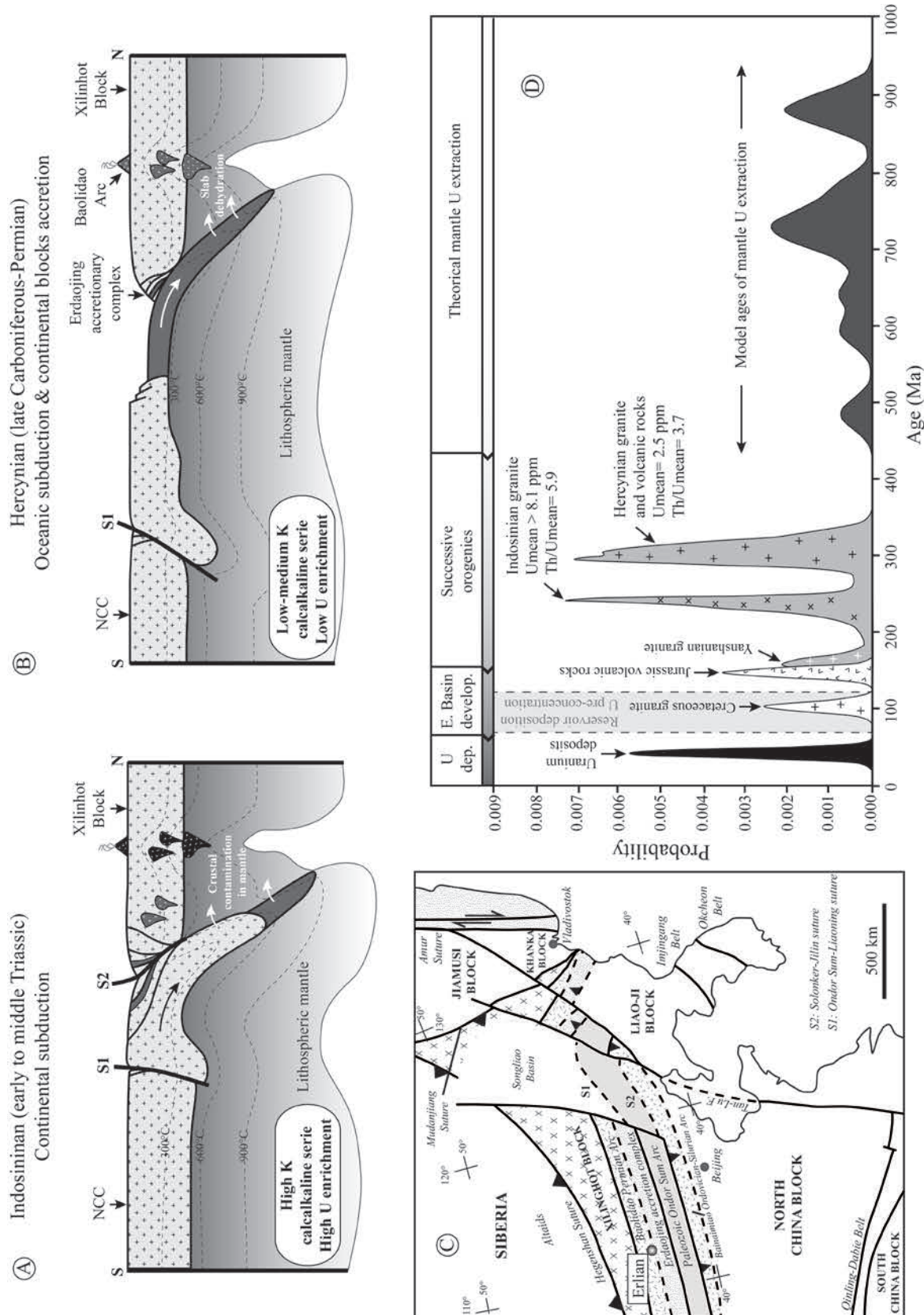


Figure 43. Geodynamic evolution model for the eastern part of the CAOB, placing emphasis on the two successive micro-continents accretion during the late Carboniferous-Permian and the early-middle Triassic, and integrating U enrichment through time until the formation of the deposits hosted in the Erlian Basin. A= model cross section of the oceanic subduction and the block accretion during the late Carboniferous-Permian (modified

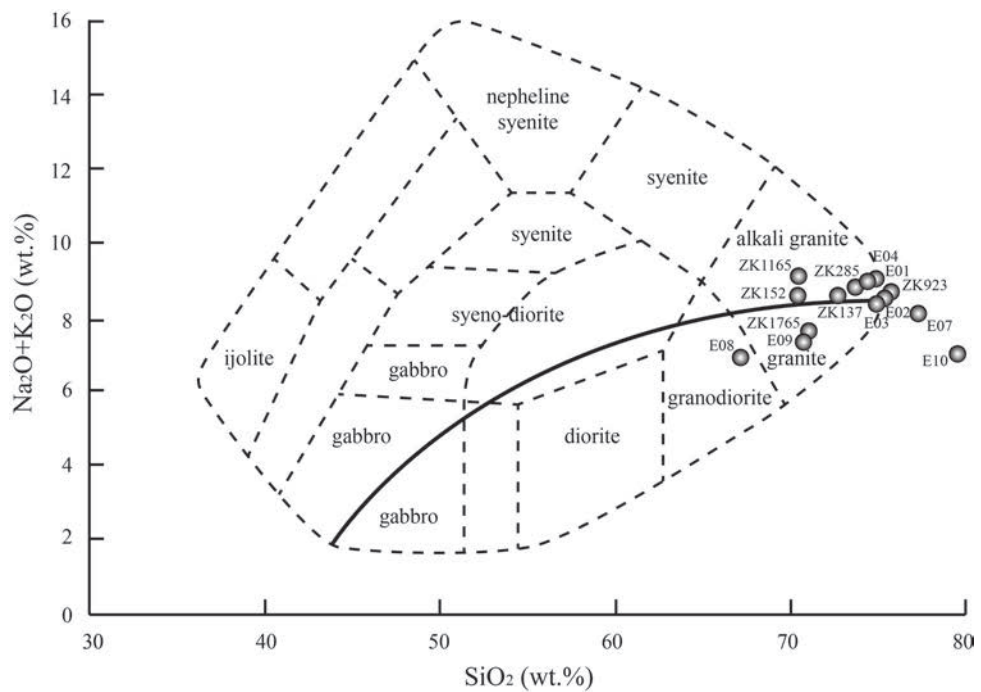
after Lin et al., 2008); B= model cross section of the continental subduction and the block accretion during the early-middle Triassic (modified after Lin et al., 2008); C= Tectonic map of northeast China (modified after Lin et al., 2008); D= Evolution diagram of geological event related to U enrichment through time in northeast China.

11. Conclusions

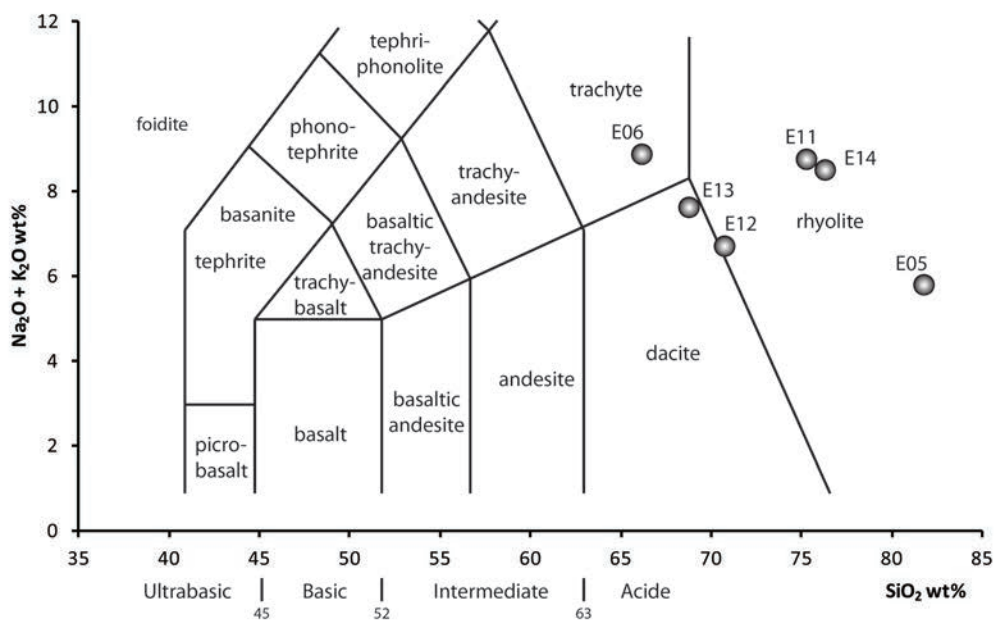
Hercynian and Indosinian granites are largely occurring in the CAOB and are widespread in the basement of the Erlian Basin. Both generations of granite are derived from an enriched mantle and characterised by calcalkaline magmatic series: (i) Hercynian granites correspond to a low-medium-K calcalkaline association derived from a moderately enriched mantle and emplaced during the late Carboniferous-Permian oceanic subduction; (ii) Indosinian granites correspond to a high-K calcalkaline association derived from an enriched mantle that have likely been contaminated by crustal material during the early-middle Triassic continental subduction that occurred in northeast Asia. The contamination of the mantle by sediments or continental crust material explains the high incompatible element enrichment (especially U) of the initial magmas, which have been further enriched by a high degree of crystal fractionation, for Indosinian granites. This high enrichment in incompatible elements was expressed by the crystallization of U-Th-REE-rich accessory minerals such as U-thorite and allanite. These U-bearing minerals were metamict at the time of the sedimentation of the Saihan and Erlian formations and their U content has been released into the rock. In the weathered parts of the granites, this uranium has almost been totally leached. Masse balance calculation indicated that U-rich Indosinian granites could liberate ~15000t U/km³. Therefore, Indosinian granites correspond to a major source of uranium for the sedimentary-hosted mineralisation occurring in the Erlian Basin.

Acknowledgements

Financial support for this study was provided by AREVA Mines, the East China Institute of Technology in Fuzhou, Jiangxi and the Geological Team N°208, BOG, CNNC in Baotou, Inner Mongolia. The authors acknowledge colleagues from the East China Institute of Technology for the presentations and scientific discussions that have been organized about the geology of the Erlian Basin, as well as colleagues from the Geological Team N°208 for their field support and the access to drill cores. Authors also acknowledge Menhong from the Geological team N°208 for the translation during the field trip, M. Brouand for the acquisition of U-Pb isotopic data and other geologists from AREVA Mines for the discussions on the geodynamic evolution of eastern Asia.



Appendix 1. Classification diagram for granites from the basement of the Erlian Basin (modified after Cox et al, 1979).



Appendix 2. Classification diagram for volcanic rocks from the basement of the Erlian Basin

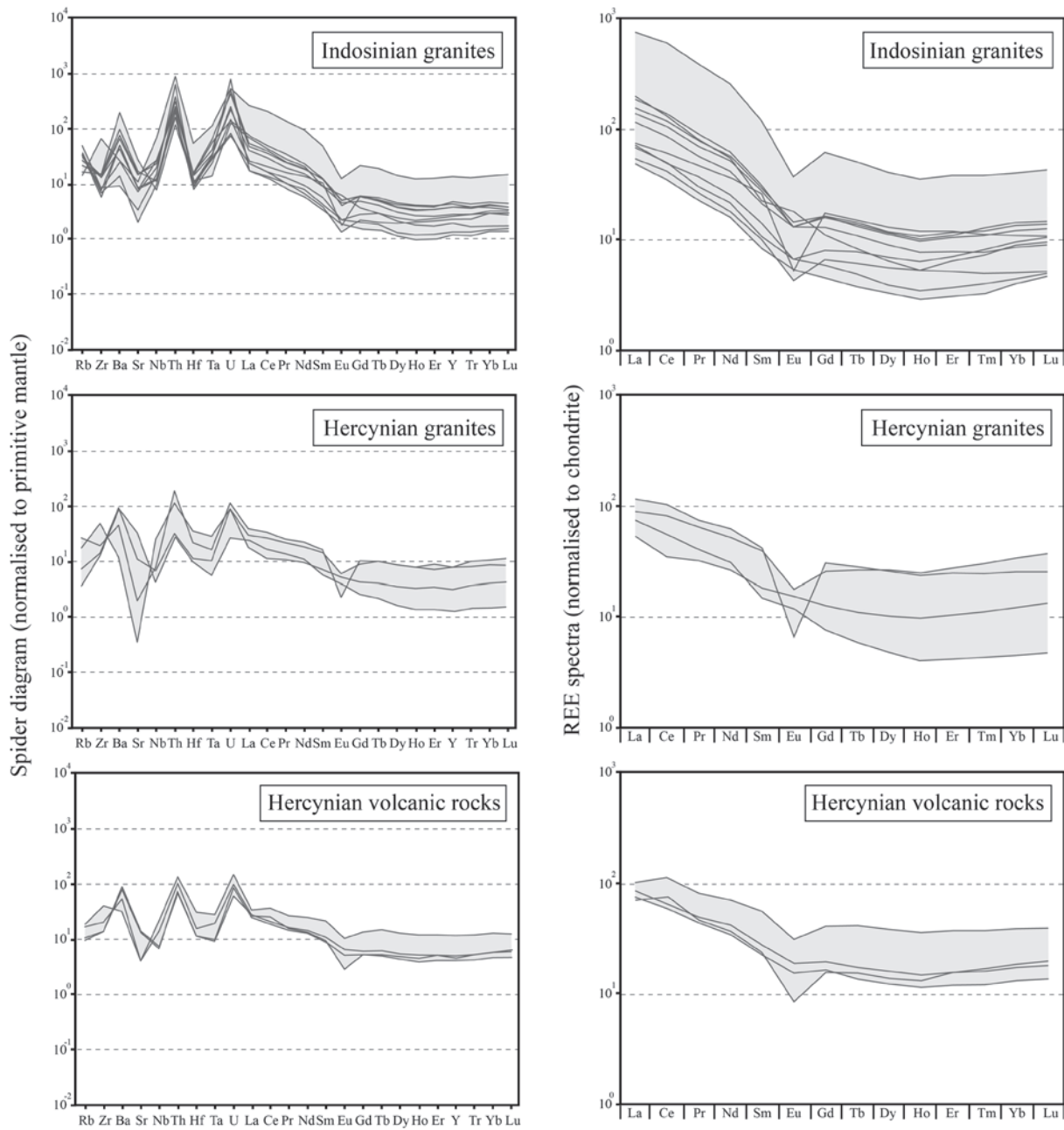
Appendix 3. Major and trace elements whole-rock geochemical data for granites and volcanic rocks from the basement of the Erlan Basin.

Sample n°	Trace elements (in ppm)										Major elements (in wt.%)										
	Ba	Hf	Rb	Nb	Sr	Ta	Th	U	Th/U	Y	Zr	SiO ₂	Al ₂ O ₃	Fe ₂ O ₃	MnO	MgO	CaO	Na ₂ O	K ₂ O	TiO ₂	P ₂ O ₅
ZK-25.8m	333.80	4.35	235.30	16.58	195.40	2.52	77.70	4.01	19.37	20.92	151.20	73.87	13.89	1.42	0.04	0.27	0.88	3.85	4.93	0.19	0.05
ZK-60.5m	439.50	18.77	41.96	253.40	4.88	84.77	14.33	5.91	66.32	223.30	65.00	14.15	6.04	0.18	2.48	1.60	4.05	2.55	1.25	0.39	
ZK-92.3m	68.92	3.58	224.80	9.28	78.81	1.48	60.19	21.34	2.82	11.17	94.54	75.95	12.87	0.67	0.02	0.08	0.77	3.60	5.06	0.08	0.00
ZK-116.5m	578.20	5.42	202.60	14.43	346.50	1.77	30.37	13.52	2.24	19.03	161.30	70.66	14.78	1.73	0.08	0.50	1.85	4.34	4.74	0.25	0.09
ZK-137.0m	497.40	5.44	184.80	16.42	336.50	2.77	24.35	11.48	2.12	21.63	155.70	72.45	14.46	1.58	0.06	0.46	1.49	4.33	4.24	0.23	0.08
ZK-152.0m	1505.00	4.22	113.60	4.81	633.70	0.59	11.25	3.41	3.29	9.44	174.60	70.23	14.75	1.88	0.03	0.63	2.09	3.89	4.54	0.33	0.11
ZK-176.5m	729.40	4.75	148.30	6.94	390.90	1.47	15.89	5.98	2.65	13.51	162.30	70.92	15.27	1.87	0.03	0.55	2.40	4.33	3.43	0.28	0.10
E01	376.40	2.75	266.90	7.62	174.60	1.26	15.35	2.30	6.67	5.73	62.85	73.57	13.93	0.76	0.02	0.20	0.64	3.90	5.08	0.12	0.06
E02	195.30	2.95	336.30	12.16	165.40	1.40	36.30	6.72	5.4	12.65	76.14	75.35	13.49	0.93	0.03	0.19	0.80	4.12	4.30	0.14	0.06
E03	368.30	2.84	232.50	7.23	207.40	1.16	19.28	2.00	9.64	6.59	82.29	74.57	13.69	1.10	0.03	0.36	1.19	3.88	4.47	0.18	0.06
E04	348.50	7.75	185.20	4.97	45.45	0.71	18.42	3.08	5.98	39.26	214.40	73.36	13.62	1.59	0.02	0.22	0.70	4.10	4.76	0.20	0.04
E05	177.80	7.40	203.70	27.18	135.50	2.12	11.20	3.05	3.67	26.94	292.90	81.82	9.06	0.88	0.00	0.20	0.19	1.14	4.67	0.27	0.04
E06	827.00	9.82	345.90	31.62	345.90	1.62	9.63	6.48	1.48	31.71	550.40	66.15	14.81	4.91	0.02	0.22	1.52	3.85	5.08	0.82	0.09
E07	91.19	12.50	120.30	15.81	8.20	1.22	11.11	2.46	4.51	38.61	543.90	76.88	10.89	1.87	0.05	0.05	0.05	4.05	4.24	0.21	0.03
E08	704.8	3.41	24.78	2.97	765.50	0.24	2.82	0.72	3.91	6.56	141.00	68.26	16.53	2.44	0.06	0.64	3.02	5.51	1.69	0.29	0.13
E09	725.50	3.97	51.00	4.29	254.50	0.45	3.12	2.45	1.27	15.44	157.20	70.60	14.22	2.40	0.06	0.62	1.66	4.47	2.68	0.30	0.09
E10	103.90	2.82	258.70	6.10	47.11	1.02	19.01	4.00	4.75	21.26	76.36	79.29	10.44	0.75	0.01	0.10	0.28	1.97	5.08	0.10	0.03
E11	420.50	6.35	119.60	8.94	96.75	0.85	10.25	2.75	3.72	25.56	229.70	75.31	12.78	1.38	0.03	0.19	0.39	4.47	4.29	0.25	0.05
E12	625.20	4.08	75.88	4.86	333.50	0.45	6.95	1.70	4.08	25.12	156.80	70.74	14.84	3.44	0.08	0.60	1.32	4.08	2.56	0.41	0.13
E13	708.70	4.27	74.15	4.68	362.50	0.43	6.83	2.39	2.85	20.34	162.90	69.07	14.38	3.44	0.11	1.02	1.88	4.50	3.00	0.41	0.13
E14	256.60	11.24	118.70	13.91	93.67	1.24	13.52	4.20	3.21	59.10	457.10	76.06	12.04	2.02	0.05	0.28	0.15	3.47	4.56	0.30	0.05

Appendix 4. REE whole-rock geochemical data for granites and volcanic rocks from the basement of the Erlian Basin.

Sample n°	REE elements (in ppm)													
	La	Ce	Pr	Nd	Sm	Eu	Gd	Tb	Dy	Ho	Er	Tm	Yb	Lu
ZK-25.8m	49.32	92.48	8.71	29.87	4.77	0.77	3.55	0.54	3.12	0.60	1.86	0.30	2.21	0.35
ZK-60.5m	188.00	389.80	38.00	123.00	18.39	2.17	12.71	1.88	10.42	1.99	6.10	0.96	6.69	1.08
ZK-92.3m	13.41	26.86	2.56	8.62	1.56	0.25	1.34	0.22	1.42	0.30	1.02	0.18	1.49	0.24
ZK-116.5m	38.69	76.33	7.58	27.67	4.62	0.84	3.32	0.49	2.83	0.54	1.67	0.27	2.00	0.31
ZK-137.0m	34.26	68.34	6.79	24.81	4.27	0.76	3.25	0.50	3.00	0.58	1.84	0.32	2.36	0.36
ZK-152.0m	49.34	84.44	7.80	26.80	3.49	1.05	2.24	0.30	1.62	0.29	0.82	0.12	0.82	0.12
ZK-176.5m	28.53	55.61	5.48	19.92	3.46	0.75	2.65	0.40	2.27	0.43	1.24	0.19	1.39	0.22
E01	12.20	22.76	2.22	7.73	1.27	0.30	0.93	0.14	0.82	0.16	0.49	0.08	0.66	0.11
E02	18.45	31.34	3.58	12.21	2.16	0.37	1.64	0.28	1.76	0.35	1.11	0.20	1.59	0.26
E03	16.77	32.25	2.90	10.23	1.64	0.38	1.19	0.18	0.97	0.19	0.58	0.09	0.72	0.12
E04	28.10	65.20	7.02	29.05	6.32	0.38	6.14	1.02	6.45	1.30	3.89	0.60	4.15	0.63
E05	30.76	62.33	6.44	24.02	4.78	0.40	4.31	0.73	4.61	0.92	2.73	0.42	2.89	0.44
E06	56.46	113.60	12.61	45.03	7.97	2.32	6.22	0.94	5.49	1.06	2.95	0.44	2.92	0.47
E07	21.48	51.28	6.14	24.28	5.95	1.01	5.32	0.99	6.60	1.39	4.36	0.74	5.49	0.91
E08	18.14	34.92	3.82	14.50	2.25	0.67	1.53	0.21	1.20	0.22	0.65	0.10	0.72	0.11
E09	12.85	21.93	3.03	12.53	2.77	0.87	2.54	0.41	2.64	0.54	1.65	0.27	1.99	0.32
E10	18.65	39.15	4.51	17.49	4.00	0.30	3.56	0.56	3.32	0.67	1.91	0.28	1.80	0.27
E11	18.24	49.51	4.46	17.22	3.61	0.48	3.17	0.57	3.70	0.78	2.48	0.42	3.03	0.48
E12	20.71	41.38	4.65	19.77	4.25	1.12	3.94	0.63	4.03	0.83	2.48	0.40	2.86	0.45
E13	18.99	39.83	4.20	17.33	3.67	0.89	3.35	0.53	3.31	0.68	2.03	0.32	2.31	0.36
E14	24.65	70.90	7.70	33.30	8.58	1.79	8.29	1.52	9.70	2.00	5.94	0.92	6.37	0.97

Appendix 5. Spider diagrams and REE patterns for granites and volcanic rocks from the basement of the Erlian Basin.



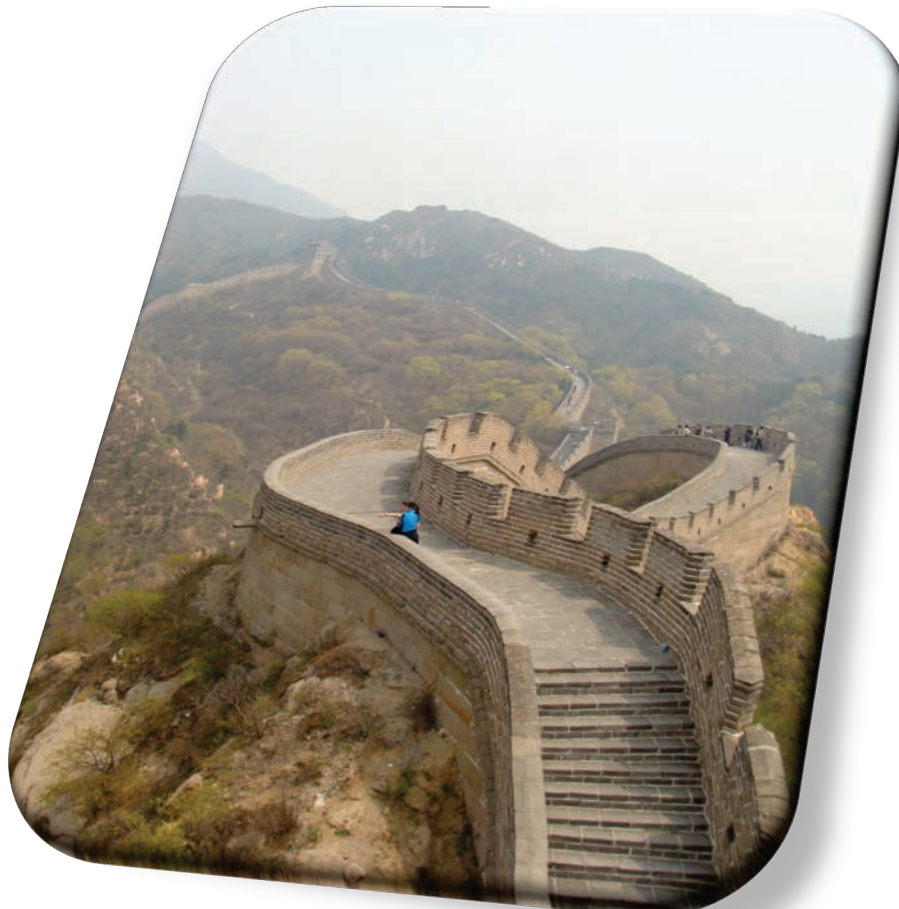
PARTIE C :

GENESE DES MINERALISATIONS URANIFERES

DANS LE BASSIN D'ERLIAN

CHAPITRE 5 :

LES GISEMENTS D'URANIUM DE TYPE GRES



1. Généralités sur les gisements de type grès

Les gisements d'uranium de type grès sont définis comme correspondant à des minéralisations uranifères épigénétiques qui apparaissent en imprégnation ou remplacement dans des formations gréseuses fluviatiles, lacustres et deltaïques (Finch et Davis, 1985). La minéralisation se met généralement en place dans des grés de granulométrie moyenne à grossière qui se sont déposés en environnement continental fluviatile ou littoral. Les intercalaires de shale ou de facies argileux constituent des horizons de roches imperméables qui permet de confiner la minéralisation. Ces « aquitars » constituent généralement les bornes inférieures et supérieures des grès minéralisés.

L'uranium précipite en conditions réductrices qui peuvent être causées par différents agents réducteurs présents au sein des grès tels que la matière carbonée (débris de plantes détritiques, algues marines...), les sulfures (pyrite, H₂S), les hydrocarbures (pétrole, gaz) et des roches volcaniques intercalées contenant de grandes quantités de minéraux ferromagnésiens telle que la chlorite. Les âges de ces minéralisations s'étalent du Paléozoïque au Tertiaire. Les minéralisations d'âge Protérozoïques sont plus rares. Les environnements sédimentaires favorisant la formation de ce type de gisement d'uranium correspondent aux séquences molassiques des systèmes fluvio-lacustres qui se développent entre les zones de subduction et les mers intracratoniques, les bassins intracontinentaux et les systèmes fluviatiles littoraux (Everhart, 1985).

Les gisements de type grès représentent près de 30% des ressources mondiales en uranium. Les gisements de ce type sont communément de basses teneurs (0.05-0.4% U) et constituent des corps minéralisés de petite à moyenne taille pouvant atteindre 50 000t U (OECD/NEA/IAEA, 2008). Les principaux minéraux d'uranium de ces gisements sont la pechblende et la coffinite. D'autre part, l'exploitation de ces gisements par des méthodes in situ de lessivage et récupération les rend particulièrement attractifs d'un point de vue économique.

2. Une classification sommaire

Il existe quatre principaux types de gisements de type grès d'après les classifications de Cuney et Kyser (2008) et de l'OECD/NEA/IAEA (2012); (**Figure 44**).

(i) Le type basal se met en place dans des sédiments peu triés et faiblement consolidés au sein de paléo-vallées incisées dans les roches du socle souvent isolées au toit par des plateaux basaltiques ou par des horizons sédimentaires imperméables à semi-imperméable. L'uranium est principalement associé avec des débris de plantes formant des gisements lenticulaires qui représentent individuellement plusieurs centaines de tonnes à 20 000t U avec des teneurs allant de 0.01% à 3%. Le gisement du Blizzard au Canada est un exemple caractéristique du type basal (Boyle, 1982).

(ii) Le type tabulaire est irrégulier, de morphologie lenticulaire plus ou moins étendues et apparaît parallèle au litage sédimentaire. On le trouve dans les formations gréseuses continentales intercalées de shale, plus particulièrement dans les paléo-vallées en incision des unités sédimentaires sous-jacentes. Les gisements tabulaires peuvent être subdivisés en différentes sous-classes, notamment en fonction du type de matière organique avec laquelle ils sont associés (MO détritique vs MO redistribuée de type bitume). Le district du lac Ambrosia situé dans l'Est du plateau du Colorado, possède des ressources estimées en uranium de 238 000t U (Finch, 1996) principalement localisées dans des gisements de type tabulaire.

(iii) Le type « roll front » représente des gisements de forme convexe qui recoupent le litage sédimentaire des grès encaissants et sont orientés en fonction du gradient hydrologique. Ce type de gisement se distingue par contact prononcé entre la zone oxydée par les eaux oxydantes de surface qui se sont infiltrée dans le réservoir gréseux et la partie réduite de ce réservoir. La minéralisation uranifère apparaît au contact rédox mais peut diffuser de manière plus ou moins étendue en aval du front. Les ressources de ce type de gisement varient de quelques centaines à quelques milliers de tonnes d'U. Les gisements encaissés dans les bassins du Wyoming aux USA sont les meilleurs exemples de ce type de minéralisation uranifère.

(iv) Le type tectonolithologique est discordant à la stratification et se met en place le long des zones de failles perméables, qui recoupent des unités sédimentaires gréseuses. L'uranium précipite dans les zones de faille en association avec de la matière organique détritique ou des hydrocarbures. Les ressources de ce type de gisement varient de quelques centaines de tonnes à 5000t U. Un exemple caractéristique des minéralisations de type tectonolithologiques est le district de Lodève (France).

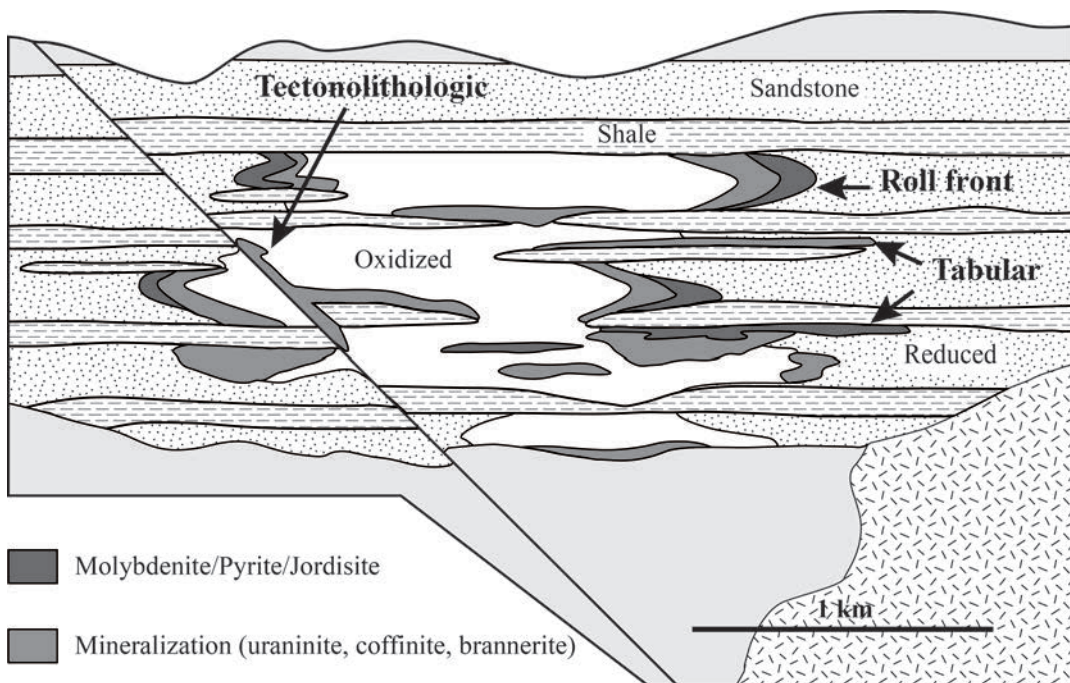


Figure 44. Coupe schématique montrant la distribution des principaux types de gisement d'uranium encaissés dans les grès ainsi que la distribution des grès réduits et oxydés (modifié d'après Cuney et Kyser, 2008).

Un dernier type de gisement peut être évoqué. Celui-ci n'est pas encaissé dans des unités gréseuses mais est souvent associé aux environnements de dépôt sédimentaires dans lesquels se développent les chenaux fluviatiles le plus fréquemment à l'origine des horizons gréseux perméables pièges pour les minéralisations de type grès. Il s'agit des concentration et/ou minéralisations d'uranium synsédimentaires qui se mettent en place dans les environnements marécageux ou de lac peu profond qui se développent au sein de la plaine d'inondation fluviatile. Dans ce cas, l'uranium est le seul métal en quantité significative (Cuney et Kyser, 2008). Les minéralisations apparaissent au sein des faciès réduits riches en matière organique. L'uranium se trouve principalement en adsorption sur les minéraux argileux ou complexé à la matière organique (Mueller et Halbach, 1983). Ce type de minéralisation représente généralement quelques centaines de tonnes d'U (Owen, 1990) mais peut être reconcentrée au cours de la diagenèse (Mueller et Halbach, 1983).

3. Généralités sur les gisements de type roll

Parmi les gisements de type grès, les types tabulaires et roll front sont les plus fréquemment rencontrés. L'accent sera mis sur les gisements de type roll front qui font l'objet de principal de ce travail de thèse et les concentrations synsédimentaires associées.

Les gisements d'uranium de type roll (Granger et Warrens, 1969; Rackley, 1972; Devoto, 1978; Goldhaber et al., 1978; d'Adams et Smith, 1981; Reynolds et al., 1982; Reynolds and Golhaber, 1983; Min et al., 2005a, 2005b; Bo and Kuan, 2006; Cai et al., 2007a; 2007b; Nie et al., 2007; Fan et al., 2008; Zhang et al., 2008; 2010; Munara, 2012) illustrent l'importance des phénomènes d'oxydo-réduction dans les bassins sédimentaires. La formation de ces gisements résulte de la infiltration d'eaux de surface oxydantes au sein d'unités sédimentaires perméables réductrices, à la suite de mouvements tectoniques. L'infiltration des eaux météoriques va progressivement oxyder l'encaissant et mettre en solution un certain nombre d'éléments mobiles en conditions oxydantes. Un front d'oxydo-réduction va se former et se déplacer de manière prograde au sein de la formation hôte (Granger et Warrens, 1969; Harshman, 1972; Rackley, 1972). Les caractéristiques de la roche hôte sont modifiées et montrent la zonation géochimique suivante en fonction de la direction d'écoulement: une zone oxydée, une zone minéralisée et une zone réduite.

Ainsi, les eaux d'infiltration vont progressivement s'enrichir en divers éléments (U, V, Cu, Fe, Se, Re, Mo...) par altération des minéraux disséminés dans la formation hôte et/ou apporté par les eaux de surface qui ont pu les lessiver dans des roches en surface (par exemple uranium de source granitique ou volcanique). De part leur capacité à changer de valence, ces éléments vont être impliqués dans les réactions redox. Les éléments à considérer sont (i) l'oxygène dissous dans les solutions de sub-surface, (ii) le fer sous forme ferreux et ferrique, et (iii) les espèces du soufre (sulfures, sulfates, polysulfures...). La présence de matière organique et de bactéries (sulfato-oxydantes ou réductrices, ferro-oxydantes...) va également modifier l'état redox de la solution porteuse de la minéralisation. Les solutions initialement oxydantes qui percolent, perdent progressivement leur caractère oxydant au contact de la formation réduite, impliquant des réactions chimiques ou biochimiques. A ces processus peuvent être également associés des variations du pH. Ainsi, les solutions de surface sont initialement légèrement acides du fait du CO₂ dissout qu'elles contiennent. Puis, elles deviennent progressivement alcalines par équilibrage avec les feldspaths et/ou carbonates et/ou tuffs volcaniques des sédiments. L'évolution des conditions eH-pH des eaux de recharge lors de leur infiltration conditionne le dépôt des éléments dans l'ordre prévu par les équilibres

physico-chimiques et déductible de l'examen des diagrammes de phase. Ainsi, les zonations minéralogique au niveau du front froment une séquence logique, caractéristique de la précipitation différentielle des éléments de la solution minéralisante, allant des minéraux nécessitant des conditions potentiels rédox de plus en plus bas pour leur précipitation depuis l'amont à l'aval du roll. Ainsi, la zone de transition entre les conditions oxydantes et les conditions réductrices constitue une barrière géochimique par rapport au transfert de l'uranium et de nombreux autres éléments, dont le fonctionnement est en grande partie basé sur des phénomènes rédox (eH) et acido-basique (pH). L'étude de cette zone est primordiale afin d'appréhender les conditions physico-chimiques nécessaires pour la précipitation de l'uranium.

Cependant de nombreux autres paramètres tels que la température, la pression, les pressions partielles en O₂, CO₂ et H₂S, la présence d'ions ou de complexes ioniques organiques ou inorganiques et la présence de bactéries, la disponibilité de l'uranium et des autres métaux sensibles aux rédox dans les eaux s'infiltrant et dans les formations percolées, les variations de perméabilité de ces formations, leur degré de confinement par des aquitard qui peuvent significativement modifier les caractéristiques géochimiques du gisements, sont également à prendre en compte. Par exemple, le contrôle biologique de la minéralisation uranifère peut modifier l'abondance, la distribution et la texture des sulfures de fer (Reynolds et al., 1982). Dans certains gisements, la matière organique, généralement abondante, est supposée avoir contrôlé la distribution de la minéralisation uranifère soit directement à travers des processus de complexation, adsorption et réduction, soit indirectement en fournissant l'énergie nécessaire pour la réduction bactérienne de l'uranium (Rackley, 1972). Dans le gisement de Wuyiyi (Chine), Min et al. (2005a, 2005b) montrent que la dégradation microbienne de la matière organique a permis de maintenir un environnement réducteur, dû à la production de CH₄, H₂S ou H₂SO₃²⁻, favorable à la réduction de l'uranium. L'influence des réactions biochimiques est également mise en évidence par la présence de pyrite framboïdale (Reynolds et al., 1982; Min et al., 2005a, 2005b). Dans d'autres gisements, par exemple dans bassin Tertiaire du Wyoming ou au Sud du Texas (Benavides, Felder, Lamprecht), la présence d'une matière organique très dispersée ne permet pas à elle seule d'expliquer les fortes concentrations d'uranium. D'une manière générale deux hypothèses ont été avancées pour expliquer la formation des gîtes uranifères de type roll front: (i) un modèle chimique et (ii) un modèle biogénique.

- (i) Dans le cas d'un modèle chimique classique (**Figure 45**; Devoto, 1978), une oxydation inorganique de la pyrite par la solution minéralisante permet de fournir des espèces soufrée métastables capables de réduire l'uranium (Granger et Warren, 1969)

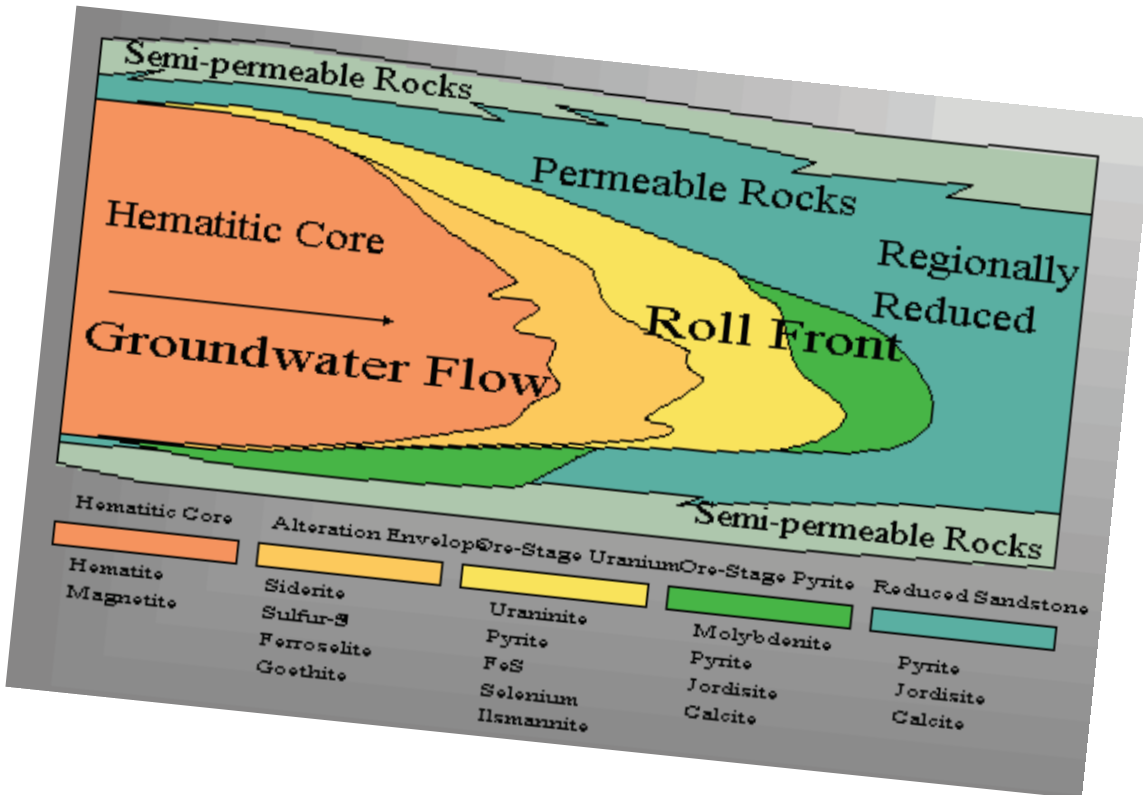


Figure 45. Coupe schématique d'un gisement de type roll montrant les zonations minéralogiques classiques de ce type de minéralisation (Devoto, 1978).

- (ii) Dans le cas d'un modèle biogénique (Jensen, 1958; Lizitsyn et Kuznetsova, 1967; Belyi et al., 1972; Rackley, 1972), les bactéries sulfato-réductrices sont responsables indirectement de la réduction de l'uranium par la production de composés chimiques tel que le H₂S.

- (iii) Un troisième modèle peut cependant être évoqué, celui d'Adams et Smith (1981), qui propose la migration secondaire d'hydrocarbures le long des failles recoupant les réservoirs gréseux comme agent réducteur pour la minéralisation uranifère (**Figure 46**).

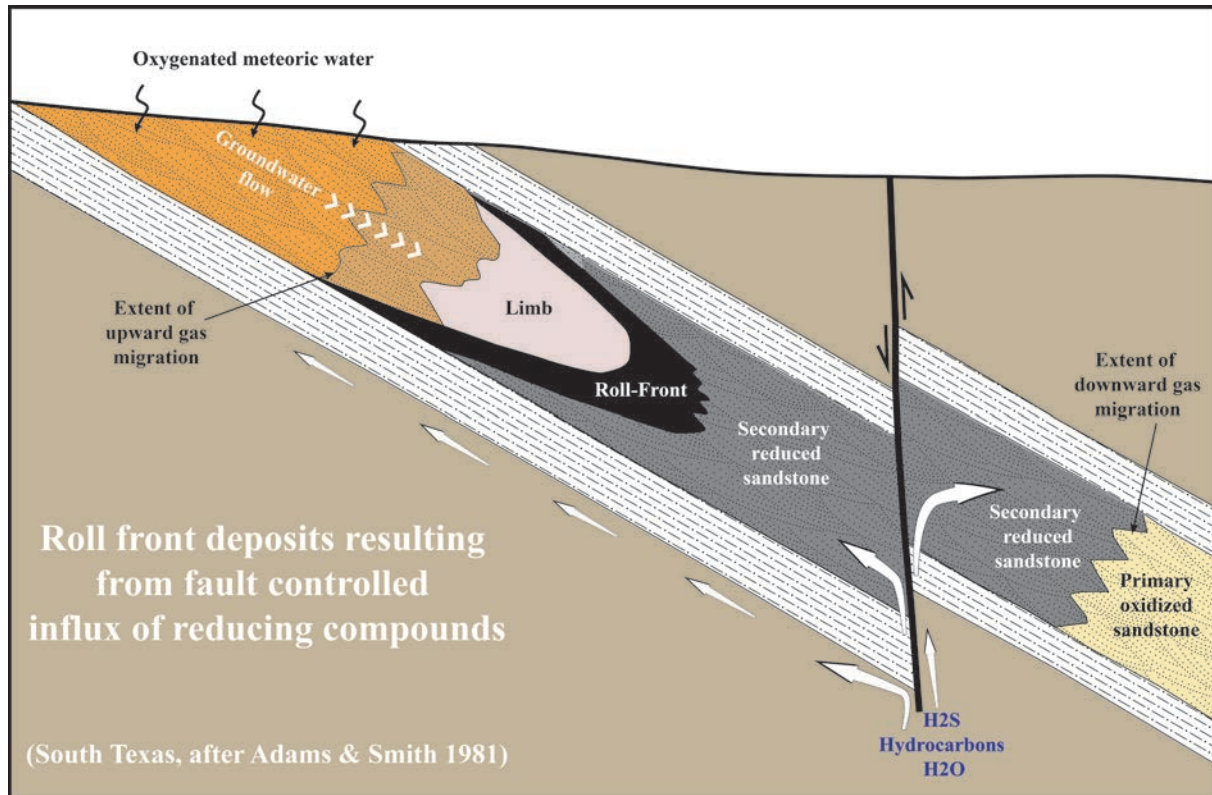


Figure 46. Coupe schématique du modèle de gisement roll front d'Adams et Smith (1981) impliquant la migration secondaire d'hydrocarbures le long des failles recouvrant les réservoirs gréseux qui encaissent la minéralisation.

CHAPITRE 6:

LES MINERALISATIONS SYN-SEDIMENTAIRES VS DIAGENETIQUE DANS LE BASSIN D'ERLIAN



Article 3: The Nuheting Deposit, Erlian Basin, China: Synsedimentary vs Diagenetic Uranium Mineralization.

Christophe Bonnelli^a, Michel Cuney^a, Fabrice Malartre^a, Raymond Michels^a, Xiaodong Liu^b,
Yunbiao Peng^c

^aUniversité de Lorraine, GéoRessources-CNRS-CREGU, BP239, F54506 Vandoeuvre-les-Nancy, France

^bEast China Institute of technology, 56 Xuefu Road , Linchan, 344000 Fuzhou, Jiangxi, China

^cGeological Team No.208, BOG, CNNC, Baotou, Inner Mongolia, China

Paper to be submitted in Ore Geology Reviews

1. Abstract

Sedimentary units deposited during the post-rift stage of the Erlian Basin located in northeast China present an alternation of sandstone and mudstone layers. This sedimentological architecture is at the origin of confined permeable reservoir hosting sandstone-type uranium deposits. The study of the Nuheting deposit offered the opportunity to identify synsedimentary uranium concentration and diagenetic mineralization hosted in mudstone layers that could slightly contribute as uranium source in the genesis of sandstone-hosted uranium deposits. Detailed petrographical and geochemical study of drill-core samples from the Nuheting deposit led to the characterization of different stages related to the formation of uranium ore bodies and allowed to propose a new metallogenetic model. Uranium mineralization of the Nuheting deposit is mainly hosted in dark grey silty mudstone of wetland depositional environment of the late Cretaceous Erlian Formation. Petrographical observations and EMP analysis evidenced a large amount of uranium adsorbed on clay minerals corresponding to synsedimentary concentration. Trace elements on pyrite analyzed by LA-ICPMS and whole-rock geochemical data led to the characterization of a diagenetic uranium mineralization. Mo and Se enrichment and their incorporation in pyrite highlight reducing conditions within the host-rock during the diagenesis of the Erlian Formation. Uranium was desorbed from clay minerals and then, redistributed *in situ* and redeposited on pyrite crystals mainly as coffinite. Finally an epigenetic stage of cementation was identified with sulphate and carbonate minerals which may enclose some uranium mineralization. This epigenetic stage of fluid circulation may be responsible for minor uranium remobilization. Therefore the Nuheting deposit is dominantly diagenetic-related and experienced three main stages of uranium mineralization: (i) a synsedimentary uranium concentration, (ii) a diagenetic *in situ* uranium remobilization and redeposition on pyrite and (iii) an epigenetic cementation. Rock-Eval pyrolysis realized on samples revealed that the organic matter contained in host-rocks of the Nuheting deposit is of type IV, inherited from land plant, and do not contain free hydrocarbons. Therefore our results do not support that hydrocarbons be involved as a reducing agent for uranium mineralization.

Keywords: Erlian Basin; Nuheting uranium deposit; metallogenetic model; diagenetic-related.

2. Introduction

Since the 1980's Mesozoic sedimentary basins of northeast China located at the southeastern edge of the Central-Asia Uraniferous Province (CAUP) became more and more prospective for uranium deposit discoveries. The CAUP represents one of the largest metallogenic provinces in the world with uranium ore deposits located from the Transbaikal region in Russia, in southern Kazakhstan, in Uzbekistan, in Mongolia and in North China (OECD-NEA/IAEA, 2010). In China, excepted granite and volcanic-related uranium deposit types, the main type of uranium deposit discovered in this area is sandstone-hosted with both roll front and tabular-shaped ore bodies (Dahlkamp, 2009; OECD-NEA/AIEA, 2010), which currently represents one of the most interesting uranium resources with respect to using *in situ* recovery (ISR) for their extraction. Among the five major uranium districts of China (Dahlkamp, 2009), the Yinshan-Liaohe district located in northeast China presents the largest number of sandstone-hosted uranium deposits with the roll front-type deposits in the Erlian Basin (e.g., Mangheite and Huhe deposits, Dahlkamp, 2009; Saihangaoobi and Bayinwula roll-front deposits, Nie et al., 2007; Fan et al., 2008), in the Ordos Basin (e.g., Dongsheng area, Cai et al., 2007) and more limited uranium mineralization in the Songliao Basin. In the Erlian basin, several mudstone-hosted uranium deposits (e.g., Nuheting, Subeng and Naomugen deposits; Dahlkamp, 2009; Li and Kuang, 2010) were also identified within the upper member of the Erlian Formation. The present study of the tabular-shaped Nuheting deposit aims to evidence and to characterize a stage of synsedimentary uranium concentration and then to determine how and to which extend this pre-concentration may have been affected by diagenetic and/or epigenetic processes. Indeed, Zhou et al. (2002) suggested a synsedimentary-related ore formation, Li and Kuang (2010) proposed that a syn-sedimentary uranium mineralization stage has been remobilized *in situ* during an epigenetic stage whereas Niu et al. (1995) and Zhang and Ding (1996) discussed about a genetic relationship between oil-gas fields and uranium mineralization more likely considering an epigenetic mineralizing process. The following study of the Nuheting deposit results of a collaborative work between the GeoRessources laboratory of Lorraine University (France), the East China Institute of Technology (ECIT) and the Chinese National Nuclear Corporation (CNNC). In 2011 a field mission was carried out in the Erlian Basin in order to characterize the geological setting of the Nuheting area and to collect drill-core samples of the Nuheting deposit.

3. Geological setting

3.1. The Erlian Basin

The Erlian Basin (or Eren Basin) is located in northeast China (**Figure 47**), Inner Mongolia, close to the border between China and Mongolia. It is an intracontinental basin formed during the Mesozoic continental extension of eastern Asia (Charles, 2010; Ren et al., 2002) and covering an area of approximately 130 000 km² (Dou and Chang, 2003; Wei et al., 2005).

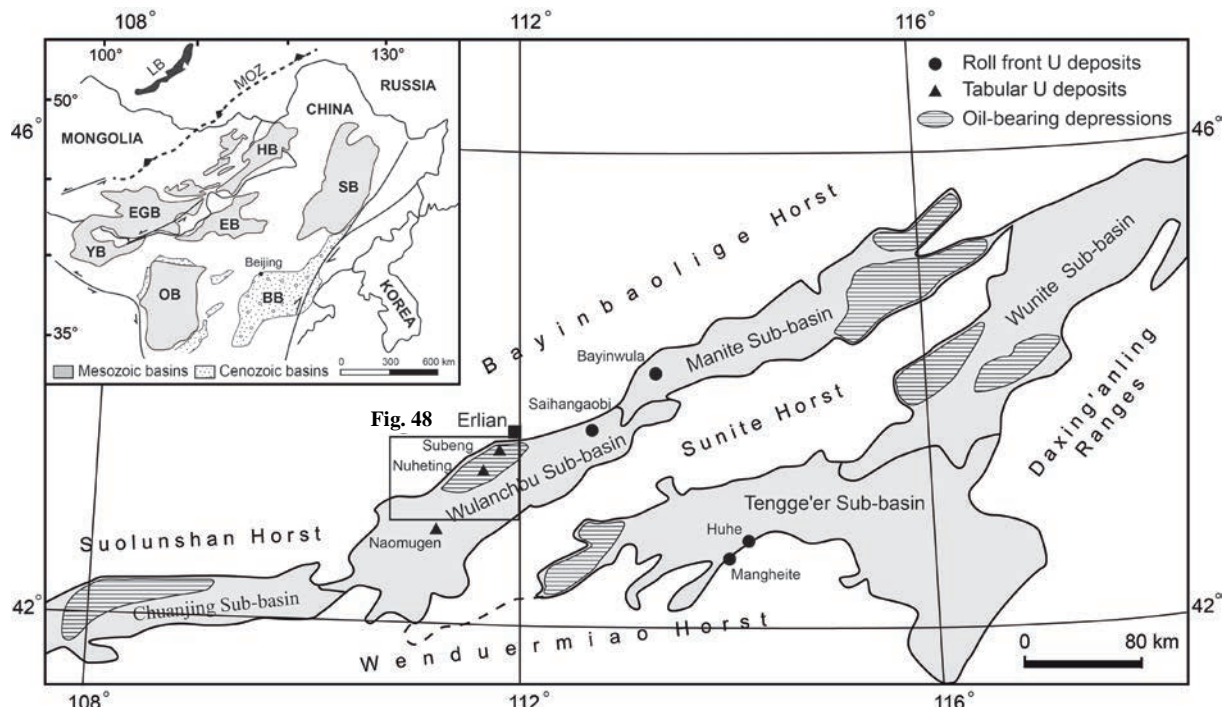


Figure 47. Structural map of the Erlian Basin showing the distribution of different types of uranium deposits and oil-bearing depressions (modified after Bonnelli et al., accepted; CNNC, unpublished data; Dahlkamp, 2009; Dou et al., 1998; Meng, 2003; Wei et al., 2005). U=uranium, BB=Bohai Basin, EB=Erlian Basin, EGB=East Gobi Basin, HB=Hailar Basin, OB=Ordos Basin, SB=Songliao Basin, YB=Yingen Basin, LB=Lake Baikal, MOZ=Mongol-Okhotsk Zone.

It is composed of five major sub-basins as following (**Figure 47**): the Chuanjing Sub-basin to the West, the Wulanchabu Sub-basin in the central-west part, the Manite Sub-basin in the central-north, the Tengge'er Sub-basin in the southeastern part and the Wunite Subbasin to the northeast (Dou and Chang, 2003; Dou et al., 1998; Wei et al., 2005). These sub-basins are framed by a series of horsts or ranges oriented ENE-WSW: the Daxing'anling Ranges to the East, the Bayinbaolige Horst to the North and the Suolunchan Horst more to the West, and finally the Wenduermiao Horst to the South. The Sunite Horst occupies the central part of the

Erlian Basin and divides it in two different main parts (Dou et al., 1998; Wei et al., 2005), north and south (Dou and Chang, 2003).

The Erlian Basin lies on a folded and metamorphised basement corresponding to the southern margin of the Xing'an or Xing Meng Mongolian Orogenic Belt (Dou and Chang, 2003; Lin et al., 2001; Wei et al., 2005). This basement is mainly composed of both Paleozoic and early Mesozoic intermediate to felsic granitic plutons (Dahlkamp, 2009; Davis et al., 2001; Ge et al., 2007; Guo et al., 2004; Miao et al., 1998; Su et al., 2007; Wang et al., 1998; Wu et al., 2000a, 2000b, 2002, 2005a, 2005c, 2007; Yang et al., 2007; Zhou et al., 2010), mafic to felsic volcanic rocks (Ge et al., 2007; Zhou et al., 2010) and Proterozoic to Paleozoic sedimentary or metasedimentary units (Wu et al., 2005b; Zhou et al., 2010). Part of granitic and volcanic rocks mentioned above may have represented primary uranium source for the basin-hosted uranium mineralization as some biotite-granites show an average of 4-13 ppm uranium and a Th/U ratio of 5.6-11.1 (Dahlkamp, 2009). This basin was divided in about 52 half-graben-shaped depressions (Dou and Chang, 2003; Meng et al., 2003) controlled by a normal-fault system and developed during three main tectonic-stratigraphic stages: (i) a pre-rift stage mainly characterized by the emission of late Jurassic to very early Cretaceous volcanic rocks of the Qinganling Group (156.0 – 142.6 Ma; Chen and Cheng, 1997; Graham et al., 2001; Wang et al., 2006), which corresponds to the initiation of the rifting; (ii) a syn-rift stage characterized by the deposition of early Cretaceous sedimentary units (Cai et al., 1990; Dou et al., 1998; Gou et al., 1986; Ren et al., 1998; Sha, 2007): the Arshan Formation (K_{1ba}) dominated by alluvial, fluvial and shallow lacustrine environments and the Tengge'er Formation (K_{1bt}) dominated by deep to semi-deep lacustrine environment; and (iii) a post-rift stage characterized by a switch from tectonic to thermal subsidence and the deposition of the early Cretaceous Saihan Formation (K_{1bs}) and the late Cretaceous Erlian Formation (K_{2e}), both dominated by fluvial and shallow lacustrine environments (Currie and Eberth, 1993; Lin et al., 2001; Meng et al., 2003; Van Itterbeeck et al., 2005, 2007; Bonnetti et al., accepted).

3.2. The Nuheting deposit

The Nuheting deposit was discovered in 1990 in the central-north of the Wulanchabu Sub-basin (Fig. 1), about 40 km to the southwest of Erlian city (**Figure 48**). Uranium resources are estimated in excess of 10 000t U (Dahlkamp, 2009) at a grade ranging from 0.03 to 0.1% U. The deposit is hosted in the Erennaor Sag, within the upper member of the late Cretaceous Erlian Formation (Li and Kuang, 2010) and is tabular in shape. It consists of an upper main ore body (0.7-1.3 m thick) and several lower sporadically distributed smaller ore bodies (Dahlkamp, 2009). The main ore body is very shallow, blanket shaped, and located at the top of the mineralized sequence. It represents more than 90 % of the total resources. The uranium mineralization is mainly hosted in pyrite and organic matter-rich dark grey silty mudstones. Only a minor proportion occurs in siltstones and sandstones (Yan et al., 2010).

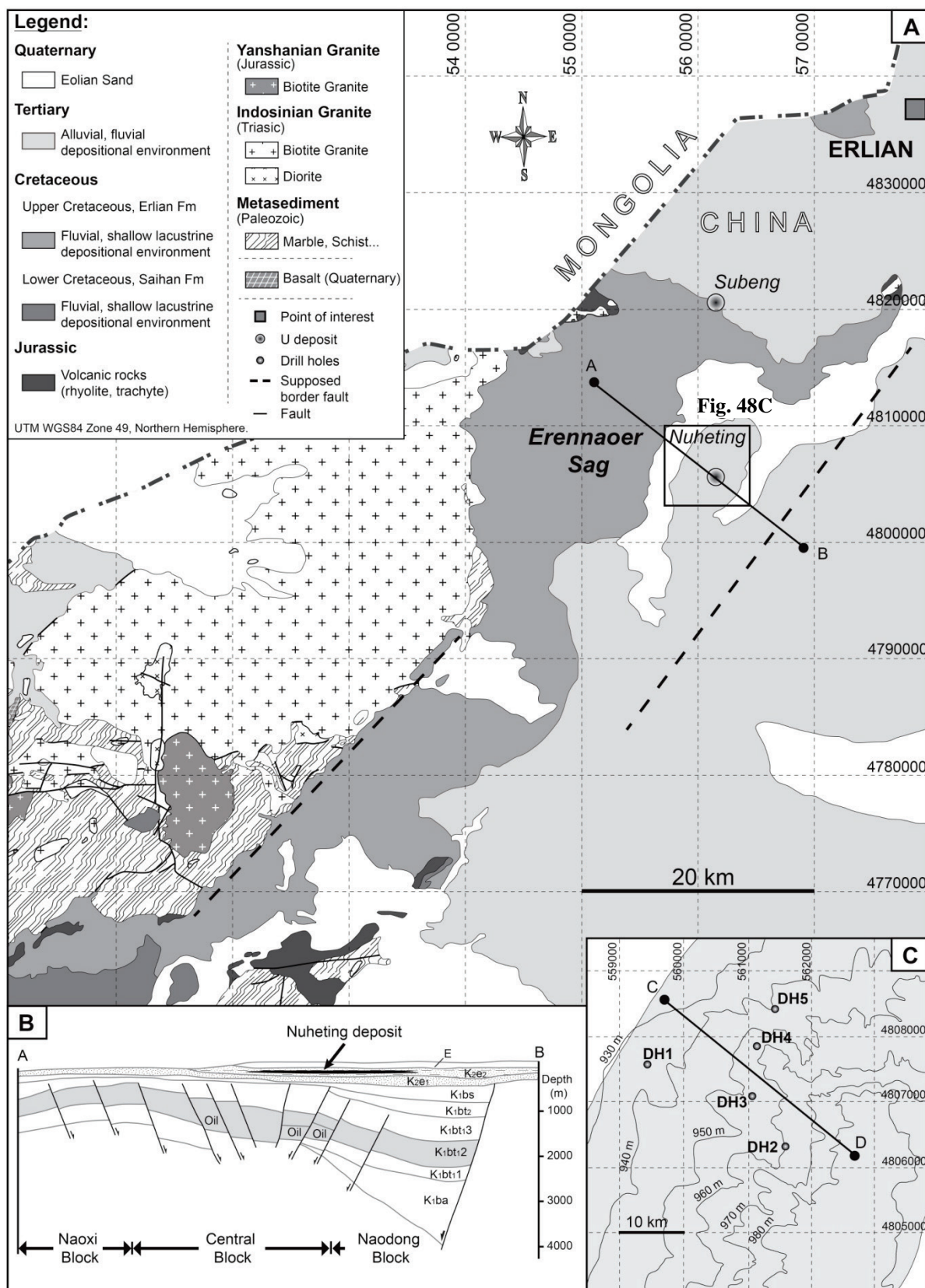


Figure 48. A= geological map of the central-northern part of the Wulanchabu Sub-basin, Erlian Basin (after CNNC, unpublished data). Fm= formation; U= uranium. This map shows the location of A-B cross-section (Fig. 48B) and the location of the Nuheting area (Fig. 48C). B= cross-section of the Erennaoer Sag (after Dahlkamp,

2009). K_1ba = Arshan Formation; K_1bt_1 , K_1bt_2 , K_1bt_3 and K_1bt_2 = Tengge'er Formation; K_1bs = Saihan Formation; K_2e_1 = lower member of the Erlian Formation; K_2e_2 = upper member of the Erlian Formation; E= Eogene. C= topographic map of the Nuheting area showing the location of drill holes DH1 to DH5 (after CNNC, unpublished data).

4. Materials and methods

Complementary methods were used in order to characterize the different stages of uranium mineralization leading to the formation of the Nuheting deposit. A total of five drill holes (DH1 to DH5, **Figure 48C**) from the Nuheting deposit were logged and sampled during the field trip realized in 2011. From bottom to top every sedimentary facies of both DH2 and DH3 were sampled in order to get geochemical profiles showing uranium mineralization evolution. Whole-rock geochemistry was realized at the rock and mineral service of analysis (SARM, CRPG) in Nancy, France. A total of seventeen drill-core samples were used for petrographical/mineralogical study which was carried out at the GeoRessources laboratory using optical microscope (reflected light and fluorescence) and at the microanalytical facility of the Lorraine University (SCEM, Nancy, France) using: (i) a Hitachi S-4800 scanning electron microscope (SEM) and (ii) a CAMECA SX100 electron microprobe (EMP). Clay minerals determination was realized at the LIEC laboratory (Nancy, France) by X-ray diffraction using a D8 Bruker diffractometer. The clay mineral fraction ($<2\mu m$) was extracted from samples and deposited on thin sections which were analysed according to three different ways: (i) oriented clay mineral fraction, (ii) ethylene glycol saturated and (iii) heated at $550^{\circ}C$ during 4 hours. Each diffractogram was measured in the 2-Theta domain. Organic matter typology and maturity were determined by Rock-Eval VI pyrolysis (REP) at Weatherford Laboratories (Texas, USA). The distribution of uranium mineralization as well as other high-density minerals like pyrite was visualized by XR-tomography using a Phoenix nanotom microtomograph. 1440 images at a resolution of $6\mu m$ Voxet over 360° on a mineralized sample (1 cm^3) of the Nuheting deposit have been recorded using a beam at 98 kv (voltage) and $75\mu A$ (current). Finally, trace element concentrations in pyrite (Zhao et al., 2011) have been measured on two mineralized samples of the Nuheting deposit using a laser ablation inductively coupled plasma mass spectrometry (LA-ICPMS) at the GeoRessources laboratory of Nancy. Laser sampling was performed with a 193 nm GeoLas Pro ArF Excimer laser (Microlas®, Göttingen, Germany) equipped with beam homogenisation optics. Ablation was performed by focussing the beam at the sample surface with a constant fluence of 10 J.cm^{-2} and constant repetition rate of 5 Hz. Helium was used as a carrier gas to transport the laser-

generated aerosols from the ablation cell to the ICP-MS. Argon as a make-up gas was mixed with the carrier gas via a T-connector before entering the ICP torch. Typical flow rates of 0.5 l min⁻¹ for He and 0.96 l min⁻¹ for Ar were used (Lach et al., 2013). For each experiment, a 16 µm spot size has been used and eleven trace elements (Cu, Zn, As, Se, Mo, V, Ni, Co, Cd, Te, Bi) were analyzed. All data were acquired as raw counts (cps) using the time resolved mode. For each individual analysis (external standard and samples), the background was measured before ablation during 20 s and its return to initial value was checked before ablating a new zone. Signal intensity integration of trace element masses was realized during the plateau regime. Signal acquisition of sample was stopped after 150 pulses (10 to 30 s at 5 Hz) and recorded during 80 s (including 20 s of background acquisition and 10 to 30 s of ablation). The sulfide external standard Mass-1 (called PS-1 in Wilson et al., 2002) was used as reference material and Fe concentration of pyrite analyzed as internal standard. Then data processing was realized using the LASP software (Leisen, 2011) in order to convert raw counts for every measured trace element into concentration (in ppm).

5. Sedimentology and petrography of the host-rock

5.1. Sedimentology of the Erlian Formation

The Nuheting deposit located in the Erennaor Sag of the Wulanchabu Sub-basin is hosted in the late Cretaceous Erlian Formation (Cai et al., 1990; Currie and Eberth, 1993; Van Itterbeeck et al., 2005, 2007; Bonnetti et al., accepted). The Erlian Formation is about 50 m thick in the study area and presents two different members (**Figure 49**): (i) a lower member dominated by stacked channels of braided river system and (ii) an upper member dominated by overbank deposits. The lower member shows facies association of channels characterized by very coarse to fine-grained sand with either trough or planar crossbeds and very minor siltstone occurrence, and sandy bedforms that may occur as channel fills, crevasse splays or minor bars. This member is secondarily oxidized (**Figure 49**), as some remnants of reduced sandstone have been observed, indicating that oxygenated groundwater has flowed through. The lateral extend of this secondary oxidation is of kilometre scale. The lower member corresponds to a braided fluvial environment with minor preserved floodplain deposits (Bonnetti et al., accepted). The upper member mainly presents sedimentary facies of crevasse splays and floodplain fines. These facies especially floodplain fines are composed of fine to very fined-grained sand, silt and mud that may build sheets of many kilometres in lateral extension. They correspond to overbank sheet flow, floodplain ponds and swamps. These type

of depositional environments dominated by floodplain deposits are highly favourable for preserving detrital organic matter like phytoclasts and coal debris because of their suboxic to anoxic characteristics (Casagrande, 1987; Diessel, 1992; Miall, 1996). The upper member of the Erlian Formation is overbank dominated fluvial environment (Bonnetti et al., accepted) and shows minor channel occurrence (anastomosed or abandoned channel).

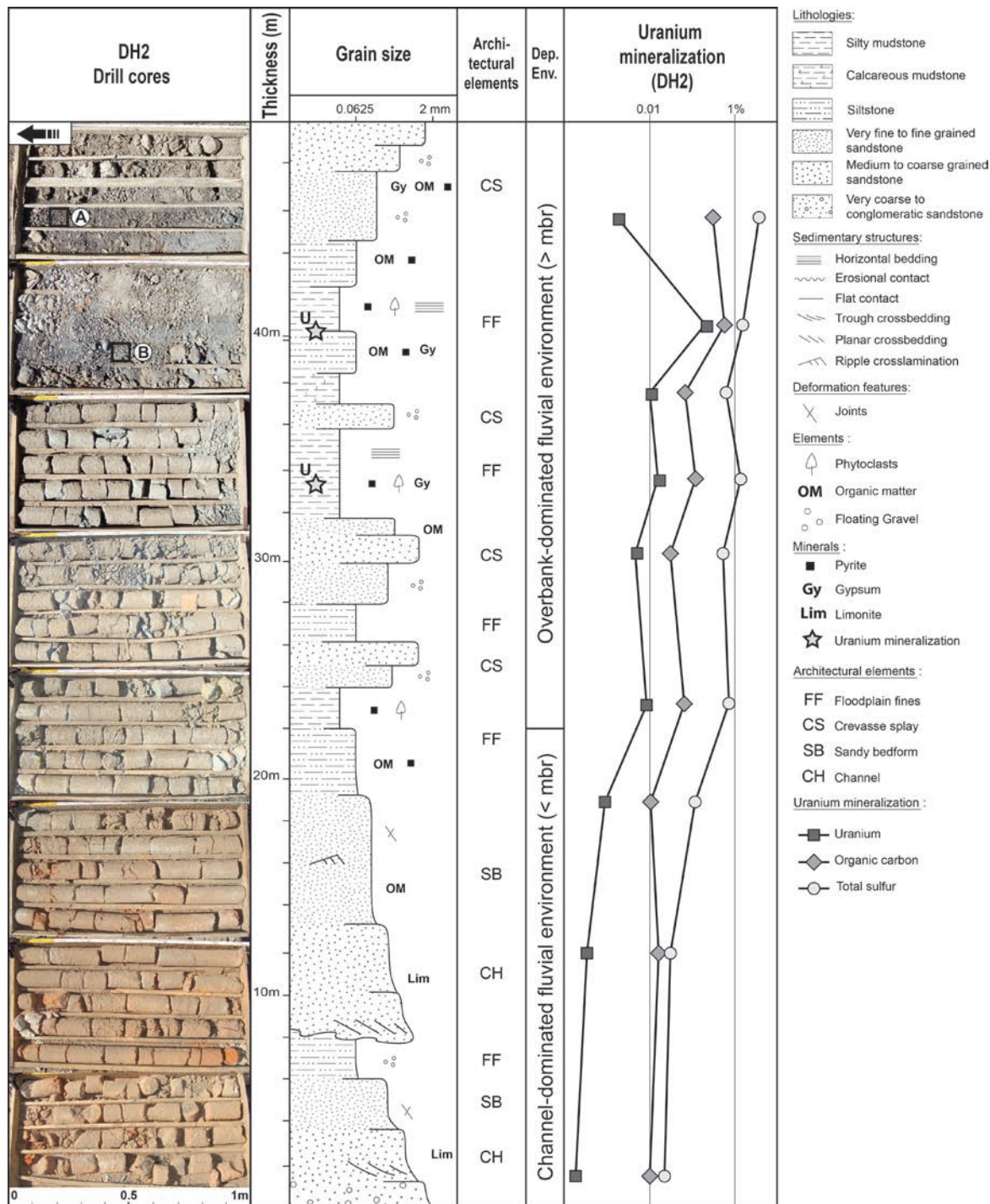


Figure 49. Sedimentological log of the Erlian Formation correlated to the geochemical profile of DH2 showing the evolution of uranium, organic carbon and total sulfur (modified after Bonnetti et al., accepted). Black squares

A and B show the location in the log of the main host-facies presented in figure 50. Dep. Env.= depositional environment; < mbr = lower member; > mbr = upper member.

5.2. Characteristics of the host-rock

5.2.1. Lithofacies

According to Yan et al. (2010) uranium mineralization in the Nuheting deposit is mainly hosted in organic matter and pyrite-rich dark grey silty mudstone (~52 %) and in siltstone (~37 %). A minor proportion is hosted in sandstone (~7 %) and calcareous mudstone (~0.5 %). Indeed uranium content in the sedimentary facies presented in **Figure 49** shows that black silty mudstone with root network deposited in swamp (Bonnetti et al., accepted; **Figure 50A**) and dark grey silty mudstone deposited in floodplain ponds host the main part of the mineralization with uranium content ranging from 100 to 3500 ppm based on geochemical profiles realized on DH2 and DH3 drill holes (**Figure 49; Appendix 9**). Both facies of silty mudstone occur in the upper member of the Erlian Formation and uranium mineralization is correlated to high content of both organic carbon and total sulfur (**Figure 49**). As observed in **figure 50B** than mud facies, secondary oxidation may occur along silty or sandy beds of the mudstone due to a better permeability. Most of the uranium mineralization appeared to be facies-controlled.

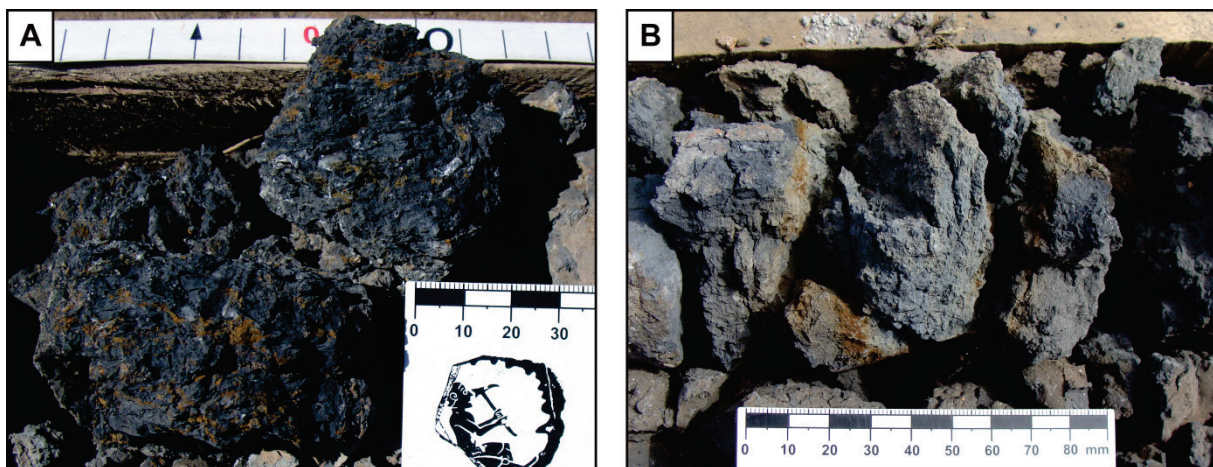


Figure 50. Main lithofacies hosting the uranium mineralization of the Nuheting deposit. A= root network and gypsum-bearing black mudstone of swamp; B= massive dark grey silty mudstone of floodplain pond with secondary oxidation along silt-dominant beds.

5.2.2. Petrography/mineralogy

Most of the lithofacies from the Erlian Formation, sandstones, siltstones and mudstones, have quartz and feldspar contents indicating a sandstone composition (**Appendix 6**). The clayey matrix is more or less dominant depending of the facies. Moreover, part of these lithologies has been carbonated especially sandstones, but also affecting fine grained facies (**Appendix 6**). Both lithofacies hosting the major part of the uranium mineralization, silty mudstone and siltstone (Yan et al., 2010), present subangular to subrounded detrital grains that are supported by a clayey matrix, more or less dominating and corresponding to mudstone to siltstone lithologies. Isolated coarse grains or small gravels of lithic grain (carbonate, granitic or volcanic composition; **Figure 51A**), quartz or feldspar often occur in the matrix. The major mineral assemblage of these facies is composed of quartz, alkali-feldspar, plagioclase (**Figure 51B**), biotite and chlorite (**Figure 51C**). The detrital accessory mineral assemblage is epidote (**Figure 51D**), monazite (**Figure 51E**), Fe/Ti oxides (**Figure 51F**), zircon (**Figure 51G**) and titanite (**Figure 51H**). The clay mineral assemblage identified for the lithofacies hosting the mineralization of the Nuheting deposit is interstratified clay minerals, smectite, chlorite, palygorskite, illite and kaolinite (**Appendix 8**). The occurrence of palygorskite may highlight a confined environment alternating between dry and humid periods. Among the most abundant U-bearing detrital minerals like monazite, zircon and Fe/Ti oxides: (i) zircon shows uranium content ranging from 0 to 0.1 wt.% UO₂ (EMP analysis) but behaves as refractory mineral (not altered in host-rock, low to moderate Zr content in whole rock), (ii) monazite presents a relatively high uranium concentration from 0.1 to 1.0 wt.% UO₂ (**Table 12**) but is also a refractory mineral (not altered in the host-rock, low to moderate Ce content in whole rock) and in most geological conditions (iii) Fe/Ti oxide may contain 0.01 to 0.1 wt.% UO₂ but not systematically, depending if they are Fe-dominant (**Table 13**: 56/14-1 and 56/14-2) or Ti-dominant (**Table 13**: 56/2-1, 56/3-1, 56/4-2 and 56/6-2) oxides. Indeed Ti-dominant Fe/Ti oxides often present significant uranium contents (~1000 ppm U) whereas Fe-dominant Fe/Ti oxides do not. In addition, some very rare occurrences of U-thorite crystals were observed as well. Therefore detrital contribution in whole-rock uranium content appeared to be very minor.

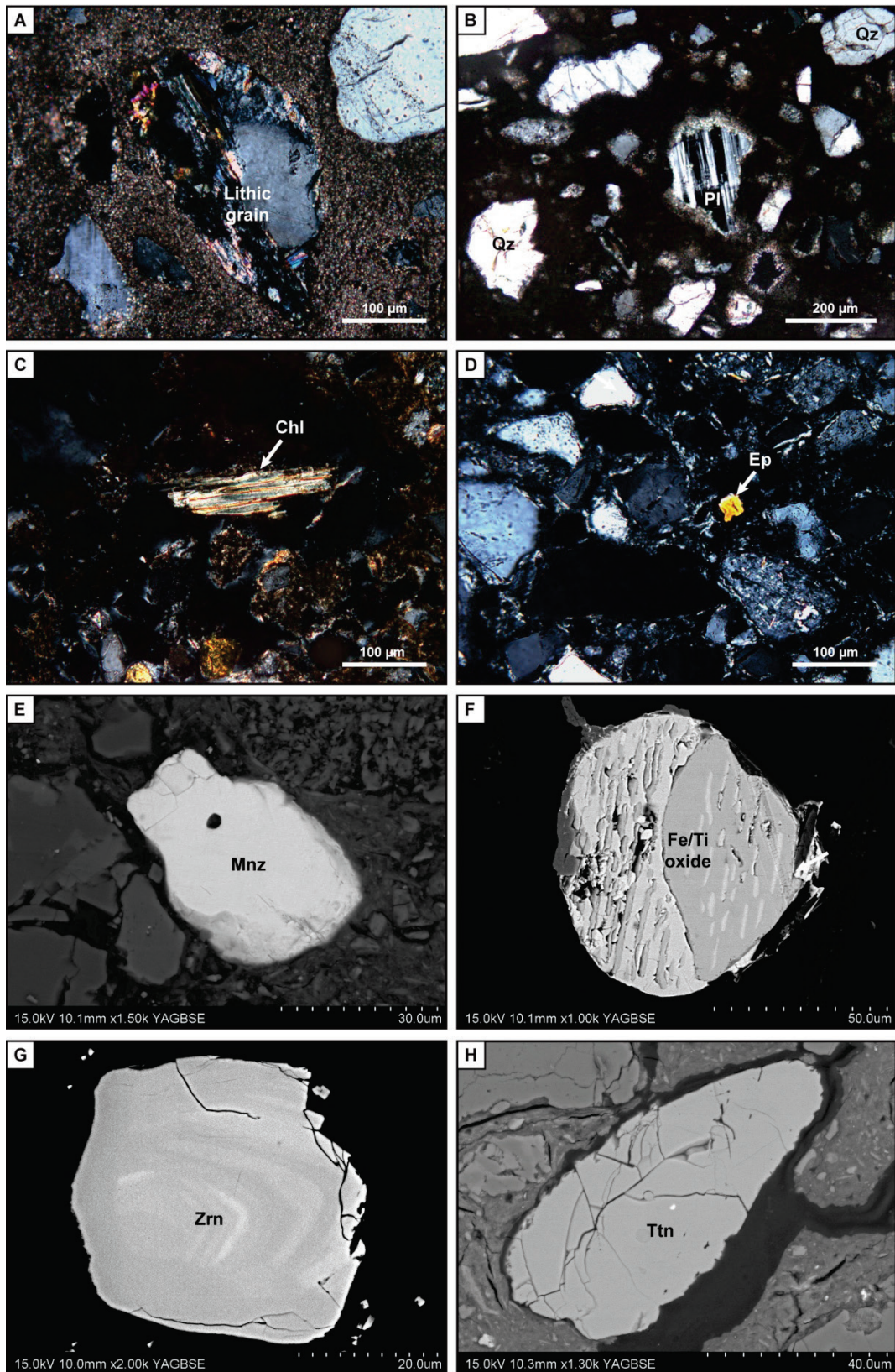


Figure 51. Main detrital minerals of the host-rock. A= lithic grain; B= plagioclase (Pl); C= chlorite (Chl); D= epidote (Ep); E= monazite (Mnz); F= Fe/Ti oxide; G= zircon (Zrn); H= titanite (Ttn).

Table 12. Representative EMP analysis of monazites occurring in the host-rock of the Nuheting deposit.

Location		Nuheting deposit					
Mineral		Monazite					
Sample		DH2-63.7m		DH3-54.6m			
Analysis n°		637-A	637-B	546-A	546-B	546-C	M11-A
Oxides (wt.%)							
P ₂ O ₅		27.29	27.34	27.18	27.66	27.92	27.91
SiO ₂		1.75	1.80	2.17	2.08	2.06	1.55
CaO		1.24	1.28	0.55	0.57	0.56	0.65
Y ₂ O ₃		2.13	2.13	1.73	1.72	1.69	2.00
La ₂ O ₃		13.64	13.49	14.27	13.91	13.95	11.76
Ce ₂ O ₃		25.55	27.35	27.75	27.74	27.92	27.05
Pr ₂ O ₃		3.13	3.14	3.18	3.25	3.38	3.28
Nd ₂ O ₃		10.08	9.97	10.56	11.08	10.95	11.42
Sm ₂ O ₃		1.54	1.53	1.90	1.93	1.90	1.91
Gd ₂ O ₃		1.21	1.24	1.33	1.24	1.45	1.38
PbO		0.13	0.15	0.13	0.00	0.11	0.05
ThO ₂		9.79	9.78	9.29	8.70	8.72	9.04
UO ₂		0.40	0.40	0.49	0.44	0.45	0.11
Total		99.57	99.62	100.54	100.33	100.64	98.12
Oxygens		4	4	4	4	4	4
Cations							
P		0.924	0.924	0.916	0.927	0.922	0.949
Si		0.070	0.072	0.086	0.082	0.082	0.062
ΣT-site		0.994	0.996	1.002	1.009	1.004	1.011
Ca		0.053	0.055	0.023	0.024	0.024	0.028
Y		0.045	0.045	0.037	0.036	0.036	0.043
La		0.201	0.199	0.210	0.203	0.204	0.174
Ce		0.403	0.400	0.404	0.402	0.405	0.398
Pr		0.046	0.046	0.046	0.047	0.049	0.048
Nd		0.141	0.142	0.150	0.157	0.155	0.164
Sm		0.021	0.021	0.026	0.026	0.026	0.026
Gd		0.016	0.016	0.018	0.016	0.019	0.018
Pb		0.001	0.002	0.001	0.000	0.001	0.001
Th		0.089	0.089	0.084	0.078	0.079	0.083
U		0.004	0.004	0.004	0.004	0.004	0.001
Σa-site		1.020	1.018	1.004	0.993	1.001	0.984
% Huttonite		0.07	0.07	0.08	0.08	0.08	0.06
% Brabantite		0.11	0.11	0.05	0.05	0.05	0.17
% Monazite		0.87	0.86	0.89	0.88	0.89	0.87

Table 13. Representative EMP analysis of Fe/Ti oxides occurring in the host-rock of the Nuheting deposit.

Location		Nuheting deposit					
Mineral		Fe/Ti oxide					
Sample		DH3-56.0m					
Analysis n°		56/2-1	56/3-1	56/4-2	56/6-2	56/14-1	56/14-2
Oxides (wt.%)							
SiO ₂		0.42	0.40	1.29	0.23	0.05	0.05
TiO ₂		56.67	55.51	76.38	55.83	39.80	16.00
Al ₂ O ₃		0.04	0.23	0.27	0.06	0.00	0.02
FeO		31.77	32.72	9.88	35.23	55.38	74.61
MnO		5.53	2.18	0.29	2.22	1.77	0.39
MgO		0.04	0.13	0.06	0.04	0.02	0.00
Cr ₂ O ₃		0.00	0.03	0.03	0.00	0.05	0.11
V ₂ O ₃		1.80	2.01	2.86	1.84	1.59	1.24
CoO		0.00	0.02	0.00	0.02	0.02	0.05
UO ₂		0.03	0.19	0.11	0.07	0.02	0.00
Total		96.31	93.43	91.17	95.53	98.72	92.48
Oxygens		3	3	3	3	3	3
Cations							
Si		0.010	0.010	0.029	0.006	0.001	0.002
Ti		1.062	1.065	1.312	1.058	0.813	0.405
Al		0.001	0.007	0.007	0.002	0.000	0.001
Fe		0.662	0.698	0.189	0.742	1.257	2.100
Mn		0.117	0.047	0.006	0.047	0.041	0.011
Mg		0.001	0.005	0.002	0.002	0.001	0.000
Cr		0.000	0.001	0.001	0.000	0.001	0.003
V		0.030	0.034	0.043	0.031	0.029	0.028
Co		0.000	0.001	0.000	0.001	0.001	0.002
U		0.001	0.008	0.004	0.003	0.001	0.000

6. Characterization of the organic matter

6.1. Petrography

Organic matter-rich samples collected in drill holes of the Nuheting deposit were studied by fluorescence optical microscopy in order to characterize the petrography of the organic matter. The structured elements identified in the samples of the mineralized sequence are of both terrigenous and aquatic origin. Indeed, a large amount of phytoclasts (non-fluorescent, biostructure = plant cell) and coal fragments (non-fluorescent, biostructure = fibrous or laminae; Durand, 1980; **Figure 52A**) as well as some megaspores (fluorescent; **Figure 52B**) and pollen indicate a dominant contribution of terrigenous organic matter in the overbank deposits of the Erlian Formation. The frequent occurrence of Tasmanaceae-type algae or Thrombolite-type microbial structure (fluorescent; Durand, 1980; Olivier et al, 2003; **Figure 52C, D**) characterizes a subaquatic to aquatic depositional environment (Durand, 1980). No

evidence of fluorescent material that could correspond to free hydrocarbons was identified in the matrix or in-filling fractures.

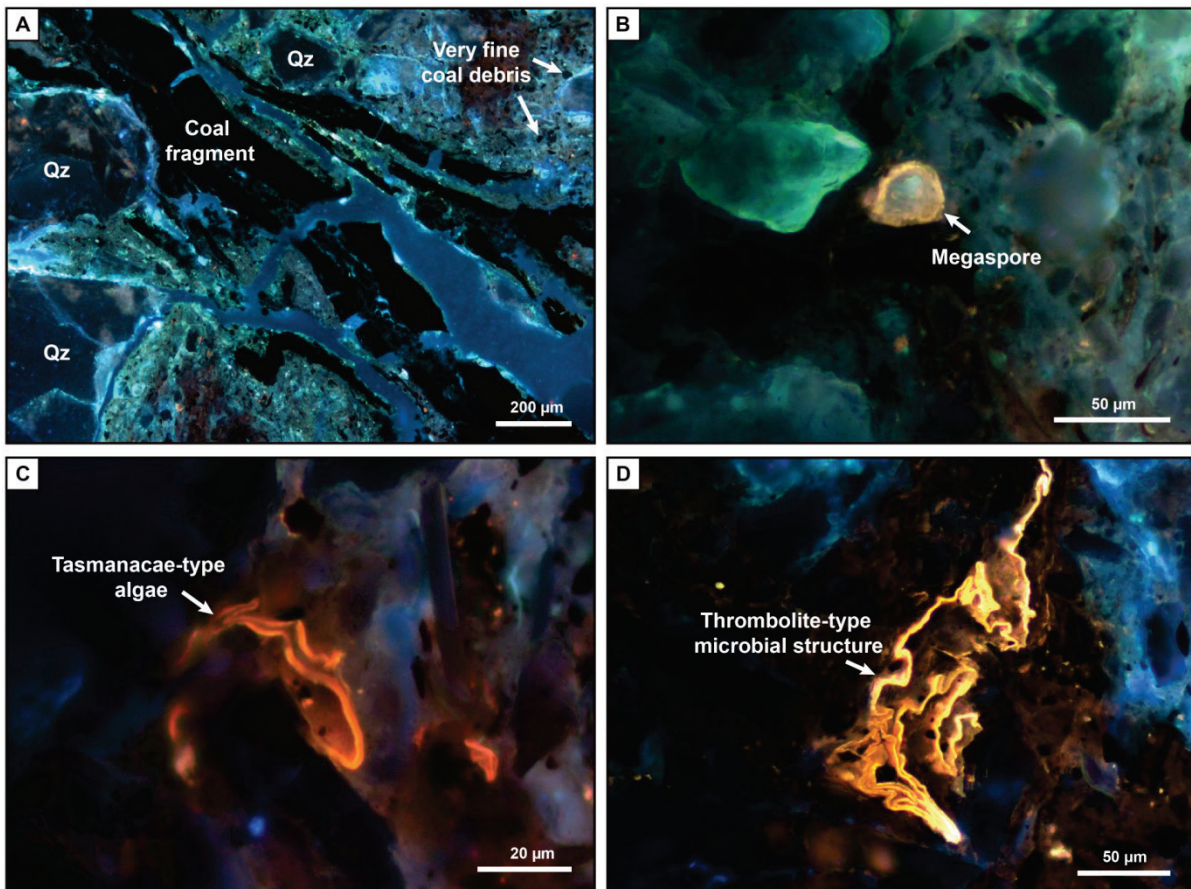


Figure 52. Structured elements of organic matter occurring in the host-rock of the Nuheting deposit. A= coal fragment; B= megasporite; C= Tasmanacae-type algae; D= Thrombolite-type microbial structure. Qz= quartz.

6.2. Typology

In order to characterize the typology of organic matter occurring in overbank deposits of the Erlian Formation Rock-Eval pyrolysis (REP) was realized on samples from DH1, DH2, DH3 and DH5 including mineralized samples (**Table 13**; **Appendix 12**). First of all, the total organic carbon (TOC) content of analyzed samples displays low values ranging from 0.10 to 0.82 wt.%. Moreover mineralized samples like DH2-50.9 m and DH3-54.6 m (**Appendix 6**) present organic matter content of respectively 0.63 and 0.55 wt.% TOC. Preliminary evaluation by REP of free hydrocarbon (HC) in host-rock of the Nuheting deposit revealed an extremely low content of thermodesorbed HC with S1 values of 0.01-0.02 mg HC/g sample. REP S2 range from 0.02 to 0.37 mg HC/g sample (**Table 14**) and indicate a very low petroleum potential (Espitalie et al., 1985).

Table 14. Rock-Eval pyrolysis (REP) results from overbank deposit samples of the Erlian Formation (using REP interpretation methods Espitalie et al., 1985).

Drill holes	DH1		DH2		DH3			DH5
Depth (m)	11.4	20.4	53.2	55.7	48.0	54.6	55.7	26.2
TOC (%) Total organic carbon	0.10	0.34	0.17	0.14	0.19	0.39	0.82	0.72
S1 (mg HC/g sample) Free hydrocarbons (HC)	0.01	0.01	0.01	0.01	0.01	0.01	0.02	0.02
S2 (mg HC/g sample) HC generated through thermal cracking	0.03	0.02	0.07	0.04	0.04	0.09	0.37	0.32
S3 (mg CO ₂ /g sample) Amount of CO ₂ produced during pyrolysis	0.31	0.29	0.15	0.23	0.27	0.31	0.43	0.32
T _{max} (°C) Temperature at top of S2 peak	404	409	398	416	402	419	390	385
HI (mg HC/g TOC) Hydrogen index	30	6	41	29	21	23	45	44
OI (mg CO ₂ /g TOC) Oxygen index	310	85	88	164	142	79	52	44

Organic matter of the analyzed samples displays a very low hydrogen index (HI) with data ranging from 6 to 45 mg HC/g TOC and a relatively high to very high oxygen index (OI) with data from 44 to 310 mg CO₂/g TOC (**Table 14**). T_{max} values are lower than 435 °C and characterize thermally immature organic matter (Espitalie et al., 1985) occurring in the host-rock. This organic matter is of type IV (**Figure 53**; Demaison et al., 1983). Petrographical observations combined with REP analyses confirm that most of the organic matter is derived from land plants, even though trace contribution of algal input may be observed under the microscope (**Figure 52**). Very high values of OI (like 142 mg CO₂/g TOC for DH3-48.0 m or 310 mg CO₂/g TOC for DH1-11.4 m) associated with very low HI and the predominance of macerals characterizing higher plants input may be evidence for degraded type III kerogen (e.g. type IV kerogen).

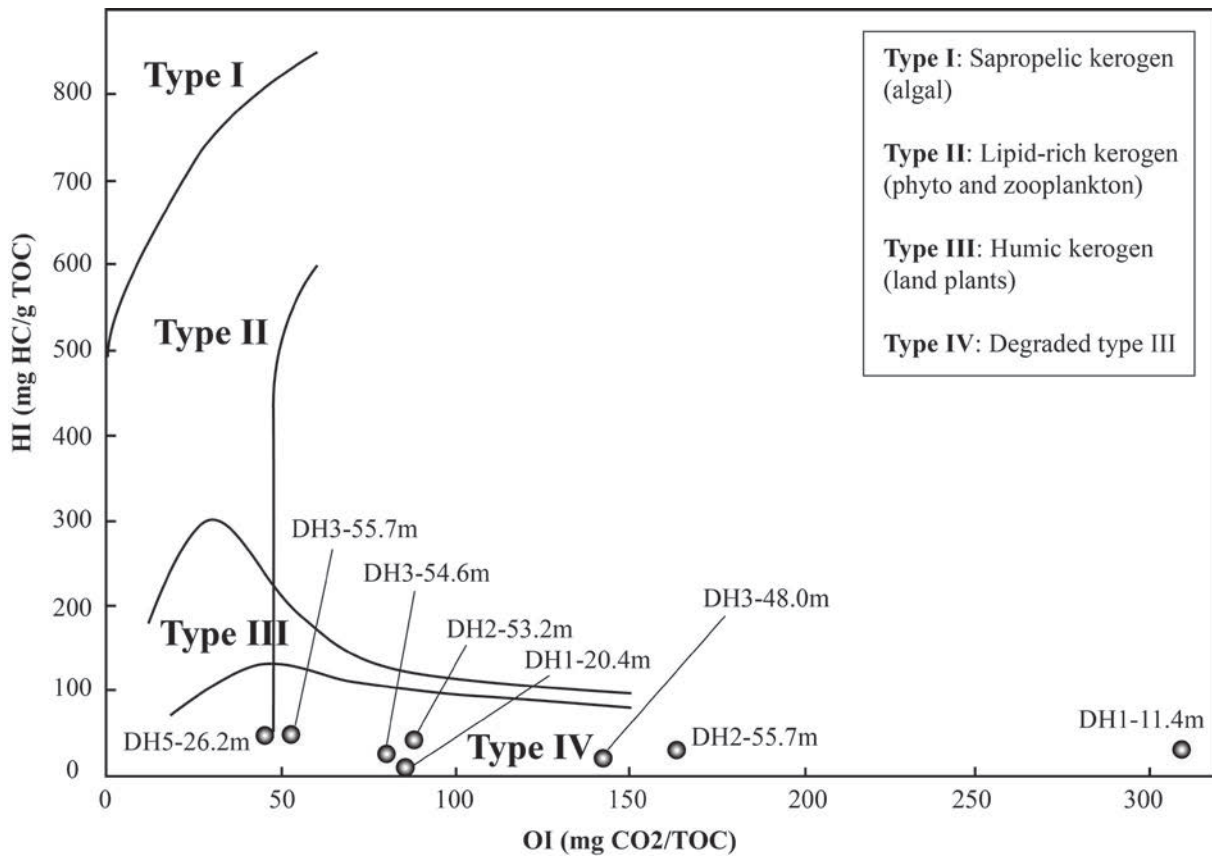


Figure 53. HI vs OI diagram showing the typology of organic matter of overbank deposits occurring in the Erlian Formation (modified after Herbin and Deroo, 1979; Demaison et al., 1983).

7. Uranium mineralization stages

The different stages of uranium mineralization of the Nuheting deposit were characterized mainly on mineralized samples from DH2 and DH3 drill cores and on other samples from DH1, DH4 and DH5 drill cores (see sample geochemical composition in **Appendix 6**; **Appendix 7**; **Appendix 8**; **Appendix 10**; **Appendix 11** and **Appendix 12**).

7.1. Disseminated uranium concentration

Uranium concentration occurs as fine disseminations in the both main host-facies of swamp type and floodplain pond type. Indeed, uranium does not occur as proper minerals but is largely adsorbed on clay minerals (Dahlkamp, 2009; Li and Kuang, 2010) as observed in **Figure 54A, B** where the clayey matrix shows irregularly enriched uranium background with respectively uranium content of 13.41 wt.%, 5.70 wt.% and 8.84 wt.% for the EMP analytical spots 312-1, 312-2 and 312-3 (**Figure 54A**).

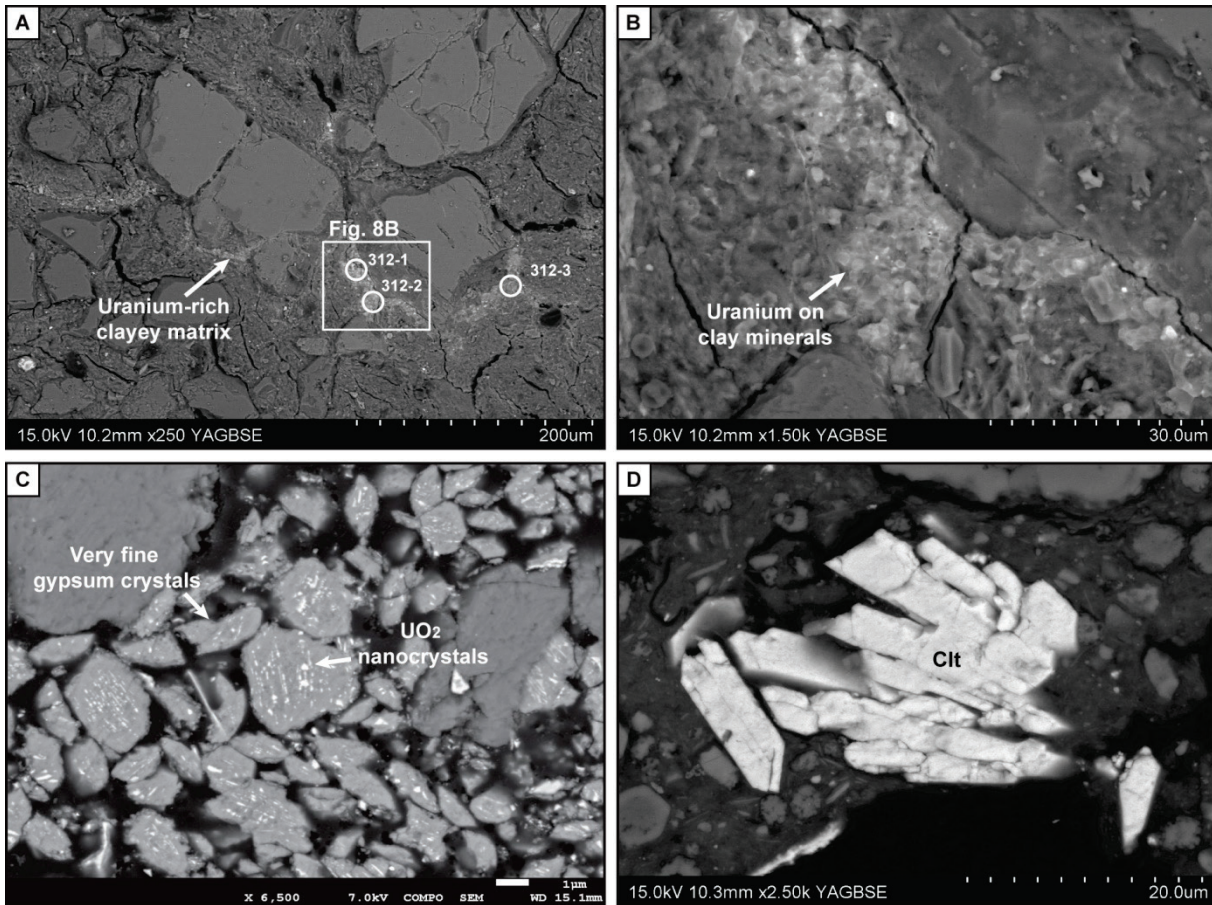


Figure 54. Characterization of synsedimentary uranium concentration in the host-rock of the Nuheting deposit. A= uranium-rich clayey matrix of silty mudstone, location of EMP data-points; B= uranium-rich clayey matrix; C= UO_2 nanocrystals within very fine gypsum crystals; D= celestite (Clt).

Primary sulphate minerals (**Figure 54C, D**), gypsum (CaSO_4) and celestite (SrSO_4), were observed in mineralized silty mudstone of overbank deposits and have likely crystallized shortly after sediment deposition (Bonnetti et al, accepted). These sulfate minerals especially gypsum include UO_2 nanocrystals (**Figure 54C**) which tend to be distributed along cleavage planes. Therefore uranium adsorption on clay minerals of the sedimentary facies hosting the uranium mineralization and UO_2 nanocrystals included within primary sulfate minerals are both interpreted as synsedimentary uranium concentration occurring in the depositional environment of the upper member of the Erlian Formation.

7.2. Uranium minerals associated with pyrite and organic matter

In the same sedimentary facies that host synsedimentary finely disseminated uranium concentration, uranium minerals coffinite (USiO_4) and/or pitchblend (UO_2) tend to replace diagenetic pyrite crystals.

7.2.1. Distribution of the mineralization

The 3D textural distribution of high-density minerals, such as pyrite, pyritized organic matter or uranium minerals, is visualized by XR-tomography imagery in the mineralized sample DH2-50.9m (**Figure 55A**). High-density minerals occur as dissemination in the matrix of the rock and mainly along a series of parallel planes corresponding to the sedimentary bedding of the silty mudstone hosting the mineralization. Moreover, elongated elements that may correspond to pyritized fragments of organic matter are also oriented parallel to the bedding. SEM observations (**Figure 55B, C, D**) show that the uranium mineralization is associated with pyrite or pyritized organic matter and disseminated in the host-rock (**Figure 55C, D**) but essentially distributed along the sedimentary bedding as also shown in the 3D imagery by XR-tomography. In **figure 55B**, the U mineralization is hosted by silt-dominant beds of the host-rock (slightly more permeable), the fracture results from thin section preparation.

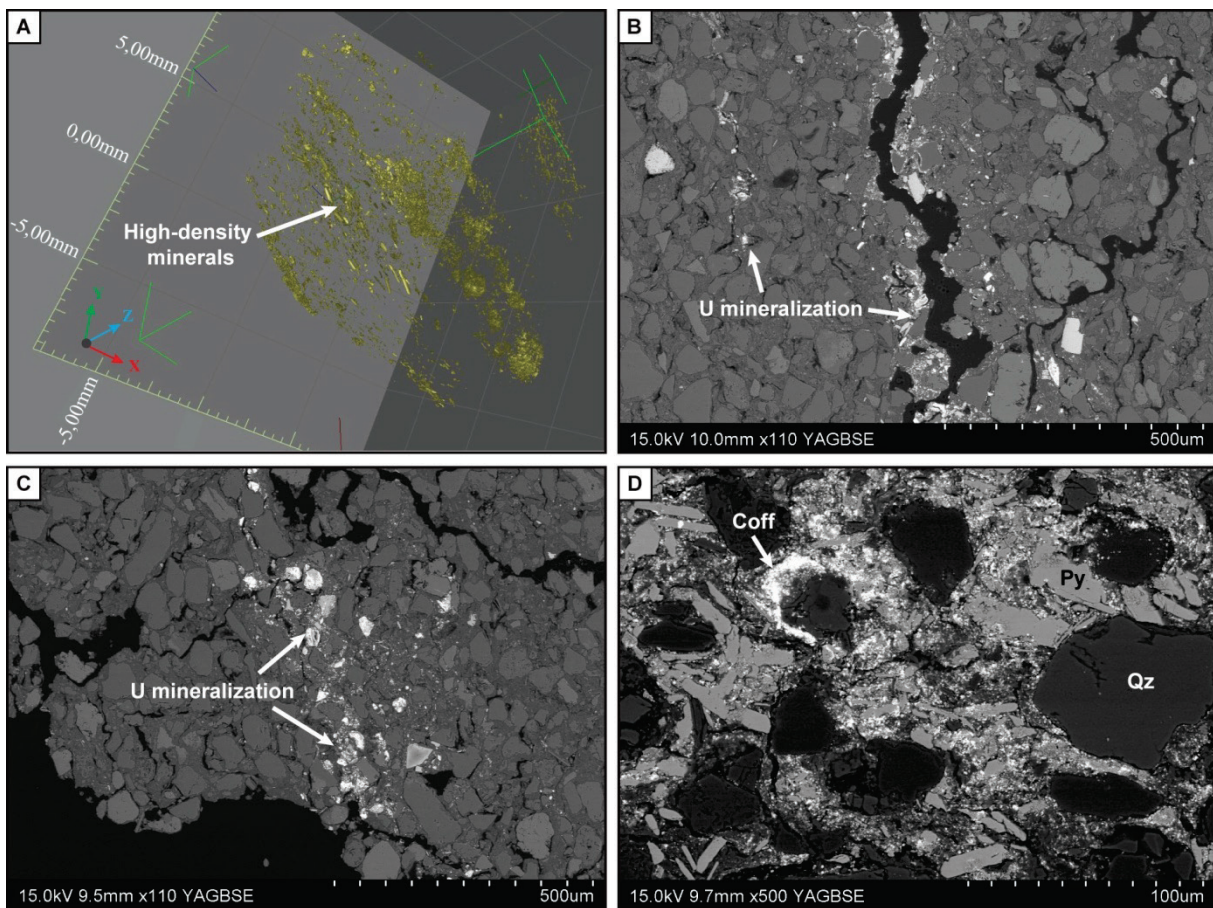


Figure 55. Diagenetic uranium mineralization distribution in mineralized samples of the Nuheting deposit. A= RX-tomography 3D imagery showing the distribution of high-density minerals; B= uranium mineralization along secondary induced fracture; C= uranium mineralization along pyrite and organic matter-rich level; D= uranium mineralization disseminated in the host-rock. Coff.= coffinite; Py= pyrite; Qz= quartz.

7.2.2. Pyrite typology and its trace element signature

In mineralized samples of the Nuheting deposit, pyrite offers three different textural shapes, respectively in order of abundance: (i) as epigeny of organic matter fragments; (ii) as subidiomorphic to idiomorphic crystals and (iii) as cement in the matrix. The trace element composition of these pyrites measured by LA-ICPMS (**Figure 56**; **Table 15** and **Table 16**) aimed: (i) to characterize the trace element signature of each population and (ii) to determine if they are cogenetic.

The three pyrite populations present significant As, Se and Mo concentrations and minor amount of Ni, Co, Cu, Zn, V and Cd. Te and Bi contents are extremely low or below the detection limit. The three populations of pyrite analyzed are characterized by distinct trace elements contents.

Pyrite in epigeny of organic matter (n= 6) is mainly frambooidal and displays very high content of Mo (from 11168 to 69678 ppm; mean= 28466 ppm; σ = 24292 ppm), Se (from 3560 to 6728 ppm; mean= 5482 ppm; σ = 1083 ppm) and As (from 2055 to 6690 ppm; mean= 3641 ppm; σ = 1603 ppm); (**Table 16**). Mo is largely predominant in the trace element signature (**Figure 57C**). Cu, Zn (except for DH2-50.9m/1-2a, **Table 16**), Ni and Co occur in a minor proportion.

Pyrite cement and idiomorphic pyrite (n= 13) have the same trace element signature (**Figure 57A**). They are characterized by high contents of Se (from 117 to 11078 ppm; mean= 1763 ppm; σ = 2912 ppm), Mo (from 1 to 649 ppm; mean= 126 ppm; σ = 189 ppm) and As (from 1 to 353 ppm; mean= 142 ppm; σ = 114 ppm), and minor amount of Cu, Zn, Ni and Co (**Table 15**). Se is largely predominant in the trace element signature (**Figure 57B**).

Both main pyrite populations present negligible V content (**Table 15**; **Table 16**).

Therefore two main populations of pyrite can be differentiated from their trace element signature: (i) frambooidal pyrite in epigeny of organic matter and (ii) pyrite cement and idiomorphic pyrite. Secondary pyrite cement and idiomorphic pyrite are cogenetic and occurred at the diagenetic stage of the Nuheting deposit. As both populations of pyrite previously characterized are partly replaced by uranium minerals and present the same their trace element signature, they are most probably cogenetic and related to the diagenetic stage of the Nuheting deposit.

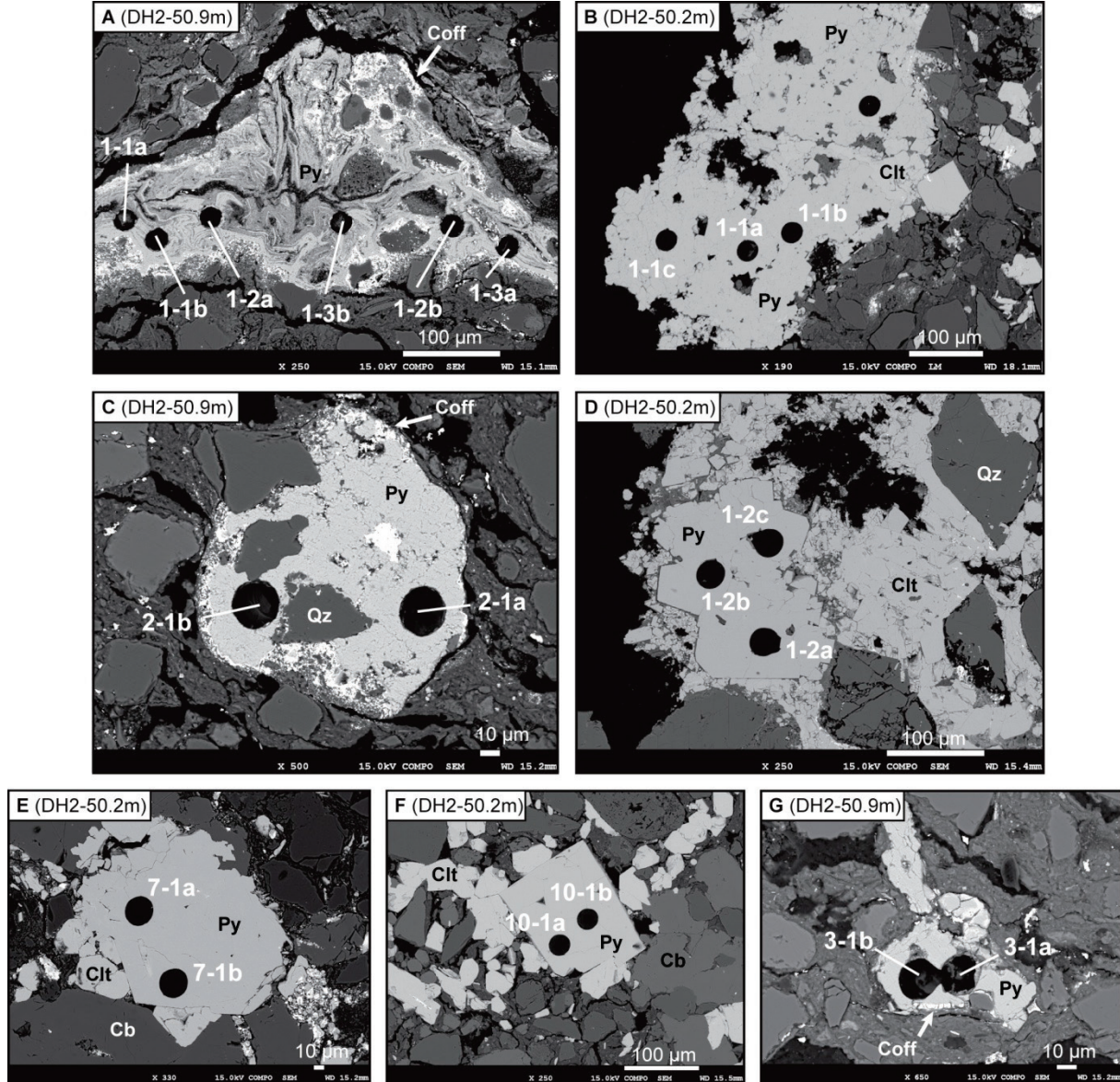


Figure 56. Location of ICPMS ablation spots on the different populations of pyrite. A= pyritized organic matter; B= pyrite cement; C= pyrite cement; D, E, F and G= idiomorphic pyrite. Cb= carbonate; Clt= celestite; Coff.= coffinite; Py= pyrite; Qz= quartz.

Table 15. Trace element composition of idiomorphic pyrite and pyrite cement. DH= Drill hole, Loc.= location; Tot.= total.

Loc.	Nuheting deposit												
	Type	Idiomorphic pyrite or pyrite cement											
DH		DH2-50.2m									DH2-50.9m		
N°	1-1a	1-1b	1-1c	1-2a	1-2c	7-1a	7-1b	10-1a	10-1b	2-1a	2-1b	3-1a	3-1b
Major elements by EMP analysis (Element wt.%)													
S	53.37	53.89	53.05	53.31	53.62	53.70	53.31	53.82	53.79	52.77	52.55	54.31	54.33
Fe	46.43	46.09	46.49	46.58	46.47	46.91	46.61	46.45	46.09	45.08	44.89	46.96	46.81
Tot.	100.20	100.70	99.82	100.28	100.32	100.75	100.32	100.48	100.44	98.19	97.8	101.55	101.34
Trace elements by LA-ICPMS (ppm); error is about 30-50%													
Cu	12	15	21	9	11	3	<LOD	1	3	6	7	28	9
Zn	7	6	19	2	4	2	<LOD	<LOD	<LOD	56	60	11	2
As	203	232	24	5	31	353	147	56	1	125	162	283	225
Se	976	860	454	395	684	858	888	790	117	1151	1203	11078	3477
Mo	85	101	15	5	36	101	27	7	1	403	649	147	61
V	<LOD	<LOD	2	9	<1	<LOD	<LOD	<LOD	<LOD	2	7	27	8
Ni	32	35	5	<LOD	2	<LOD	<LOD	<LOD	<LOD	97	139	60	29
Co	19	20	2	<LOD	<LOD	2	<LOD	<LOD	<LOD	54	92	9	5
Cd	<LOD	2	<LOD	<LOD	<LOD	1	<LOD	<LOD	<LOD	2	2	2	<LOD
Te	<LOD	<LOD	<LOD	<LOD	<LOD	<LOD	<LOD	<LOD	<LOD	1	1	<LOD	
Bi	<LOD	<LOD	<LOD	<LOD	<LOD	<LOD	<LOD	<LOD	<LOD	<LOD	<LOD	<LOD	

Table 16. Trace elements composition of framboidal pyrite in epigeny of organic matter. DH= Drill hole, Loc.= location; Tot.= total.

Loc.	Nuheting deposit					
	Type	Pyrite epigeny on organic matter				
DH		DH2-50.9m				
N°	1-1a	1-1b	1-2a	1-2b	1-2a	1-3b
Major elements by EMP analysis (Element wt.%)						
S	52.65	52.36	52.56	51.41	49.64	51.68
Fe	45.17	44.97	44.38	43.56	43.90	44.79
Tot.	98.24	97.82	97.72	95.57	94.21	97.07
Trace elements LA-ICPMS (ppm) ; error is about 50%						
Cu	133	7	12	10	24	27
Zn	82	69	54	105	7858	57
As	6690	2807	3281	2055	3808	3210
Se	5880	5141	6728	3560	5518	6070
Mo	69678	17096	32999	11168	35191	42268
V	47	6	11	14	30	19
Ni	150	246	143	392	350	199
Co	81	156	97	216	178	119
Cd	50	40	37	48	169	32
Te	<LOD	<LOD	3	1	3	<LOD
Bi	<LOD	<LOD	<LOD	<LOD	<LOD	<LOD

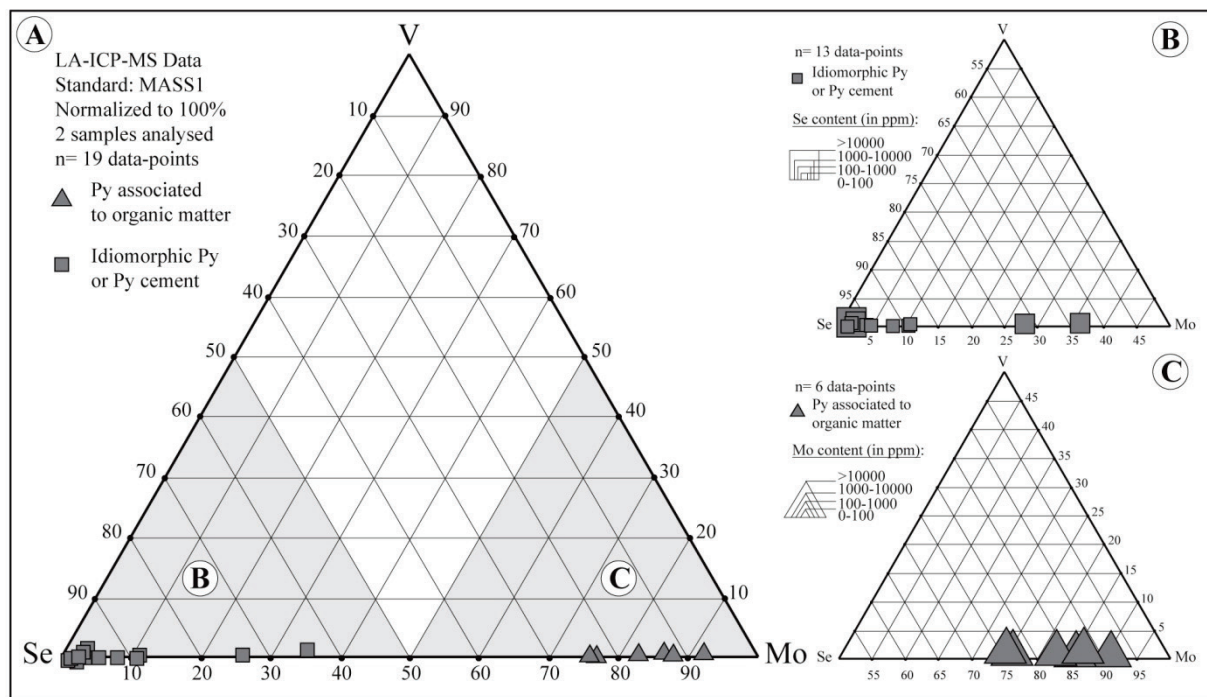


Figure 57. Se, V, Mo diagram permitting the characterization of two populations of pyrite. The Se-rich group represents pyrite cement and idiomorphic pyrite; the Mo-rich group represents pyrite replacing organic matter. Py= pyrite.

7.2.3. Uranium minerals

The uranium minerals in the Nuheting deposit are associated with: (i) pyritized organic matter (**Figure 58A, B, E, F**), (ii) pyrite cement (**Figure 58C**) or idiomorphic pyrite (**Figure 58D**) and (iii) pyritized sulfate (**Figure 58G, H**). The main uranium mineral is coffinite. Pitchblend occurs in minor proportion (Dahlkamp, 2009; **Table 17**). Organic matter fragments like higher plant debris (**Figure 58A, B**) and thrombolite-type microbial structures (**Figure 58E, F**) were first partly to totally replaced by pyrite and then partly to totally epigenized by coffinite. Coffinite also occurs at the edge of pyrite cement with quartz grain inclusions and may replace sub-idiomorphic to idiomorphic pyrite crystals (**Figure 58D**). Botryoidal coffinite also occurs at the edge of quartz grains (**Figure 58E**). Finally, in the same way as for organic matter, primary sulphate minerals gypsum and celestite are first replaced by pyrite and then epigenized by coffinite (**Figure 58G, H**).

All these petrographical and mineralogical observations evidence two episodes during the mineralizing event in the Nuheting deposit: (i) during the diagenetic stage, in the sediments of the Erlian Formation, different types of pyrite are formed, replacing organic matter fragments or still replacing primary sulphate minerals, cementing the matrix of the sediments, as isolated subidiomorphic to idiomorphic pyrite crystals, and (ii) deposition of uranium essentially occurring as coffinite replacing diagenetic pyrite crystals.

EMP analyses (**Table 17**) of coffinite show that silica ($7.17 < \text{SiO}_2 < 9.33$ wt.%) is largely substituted by phosphorous ($7.01 < \text{P}_2\text{O}_5 < 9.11$ wt.%) and uranium ($53.47 < \text{UO}_2 < 67.82$ wt.%) by calcium ($5.43 < \text{CaO} < 7.57$ wt.%). Small amounts of Zr detected in coffinite (up to 0.93 wt.% ZrO_2) may indicate a volcanic contribution within the host sediment.

EMP analyses (**Table 17**) of pitchblende show that uranium ($70.38 < \text{UO}_2 < 72.25$ wt.%) is largely substituted by calcium ($5.43 < \text{CaO} < 7.57$ wt.%), phosphorous ($3.51 < \text{P}_2\text{O}_5 < 6.77$ wt.%) and silica ($1.78 < \text{SiO}_2 < 5.68$ wt.%). Therefore, pitchblende may likely occur as a fine admixture of P-rich coffinite.

Elevated FeO content in uranium minerals (up to 9.06 wt.%; **Table 17**) may likely correspond to pyrite pollution of EMP analyses.

Therefore the dominant uranium mineral of the mineralization at the Nuheting deposit is P-rich coffinite which crystallizes during the diagenetic evolution of the sediments from the Erlian Formation, after new formation of pyrite.

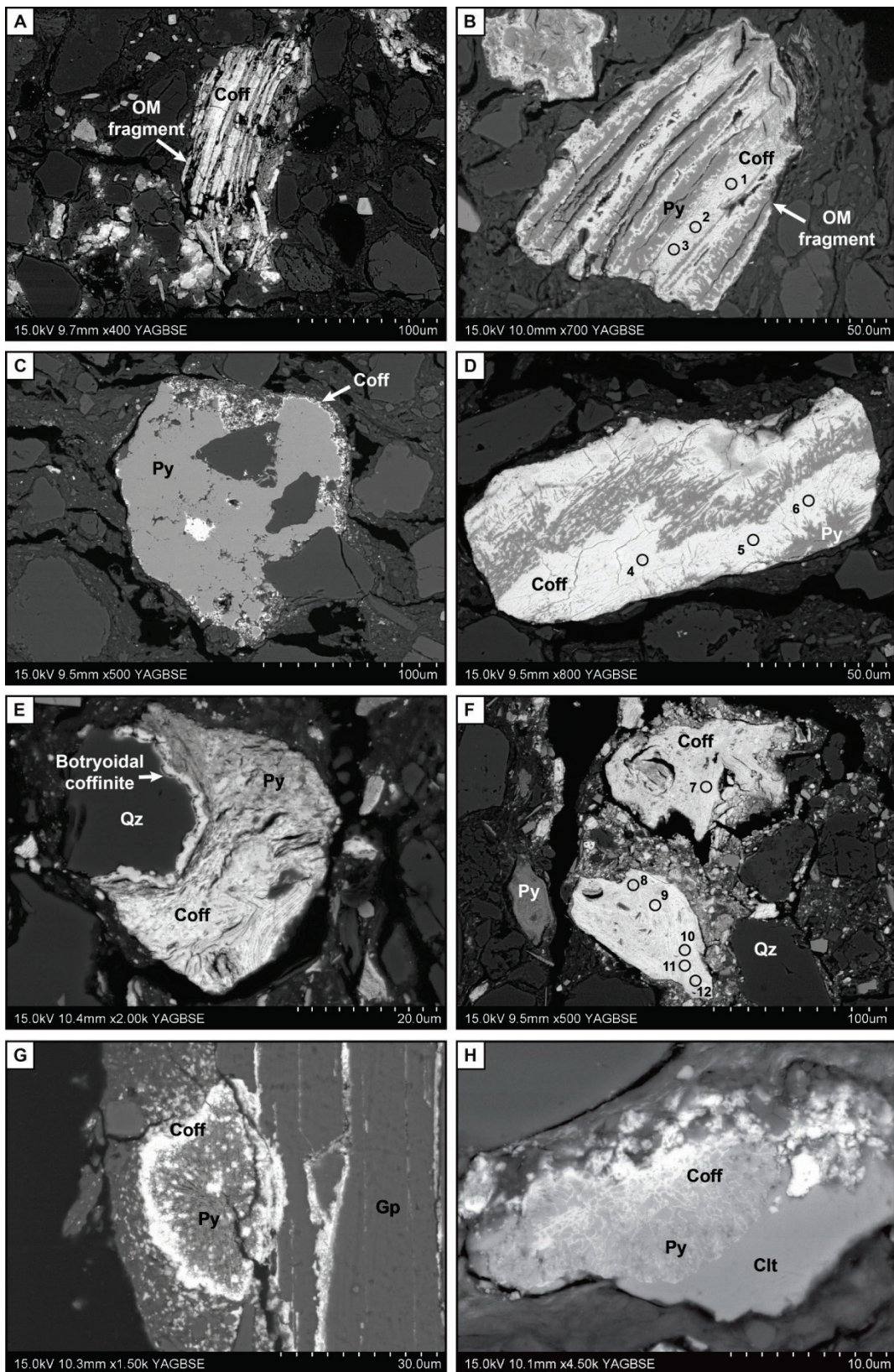


Figure 58. Uranium mineralization from the Nuheting deposit. A= organic matter fragment replaced by coffinite; B= pyritized organic matter fragment replaced by coffinite; C= coffinite at the edge of the pyrite cement; D= coffinite epigeny of a sub-idiomorphic pyrite crystal; E= coffinite replacing pyritized thrombolite-type microbial structure and botryoidal coffinite deposited at the margin of a quartz grain with evidence of quartz corrosion; F= coffinite replacing pyritized thrombolite-type microbial structure; G= coffinite replacing a

pyritized gypsum crystal; H= coffinite replacing a pyritized celestite crystal. OM= organic matter; Coff.= coffinite; Py= pyrite; Qz= quartz; Gp= gypsum; Clt= celestite.

Table 17. Representative EMP analyses on uranium minerals from the Nuheting deposit.

Location		Nuheting deposit											
Drill hole		DH2-50.9m											
Mineral		Coffinite						Pitchblende					
N°		1	2	3	4	5	6	8	11	7	9	10	12
Oxides (wt.%)													
SiO ₂		8.98	8.91	8.99	9.27	9.33	8.32	7.79	7.17	2.33	3.70	1.78	5.68
Al ₂ O ₃		0.13	0.14	0.10	0.18	0.19	0.19	0.10	0.13	0.07	0.10	0.09	0.70
FeO		3.83	4.53	3.13	0.40	1.14	9.06	0.23	0.07	1.98	1.64	3.04	0.77
MgO		0.16	0.20	0.17	0.20	0.23	0.18	0.10	0.15	0.15	0.19	0.21	0.15
CaO		6.89	7.13	7.57	7.22	6.97	5.43	6.68	6.92	4.35	5.99	4.69	6.60
K ₂ O		0.28	0.23	0.22	0.28	0.24	0.19	0.32	0.36	0.36	0.41	0.38	0.40
P ₂ O ₅		9.04	8.99	9.11	8.02	7.84	7.01	7.66	7.99	3.71	5.60	3.51	6.77
V ₂ O ₃		0.00	0.00	0.00	0.01	0.00	0.12	0.00	0.00	0.00	0.00	0.00	0.00
ZrO ₂		0.37	0.41	0.50	0.93	0.87	0.52	0.00	0.06	0.01	0.06	0.00	0.08
Y ₂ O ₃		0.07	0.07	0.10	0.41	0.38	0.32	0.00	0.00	0.00	0.00	0.00	0.00
PbO		0.03	0.02	0.02	0.00	0.00	0.02	0.00	0.00	0.00	0.00	0.00	0.00
ThO ₂		0.00	0.00	0.00	0.01	0.00	0.00	0.00	0.00	0.00	0.00	0.00	0.00
UO ₂		62.10	62.13	61.70	62.04	62.00	53.47	64.64	67.82	70.64	72.25	72.14	70.38
Total		92.45	93.43	92.06	89.88	89.96	85.11	88.12	91.47	83.94	90.24	86.05	92.02
Oxygens		4	4	4	4	4	4	4	4	2	2	2	2
Cations													
Si		0.468	0.460	0.467	0.502	0.506	0.472	0.453	0.409	0.092	0.124	0.07	0.174
Al		0.008	0.009	0.006	0.011	0.012	0.013	0.007	0.009	0.003	0.004	0.004	0.025
Fe		0.167	0.195	0.136	0.018	0.052	0.430	0.011	0.003	0.065	0.046	0.099	0.020
Mg		0.012	0.15	0.016	0.016	0.019	0.015	0.009	0.013	0.009	0.009	0.012	0.007
Ca		0.385	0.394	0.422	0.419	0.405	0.330	0.416	0.423	0.184	0.215	0.196	0.217
K		0.019	0.015	0.015	0.019	0.017	0.014	0.024	0.026	0.018	0.017	0.019	0.016
P		0.399	0.393	0.401	0.368	0.360	0.336	0.377	0.386	0.124	0.159	0.116	0.176
V		0.000	0.000	0.000	0.000	0.000	0.004	0.000	0.000	0.000	0.000	0.000	0.000
Zr		0.009	0.010	0.013	0.025	0.023	0.014	0.000	0.002	0.000	0.001	0.000	0.001
Y		0.002	0.002	0.003	0.012	0.011	0.010	0.000	0.000	0.000	0.000	0.000	0.000
Pb		0.000	0.000	0.000	0.000	0.000	0.000	0.000	0.000	0.000	0.000	0.000	0.000
Th		0.000	0.000	0.000	0.000	0.000	0.000	0.000	0.000	0.000	0.000	0.000	0.000
U		0.720	0.713	0.714	0.747	0.748	0.675	0.836	0.860	0.620	0.538	0.627	0.480

7.3. Post ore-stage

Finally, the uranium mineralization from the Nuheting deposit is partially sealed by a cement dominantly composed of celestite and minor barite, and carbonates (**Figure 59**). This cement may totally (**Figure 59A**) or partly (**Figure 59B**) occupy the matrix of the sedimentary facies hosting the uranium mineralization. The cementation may involve dissolution/replacement processes or secondary fracturation regarding the low permeability of the host-facies. Nevertheless, silt-dominant beds of the silty mudstone are more largely cemented during the epigenetic stage of fluid circulation. Sulfate and carbonate minerals are intimately associated together in the cement (**Figure 59A**) which is indicating a cogenetic crystallization. The cement is surrounding coffinite frequently until its complete inclusion, showing that the epigenetic stage of cementation is late relatively to the uranium mineralization.

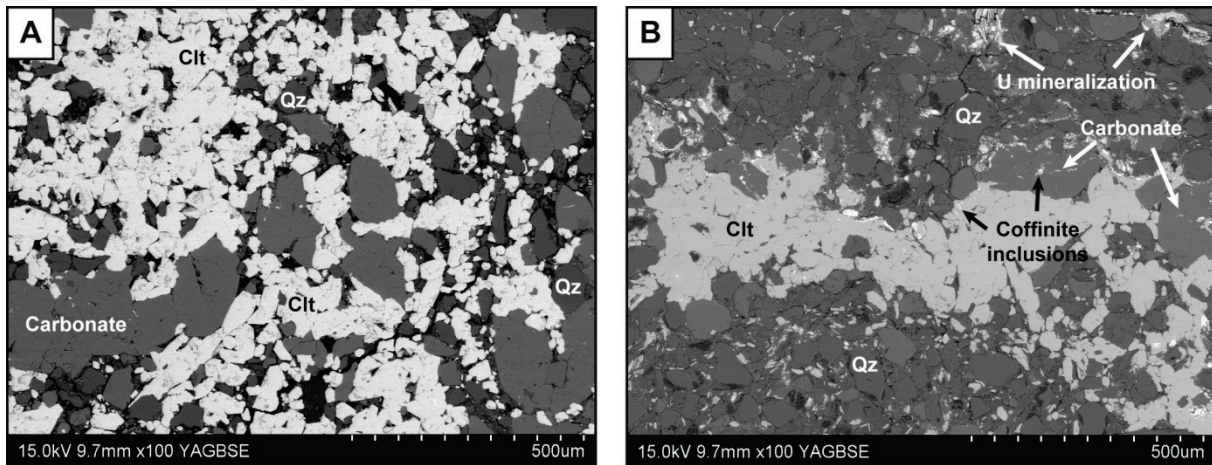


Figure 59. Late cementation of uranium mineralization in the Nuheting deposit. A= sulfate and carbonate cement; B= cementation of the uranium mineralization. Clt= celestite; Qz= quartz; U= uranium.

8. Discussion

In northeastern China, much scientific attention was focused on intracontinental sedimentary basins formed during the Mesozoic continental extension of eastern Asia (Charles, 2010; Ren et al., 2002) for their potential in energy resources (e.g. the Jixi, Boli, Shuangyashan, Hegan and Fuxin coal basins, RTMCFEH, 1986; the Daqing and Liaohe oil and gas fields, Ye et al., 1990; and the sandstone-hosted uranium deposits in the Erlian and Ordos basins, Cai et al., 2007; Dahlkamp, 2009).

The study of the Nuheting deposit presented in this paper evidences the formation of a synsedimentary uranium concentration which may have occurred at the scale of the basin. At Nuheting, this primary U concentration has been redistributed, mainly *in situ*, later during the diagenetic evolution of the sediments belonging to the Erlian Formation. This means that uranium-rich rocks were present in the source area providing the material during the sedimentation of the Erlian Formation. Such syn-sedimentary uranium enrichment may represent a characteristic of this sedimentary unit in the Erlian Basin.

8.1. Sedimentology of the Erlian Basin

The Erlian Basin is characterized by the deposition of the Saihan and the Erlian formations during a post-rift stage. Their sedimentological record exhibits sandstone layers consisting of amalgamated channels or sandy bedforms of braided river system alternating with more or less continuous mudstone layers belonging to overbank deposits (Bonnetti et al., accepted). This alternation is at the origin of confined permeable sandstone layers corresponding to favourable host-rocks for roll front-type uranium deposits. The Erlian Formation consists of two different members in the Nuheting area: (i) a sandstone dominated lower member and (ii) a mudstone dominated upper member (**Figure 60**).

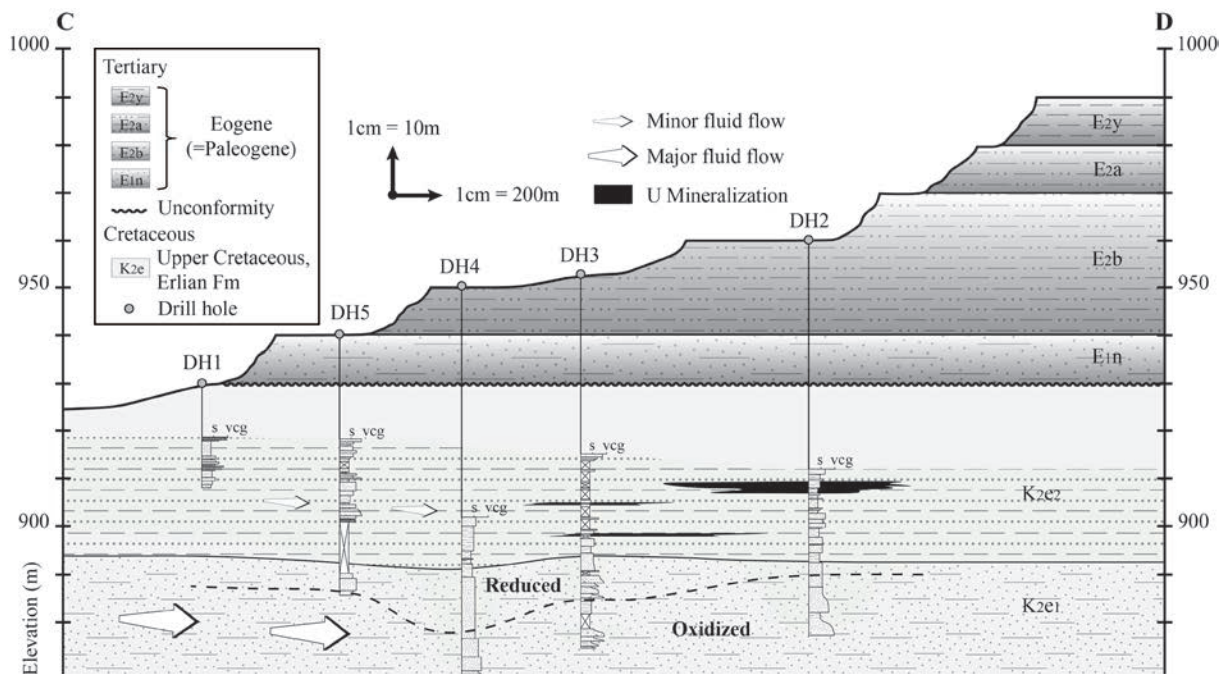


Figure 60. Drill hole cross-section of the Nuheting deposit. The cross-section C-D is located in figure 48C. K₂e₁= lower member of the Erlian Formation; K₂e₂= upper member of the Erlian Formation; s= silt; vcg= very coarse grain.

The sandstone member (K_{2e1}) generally presents evidences of a secondary oxidation (remnants of reduced sandstone within the oxidized sandstone), especially at the bottom, where the coarser grained facies are located. The finer grained facies, richer in clay mineral and close to the contact with the mudstone member are still reduced (**Figure 60**) or slightly oxidized. No uranium mineralization was observed in the sandstone member or at the contact with the mudstone member in the Nuheting area. All the mineralization occurs as tabular lenses within the mudstone member (**Figure 60**) and is controlled by organic and pyrite-rich sedimentary facies deposited in swamps and floodplain ponds. These last depositional environments, similar to mountain wetland environment (Cuney and Kyser, 2008; Owen and Otton, 1995), represent reduced environments that are favourable for the preservation of organic matter and the concentration of uranium, due to their suboxic to anoxic conditions (Casagrande, 1987; Diessel, 1992; Miall, 1996). During the deposition of sediments, uranium is concentrated by adsorption of U (VI) on clay minerals (Bachmaf and Merkel, 2010; Li et al., 2013), iron oxides and hydroxides or more generally by sorption on organic material complexing uranyl ion, UO_2^{2+} (Owen and Otton, 1995). Metals are initially only loosely adsorbed to organic material but is subsequently reduced to tetravalent uranium (Nakashima et al., 1984). Wetland uranium concentration ranges in size from less than hundred kilograms (U content) to 500 tonnes and in grade from slight enrichment (a few tens of ppm) to about 30 % in uraniferous peat in Sweden (Cuney and Kyser, 2008; Otton, 1984). Therefore, when uranium-bearing water encounters wetland depositional environments uranium will be concentrated in these sediments.

8.2. Nature and evolution of the organic matter

Petrographic observations of the organic matter occurring in the host-rocks of the Nuheting deposit and globally in overbank deposits of the Erlian Formation reveal two origins: (i) terrigenous, as coaly phytoclasts occurring in large amounts and (ii) aquatic, as Tasmanacae-type algae and thrombolite-type microbial structures. According to Rock-Eval data, the organic matter is: (i) dominantly of type IV (degraded type III) inherited from land plants, (ii) thermally immature with a very low petroleum potential and (iii) devoid of free hydrocarbons. The burial of the organic matter-rich sediments belonging to the Erlian Formation has been very shallow and thermal maturation has occurred. Hence, no hydrocarbon was produced by thermal cracking within the formation. However, very locally migrated hydrocarbons along structures have been described by Zhang and Ding (1996) and Niu et al. (1995). These

hydrocarbons come from deeper oil reservoir (Zhao and Fang, 2007) and were produced from lacustrine mudstone of the early Cretaceous Tengge'er Formation. In the Nuheting deposit, identified hydrocarbons or related products due to degradation are mainly CH₄, CO₂ and H₂S (Dahlkamp, 2009). Locally, uranium mineralization associated with migrated hydrocarbons has been described (Zhang and Ding, 1996; Niu et al., 1995). However, the low permeability of the host-rocks and the absence of free hydrocarbons in the mineralized sequence that we have analyzed do not support these observations. In addition, the very low hydrogen index (HI) and the high to very high oxygen index (OI) of some samples would indicate a degradation of organic matter that could be related to bacterial activity as shown by the local occurrence of framboidal pyrite in epigeny of coaly phytoclasts. Here, organic matter degradation due to sulphate-reducing bacteria (SRB) would explain the H₂S and CO₂ anomalies (Machel, 2001) detected above the Nuheting deposit as reported by Dahlkamp (2009).

8.3. A metallogenetic model for the Nuheting deposit

The Nuheting uranium deposit experienced three main stages: related to uranium mineralization (**Figure 61**): (i) a synsedimentary stage with uranium trapping in the sediments, (ii) a diagenetic stage with uranium remobilization/recrystallization and (iii) an epigenetic stage of cementation of the uranium mineralization. First of all, the contribution of U-bearing detrital minerals appears to be minor as zircon and monazite are present in very small amounts and behave as refractory minerals, and thus will not release their uranium content. Only the Fe/Ti oxides and hydroxides are leachable but contain limited amounts of uranium (0.0 to 0.1 wt.% UO₂).

8.3.1. Synsedimentary uranium concentration

Uranium was first concentrated in wetland sediments of the upper member of the Erlian Formation. It has been largely adsorbed to clay minerals as mentioned by all authors (Li and Kuang, 2010; Niu et al., 1995; Zhang and Ding, 1996; Zhou et al., 2002) and occurred in a minor proportion as UO₂ nanocrystals in gypsum crystals.

8.3.2. Diagenetic uranium mineralization

During diagenesis, large amounts of pyrite crystallized. Two morphological types of pyrite are characterized by specific trace element signatures: (i) pyrite cement and idiomorphic pyrite enriched in selenium and (ii) frambooidal pyrite in epigeny of organic matter enriched in molybdenum. Elements such as Se, Mo, As and Ni are enriched in the host-rock and their incorporation in pyrites is characteristic of reducing conditions (Howard, 1977; Amrhein et al., 1993; Wang et al., 2011) which is in favour of uranium mineralization. Se-dominant or Mo-dominant trace element signature of pyrite respectively disseminated in the matrix or in epigeny of organic matter may depend of the redox potential (Dahlkamp, 2009). In the Nuheting deposit, synsedimentary concentration is redistributed *in situ* by desorption of uranium adsorbed on clay minerals and then, mineralized as coffinite and pitchblende replacing pyrite crystals and previously pyritized organic matter (**Figure 61**).

8.3.3. Epigenetic cementation

Finally the uranium mineralization of the Nuheting deposit was partially sealed by a late stage of cementation characterized by sulphate (celestite and barite) and carbonate crystallization (**Figure 61**). Uranium mineralization often occurs as inclusion in the cement. Therefore this epigenetic stage of cementation highlights a late fluid circulation. As no evidence of secondary oxidation and uranium minerals dissolution were observed in the cemented parts of the host-rock, the solution involved in the cementation was unlikely under oxidizing conditions.

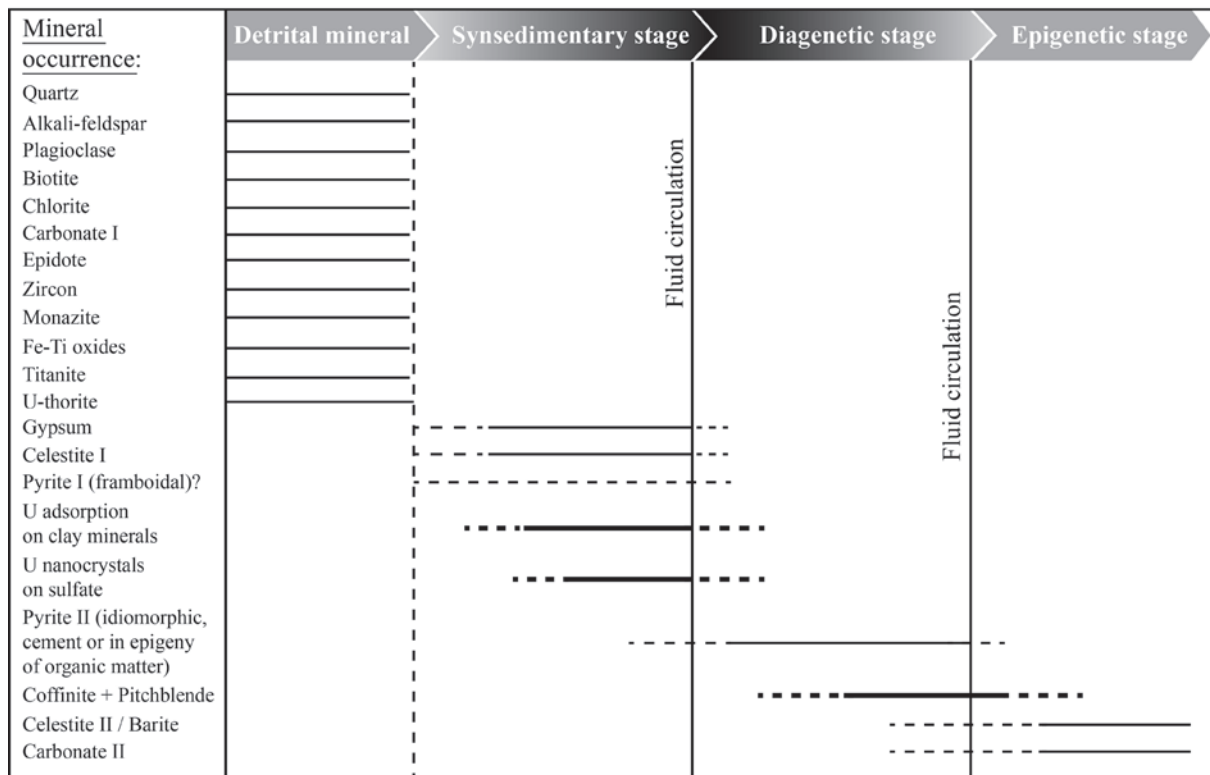


Figure 61. Mineral succession diagram of the different stages related to uranium mineralization of the Nuheting deposit.

It is now possible to summarize a metallogenetic model for the Nuheting deposit presented schematically in **figure 62**. The Nuheting deposit results from three stages of uranium deposition and remobilization: (i) a synsedimentary stage with trapping of uranium in a wetland environment during the deposition of sediments belonging to the upper member of the Erlian Formation, which most probably bring most if not all the uranium stock present in the deposit, (ii) a diagenetic stage with new formation of pyrite as cement in the matrix, as isolated crystals or in replacement of the organic matter, followed by nearly *in situ* uranium remobilization and mineralization with replacement of pyrite and (iii) a late stage of cementation sealing the mineralization and possibly responsible for minor uranium remobilization.

Isotopic U/Pb dating by TIMS of the uranium minerals from the Nuheting deposit (Niu et al., 1995; Zhang and Ding, 1996; Li and Kuang, 2010) gives three ages at 85, 41±5 and 10 Ma. These ages may respectively correspond to the synsedimentary concentration, the diagenetic uranium remobilization and the cementation stage. All previous studies propose a first stage with synsedimentary concentration. However, Niu et al. (1995), Zhang and Ding (1996) and Li and Kuang (2010) proposed an epigenetic stage of uranium mineralization associated with

migrated hydrocarbons (Niu et al., 1995; Zhang and Ding, 1996). Our data do not allow the corroboration of this hypothesis. Moreover, the permeability of the silty mudstone hosting the mineralization is extremely weak for permitting significant fluid percolation. However epigenetic fluid circulation may be responsible for a minor remobilization of the uranium mineralization during its cementation by sulfate and carbonate minerals.

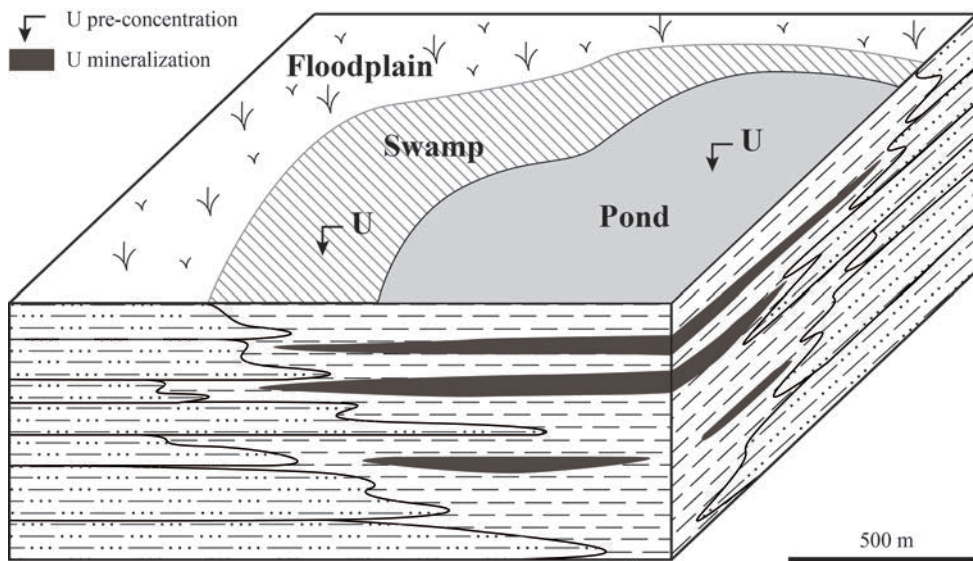


Figure 62. Schematic genetic model of the Nuheting deposit representing the synsedimentary uranium concentration during the deposition of sediments belonging to the Erlian Formation and the diagenetic uranium remobilization.

9. Conclusions

The Erlian Basin is an intracontinental basin of northeast China developed from late Jurassic to upper Cretaceous over two main tectono-sedimentary events: (i) a syn-rift stage dominated by lacustrine depositional environment and (ii) a post-rift stage dominated by fluvial and shallow lacustrine environments. Sedimentary units deposited during the post-rift stage, including Saihan and Erlian formations, present alternation of sandstone and mudstone layers. The Nuheting deposit mainly hosted in dark grey silty mudstone of the late Cretaceous Erlian Formation is a diagenetic-related uranium deposit. This deposit experienced three stages of uranium deposition and remobilization: (i) a synsedimentary stage of uranium concentration in wetland depositional environments of the upper member of the Erlian Formation which probably bring the totality of the uranium stock, (ii) a diagenetic phase of new formation of pyrite and *in situ* uranium remobilization replacing pyrite, (iii) a late stage of cementation with a minor remobilization of the uranium mineralization. The mineralized sequence of the

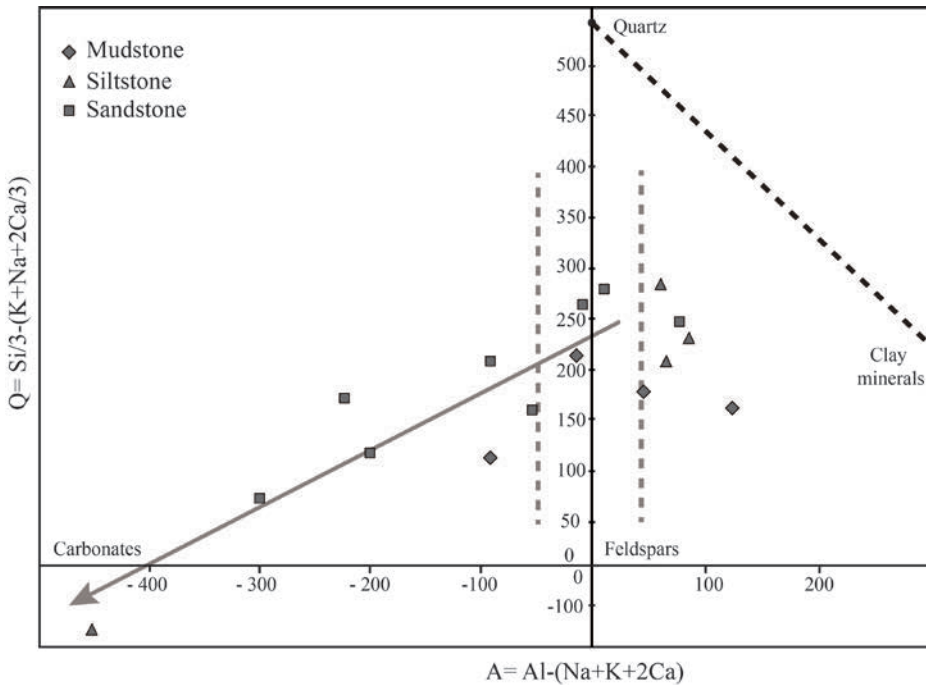
Nuheting deposit that was studied does not contain free hydrocarbons. Therefore hydrocarbons cannot be involved as a significant reducing agent for explaining the genesis of the Nuheting uranium mineralization.

Therefore, post-rift sediments of the Erlian Basin presenting a sedimentological architecture at the origin of the formation of confined permeable sandstone layers hosting roll front-type uranium deposits, may contain significant synsedimentary uranium concentration and diagenetic mineralization hosted in mudstone layers that may constitute a possible uranium source for the formation of roll front mineralization.

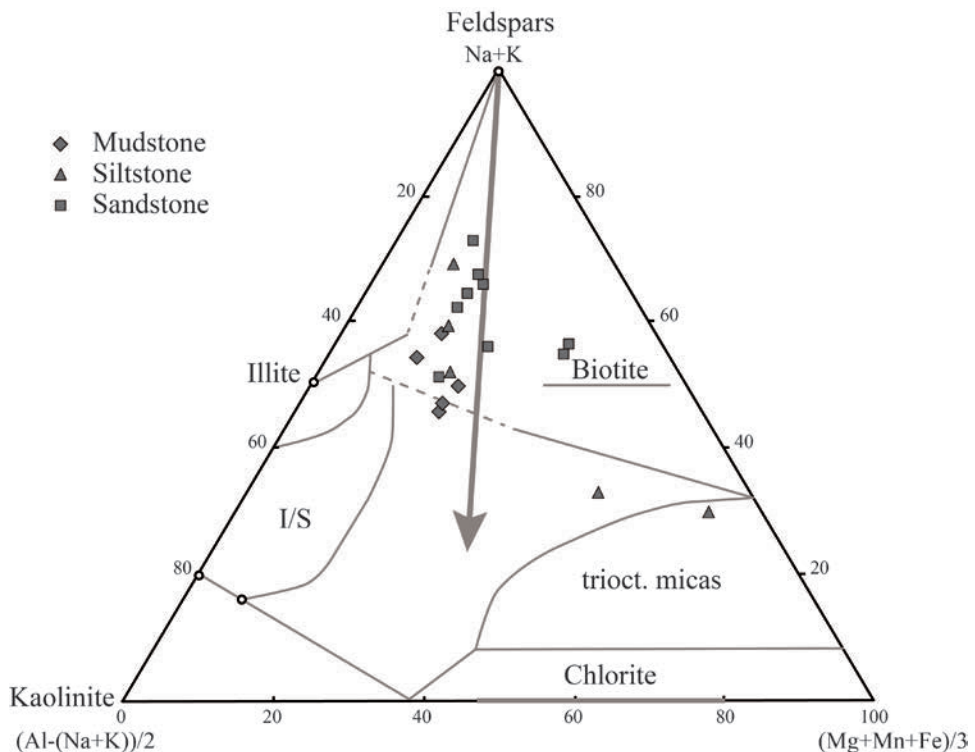
Acknowledgements

Financial support for this study was provided by AREVA Mines, the East China Institute of Technology in Fuzhou, Jiangxi and the Geological Team N°208, BOG, CNNC in Baotou, Inner Mongolia. The authors acknowledge colleagues from the East China Institute of Technology for the presentations and scientific discussions that have been organized about the geology of the Erlian Basin, and colleagues from the Geological Team N°208 for their field support and the access to drill cores. Authors also acknowledge Menhong from the Geological team N°208 for the help with translation from Chinese to English during the field trip, Li Guanglai from the East China Institute of Technology who brought to our attention several important papers on the Nuheting deposit and geologists from AREVA Mines for the discussions on uranium deposits in central Asia. Authors are indebted to Philippe Lach for the acquisition of ICPMS data, to Régine Mosser-Rück for XR analyses and to Mathieu Jouanny for his kind contribution in the realization of XR-tomography 3D imagery.

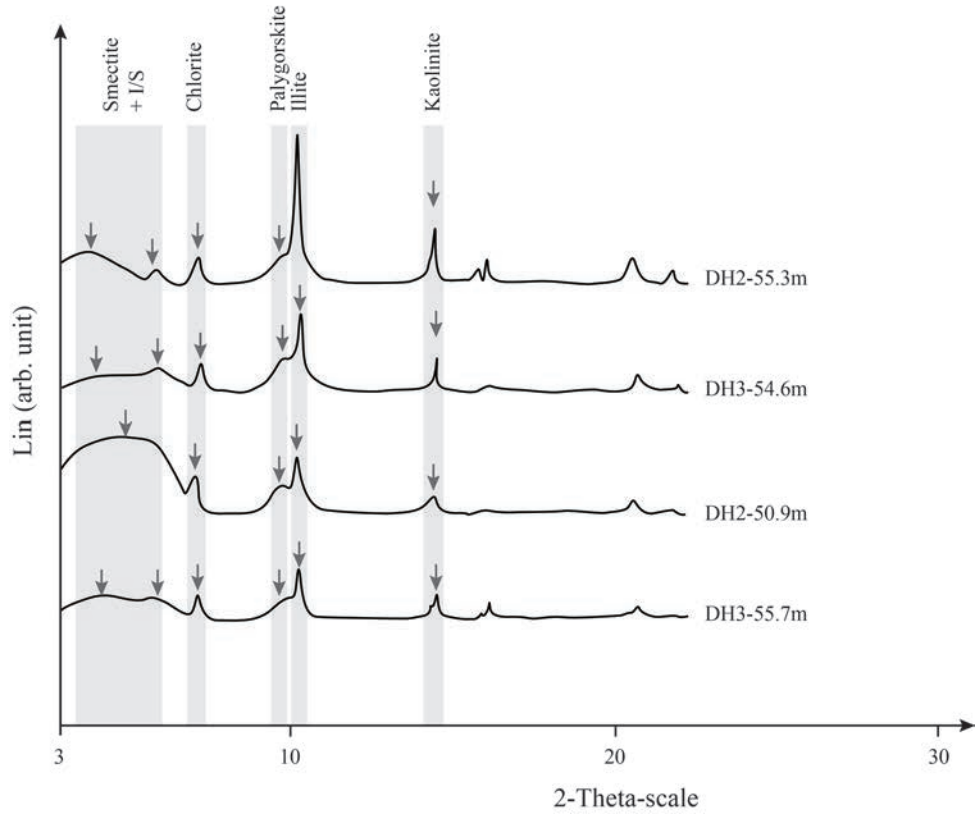
Appendix 6. Q-A diagram showing petrographic composition of sandstones, siltstones and mudstones from the Erlian Formation, in the Nuheting area. This diagram shows a carbonatation trend for part of samples from the Nuheting area.



Appendix 7. Na+K / Al-(Na+K))/2 / (Mg+Mn+Fe)/3 diagram showing the typology of clay minerals occurring in sandstones, siltstones and mudstones from the Erlian Formation, in the Nuheting area.



Appendix 8. XR spectra showing the clay minerals assemblage from the host-rock of the Nuheting deposit.



Appendix 9. Major elements whole-rock geochemical data for drill cores of the Nuheting deposit (in %).

Sample ID	SiO ₂	Al ₂ O ₃	Fe ₂ O ₃	MnO	MgO	CaO	Na ₂ O	K ₂ O	TiO ₂	P ₂ O ₅	PF	Total	Corg	Stot
DH2-48.1m	52.54	8.91	2.09	0.02	1.95	8.42	0.78	2.45	0.35	0.13	21.91	99.54	0.32	4.03
DH2-50.9m	65.06	10.73	2.70	0.02	1.64	3.43	1.41	2.79	0.48	0.10	11.33	99.69	0.63	1.26
DH2-53.2m	33.11	7.68	2.58	0.10	10.32	14.98	0.79	1.92	0.33	0.15	27.47	99.44	0.06	0.61
DH2-55.3m	58.89	13.07	4.38	0.06	3.33	2.87	1.37	3.29	0.56	0.23	12.48	100.52	0.15	1.26
DH2-57.4m	61.85	6.32	1.34	0.05	5.13	7.41	1.13	2.33	0.18	0.06	13.56	99.36	0.03	0.52
DH2-62.8m	67.42	12.83	3.76	0.03	1.80	1.05	1.76	3.46	0.49	0.13	7.44	100.14	0.07	0.80
DH2-67.2m	52.78	8.19	1.28	0.04	6.65	10.00	1.59	2.55	0.23	0.03	17.04	100.37	0.01	0.12
DH2-72.6m	60.33	11.46	3.52	0.04	3.69	4.51	1.76	3.06	0.41	0.10	11.81	100.70	0.02	0.03
DH2-80.2m	76.59	9.41	1.65	0.03	1.34	1.45	1.83	3.14	0.25	0.03	4.65	100.36	0.01	0.02
DH3-48.0m	62.13	12.65	4.59	0.04	2.35	2.01	1.30	3.40	0.51	0.18	11.89	101.04	0.13	1.66
DH3-54.6m	74.35	10.11	2.00	0.02	1.07	0.57	1.49	3.46	0.32	0.09	6.54	100.01	0.55	0.71
DH3-55.7m	67.73	11.07	3.83	0.06	1.30	0.53	1.65	3.23	0.41	0.03	10.43	100.27	0.89	1.77
DH3-56.0m	66.19	9.21	3.45	0.03	1.01	4.71	1.38	2.92	0.31	0.04	10.67	99.91	0.67	1.71
DH3-63.7m	22.15	3.17	0.90	0.12	0.62	39.38	0.57	0.97	0.11	0.03	32.01	100.01	0.06	0.12
DH3-76.4m	73.55	9.66	2.19	0.03	1.90	2.25	1.67	3.15	0.30	0.05	6.36	101.10	0.05	0.02
DH5-26.0m	19.60	2.12	1.11	0.08	6.61	23.23	0.33	0.81	0.09	0.07	25.13	79.16	0.06	8.39
DH5-26.2m	63.64	10.97	3.95	0.07	2.37	1.50	0.78	2.80	0.47	0.15	12.51	99.21	0.93	1.43

Appendix 10. RE elements whole-rock geochemical data for drill cores of the Nuheting deposit (in ppm).

Sample ID	La	Ce	Pr	Nd	Sm	Eu	Gd	Tb	Dy	Ho	Er	Tm	Yb	Lu
DH2-48.1m	15.75	34.30	3.84	15.36	3.09	0.67	2.68	0.41	2.38	0.45	1.30	0.19	1.32	0.20
DH2-50.9m	18.96	38.74	4.35	18.41	3.69	0.81	3.21	0.49	2.96	0.59	1.77	0.27	1.95	0.31
DH2-53.2m	17.46	35.85	3.75	14.93	3.00	0.62	2.61	0.39	2.34	0.45	1.31	0.19	1.35	0.21
DH2-55.3m	29.71	62.45	6.68	27.59	5.35	1.14	4.59	0.70	4.06	0.77	2.17	0.32	2.15	0.33
DH2-57.4m	9.75	19.68	2.24	9.04	1.82	0.42	1.63	0.24	1.46	0.28	0.82	1.12	0.87	0.13
DH2-62.8m	25.07	53.32	5.89	23.65	4.73	1.01	4.08	0.62	3.67	0.69	1.97	0.29	1.98	0.30
DH2-67.2m	12.50	24.03	2.91	11.81	2.36	0.53	2.02	0.31	1.88	0.36	1.06	1.64	1.12	0.17
DH2-72.6m	20.84	42.99	4.85	19.5	3.82	0.83	3.33	0.50	2.94	0.57	1.65	0.25	1.72	0.26
DH2-80.2m	12.80	25.85	2.88	11.45	2.23	0.51	1.91	0.29	1.73	0.33	1.01	0.15	10.8	0.16
DH3-48.0m	25.43	55.19	5.91	23.63	4.64	1.01	4.08	0.61	3.70	0.72	2.08	0.31	2.09	0.32
DH3-54.6m	11.13	41.02	5.75	24.90	4.82	1.18	4.77	0.68	4.23	0.89	2.62	0.37	2.44	0.39
DH3-55.7m	10.74	21.75	2.45	9.73	1.88	0.44	1.62	0.26	1.65	0.34	1.04	0.16	1.19	0.19
DH3-56.0m	14.63	27.79	3.01	11.82	2.30	0.53	1.94	0.30	1.81	0.34	1.03	0.16	1.137	0.18
DH3-63.7m	31.52	51.65	6.73	26.94	5.41	1.26	4.78	0.76	4.40	0.86	2.43	0.36	2.41	0.36
DH3-76.4m	14.97	30.23	3.473	13.52	2.70	0.58	2.24	0.34	1.94	0.38	1.11	0.16	1.16	0.18
DH5-26.0m	4.86	9.18	1.06	4.29	0.86	0.17	0.74	0.11	0.72	0.15	0.47	0.07	0.51	0.08
DH5-26.2m	19.93	41.30	4.90	19.43	3.84	0.79	3.21	0.48	2.79	0.54	1.60	0.24	1.73	0.28

Appendix 11. Trace elements whole-rock geochemical data for drill cores of the Nuheting deposit (in ppm).

Sample ID	As	Ba	Be	Bi	Cd	Co	Cr	Cs	Cu	Ga	Ge	Hf	Mo	Nb
DH2-48.1m	1.50	299.70	1.24	0.23	0.16	4.35	37.12	4.24	13.12	10.72	1.07	3.57	2.57	6.03
DH2-50.9m	40.44	417.30	1.72	0.26	3.98	14.67	45.95	4.19	49.15	12.17	1.35	6.41	404.00	7.25
DH2-53.2m	5.19	247.40	1.24	0.23	0.24	7.09	35.69	3.88	29.33	10.14	0.66	2.69	22.23	5.51
DH2-55.3m	21.91	478.60	1.99	0.45	0.62	10.70	56.24	6.42	27.21	16.94	1.38	5.02	47.42	8.47
DH2-57.4m	4.20	492.20	0.88	0.13	0.15	2.04	20.33	2.43	8.72	6.98	0.83	2.08	14.77	3.75
DH2-62.8m	7.20	462.80	1.90	0.28	0.27	7.52	50.92	6.11	15.46	16.15	1.43	4.64	5.50	8.21
DH2-67.2m	1.23	523.3	1.35	0.18	0.14	4.73	19.54	3.11	12.10	9.71	0.82	2.73	2.49	4.86
DH2-72.6m	6.73	526.2	1.84	0.35	0.15	7.25	35.83	5.32	40.40	14.32	1.49	3.88	1.40	8.16
DH2-80.2m	4.72	486.70	1.45	0.20	0.11	3.42	20.33	3.75	10.52	10.84	1.15	3.82	0.74	5.92
DH3-48.0m	11.86	490.3	1.86	0.34	0.88	10.48	49.61	6.14	19.97	16.19	1.26	4.48	96.31	8.64
DH3-54.6m	14.07	459.20	1.62	0.21	0.80	5.39	29.35	3.94	16.01	12.40	1.71	3.66	412.90	6.02
DH3-55.7m	8.73	537.60	1.68	0.24	0.24	7.26	36.83	4.68	17.79	12.67	1.40	4.04	45.22	6.86
DH3-56.0m	6.96	555.20	1.29	0.40	0.25	4.71	32.35	3.89	25.21	10.76	1.27	3.28	37.76	5.23
DH3-63.7m	2.92	284.70	0.47	0.11	<LOD	3.52	11.95	1.21	9.59	3.98	0.42	1.14	0.79	1.89
DH3-76.4m	5.47	621.90	1.36	0.16	0.11	4.50	26.62	4.00	24.97	11.15	1.25	3.36	1.58	6.07
DH5-26.0m	8.20	481.70	<LOD	<LOD	0.13	1.15	7.77	0.90	4.01	2.47	0.29	1.31	10.48	1.61
DH5-26.2m	26.98	512.60	1.65	0.32	0.72	9.43	48.2	6.26	35.05	13.95	1.41	5.17	38.00	8.20

Appendix 12 Trace elements whole-rock geochemical data for drill cores of the Nuheting deposit (in ppm).

Sample ID	Ni	Pb	Rb	Sb	Sn	Sr	Th	U	V	W	Y	Zn	Zr
DH2-48.1m	13.09	13.89	94.82	0.61	1.66	880.5	6.21	18.80	42.93	0.99	13.46	46.73	144.40
DH2-50.9m	33.65	89.82	94.78	2.17	2.97	2696.00	6.73	2247.00	50.22	1.81	19.56	127.80	227.40
DH2-53.2m	19.27	13.08	69.67	0.94	1.63	711.80	6.20	105.5	44.37	1.00	13.69	51.49	110.10
DH2-55.3m	32.83	40.56	117.90	1.40	2.29	2436.00	10.01	156.10	67.84	1.66	25.01	68.75	177.40
DH2-57.4m	7.11	13.01	83.65	0.31	1.65	4015.00	3.62	50.69	25.57	0.60	9.41	16.98	81.48
DH2-62.8m	20.70	19.84	118.40	1.03	2.64	221.50	9.14	90.09	76.92	1.58	21.04	60.19	185.90
DH2-67.2m	10.96	23.05	99.51	0.33	1.54	242.80	5.20	8.31	37.44	0.72	11.29	26.33	108.10
DH2-72.6m	17.76	20.30	118.90	1.12	6.80	245.90	9.19	3.12	83.69	1.45	17.85	49.97	157.6
DH2-80.2m	9.38	20.35	123.10	0.55	1.44	189.60	6.70	1.71	39.60	0.84	10.12	33.24	158.90
DH3-48.0m	26.83	53.52	117.50	1.49	2.82	3200.00	9.45	402.20	65.64	1.46	23.68	60.08	177.20
DH3-54.6m	14.45	37.32	122.00	1.21	1.61	167.70	5.93	3457.00	34.37	1.07	38.04	55.63	171.4
DH3-55.7m	17.67	21.00	116.20	1.00	1.76	2338.00	7.00	21.84	48.06	1.21	10.60	39.00	163.50
DH3-56.0m	14.92	21.87	108.20	0.52	1.74	25.92	5.89	88.50	38.69	0.90	10.63	28.81	132.10
DH3-63.7m	8.24	7.88	36.76	0.26	1.96	226.10	3.17	32.84	17.16	0.32	24.57	<LOD	48.15
DH3-76.4m	11.70	17071	117.90	0.80	4.07	184.10	7.08	1.99	49.57	0.98	11.48	30.56	134.40
DH5-26.0m	4.69	7.80	28.88	0.36	0.84	10970.00	1.56	93.71	10.81	0.31	5.43	<LOD	55.94
DH5-26.2m	23.68	26.16	117.00	1.77	3.27	194.80	8.95	54.07	83.11	1.37	15.99	67.15	213.60

CHAPITRE 7:

LES MINERALISATIONS DE TYPE ROLL FRONT DANS LE BASSIN D'ERLIAN



Article 4: The multiple roles of sulphate-reducing bacteria and Fe-Ti oxides in the genesis of the Bayinwula roll front-type uranium deposit, Erlian Basin, NE China.

Christophe Bonnetti^a, Michel Cuney^a, Raymond Michels^a, Laurent Truche^a, Fabrice Malartre^a,
Xiaodong Liu^b, Jianxing Yang^c

^aUniversité de Lorraine, GéoRessources-CNRS-CREGU, BP239, F54506 Vandoeuvre-lès-Nancy, France

^bEast China Institute of technology, 56 Xuefu Road , Linchan, 344000 Fuzhou, Jiangxi, China

^cGeological Team No.208, BOG, CNNC, Baotou, Inner Mongolia, China

Paper to be submitted in Chemical Geology

1. Abstract

The Bayinwula roll front-type uranium deposit is hosted in sandstones of the Saihan Formation deposited during the post-rift stage of the Erlian Basin. The present study aims to characterize: (i) the roles of sulphate reducing bacteria and (ii) the roles of Fe-Ti oxides in the genesis of the Bayinwula deposit. Drill cores of the host-sandstone have been investigated with emphasis on petrographical observations, whole rock geochemistry and geochemical/mineralogical study of Fe-Ti oxides, iron disulphide, uranium minerals (EMP, LA-ICPMS), organic matter (Rock-Eval pyrolysis, GC-MS). $\delta^{34}\text{S}$ has been measured in situ by SIMS on the different generation of iron disulphides.

Within sandstones, pre-ore uranium enrichment was identified on altered Fe-Ti oxides (38.5 % of the whole-rock U content) and constitutes a major source of uranium for the mineralization. Rock-Eval and GC-MS data indicate that organic matter occurring in the host-sandstone is mainly inherited from land plants and corresponds to kerogens of type IV. No migrated hydrocarbons were identified. Framboidal and collomorph ore-stage iron disulphides have moderate to high concentration of As, Ni and Co and have a light sulphur isotope signature characterized by $\delta^{34}\text{S}$ values from -30.54 to -7.47‰, suggesting that sulphur originated from bacterial sulphate reduction (BSR). A late generation of pyrite is characterized by BSR was responsible for (i) the liberation of U from the Fe-Ti oxides, (ii) the generation of ore-stage iron disulphide, (iii) the production of a secondary H₂S-rich reducing barrier involved in the reduction of U(VI) and the precipitation of U(IV). Uranyl and sulphate ions were carried out through the host sandstone by low temperature oxygenated groundwater at pH ranging from 6.35 to 8.48 conditions favourable for uranium transportation dominantly as UO₂(HPO₄)₂²⁻ complexes. At the redox front, U(IV) was precipitated as P-rich coffinite and ningyoite dominantly as epigeny of ore-stage iron disulphide which have partly to totally replaced organic matter and Fe-Ti oxides. Therefore the mineralogical, geochemical and isotopic characteristics of the Bayinwula roll front uranium deposit support a biogenic model.

Keywords: Erlian Basin; Bayinwula uranium deposit; roll front; sulphate-reducing bacteria; Fe-Ti oxide.

2. Introduction

Central Asia represents one of the largest uraniferous provinces in the world, with uranium ore deposits located from the Transbaikal area in Russia, in southern Kazakhstan, in Uzbekistan, in Mongolia and in northern China. In comparison with other world class provinces (Canada, Australia and Africa), which are associated with Archaean to Paleoproterozoic basements, the present study area provides an opportunity to investigate genetic conditions of uranium deposits generated within a very young uraniferous province. Most the deposits discovered in this province are of sandstone-hosted tabular or roll-front type (Dahlkamp, 2009; OECD-NEA/IAEA, 2010) which currently represents one of the most economic uranium resources with respect to using in situ recovery (ISR) for their extraction. In northern China a large amounts of sandstone-hosted uranium deposits have been discovered in Mesozoic sedimentary basins. From West to East, uranium deposits are hosted in the Yilli Basin (e.g., the Wuyier, Wuyiyi, Wuyisan and Shihongtan deposits, Min et al., 2005a; 2005b), in the Ordos Basin (e.g., the Dongsheng deposit, Cai et al., 2007a; 2007b), in the Erlian Basin (e.g., the Saihangaoi and Bayinwula deposits, Bo and Kuan, 2006; Nie et al., 2007; Fan et al., 2008; Zhang et al., 2008; 2010) and in the Kailu Basin (Cai and Li, 2008). The uranium mineralization of sandstone-hosted deposits has generally been attributed to U (VI) reduction by sulphides and organic matter under low temperature conditions (e.g., Rackley, 1972; Reynolds and Goldhaber, 1982). For uranium deposits of the Yilli and Ordos basins, authors proposed biogenic mechanisms involved in both sulphate reduction and uranium mineralization (Min et al., 2005a; 2005b; Cai et al., 2007a; 2007b), with the contribution of sulphate-reducing bacteria (SRB). The previous works realized on uranium deposits from the South Texas district (e.g., Goldhaber et al., 1978; Reynolds et al., 1982; Reynolds and Golhaber, 1983) have shown the critical role of understanding the genesis of iron disulphides for the formation of the uranium mineralization. Biogenic and nonbiogenic processes of uranium ore formation were identified (Reynolds et al., 1982).

In fact, most of proposed genetic models for roll front deposits emphasize the role of bacterial metabolic processes in the genesis of ore-stage iron disulphides (Jensen, 1958; Lizitsyn and Kuznetsova, 1967; Belyi et al., 1972; Rackley, 1972). Several reactants are needed for bacterial sulphate reduction (BSR; Machel, 2001): sulphate (SO_4^{2-}), reactive organic matter and iron (Fe^{2+}). Sulphate is argued to originate from preore-stage pyrite oxidation and carried with oxidized groundwater flowing downdip into reduced sandstone. Then, it is partially to totally reduced by heterotrophic SRB using local organic matter as a substrate. The source of

iron likely corresponds to detrital Fe-Ti oxides (Reynolds and Goldhaber, 1978) or other Fe-rich detrital minerals of the host sandstone. Moreover, BSR is known to produce a large amount of CO₂ and dissolved reduced sulphur species (H₂S, HS⁻; Machel, 2001) that may create a strong reducing barrier for precipitating uranium (Lizitsyn and Kuznetsova, 1967; Hua et al., 2006). The produced dissolved sulphides are strongly enriched in ³²S (i.e., isotopically light) compared to the initial sulphate ions (Thode et al., 1951). Consequently, pyrite precipitating from these sulphides will be enriched in ³²S. Therefore, strongly negative δ³⁴S values associated with sandstone-hosted uranium deposits has been taken as one line of evidence for results from BSR (Jensen, 19518; Belyi et al., 1972).

The purpose of this paper is to evidence the multiple roles of SRB in the genesis of the uranium mineralization within the Bayinwula roll front deposit located in the Erlian Basin. In this paper, mineralogical and geochemical relations between U-rich Fe-Ti oxides, detrital organic matter and ore-stage iron disulphides occurring in the early Cretaceous Saihan Formation sandstones, hosting the uranium mineralization, are presented. Several approaches were employed to determine the metallogenetic model of the Bayinwula deposit. The study focused on (i) petrography and geochemistry of the host sandstone, (ii) Fe-Ti oxides mineralogical/chemical data and (iii) ore-stage iron disulphide petrography coupled with in situ determination of sulphur isotopic composition by SIMS and trace element signature analyzed by LA-ICPMS and (iv) uranium ore mineral distribution and composition by SEM and EMP.

3. Geological setting

3.1. The Erlian Basin

The Erlian Basin (or Eren Basin) is located in northeast China (**Figure 63**), Inner Mongolia, close to the border between China and Mongolia. It is an intracontinental basin formed during the Mesozoic continental extension of eastern Asia (Ren et al., 2002; Charles et al., 2013) and covering an area of approximately 130 000 km² (Dou and Chang, 2003; Wei et al., 2005).

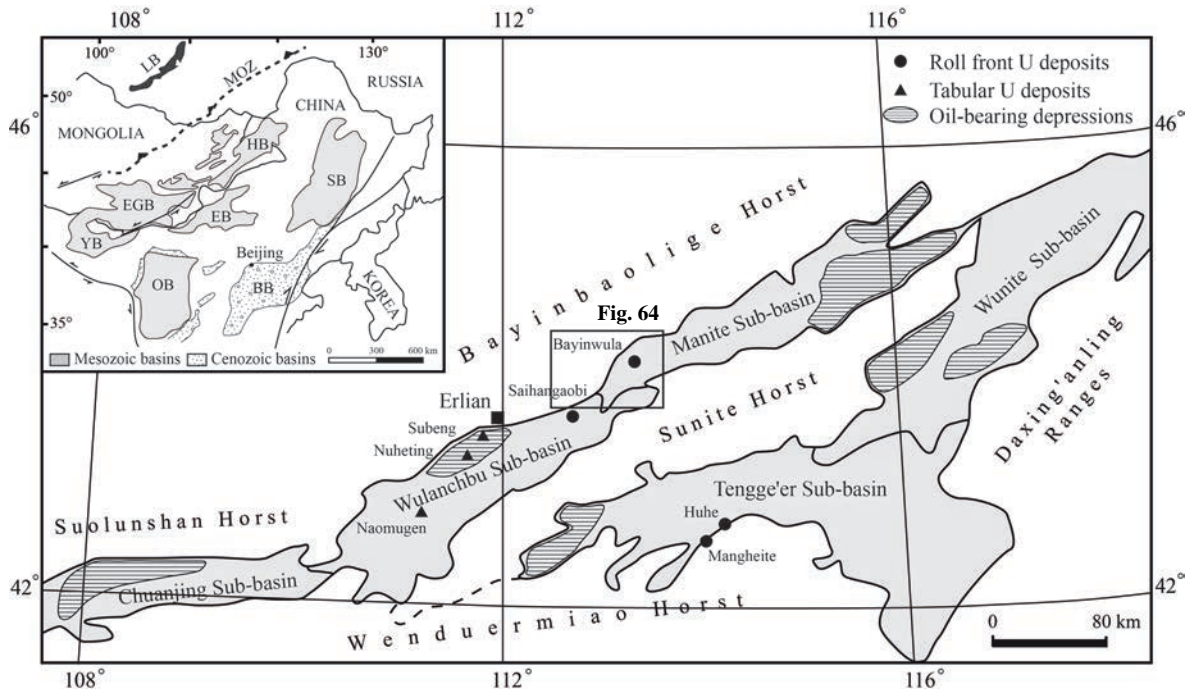


Figure 63. Structural map of the Erlian Basin showing the distribution of different types of uranium deposits and oil-bearing depressions (modified after CNNC, unpublished data; Dou et al., 1998; Meng, 2003; Wei et al., 2005; Dahlkamp, 2009; Bonnelli et al., accepted). U= uranium, BB= Bohai Basin, EB= Erlian Basin, EGB= East Gobi Basin, HB= Hailar Basin, OB= Ordos Basin, SB= Songliao Basin, YB= Ying Basin, LB= Baikal Lake, MOZ= Mongol-Okhotsk Zone.

It is composed of five major sub-basins as following (**Figure 63**): the Chuanjing Sub-basin to the West, the Wulanchabu Sub-basin in the central-west part, the Manite Sub-basin in the central-north, the Tengge'er Sub-basin in the southeastern part and the Wunite Subbasin to the northeast (Dou et al., 1998; Dou and Chang, 2003; Wei et al., 2005). These sub-basins are framed by a series of horsts or ranges oriented ENE-WSW: the Daxing'anling Ranges to the East, the Bayinbaolige Horst to the North and the Suolunchan Horst more to the West, and finally the Wendurmiao Horst to the South. The Sunite Horst occupies the central part of the Erlian Basin and divides it in two different main parts (Dou et al., 1998; Wei et al., 2005), north and south.

The Erlian Basin lies on a folded and metamorphised basement corresponding to the southern margin of the Hercynian Xing'an or Xing Meng Mongolian Orogenic Belt (Dou and Chang, 2003). This basement is mainly composed of both Paleozoic and early Mesozoic intermediate to felsic granitic plutons (Wu et al., 2005a, 2005b, 2005c), mafic to felsic volcanic rocks (Chen and Chen, 1997; Ying et al., 2010) and Paleozoic sedimentary or metasedimentary units (Wu et al., 2005b; Zhou et al., 2010). Part of granitic and volcanic rocks mentioned above may have represented primary uranium source for the basin-hosted uranium

mineralization as some biotite-granites show an average of 4-13 ppm uranium and a Th/U ratio of 5.6-11.1 (Dahlkamp, 2009). This basin is divided into about 52 half-graben-shaped depressions (Dou and Chang, 2003; Meng et al., 2003) controlled by a normal-fault system and developed during three main tectonic-stratigraphic stages: (i) a pre-rift stage mainly characterized by the emission of late Jurassic to very early Cretaceous volcanic rocks of the Qinganling Group (156.0 – 142.6 Ma; Cheng and Cheng, 1997; Graham et al., 2001; Wang et al., 2006), which corresponds to the initiation of the rifting; (ii) a syn-rift stage characterized by the deposition of early Cretaceous sedimentary units (Gou et al., 1986; Cai et al., 1990; Sha, 2007): the Arshan Formation (K_{1ba}) dominated by alluvial, fluvial and shallow lacustrine environments and the Tengge'er Formation (K_{1bt}) dominated by deep to semi-deep lacustrine environment; and (iii) a post-rift stage characterized by a switch from tectonic to thermal subsidence and the deposition of the early Cretaceous Saihan Formation (K_{1bs}) and the late Cretaceous Erlian Formation (K_{2e}), both dominated by fluvial and shallow lacustrine environments (Currie and Eberth, 1993; Lin et al., 2001; Van Itterbeeck et al., 2005, 2007; Bonnetti et al., accepted).

3.2. *The Bayinwula deposit*

The Bayinwula deposit is located in the western part of the Manite Sub-basin (**Figure 63**), about 100 km to the East of Erlian city and 20 km to the North-West of Sunite city.

This deposit is of roll front-type (**Figure 64**) and hosted in sandstone layers of the early Cretaceous Saihan Formation (Nie et al., 2007; Fan et al., 2008), situated in an interval between 100 m and 160 m of depth. The uranium mineralization is low grade and presents a mean at 100-300 ppm U. The Bayinwula roll front deposit occurs in the central part of the basin and developed from NW to SE. It is composed of three main ore bodies (Nie, 2008) which extend over seven kilometres along the redox front and a few hundred of metres wide. The uranium mineralization is hosted in medium to coarse-grained sandstone, rarely fine-grained, and mainly occurs as coffinite associated with pyrite and organic matter.

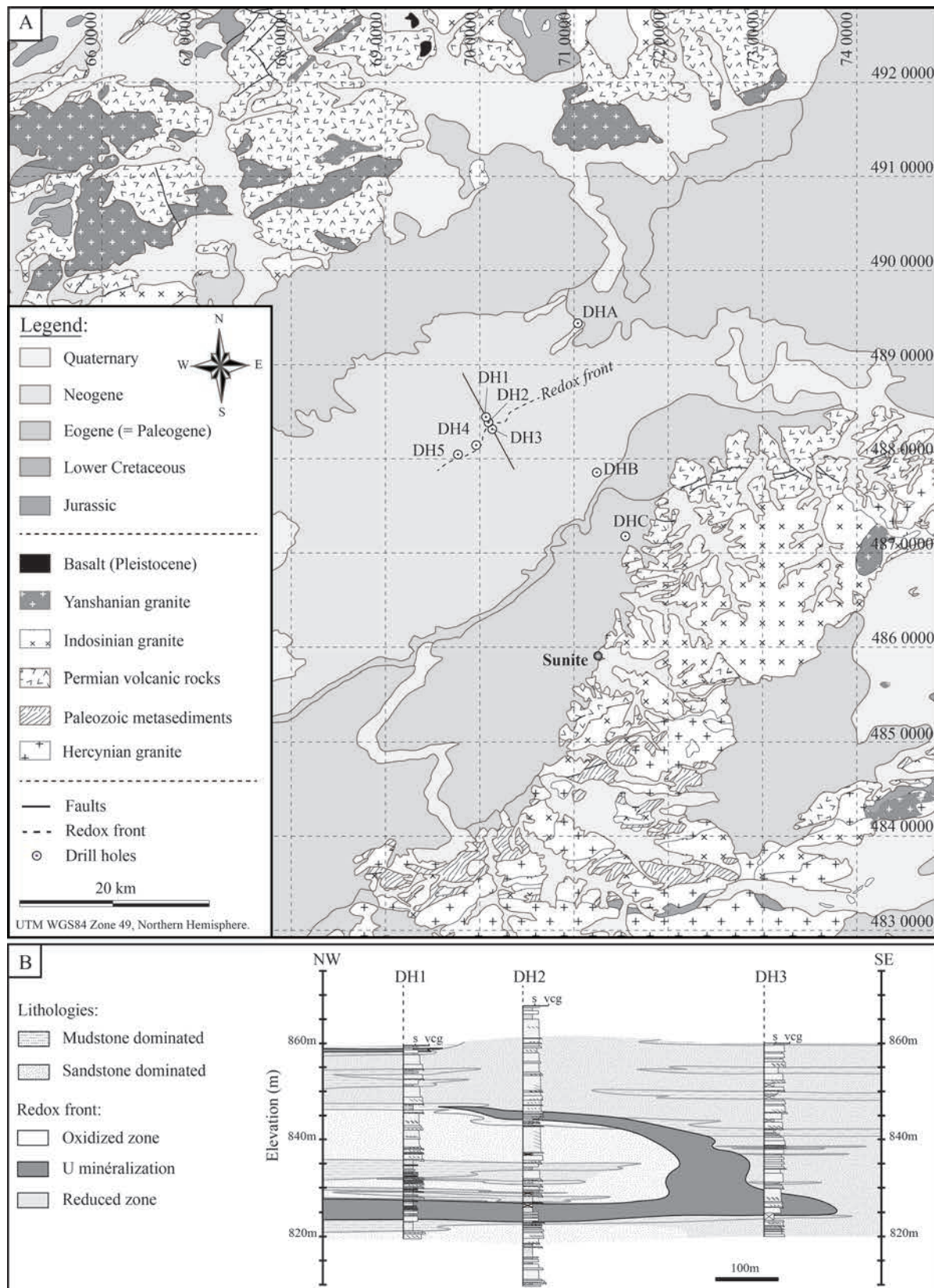


Figure 64. A= geological map of the western part of the Manite Sub-basin, Erlian Basin (after CNNC, unpublished data). This map shows the location of studied drill-holes (DH) and the position of the cross-section presented in figure 86B, from DH1 to DH3. B= drill-hole cross-section of the Bayinwula deposit. S=silt; vcg=very coarse grained sand.

4. Materials and methods

A total of eight drill holes (**Figure 64**), including three regional stratigraphic drill holes (DHA to DHC) and five drill holes through the Bayinwula deposit, were logged and sampled. Stratigraphic drill holes were used as a reference to determine the petrographic, mineralogical and geochemical characteristics of the host sandstone before the roll front formation, mainly regarding the uranium geochemical background, the chemical composition and the typology of organic matter and pyrites. Drill holes through the Bayinwula deposit, especially DH1 to DH3 used to draw a NW-SE cross-section, were examined in order to characterize the mineralogical reactions particularly involved in the formation of the ore body. Sixty-three drill-core samples were used for the geochemical/mineralogical study. Whole-rock geochemical analyses were realized at the SARM-CRPG in Nancy, France. The mineralogical study was carried out in the GeoRessources laboratory (France) using optical microscope (reflected light and fluorescence) and at the microanalytical facility of the Lorraine University (SCMEM, Nancy, France) using: (i) a JEOL J7600F scanning electron microscope (SEM) and (ii) a CAMECA SX100 electron microprobe (EMP). Mineralogical characterization of Fe-Ti oxides was realized at the GeoRessources laboratory by Raman spectroscopy using a LabRAM HR (Horiba Jobin Yvon) spectrometer equipped with a 600 gr.mm⁻¹ grating and an Edge filter. The excitation beam is provided by a Stabilite 2017 Ar⁺ laser (Spectra Physics, Newport Corporation) at 457.9 nm and a power of 200 mW, focused in the capillary using a ×50 objective (Olympus). Acquisition time is optimized to have the spectrum maximum intensity between 1/3rd and 2/3rd of the CCD saturation level (i.e. 20,000-40,000 counts). The spectra are accumulated 10 times. The resulting signal-to-noise ratio (S/N) is by far lower than 1 %. Clay minerals determination was realized at the LIEC laboratory (Nancy, France) by X-ray diffraction using a D8 Bruker diffractometer. The clay mineral fraction (<2μm) was extracted from samples by application of the Stoke's law and deposited on thin sections which were further analysed according to three different ways: (i) oriented clay mineral fraction, (ii) ethylene glycol saturated and (iii) heated at 550°C during 4 hours. Each diffractogram was measured in the 2-Theta domain. Organic matter typology and maturity were determined by Rock-Eval VI pyrolysis (REP) at Weatherford Laboratories (Texas, USA). Trace element concentrations in pyrite (Zhao et al., 2011) have been measured on three samples using a laser ablation inductively coupled plasma mass spectrometry (LA-ICPMS) at the GeoRessources laboratory of Nancy. Laser sampling was performed with a 193 nm GeoLas Pro ArF Excimer laser (Microlas®, Göttingen, Germany) equipped with beam homogenisation optics. Ablation

was performed by focussing the beam at the sample surface with a constant fluence of 10 J.cm⁻² and constant repetition rate of 5 Hz. Helium was used as a carrier gas to transport the laser-generated aerosols from the ablation cell to the ICP-MS. Argon as a make-up gas was mixed with the carrier gas via a T-connector before entering the ICP torch. Typical flow rates of 0.5 l min⁻¹ for He and 0.96 l min⁻¹ for Ar were used (Lach et al., 2013). For each experiment, either a 10 or 16 μm spot size has been used and 8 trace elements (As, Ni, Co, Zn, Cu, Mo, Se, V) were analyzed. Regarding to the small spot size, the relative error on concentrations are about 30%. All data were acquired as raw counts (cps) using the time resolved mode. For each individual analysis (external standard and samples), the background was measured before ablation during 20 s and its return to initial value was checked before ablating a new zone. Signal intensity integration of trace element masses was realized during the plateau regime. Signal acquisition of sample was stopped after 150 pulses (10 to 30 s at 5 Hz) and recorded during 80 s (including 20 s of background acquisition and 10 to 30 s of ablation). The sulphide external standard Mass-1 (called PS-1 in Wilson et al., 2002) was used as reference material and pyrite Fe content analyzed by EMP as internal standard. Then data processing was realized using the LASP software (Leisen, 2011) in order to convert raw counts for every measured trace element into concentration (in ppm). Finally, the same three same samples of the host sandstone were investigated for *in situ* analysis of sulphur isotopes on pyrite by SIMS using CAMECA IMS 1270 microprobe at the CRPG, Nancy. The data were integrated as ³²S/³⁴S ratio ($\delta^{34}\text{S}$ in ‰) and normalized to the troilite phase of the Canyon Diablo V-CDT meteorite (Ding et al., 1999). The spot size was about 25 μm of diameter.

5. Sedimentology of the Saihan Formation

The Saihan Formation is part of the post-rift sediments deposited in the Erlian Basin. The Bayinwula deposit is hosted in permeable sandstone layers of the upper member of this formation (**Figure 65**).

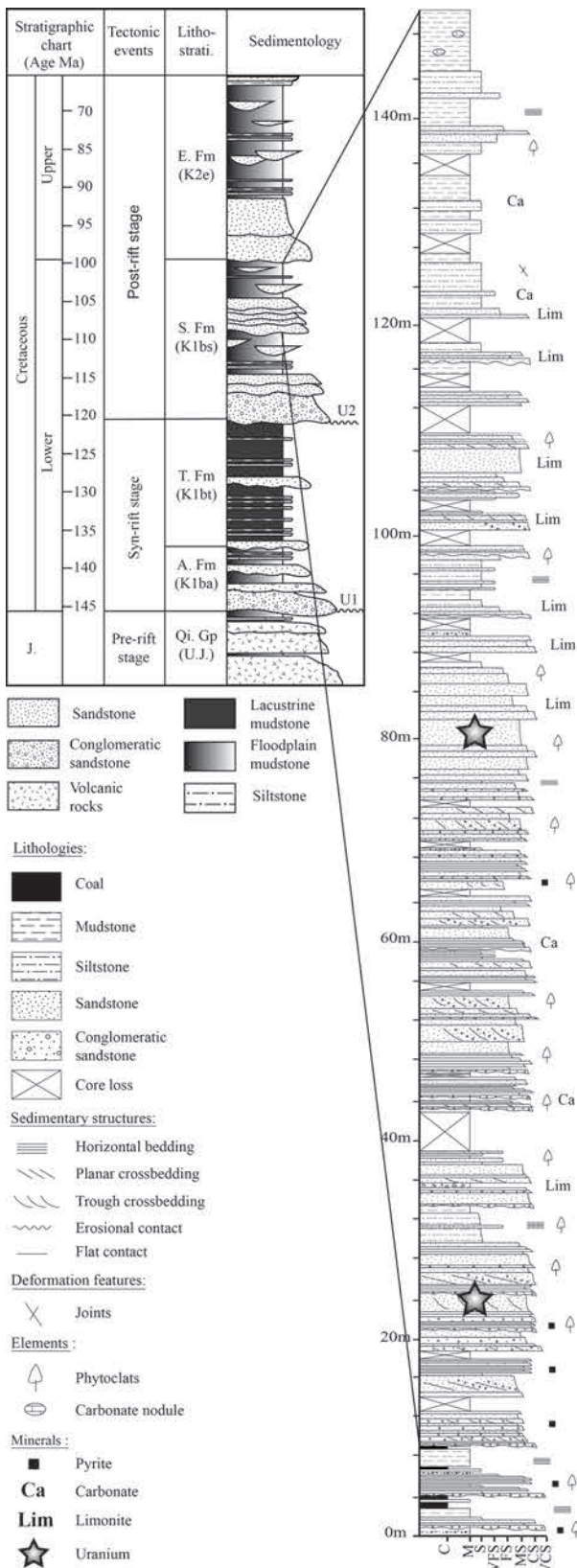


Figure 65. Sedimentological log of the upper member of the Saihan Formation with the location of roll front-type uranium mineralization. This detailed log is located on the inserted global tectonic-stratigraphic log of the Erlian Basin (modified after Gou et al., 1986; Cai et al., 1990; Dou et al., 1998; Graham et al., 2001; Lin et al., 2001; Meng, 2003; ICS, 2006; Sha, 2007). C= coal; M= mud; S= silt; VFS= very fine sand; FS= fine sand; MS= medium sand; CS= coarse sand; VCS= very coarse sand.

Based on stratigraphic and sedimentological study realized by Bo and Kuan (2006), Nie et al. (2007), Fan et al. (2008), Zhang et al. (2010) and field observations made on the stratigraphic drill holes, the sediments of the upper member of the Saihan Formation represent a braided river system alternating with sandstone dominated and overbank dominated depositional environments. The boundary between the lower and upper members of the Saihan Formation is marked by coal seams occurring at the top of the lower member. Sedimentary facies formed in braided channels correspond to a lithofacies combination of gravel and very coarse to fine-grained sand showing fining-upward trends. Gravels are more or less stratified, sometimes pebbly and correspond to minor channel fills. They occur as 10 cm – 1 m thick layers located at the bottom of channels. These sediments are clast-supported and mainly composed of lithoclasts, sub-angular to sub-rounded quartz and feldspar grains. Sandstones are poorly sorted and very coarse to fine-grained, clast-supported and composed of sub-angular to sub-rounded quartz and feldspar grains. Sandstone units comprise 10 cm to 5 m thick layers displaying either trough or planar crossbeds. Overbank sedimentary facies are represented by a combination of floodplain fines and crevasse splays. Floodplain fines correspond to deposits of overbank sheet flows, floodplain ponds and swamps. They form more or less continuous sheet-like layers that can extend laterally for several km, with thicknesses of tens of meters (Miall, 2010). Floodplain fines are mainly composed of very fine-grained sand, silt and mud often occurring with poorly sorted floating gravels or coarse quartz grains. Crevasse splays occur as lenses from 10 cm to 5 m thick probably extending laterally for several kilometers (Miall, 2010), and correspond to delta-like progradation from a crevasse channel into the floodplain. Deposits are characterized by massive layers of sand, silt and mud frequently associated with floating gravels and coarse quartz grains. This facies architecture is at the origin of the confined permeable sandstone layers hosting the uranium mineralization (Bonnetti et al., accepted).

6. Pre-ore uranium concentration

6.1. Uranium content of the host sandstone

Whole-rock geochemical data from drill-core samples of the Bayinwula area were classified into different categories according to the position of the samples compared to the location of the mineralization: (i) reduced sandstone, (ii) oxidized sandstone, and (iii) mineralized sandstone. In order to characterize the pre-ore uranium content within the primary reduced sandstone, only non-mineralized samples were used in the calculation. Moreover, the average

uranium content was calculated on 23 samples by using whole-rock geochemical data from both reduced sandstone surrounding the roll front and reduced sandstone collected in stratigraphic drill holes which are located more than 10 km away from the deposit. Uranium geochemical background in the reduced sandstone is ranging from 2.44 to 70.31 ppm (**Appendix 15, Appendix 16**) with a standard deviation of 18.58 ppm and with a mean value of 30.36 ppm. In oxidized sandstone, uranium contents calculated of 16 samples range from 1.97 to 14.80 ppm with a standard deviation of 4.20 ppm and a mean value of 6.79 ppm. Therefore, there is a difference of more than 20 ppm between the uranium content in reduced and oxidized sandstone, indicating a significant uranium leaching by oxidizing groundwater.

6.2. Sandstone petrography and U-bearing minerals

The host sandstone of the Bayinwula deposit is globally of arenite sand to sandstone composition and is mainly grain-supported, except for very fine-grained sandstone which can be slightly matrix-supported (**Appendix 13, Appendix 14, Appendix 17, Appendix 18**). Sandstones from stratigraphic drill holes, especially reduced sandstones, are richer in clay minerals compared to sandstones from the Bayinwula deposit and thus less permeable. In the Bayinwula deposit, oxidized sandstone tends to be richer in clay minerals than the reduced sandstone. Sandstones do not show evidence of carbonatation. They are composed of (i) rock fragments (granitic and volcanic composition) and (ii) individual detrital minerals such as quartz, K-feldspar, plagioclase, biotite and chlorite. Sandstones are fined to very coarse grained, poorly sorted, and show sub-angular to sub-rounded grains. Feldspars are frequently altered. Clay minerals assemblage is smectite-illite-kaolinite for oxidized samples and smectite-illite±kaolinite for reduced samples (**Appendix 18, Appendix 19**). Detrital accessory minerals are epidote, zircon, monazite, Fe-Ti oxide (mainly ilmenite and minor rutile occurrences) and some titanite and apatite. Among U-bearing detrital minerals the most represented ones in the host sandstone are monazite (**Figure 66A**), zircon (**Figure 66B**) and Fe-Ti oxide (**Figure 66C, D**).

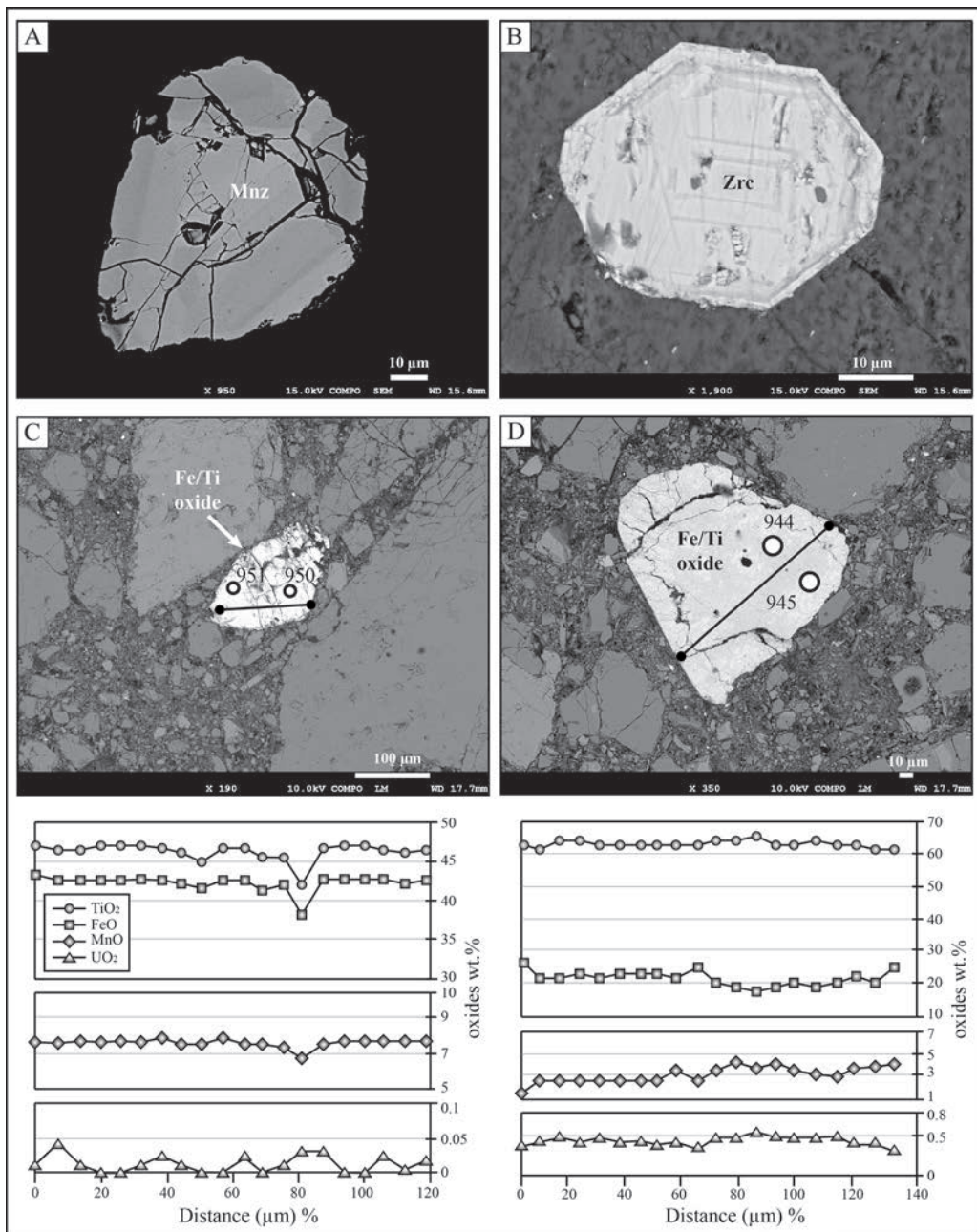


Figure 66. U-bearing minerals occurring in the host sandstone. A= monazite (Mnz); B= zircon Zrc); C= weakly altered Fe-Ti oxide in the reduced sandstone with EMP analysis profile below; D= strongly altered Fe-Ti oxide in the reduced sandstone with EMP analysis profile below. Black circles in C and D correspond to Raman analyses spots.

Uranium content is ranging from 0.0 to 0.5 wt.% UO₂ in monazite and from 0.0 to 0.1 wt.% UO₂ in zircon. However monazite as well as zircon does not show any evidence of alteration (**Figure 66A, B**) in both reduced and oxidized zones. Therefore their uranium content appears to be refractory to oxidizing groundwater leaching. Fe-Ti oxides are major dominant U-bearing minerals and are concentrated in the heavy mineral-rich layers of the host-sandstone. In the reduced part of the sandstone Fe-Ti oxides are generally already strongly altered. Raman spectra of the less altered grains match with an ilmenite composition (**Figure 66C, Appendix 20**). These grains have low uranium content, a few hundreds of ppm when detected (**Figure 66C; Table 18**: DH3-118.0m 4/4). Raman spectra of the most altered grains indicate that they are constituted of an intimate mixture of hematite and anatase micrograins (**Figure 66D, Appendix 21**). The characteristic alteration of these Fe-Ti oxides is also evidenced by a strong depletion of their Fe content (**Figure 67**) compared to ilmenite stoichiometric composition (i.e., 46.65 wt.% FeO; Deer et al., 1962). Strongly altered grains show high uranium concentration ranging from 0.08 to 0.52 wt.% (**Figure 66D, Figure 67B; Table 18**: DHB-64.2m 2/1, 3/1; DH2-111.8m 1/12, 1/13, 1/17; DH3-118.0m 8/7, 9/8). In the oxidized zone of the host-sandstone, Fe-Ti oxides are much less abundant than in the reduced zone. They are weakly to strongly altered by oxygenated groundwater and tend to be hematized. Altered grains show an extremely low uranium content (**Table 18**: DH2-128.0m 2/2) indicating that a significant part of this uranium concentration has been leached out. Rare and relatively preserved grains may still show similar U content as Fe-Ti oxides observed in the reduced zone (Table 1: DH2-128.0m 2/1). In the opposite, Fe-Ti oxides grains observed in the host-sandstone downdip of the roll front, corresponding to the pyritized zone (e.g., Devoto, 1978), present a second alteration corresponding to their replacement by iron disulphide. These grains show very high uranium concentration, about a few wt.% UO₂ (**Table 18**: DH5-114.0m 1/1, 2/2).

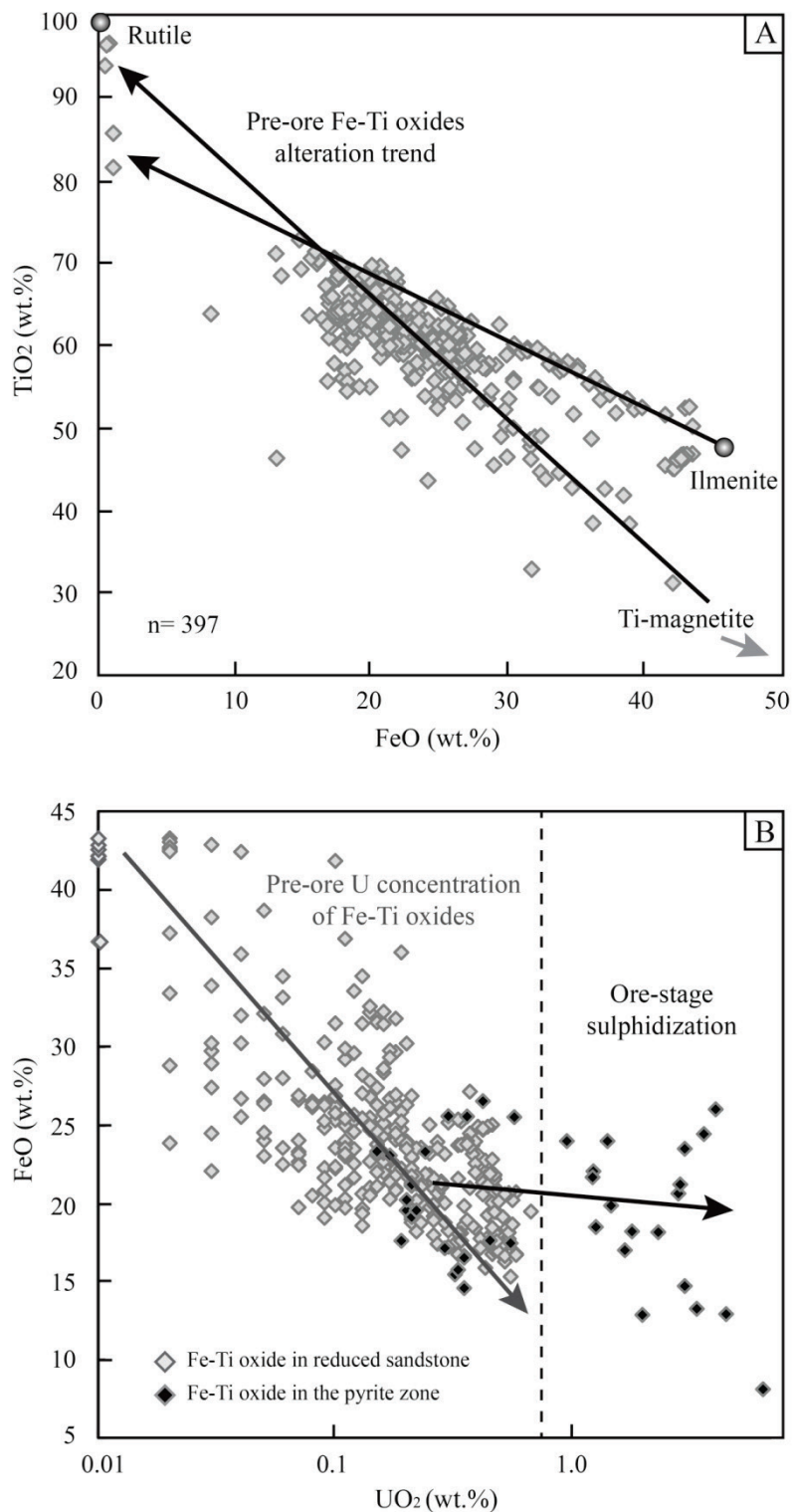


Figure 67. EMP analyses realized on Fe-Ti oxides from the reduced host sandstone and the pyrite zone of the Bayinwula deposit. A= FeO vs TiO₂ diagram showing pre-ore Fe-Ti oxides alteration trend; B= UO₂ vs FeO diagram showing pre-ore uranium concentration on Fe-Ti oxides and uranium over concentration related to ore-stage sulphidization.

Table 18. Representative EMP analyses on Fe-Ti oxide from the Bayinwula deposit.

Location		Bayinwula area									
Mineral		Fe-Ti oxides									
Sample	DH2-128.0m		DHB-64.2m		DH2-111.8m			DH3-118.0m		DH5-114.0m	
Analysis n°	2/1		2/1		1/12	1/13	1/17	4/4		1/1	
Oxides (wt.%)											
SiO ₂	1.22	2.45	0.96	1.06	0.87	0.28	1.03	0.03	0.64	1.91	1.11
TiO ₂	62.12	68.30	62.09	61.94	64.89	57.92	62.79	46.86	63.05	71.26	53.52
Al ₂ O ₃	0.52	0.65	0.35	0.39	0.29	0.09	0.22	0.05	0.52	0.43	0.28
FeO	22.98	20.70	21.72	20.09	19.24	28.49	21.85	42.75	27.20	12.94	26.07
MnO	3.85	0.37	0.84	0.57	5.17	9.22	3.08	7.63	1.56	0.84	1.05
MgO	0.14	0.17	0.09	0.13	0.07	0.03	0.05	1.32	0.08	0.15	0.12
Cr ₂ O ₃	0.00	0.00	0.03	0.12	0.00	0.08	0.00	0.00	0.01	0.00	0.02
V ₂ O ₃	0.05	0.04	2.59	2.63	2.27	2.17	2.20	1.56	2.34	2.35	2.01
CoO	0.01	0.01	0.00	0.01	0.01	0.00	0.00	0.03	0.03	0.00	0.01
UO ₂	0.19	0.00	0.12	0.09	0.26	0.08	0.18	0.00	0.37	1.98	4.04
Total	91.08	92.69	88.79	87.03	93.07	98.36	91.40	100.23	95.80	91.86	88.23
Oxygens	3	3	3	3	3	3	3	3	3	3	3
Cations											
Si ⁴⁺	0.031	0.058	0.024	0.027	0.021	0.007	0.025	0.001	0.015	0.045	0.030
Ti ⁴⁺	1.171	1.216	1.174	1.184	1.178	1.060	1.165	0.901	1.135	1.253	1.086
Al ³⁺	0.015	0.018	0.010	0.012	0.008	0.003	0.006	0.002	0.015	0.012	0.009
Fe ²⁺	0.482	0.410	0.457	0.427	0.388	0.580	0.451	0.913	0.545	0.253	0.588
Mn ²⁺	0.082	0.007	0.018	0.012	0.106	0.190	0.064	0.165	0.032	0.017	0.024
Mg ²⁺	0.005	0.006	0.003	0.005	0.003	0.001	0.002	0.050	0.003	0.005	0.005
Cr ³⁺	0.000	0.000	0.001	0.002	0.000	0.002	0.000	0.000	0.000	0.000	0.000
V ³⁺	0.001	0.001	0.043	0.044	0.036	0.035	0.036	0.026	0.037	0.036	0.036
Co ²⁺	0.000	0.000	0.000	0.000	0.000	0.000	0.000	0.001	0.001	0.000	0.000
U ⁴⁺	0.001	0.000	0.001	0.001	0.001	0.000	0.001	0.000	0.002	0.010	0.024

6.3. Uranium mass balance calculation

Mass balance calculation was realized on 23 samples of the reduced sandstone and more than 400 EMP analyses of Fe-Ti oxide, monazite and zircon. It shows that monazite and zircon are negligible hosts for uranium as they represent in proportion much less than 1% of the whole-rock uranium content, but Fe-Ti oxide seems to be the major one. Assuming that all Ti content of the host sandstone (0.22 wt.% Ti) is contained in Fe-Ti oxide (35.15 wt.% Ti), the average amount of Fe-Ti oxide in the host sandstone is 6260 ppm. The average U content in Fe-Ti oxide being 0.187 wt.% U, the U amount contained in Fe-Ti oxide in whole rock is 11.7 ppm. Therefore, the average U concentration in the reduced sandstone being 30.36 ppm, U amount contained in Fe-Ti oxide represents 38.5% of the whole-rock U content.

Organic matter fragments of the reduced sandstone, which may represent another important site for U in these rocks, were not analyzed because of a lack of standard to recalculate the possible U concentration associated with.

7. Characterization of the organic matter

7.1. Petrography

Organic matter-rich samples collected in both stratigraphic drill holes and the ones from the Bayinwula deposit were studied by fluorescence optical microscopy in order to characterize the petrography of the organic matter (OM). A large amount of phytoclasts (non-fluorescent, biostructure= plant cell) and coal fragments (non-fluorescent, biostructure= fibrous or laminae; Durand, 1980; **Figure 68A, B, C**) indicates a dominant contribution of terrigenous OM in channel deposits of the Saihan Formation. The frequent occurrence of Tasmanacea-type algae (fluorescent; Durand, 1980; **Figure 68D**) characterizes a subaquatic to aquatic depositional environment (Durand, 1980). Therefore, the structured elements of the host reduced sandstone have both terrigenous and aquatic environments origin. No evidence of fluorescent material that could correspond to free hydrocarbons was identified in the matrix or in-filling fractures despite a systematic tracking of such features. In the ore zone as well as in the pyrite zone of the Bayinwula deposit OM is partially to totally replaced by iron disulphides (**Figure 70**). Only the structure of OM elements is partly preserved in the sulphides. However, in oxidized sandstone only rare and strongly altered fragments can be still observed.

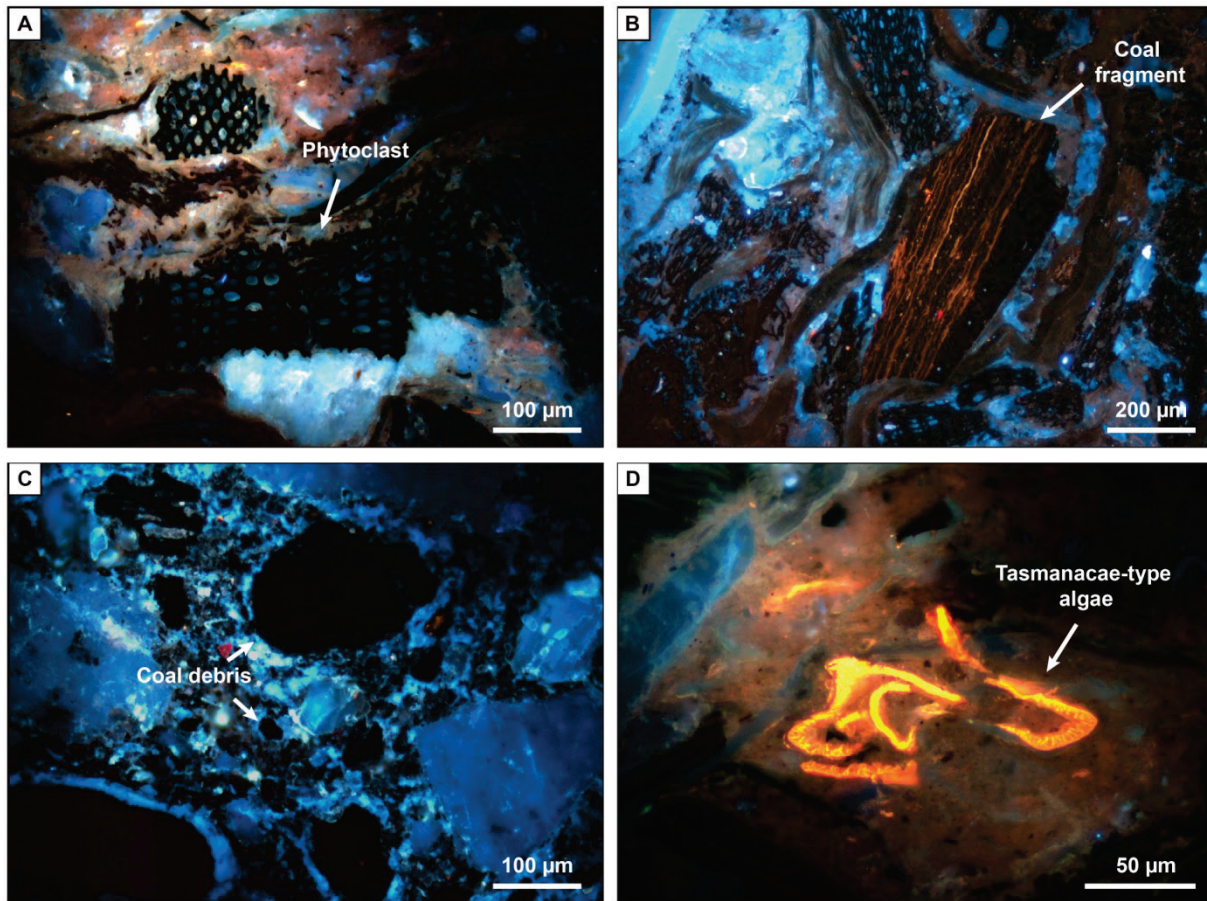


Figure 68. Structured elements of organic matter occurring in the host sandstone of the Bayinwula deposit. A= Phytoclast; B= Coal fragment; C= Fine coal debris; D= Tasmanaceae-type algae.

7.2. Typology

In order to characterize the typology of the organic matter occurring in sandstone of the Saihan Formation, Rock-Eval pyrolysis (REP) was realized on samples from both stratigraphic drill holes and drill holes from the Bayinwula deposit (**Table 19**; **Appendix 13**, **Appendix 14**). In addition a coal sample (CM08) collected in one of the large coal seams of the Saihan Formation was analyzed as a reference. First of all, the total organic carbon (TOC) content of analyzed drill-core samples displays low to elevated values ranging from 0.52 to 23.91 wt.%. Elevated TOC contents mainly identified in stratigraphic drill holes correspond to coal seams deposited in swamp environment or to a strong accumulation of OM fragment in fluvial channel sands. Samples from the reduced host sandstone located downdip to the ore zone present TOC content ranging from 0.52 to 3.38 wt.%. In the oxidized sandstone TOC is extremely low (**Appendix 13**, **Appendix 14**), from 0.00 to 0.02 wt.%, indicating that OM is globally not preserved. Preliminary evaluation by REP of free hydrocarbon (HC) in the host sandstone of the Bayinwula deposit revealed an extremely low content of thermodesorbed HC

with S1 values of 0.01-0.26 mg HC/g sample. REP S2 data are quite low, globally range from 0.11 to 2.11 mg HC/g sample (**Table 19**), and indicate a low petroleum potential (Espitalié et al., 1985). Elevated S2 values indicating a good petroleum potential are only observed for some stratigraphic drill-core samples highly rich in OM, or in coal seams (**Table 19**: CM08 and DHB-1105).

Table 19. Rock-Eval pyrolysis (REP) results from sandstone of the Saihan Formation hosting the Bayinwula deposit (using REP interpretation methods of Espitalié et al., 1985).

Location		Bayinwula area										
Drill hole		DHB					DH2	DH3				
Analysis n°	CM08	638	645	711	1008	1105	1462	1328	1356	1384	140	142
TOC (%) Total organic carbon	57.40	9.31	12.35	10.07	8.33	23.91	1.81	0.68	3.38	1.73	0.52	1.04
S1 (mg HC/g sample) Free hydrocarbons (HC)	0.39	0.04	0.06	0.03	0.04	0.26	0.02	0.04	0.04	0.03	0.01	0.01
S2 (mg HC/g sample) HC generated through thermal cracking	23.09	1.18	2.11	1.36	1.68	23.52	0.56	0.11	0.40	0.15	0.12	0.21
S3 (mg CO ₂ /g sample) Amount of CO ₂ produced during pyrolysis	16.91	4.01	4.55	3.47	3.10	10.01	1.22	0.75	2.47	1.66	0.43	0.91
T _{max} (°C) Temperature at top of S2 peak	418	546	431	529	459	428	415	311	384	367	415	385
HI (mg HC/g TOC) Hydrogen index	40	13	17	14	20	98	31	16	12	9	23	20
OI (mg CO ₂ /g TOC) Oxygen index	30	43	37	34	37	42	67	110	73	96	83	88

OM disseminated in the host sandstone displays a very low hydrogen index (HI) with data ranging from 9 to 98 mg HC/g TOC and a relatively high oxygen index (OI) with data from 34 to 110 mg CO₂/g TOC (**Table 19**). Except for some OM-rich stratigraphic drill-core samples, T_{max} values are lower than 435°C and characterize thermally immature organic matter (Espitalié et al., 1985). These data indicate that the bulk kerogen composition corresponds to type IV (**Figure 69**; Demaison et al., 1983) and inherited from land plants. Petrographical data combined with REP analyses confirm that most of the organic matter is derived from land plants, even though trace contribution of algal input may be observed under the microscope (**Figure 68D**). Elevated OI values (73 to 110 mg CO₂/g TOC; **Table 19**: DH3), mainly observed in the pyrite zone of the roll front, associated with very low HI data

and the predominance of macerals characterizing higher plants input may be evidence for degraded type III kerogen (e.g., type IV kerogen).

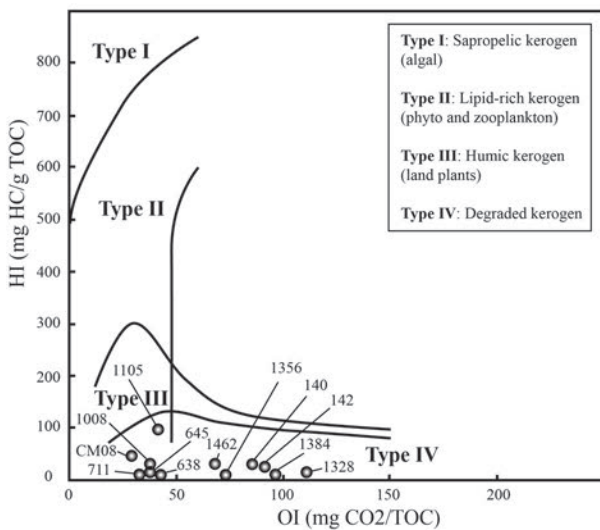


Figure 69. HI vs OI diagram showing the typology of organic matter occurring in the host sandstone of the Bayinwula deposit (modified after Herbin and Deroo, 1979; Demaison et al., 1983).

8. Ore-stage sulphidization

8.1. Petrography of iron disulphides

Preore-stage sub-idiomorphic to idiomorphic pyrite is widely distributed and disseminated in the reduced permeable sandstone of the Saihan Formation. Preore-stage pyrite was observed in the stratigraphic drill holes and in the sandstone hosting the Bayinwula deposit. Ore-stage iron disulphides are mainly located in the pyrite zone, either at the “nose” or at the lateral “wings” of the roll. They occur dominantly in epigeny of both OM fragments and Fe-Ti oxides (**Figure 70**). The common succession starts with the crystallization of framboidal FeS₂ (**Figure 70B, C, D: FeS₂ (1)**) followed by a collomorph growth (**Figure 70B, C, D: FeS₂ (2)**). Then, the two first populations may be cemented by a late stage of sub-idiomorphic FeS₂ (**Figure 70B, C, D: FeS₂ (3)**). In the pyrite zone, OM fragments are partly to totally replaced by iron disulphide. Similarly detrital Fe-Ti oxides are largely replaced by iron disulphide which also occur as overgrowth and may cement several grains (**Figure 70C, D**). In the oxidized sandstone, iron disulphides are strongly altered into hematite or limonite by oxygenated groundwater.

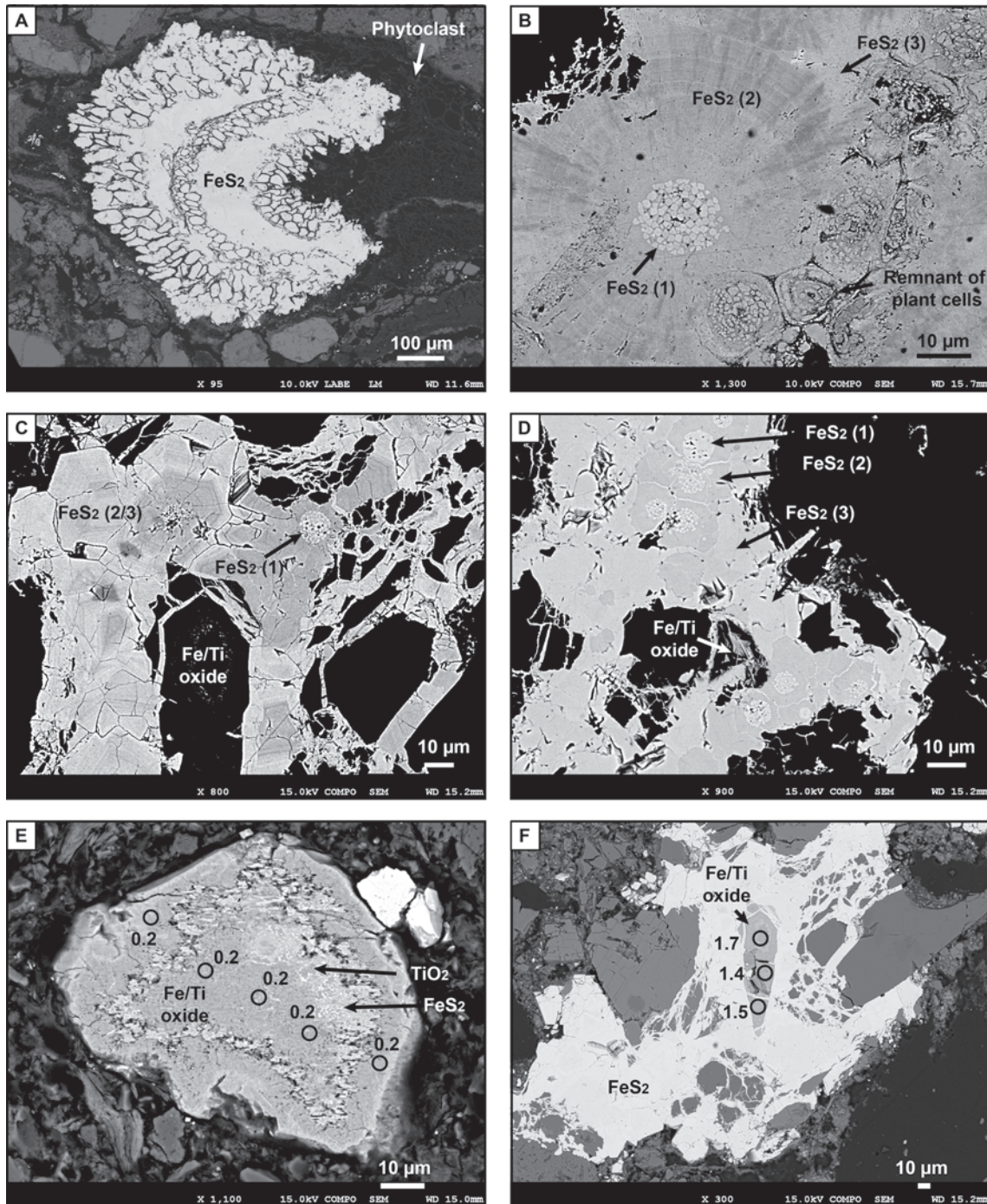


Figure 70. Ore-stage iron disulphides in epigeny of organic matter fragments and Fe-Ti oxides. A and B= iron disulphide in epigeny of organic matter; C and D= iron disulphide in epigeny of Fe-Ti oxide. FeS_2 (1)= frambooidal population; FeS_2 (2)= collomorph population; FeS_2 (3)= cement to sub-idiomorphic population. E= non-epigenized Fe-Ti oxide; F= Fe-Ti oxide epigenized into FeS_2 . Black circles and numbers indicate EMP uranium concentration in wt% UO_2 .

8.2. Sulfide trace element signature

The trace element concentrations of the different iron disulphide populations occurring in the host sandstone of the Bayinwula deposit were measured by LA-ICPMS (**Figure 71**). The trace element signature of each iron disulphide population (**Table 20**) aims: (i) to correlate it with petrographical observations and (ii) to provide constraints about the genetic processes involved in the ore-stage sulphidization. As a reference, trace element contents were measured in preore-stage FeS₂ disseminated in the host sandstone in order to compare with trace element signature of ore-stage FeS₂. Trace element concentrations in preore-stage FeS₂ are very low (**Table 20**: 1213-43b, 1213-44b): a few tens of ppm of As and Cu and only few ppm of Co, Zn and Mo.

The three populations of ore-stage FeS₂ present significant concentrations of As, Ni and Co and minor amounts of Zn, Cu and Mo. The Se and V content are extremely low or below the detection limit. Therefore the most discriminating elements to characterize the different ore-stage FeS₂ trace element signature are As, Ni and Co. The framboids (n=22) have very high contents of As (1008-2274 ppm; mean= 1531; σ_{As} = 485), Ni (108-617 ppm; mean= 320; σ_{Ni} = 173) and Co (148-562 ppm; mean= 288; σ_{Co} = 157). Collomorph FeS₂ (n=17) is characterized by moderate contents of As (346-1366 ppm; mean= 645; σ_{As} = 328), Ni (63-257 ppm; mean= 133; σ_{Ni} = 56) and Co (51-184 ppm; mean= 106; σ_{Co} = 46). Cement to sub-idiomorphic FeS₂ (n=18) displays low concentrations of As (12-316 ppm; mean= 121; σ_{As} = 103), Ni (13-157 ppm; mean= 70; σ_{Ni} = 47) and Co (0-103 ppm; mean= 41; σ_{Co} = 38). Therefore, there is a progressive decrease of As, Ni and Co concentrations from framboidal to late sub-idiomorphic FeS₂ (**Figure 72**). Moreover, preore-stage and ore-stage sub-idiomorphic FeS₂ are characterized by low to very low trace element concentrations whereas ore-stage framboidal and collomorph FeS₂ present similar trace element signatures with high contents of As, Ni and Co. Therefore, the trace elements signature may evidence two different genetic processes of FeS₂ crystallization.

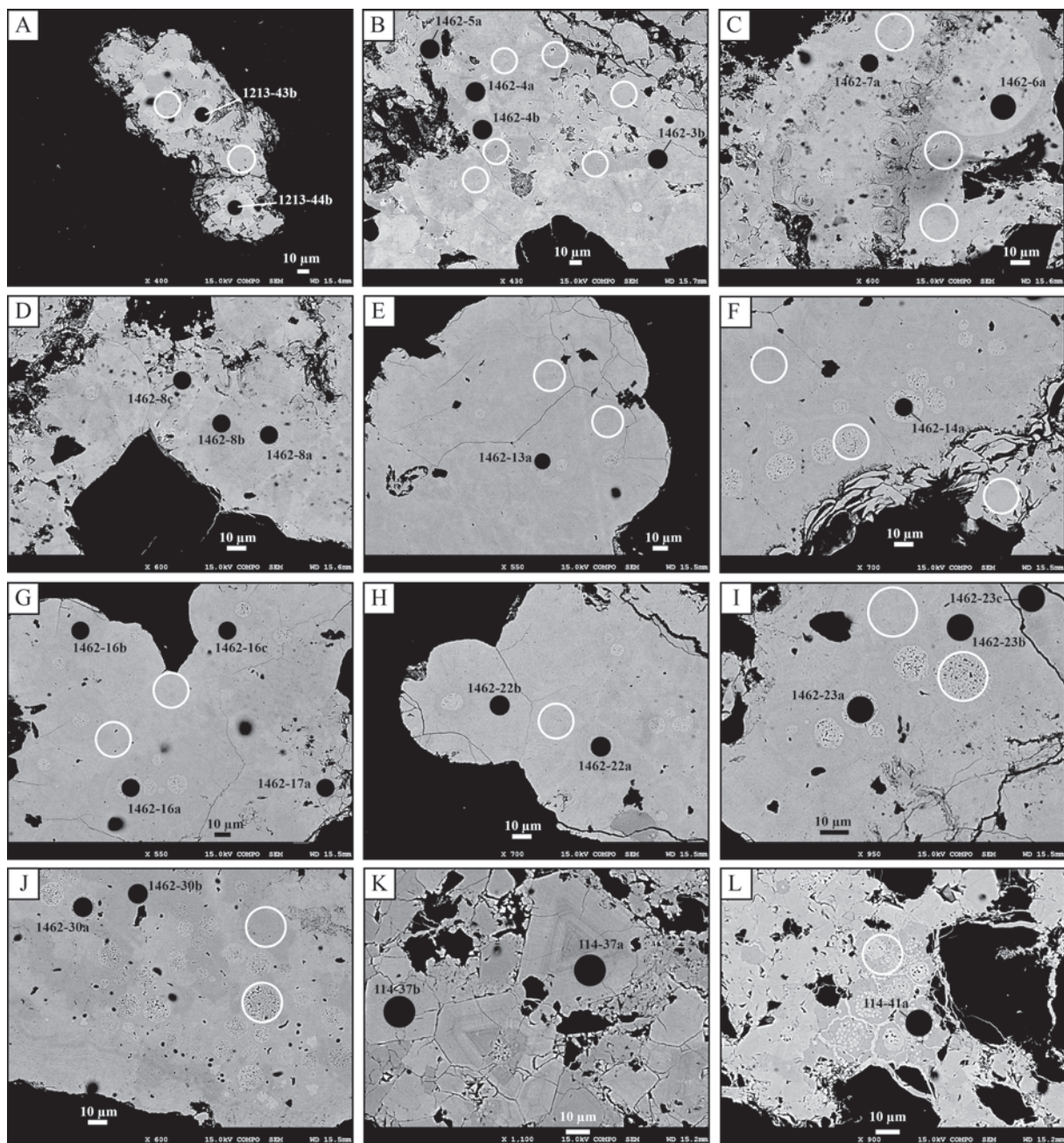


Figure 71. Representative iron disulphide populations occurring in the host sandstone of the Bayinwula deposit. Black circles indicate the location of ICPMS ablation spots realized for trace element measurement. White circles indicate the location of SIMS spots realized for stable isotopes analysis. A= preore-stage sub-idiomorphic iron FeS₂; B to J= ore-stage FeS₂ populations located in the “wings” of the roll; K and L= ore-stage FeS₂ populations located in the “nose” of the roll.

Table 20. Representative trace element concentrations of the different populations of iron disulphide occurring in the host sandstone of the Bayinwula deposit.

Location		Bayinwula deposit								
Type		Framboidal FeS ₂								
Sample		DH2-146.2m								DH5-114.0m
Analysis n°		1462-7a	1462-8a	1462-13a	1462-14a	1462-16a	1462-22a	1462-23a	1462-30a	114-41a
As		1874.85	2080.15	1065.63	1012.48	1176.00	1667.35	1008.37	1626.72	2274.62
Ni		512.99	617.21	220.03	161.83	234.30	329.96	238.61	457.66	108.85
Co		498.55	562.65	159.28	156.88	148.95	310.34	151.39	353.79	254.44
Zn		15.04	11.22	7.93	11.75	<LOD	11.93	25.29	8.66	14.92
Cu		<LOD	<LOD	<LOD	<LOD	<LOD	<LOD	<LOD	<LOD	<LOD
Mo		118.69	27.07	24.02	14.28	11.90	33.90	29.43	15.26	16.05
Se		<LOD	<LOD	<LOD	<LOD	<LOD	<LOD	<LOD	<LOD	<LOD
V		23.85	1.93	<LOD	<LOD	1.92	<LOD	<LOD	<LOD	<LOD
Type		Collomorph FeS ₂								
Sample		DH2-146.2m								DH5-114.0m
Analysis n°		1462-4a	1462-6a	1462-8b	1462-16b	1462-16c	1462-22b	1462-23b	1462-30b	114-37a
As		507.31	557.84	419.56	346.97	389.21	555.42	702.10	960.94	1366.67
Ni		149.79	121.18	82.92	111.12	139.45	257.41	111.11	63.88	163.65
Co		118.67	120.74	70.28	66.30	74.76	184.57	108.00	51.50	163.46
Zn		10.48	18.90	6.84	8.18	5.72	13.51	14.54	23.54	8.07
Cu		<LOD	5.05	<LOD	88.24	39.62	129.61	<LOD	<LOD	10.39
Mo		15.37	11.83	11.38	11.56	13.28	16.74	18.08	17.78	446.21
Se		<LOD	<LOD	<LOD	<LOD	<LOD	<LOD	<LOD	<LOD	<LOD
V		0.87	1.15	1.53	<LOD	<LOD	<LOD	<LOD	<LOD	<LOD
Type		Cement to sub-idiomorphic FeS ₂								
Sample		DH2-121.3m								DH5-114.0m
Analysis n°		1213-43b	1213-44b	1462-3b	1462-4b	1462-5a	1462-8c	1462-17a	1462-23c	114-37b
As		19.73	32.92	163.17	112.64	92.52	15.59	12.99	316.30	140.58
Ni		<LOD	<LOD	37.18	79.55	113.20	13.82	30.09	60.69	157.22
Co		4.16	9.82	92.99	24.08	28.45	<LOD	3.74	35.86	103.38
Zn		<LOD	7.09	9.80	8.03	16.25	<LOD	7.70	13.92	5.28
Cu		10.16	29.68	31.64	3.83	25.72	<LOD	<LOD	<LOD	<LOD
Mo		1.75	3.84	12.93	9.69	23.38	<LOD	4.85	9.28	32.20
Se		<LOD	<LOD	<LOD	<LOD	<LOD	<LOD	<LOD	<LOD	<LOD
V		<LOD	<LOD	0.88	0.87	1.71	1.24	<LOD	<LOD	<LOD

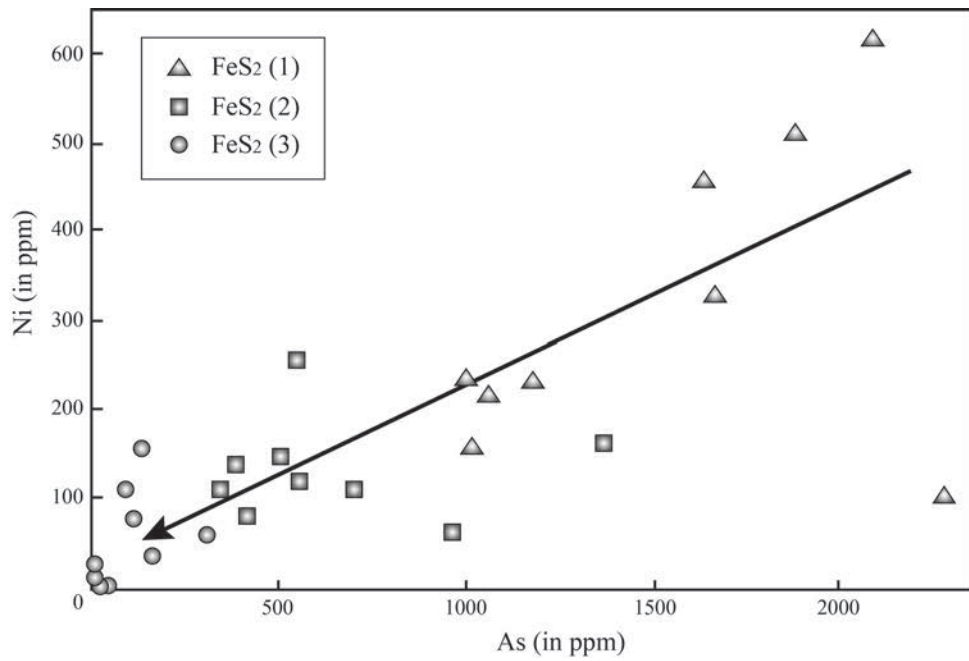


Figure 72. As vs Ni diagram showing the trace element concentrations decrease from frambooidal iron disulphides (FeS₂ (1)) to sub-idiomorphic iron disulphides (FeS₂ (3)). FeS₂ (1)= frambooidal; FeS₂ (2)= collomorph; FeS₂ (3)= sub-idiomorphic.

8.3. Sulphur isotopes

Sulphur isotopes of both preore-stage and ore-stage iron disulphides were analyzed (**Figure 73**). The $\delta^{34}\text{S}$ values of preore-stage FeS₂ (n= 5) range from -6.09 to -3.77 ‰ (mean= -4.92 ‰). As the spot size was about 25 μm of diameter and because ore-stage frambooidal FeS₂ are smaller than 20 μm , it was often analyzed with part of collomorph FeS₂. Therefore isotopic data from both populations are considered as a single episode.

Sulphur isotopic data from ore-stage FeS₂ show two distinct signatures (**Figure 73**): (i) the $\delta^{34}\text{S}$ values of frambooidal and collomorph FeS₂ (n= 24) give a very light signature from -30.54 to -7.47 ‰ (mean= -14.61‰) and (ii) sub-idiomorphic FeS₂ (n= 18) give a heavier signature from -6.93 to +18.77 ‰ (mean= 4.11 ‰).

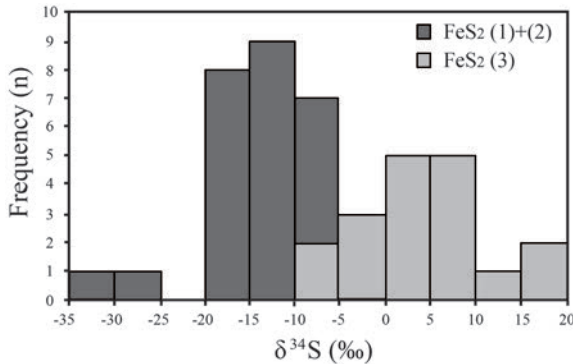


Figure 73. Sulphur stable isotopes signature of ore-stage iron disulphides. FeS₂ (1) + (2)= frambooidal + collomorph iron disulphide; FeS₂ (3)= sub-idiomorphic iron disulphide.

8.4. Ore-stage Fe-Ti oxide alteration

To constrain the physical-chemical conditions of the epigenization of the Fe-Ti oxides by iron disulphides in the pyrite zone of the roll front (**Figure 70C, D, F**), the solubility of ilmenite has been modelled. Thermodynamic calculations were carried out using the PHREEQC software package (v.3.0: Parkurst and Appelo, 1999) to determine ilmenite solubility as a function of pH and H₂S partial pressure under anoxic conditions (**Figure 74**). Calculations were performed using the LLNL database (Johnson et al. 2000). In H₂S free system, ilmenite solubility is very low over a wide range of pH condition, approximately from 5 to 11. On the contrary, when H₂S is present, ilmenite solubility increases drastically and is driven by pyrite precipitation. This model shows that ilmenite solubility is elevated in a broad range of pH when H₂S occurs in solution. Moreover, in this case iron disulphide precipitate quantitatively.

Groundwater analyzed in the Bayinwula area (Nie, 2010) is mainly composed of Cl, Na, HCO₃ and SO₄ and shows pH values ranging from 6.35 to 8.48. Over this range of pH, the presence of H₂S is required to dissolve ilmenite substantially.

Replacement of the detrital Fe-Ti oxide minerals by iron disulphides resulting from ore-stage sulphidization can be illustrated by the following reaction:



The main products of this reaction are (i) a large amount of iron disulphide precipitation and (ii) the crystallization of anatase (TiO₂) from the titanium liberated during the alteration of Fe-Ti oxides (Reynolds and Goldhaber, 1978; **Figure 70E, F**). Therefore Fe-Ti oxides represent a major source of Fe in the host sandstone for the ore-stage sulphidization.

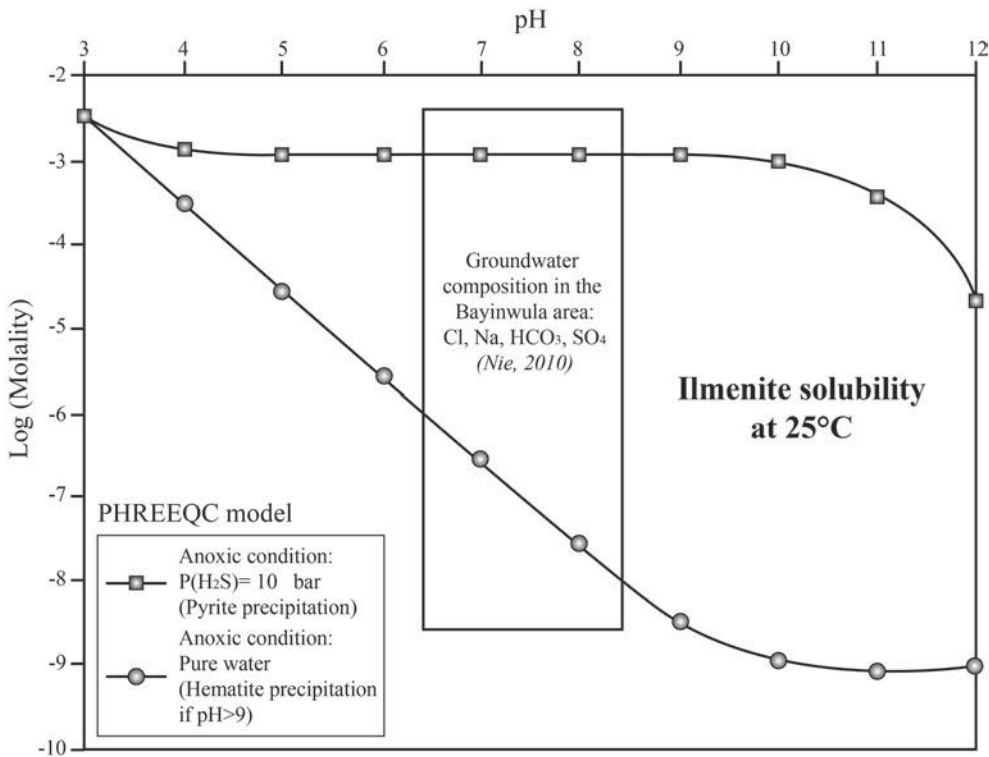


Figure 74. PHREEQC model of ilmenite solubility as a function of pH, under anoxic conditions. Two conditions are selected: (i) H_2S free system, and (ii) in the presence of 10 bar H_2S partial pressure.

Ore-stage sulphidization play a role in uranium reconcentration within the residual Ti oxide grains which exhibit high uranium contents (few wt.% UO₂, **Table 18**; **Figure 70F**) compared to the pre ore stage ones (**Figure 66C, D**).

8.5. *U mineralization*

U mineralization in the Bayinwula deposit is mainly located in the sandstone, at the “nose” of the roll front. A minor amount of ore occurs in the lateral “wings”, at the contact between the sandstone and semi-permeable mudstone sheets. Uranium minerals mainly occur as more or less complete epigeny (**Figure 75**) and occur: (i) in epigeny of FeS₂ crystals which have previously replaced organic matter fragments (**Figure 75A, C**), rarely directly at the contact with the phytoclasts (**Figure 75**) or (ii) in epigeny of FeS₂ crystals disseminated in the host sandstone (**Figure 75D, E, F**). The predominant uranium mineral is phosphorus-rich coffinite (**Table 21**). Ningyoite occurs in minor proportion. Therefore, uranium mineralization clearly post-dates sulphidization within the roll front.

In coffinite (**Table 21**) silica ($8.29 < \text{SiO}_2 < 28.51$ wt.%) is largely substituted by phosphorus ($6.79 < \text{P}_2\text{O}_5 < 13.71$ wt.%), and uranium ($25.99 < \text{UO}_2 < 56.10$ wt.%) by calcium ($2.60 < \text{CaO} < 4.67$ wt.%). Small amounts of Zr detected in coffinite (up to 1.71 wt.%) may indicate a volcanic ash contribution within the host-sediment. However, high Fe content (up to 7.63 wt.% FeO) may be related to contamination by pyrite crystals inclusions. In ningyoite (**Table 21**), the tetravalent uranium phosphate ($19.33 < \text{P}_2\text{O}_5 < 27.34$ wt.%), uranium ($22.26 < \text{UO}_2 < 27.42$ wt.%) is largely substituted by calcium ($10.26 < \text{CaO} < 13.54$ wt.%) and rare earth elements such as cerium ($5.00 < \text{Ce}_2\text{O}_3 < 8.51$ wt.%), lanthanum ($2.82 < \text{La}_2\text{O}_3 < 4.69$ wt.%), neodymium ($2.63 < \text{Nd}_2\text{O}_3 < 4.76$ wt.%) and yttrium ($1.70 < \text{Y}_2\text{O}_3 < 3.08$ wt.%).

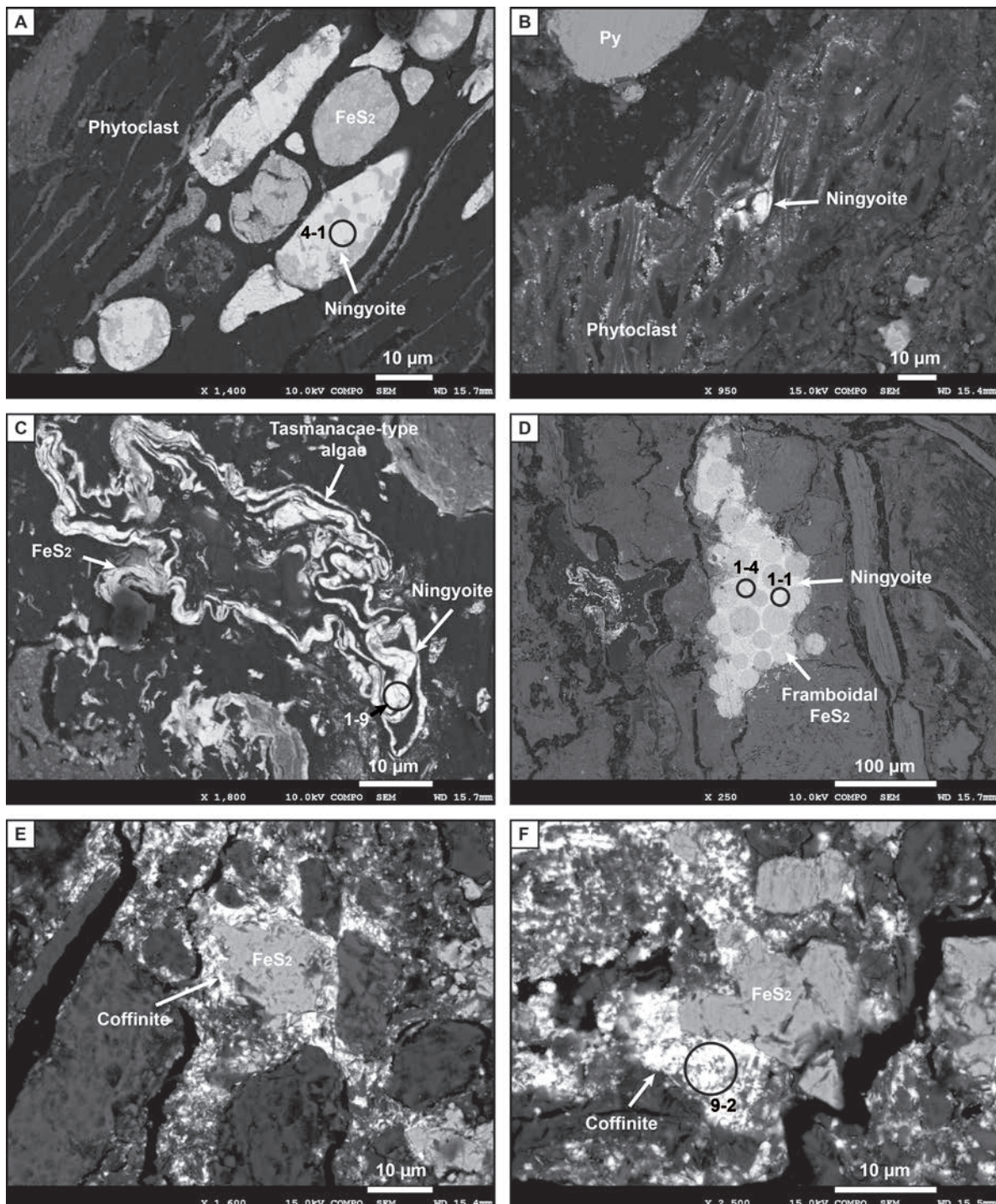


Figure 75. Uranium mineralization of the Bayinwula deposit. A= ningyoite epigeny of FeS₂ associated with organic matter; B= Ningyoite associated with organic matter; C= ningyoite epigeny of FeS₂ associated with organic matter; D= ningyoite epigeny of framboidal FeS₂; E and F= coffinite epigeny of sub-idiomorphic FeS₂.

Table 21. Representative EMP analyses of uranium mineralization from the Bayinwula deposit.

Location					Bayinwula deposit					
Drill hole		DHA-175.8m			DHB-64.5m					
Mineral		Coffinite			Ningyoite					
Analysis n°		9/2	9/10	9/11	9/12	Analysis n°	1/1	1/4	1/9	
Oxides (wt.%)										
SiO ₂		8.29	14.77	14.45	11.33	P ₂ O ₅	24.90	27.34	26.04	19.33
P ₂ O ₅		13.71	10.29	9.72	12.11	CaO	12.97	13.01	13.54	10.26
MgO		0.18	0.32	0.50	0.22	SiO ₂	0.23	0.39	0.13	0.07
Al ₂ O ₃		0.97	6.20	3.86	1.83	MgO	0.11	0.09	0.05	0.06
K ₂ O		0.30	0.19	0.35	0.27	Al ₂ O ₃	0.10	0.23	0.04	0.04
CaO		4.67	3.15	3.47	4.48	K ₂ O	0.18	0.19	0.19	0.18
ZrO ₂		1.71	1.40	1.35	1.59	FeO	1.19	1.24	0.44	13.80
ThO ₂		<LOD	<LOD	<LOD	<LOD	Y ₂ O ₃	2.63	3.08	2.55	1.70
FeO		4.41	7.63	7.28	5.46	La ₂ O ₃	4.43	4.69	4.26	2.82
TiO ₂		0.42	0.22	0.21	0.22	Ce ₂ O ₃	8.49	8.51	8.28	5.00
Y ₂ O ₃		3.36	2.68	2.10	2.86	Nd ₂ O ₃	4.67	4.76	4.07	2.63
PbO		<LOD	<LOD	<LOD	<LOD	PbO	0.18	0.04	0.13	1.45
UO ₂		56.10	44.07	34.72	48.69	UO ₂	23.95	24.02	27.42	22.26
Total		94.12	90.92	78.01	89.06	Total	84.03	87.59	87.14	79.60
Oxygens		4	4	4	4	Oxygens	8	8	8	8
Cations										
Si ⁴⁺		0.384	0.614	0.673	0.520	Cations				
P ⁵⁺		0.537	0.362	0.383	0.470	P ⁵⁺	1.821	1.871	1.850	1.593
Mg ²⁺		0.012	0.020	0.035	0.015	Ca ²⁺	1.201	1.127	1.217	1.070
Al ³⁺		0.053	0.304	0.212	0.099	Si ⁴⁺	0.020	0.032	0.011	0.007
K ⁺		0.018	0.010	0.021	0.016	Mg ²⁺	0.014	0.011	0.006	0.009
Ca ²⁺		0.232	0.140	0.173	0.220	Al ³⁺	0.010	0.022	0.004	0.005
Zr ⁴⁺		0.039	0.028	0.031	0.036	K ⁺	0.020	0.020	0.020	0.022
Th ⁴⁺		0.000	0.000	0.000	0.000	Fe ²⁺	0.086	0.084	0.031	1.124
Ti ⁴⁺		0.015	0.007	0.007	0.008	Y ³⁺	0.000	0.133	0.114	0.088
Fe ²⁺		0.171	0.265	0.284	0.209	La ³⁺	0.141	0.140	0.132	0.101
Y ³⁺		0.083	0.590	0.052	0.070	Ce ³⁺	0.269	0.252	0.254	0.178
Pb ²⁺		0.000	0.000	0.000	0.000	Nd ³⁺	0.144	0.137	0.122	0.091
U ⁴⁺		0.578	0.407	0.360	0.497	Pb ²⁺	0.004	0.001	0.003	0.038
						U ⁴⁺	0.460	0.432	0.512	0.482

9. Discussion

9.1. Sedimentology of the Saihan Formation

Sediments of the Saihan Formation are deposited during the post-rift stage of the Erlian Basin. Bo and Kuan (2006), Nie et al. (2007), Fan et al. (2008), Zhang et al. (2010) and personal observations on drill-cores has permitted to propose depositional environments typical of a braided river system alternating with sandstone dominated and overbank dominated episodes. Sandstone layers mainly correspond to stacked sandy braided channels and represent

permeable host-rock favourable for the development of roll front-type uranium mineralization. Mudstone dominated layers are more or less continuous (not greater than a few hundred meters in lateral extent; Miall, 1996) and correspond to overbank deposits. They represent good aquitars (non permeable to semi-permeable barriers) to confine in permeable sandstones the circulation of oxygenated groundwater responsible for the formation of epigenetic roll front-type uranium mineralization (Devoto, 1978). Therefore, the facies architecture related to the partitioning between sandstone dominated and mudstone dominated sedimentological record, resulting from the tectonic regime that occurred during the post-rift stage in the Erlian Basin, is at the origin of the confined permeable sandstone hosting the Bayinwula deposit.

9.2. The source of uranium

Reduced sandstone of the Saihan Formation presents an elevated uranium geochemical background with a mean at 30.4 ppm. U-bearing detrital minerals within the host sandstone are monazite, zircon, apatite and Fe-Ti oxides. Mass balance calculation shows that monazite and zircon are negligible hosts for uranium in the whole rock (less than 1 ppm), whereas altered Fe-Ti oxide contains 38.5% of the whole-rock U concentration (i.e., 11.7 ppm).

We have seen that Fe-Ti oxides are altered into a fine admixture of hematite and titanium oxides associated with a strong depletion of iron. This alteration has most probably occurred in the source of sediments or during the transport because oxidizing conditions are required for the formation of the hematite-Ti-oxide assemblage, and the host sandstone is reduced. However, the leaching of iron from Fe-Ti oxides would be easier in reducing conditions and may have occurred at least partly within the sediments. Uranium concentration in the Fe-Ti oxides may have occurred during their alteration in the source rocks or/and later within the basin. Analyses made on Fe-Ti oxides in the altered zone of the granites surrounding the basin show only a limited enrichment in uranium, up to 1000 ppm U (Bonnetti et al., 2013 in preparation). In the basin, the synsedimentary uranium concentrations, was more likely initially adsorbed on the clay mineral occurring in the matrix of sandstone or in overbank deposits and associated with the organic matter. During diagenesis, recrystallization of the clay minerals may have favoured the desorption of uranium from the clay minerals followed by re-adsorption on the altered Fe-Ti oxides within the reduced sandstone (Payne, 1999).

In the oxidized sandstone the mean uranium whole-rock uranium content of 6.8 ppm U indicates that 23.6 ppm of the pre-ore uranium concentration (with a mean of 30.4 ppm U) has been leached out by oxidizing groundwater. With a mean uranium content of 11.7 ppm, the Fe-Ti oxides which are nearly entirely replaced by pyrite represent one of the major uranium source, corresponding to a contribution of about 50% if we assume that all the uranium has been liberated from the Fe-Ti oxides. Another major source is probably the organic matter which also liberates its uranium through its pyritisation. The uranium which mainly have remain adsorbed on the clay minerals may have been more difficult to desorb if the infiltrated fluid have a pH close to the neutrality, which corresponds to the maximum adsorption of uranium on the mineral surfaces. Therefore the host sandstone itself plays a role of uranium source with a major contribution of Fe-Ti oxides and probably of organic matter through their pyritization. Concerning the relationships between organic matter and uranium two main processes are generally proposed: reduction (Nakashima, 1992) and complexation (Munier-Lamy et al., 1986).

9.3. Nature and evolution of organic matter

The nature of the organic matter occurring in the host-sandstone of the Bayinwula deposit evidenced both origins: (i) mainly terrigenous characterized by a large amount of phytoclasts and coaly fragments and (ii) from aquatic environments with the episodic presence of Tasmanaceae-type algae. Rock-Eval data revealed several important points, organic matter is: (i) dominantly inherited from land plants and corresponds to a kerogen of type IV (degraded type III), (ii) is thermally immature presenting low petroleum potential and (iii) has an extremely low content of free hydrocarbons. Therefore, organic matter-rich sandstones of the Saihan Formation have not been buried very deep and no thermal maturation has occurred indicating that no hydrocarbon was produced by thermal cracking within the formation.

9.4. SRB and ore-stage sulphidization

Sulphate reducing bacteria are responsible for a series of reactions within the roll front: (i) both organic matter and Fe-Ti oxides are epigenized by iron disulphides which in turn are replaced by the uranium minerals; (ii) during iron disulphide epigeny Fe-Ti oxides are partly to totally dissolved. Therefore the uranium adsorbed on them is liberated and become more available to be leached by oxidizing groundwater and may get more concentrated (up to few wt.% UO₂) in residual Ti-oxides; (iii) BSR produces a large amounts of dissolved sulphide,

such as H₂S (Machel, 2001), that creates a strong reducing barrier for oxidized uranium rich fluids moving downwards into the permeable sandstone and is probably the main mechanism for uranium precipitation (Lizitsyn and Kuznetsova, 1967; Hua et al., 2006; Yi et al., 2007). These processes have to be considered as occurring simultaneously in the different sections of the roll front, but successively in a given section of the roll. For example, the uranium liberated by the replacement of Ti-Fe oxides and organic matter by sulphides in the most frontal part of the roll front is leached slightly later when the oxidized brines move where the sulphides have been formed. Then, uranium will precipitate a little further downwards on previously crystallized iron sulphides when the oxidized uranium loaded solutions mix with H₂S produced by the bacteria still a little further downwards in the front.

During ore-stage sulphidization three populations of iron disulphides are characterized by their trace element concentrations and sulphur isotope signature: (i) frambooidal FeS₂ with high content of As, Ni and Co; (ii) collomorph FeS₂ with moderate concentration of As, Ni and Co; (iii) sub-idiomorphic FeS₂ with low content of As, Ni and Co. Both frambooidal and collomorph FeS₂ are characterized by light sulphur isotope signature (mean $\delta^{34}\text{S} = -14.61\text{\textperthousand}$) whereas sub-idiomorphic FeS₂ is characterized by heavy sulphur isotope signature (mean $\delta^{34}\text{S} = 4.11\text{\textperthousand}$). The frambooidal shape of the iron disulphides, their moderate to high As, Ni and Co contents, and light sulphur isotope signature support that bacterial processes have been in their genesis (Jensen, 1958; Lizitsyn and Kuznetsova, 1967; Belyi et al., 1972; Rackley, 1972). Indeed, trace elements such as As, Ni and Co tend to be incorporated in iron disulphide during BSR (Teclu et al., 2008) under reducing condition (Amrhein et al., 1993). Also, BSR typically produces isotopically light reduced sulphur species (H₂S, HS⁻; Machel, 2001) reacting with iron oxides or hydroxides to form iron disulphides. Finally, the highest OI values (up to 110 mg CO₂/g TOC) recorded by REP in samples from the pyrite zone of the roll front may be an evidence of OM biodegradation. The high phosphorus content of the uranium minerals is also probably the signature of bacterial activity. It is well known that phosphorus, which can be released either from inorganic or organic compounds, accelerates the growth of bacteria (e.g., Gächter, 1993). Certain bacteria are able to utilize even phosphorus from apatite (Hutchens et al., 2006).

9.5. Uranium mineralization

The uranium mineralization of the Bayinwula deposit is associated with organic matter and iron disulphides. Uranyl ions have been carried through the host sandstone by oxygenated groundwater and have precipitated at the redox front as phosphorus-rich coffinite and ningyoite. Both uranium minerals occur in epigeny of FeS₂ and post-date ore-stage iron sulphidization. Reduced conditions for uranyl ions precipitation are provided by H₂S-rich secondary reducing barrier developed during BSR. Sulphate reducing bacteria degrade organic matter from the host sandstone, resulting in the generation of organic acids (Landais, 1996; Machel, 2001). Subsequently, feldspars are slightly dissolved by these organic acids, supplying a silica source and likely forming organic-silica complexes (Bennett and Siegel, 1987). The organic-silica complexes might have provided the high silica activity needed to form coffinite (Brookins, 1976, Langmuir, 1978). Moreover, kaolinite detected by X-ray diffraction only in the pyrite zone where SRB were active may be evidence of feldspar alteration. In low temperature oxidized waters, the UO₂(HPO₄)₂²⁻ complex predominates at pH 4 to 7.5 (Langmuir, 1978) which corresponds to the range of pH measured in sandstones of the Bayinwula area (Nie, 2010). Organic matter may contain significant phosphorus concentration (House and Denison, 2002). Therefore, both the degradation of organic matter during BSR and its oxidation by oxygenated groundwater may supply a phosphorus source for the crystallization of both uranium minerals P-rich coffinite and ningyoite.

9.6. Metallogenic model

The present study has demonstrated the multiple roles of sulphate reducing bacteria: (i) in the precipitation of iron disulphides within the roll front, (ii) in the liberation of U from U-rich Fe-Ti oxide alteration and detrital organic matter, (iii) in the formation of a secondary reducing barrier by the liberation of H₂S, and (iv) the liberation of phosphorus from organic and/or non-organic sources. Therefore, a biogenic model for the Bayinwula roll front deposit is proposed (**Figure 76**).

9.6.1. Pre-ore Fe-Ti oxides alteration

The alteration of detrital Fe-Ti oxide is characterized by new formation of aintimate mixture of Fe-oxides and hydroxides) and Ti-oxides associated with a strong leaching of Fe content and their uranium enrichment. The alteration of the Fe-Ti oxides has probably occurred in the weathering zone of the source lithologies of the sediments and/or during their transport, because the depositional environment of the Saihan Formation is strongly reduced. Pre-ore uranium concentration (**Figure 76E**) may have occurred during Fe-Ti oxide alteration in the weathered zone of the source lithologies or/and later within the basin during diagenetic evolution of sediments. Some analyses made on the Fe-Ti oxides from weathered granites in the potential source areas have evidenced limited concentration of uranium in the altered Fe-Ti oxides. Hence, it is more likely that the uranium has been trapped on the altered Fe-Ti oxides during diagenesis, possibly from uranium desorbed from the surface of clay minerals during diagenetic recrystallization. Another significant proportion of uranium has been probably trapped on the organic matter, and on the clay minerals offering large specific surfaces (e.g., smectites).

9.6.2. Pre-ore sulphidization

Pre-ore sub-idiomorphic iron disulphides are disseminated in primary reduced sandstones of the Saihan Formation (**Figure 76E**). Their heavy sulphur isotopes signature indicates that their origin is different from the biogenic ore-stage sulphides. Infiltration of oxygenated groundwater leads to the oxidation of pre-ore iron disulphides into hematite and limonite. This oxidation has provided sulphate ions (SO_4^{2-}) that are needed for BSR (**Figure 76A, B**). Moreover, microbes including SRB have been carried to the front by meteoric waters (Abdelouas et al., 1998).

9.6.3. Ore-stage Fe-Ti oxides alteration and sulphidization

During ore-stage sulphidization Fe-Ti oxides were highly altered. Dissolved sulphides (H_2S , HS^-) produced by SRB have strongly increased their solubility. Fe-Ti oxides were partly to totally dissolved and epigenized into iron disulphide (**Figure 76D**). During this alteration, their pre-ore uranium content was reconcentrated up to few wt.% UO_2 even though a minor part of this uranium content may be provided by the roll itself. Therefore Fe-Ti oxide's pre-ore uranium content was more available for leaching by oxygenated groundwater and have contributed in the ore-stage uranium mineralization.

Bacterial sulphate reduction was responsible for ore-stage sulphidization. Coaly fragments and fossil plant debris were degraded by SRB, Fe-Ti oxides were altered and iron disulphides were produced in the pyrite zone (or BSR zone, **Figure 76E**). Therefore BSR was responsible for (i) the crystallization of iron disulphide which is the main host mineral of the uranium mineralization, and (ii) the secondary reducing barrier due to the production of dissolved sulphides such as H₂S and thus for direct or indirect U(VI) reduction and U(IV) precipitation.

9.6.4. Ore-stage U mineralization

Infiltration of oxygenated groundwater was responsible for (i) partial leaching of pre-ore uranium concentration int the Saihan Formation, (ii) oxidation of organic matter and pre-ore iron disulphide to form sulphates. Thus, uranyl sulphate ions were carried downward by oxidizing aqueous solutions through the host sandstone. At low temperature and in the range of pH measured in the Bayinwula area (pH= 6.35-8.48; Nie, 2010) the dominant uranium complex in oxidized waters was $\text{UO}_2(\text{HPO}_4)_2^{2-}$. When arriving at the redox front, U(VI) was reduced by the secondary reducing barrier formed by H₂S produced by the BSR. U(IV) was precipitated as P-rich coffinite and ningyoite as epigeny of ore-stage iron disulphide (**Figure 76A, C**).

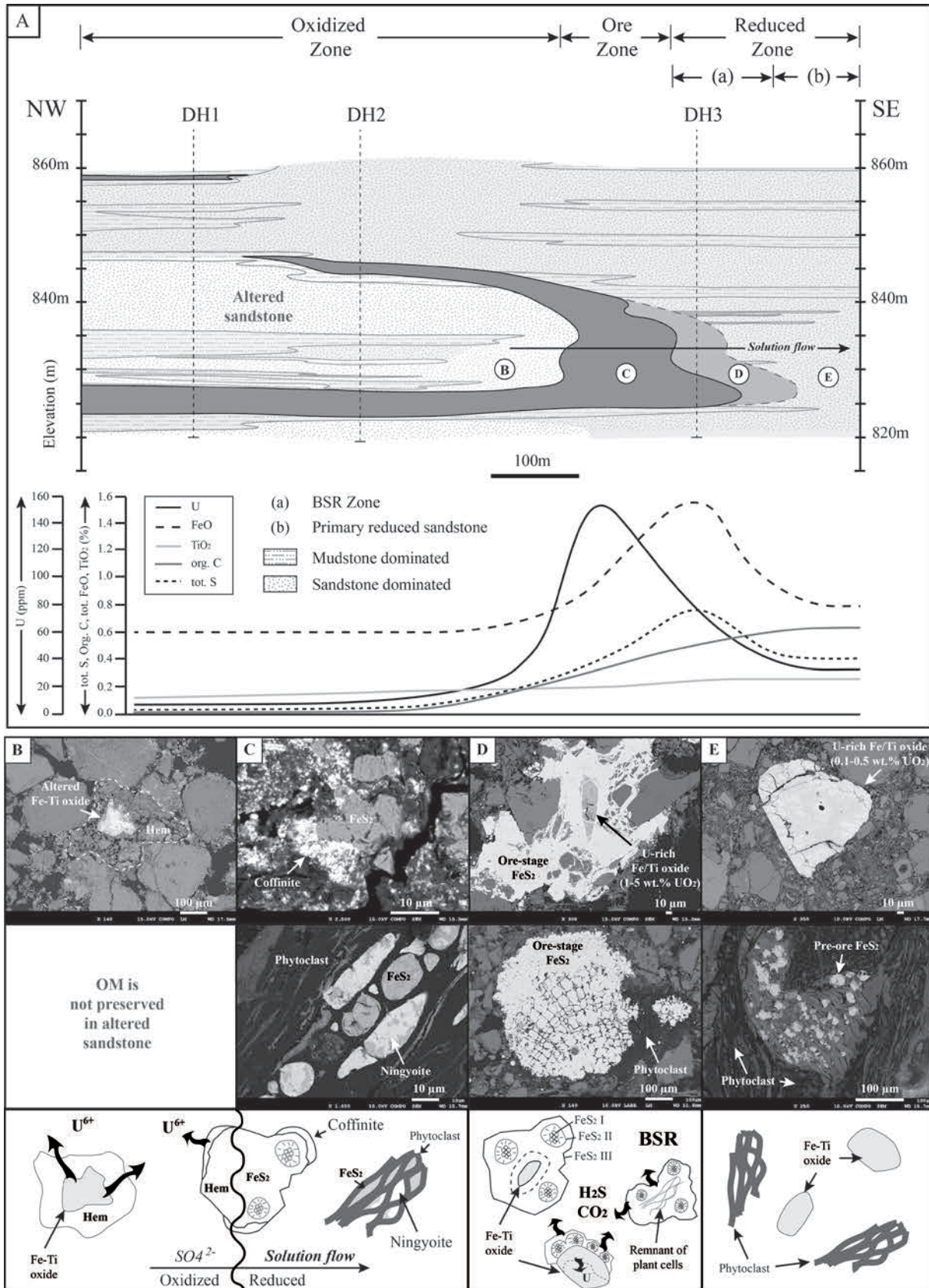


Figure 76. Metallogenetic model of the Bayinwula roll front deposit. A= drill hole cross-section of the Bayinwula deposit in correlation with geochemical zoning. B= mineral alteration and U remobilization in the oxidized zone; C= uranium mineralization associated with iron disulphide and organic matter in the ore zone; D= ore stage iron

disulphides in epigeny of Fe-Ti oxide and organic matter related to BSR occurring in the pyrite zone (or BSR zone); E= Fe-Ti oxides and organic matter in the reduced host sandstone.

10. Regional implications

As stated in the introduction, several genetic models proposed for roll front deposits emphasize the role of bacterial metabolic processes in the development of ore-stage iron disulphides (Jensen, 1958; Lizitsyn and Kuznetsova, 1967; Belyi et al., 1972; Rackley, 1972; Reynolds et al., 1982). The study of the Bayinwula roll front deposit presented in this paper evidenced a biogenic model for explaining (i) the liberation of uranium from pre-ore U-bearing phases (Fe-Ti oxides and organic matter), (ii) the crystallization of iron disulphides and (iii) the deposition of the uranium mineralization, (iv) the high P content of the uranium minerals. In northern China, at least for the sandstone-hosted uranium deposits of the Erlian, Yilli and Ordos basins it has been proved that they are related to biogenic processes involving sulphate reducing bacteria (Min et al., 2005a; 2005b; Cai et al., 2007a; 2007b). Therefore, Mesozoic intracontinental sedimentary basins of northern China may be considered as favourable geological setting for the genesis of biogenic roll front uranium deposits: (i) the post-rift tectono-stratigraphic evolution of these basins is responsible for the generation of confined permeable host sandstones for roll front uranium deposits (Bonnetti, et al., accepted), (ii) the relative abundance of type III or type IV kerogen in these host sandstones may be a discriminating factor of BSR. Moreover, a similar geological context was at least identified in the East Gobi Basin by Johnson (2004) indicating a favourable potential for the discovery of new biogenic-related roll front deposits in the Central Asia Uraniferous province.

11. Conclusions

The Bayinwula roll front uranium deposit is hosted in the reduced sandstones of the Saihan Formation that were deposited during the post-rift stage of the Erlian Basin. A biogenic model of both ore-stage iron sulphidization and uranium mineralization is proposed:

- (i) Channel sandstones deposited in a braided fluvial environment constitutes favourable permeable host-rocks for the formation of roll front uranium mineralization. The mudstone-dominated facies of overbank deposits, below and above the deposit, represents aquitars permitting the confinement of the host-sandstones for confining meteoric fluid infiltration and ore leaching solutions for their mining.

- (ii) Elevated uranium preconcentration has been trapped in the reduced sandstones of the Saihan Formation. The pre-ore uranium concentration adsorbed on altered detrital Fe-Ti oxides, and possible synsedimentary uranium trappin on organic matter and clay minerals, represent significant uranium sources in the host-sandstones.
- (iii) Organic matter occurring in the host sandstone is inherited from land plants and corresponds to a kerogen of type IV. No migrated hydrocarbons were identified.
- (iv) Bacterial sulphate reduction was responsible for the generation of ore-stage iron disulphide, the liberation of uranium from the U-rich Fe-Ti oxide and organic matter during their epigenesist by iron disulphides, the production of a secondary H₂S-rich reducing barrier and thus indirectly for U(VI) reduction and U(IV) precipitation, and for the high phosphorus content of the uranium minerals.
- (v) Low temperature oxygenated groundwater and pH conditions led to the precipitation of P-rich coffinite and ningyoite at the redox front. Uranium minerals occur in epigeny of ore-stage iron disulphide.

Favourable geological setting in Mesozoic intracontinental sedimentary basins of northern China was identified for biogenic-related roll front uranium deposits. Therefore biogenic model for sandstone-hosted uranium deposits may be common in the Central Asia Uraniferous Province which extends from Kazakhstan to Mongolia and from southern Russia to northern China.

Acknowledgements

Financial support for this study was provided by AREVA Mines, the East China Institute of Technology in Fuzhou, Jiangxi and the Geological Team N°208, BOG, CNNC in Baotou, Inner Mongolia. The authors acknowledge colleagues from the East China Institute of Technology for the presentations and scientific discussions that have been organised about the geology of the Erlian Basin, as well as colleagues from the Geological Team N°208 for field support and the access to drill cores. The authors are indebted to P. Lach for the acquisition of ICPMS data, J. Mercadier for his kind contribution in the realization of sulphur isotopes analyses and M.C. Caumon for the acquisition of Raman spectra.

Appendix 13. Whole-rock geochemistry of stratigraphic drill-core samples from the Bayinwula area. Major elements (in %), organic carbon (Corg, in %) and total sulphur (Stot, in %).

Sample ID	SiO ₂	Al ₂ O ₃	Fe ₂ O ₃	MnO	MgO	CaO	Na ₂ O	K ₂ O	TiO ₂	P ₂ O ₅	PF	Total	Corg	Stot
DHA-114.7m	82.95	8.36	0.77	0.01	0.10	0.23	1.46	4.21	0.12	<LOD	0.95	99.14	0.01	0.01
DHA-120.8m	73.77	12.54	1.39	0.02	0.48	0.68	2.36	3.46	0.51	0.03	3.84	99.08	0.02	0.01
DHA-127.5m	80.87	9.93	0.38	0.01	0.13	0.57	1.95	4.40	0.10	0.03	1.12	99.47	0.01	0.05
DHA-141.5m	76.39	11.87	1.55	0.01	0.21	0.58	2.66	4.03	0.24	0.03	2.32	99.89	0.09	0.64
DHA-156.0m	83.55	8.84	0.71	0.01	0.12	0.31	1.97	3.45	0.20	0.03	1.25	100.44	0.02	0.30
DHA-169.5m	79.97	10.24	0.72	0.01	0.15	0.41	2.19	4.01	0.19	0.03	1.46	99.36	0.03	0.03
DHA-175.8m	64.03	15.45	3.73	0.04	1.02	0.47	1.32	2.85	0.82	0.06	9.07	98.86	0.62	0.56
DHA-183.6m	75.58	12.85	1.08	0.01	0.22	0.61	2.84	4.34	0.27	0.03	2.16	99.98	0.02	0.31
DHA-186.8m	72.31	9.08	3.59	0.01	0.15	0.33	1.82	3.55	0.23	0.06	8.25	99.39	2.85	2.42
DHB-35.3m	68.14	12.39	5.51	0.02	0.80	0.57	1.56	3.23	0.46	0.12	6.56	99.35	0.01	0.01
DHB-48.4m	68.82	14.41	2.66	0.01	0.80	0.67	2.31	3.87	0.32	0.08	5.92	99.85	0.01	0.01
DHB-54.7m	67.30	14.25	3.96	0.02	0.87	0.68	2.20	3.91	0.30	0.13	6.09	99.70	0.05	0.01
DHB-63.8m	49.82	12.63	10.73	0.04	1.40	0.63	1.46	2.59	0.56	0.11	9.36	99.33	0.65	0.03
DHB-64.2m	56.86	14.71	5.64	0.03	1.88	0.72	0.84	2.78	0.891	0.10	16.23	100.60	5.21	0.29
DHB-64.5m	46.74	12.54	5.35	0.03	1.69	0.91	0.66	1.99	0.65	0.14	28.41	99.11	10.89	0.68
DHB-65.6m	67.38	14.60	4.38	0.12	1.26	0.74	2.39	3.38	0.49	0.14	5.38	100.27	0.26	0.02
DHB-71.1m	36.21	9.23	6.22	0.06	1.66	1.22	0.61	1.71	0.75	0.13	42.55	100.36	23.52	0.26
DHB-74.8m	58.96	13.62	9.48	0.28	1.82	0.93	1.71	2.89	0.68	0.20	9.27	99.83	0.94	0.07
DHB-91.8m	68.82	13.77	3.66	0.05	1.26	0.75	2.02	3.03	0.52	0.09	5.65	99.61	0.04	0.02
DHB-99.0m	65.90	15.59	3.95	0.07	1.19	0.83	2.65	4.15	0.40	0.13	5.14	100.00	0.04	0.09
DHB-100.8m	58.31	13.06	7.57	0.21	1.74	0.96	1.75	2.58	0.63	0.15	12.38	99.33	3.16	0.05
DHC-61.2m	53.74	13.08	7.17	0.07	2.03	6.73	1.50	2.61	0.72	0.21	12.05	99.89	0.06	0.03
DHC-70.4m	77.80	11.14	1.22	0.02	0.28	1.40	2.50	3.23	0.32	0.06	1.52	99.48	0.01	0.03
DHC-80.3m	80.89	8.03	2.38	0.02	0.43	0.87	1.42	2.76	0.21	0.09	2.18	99.36	0.02	0.01
DHC-83.2m	77.27	9.60	2.69	0.03	0.76	1.25	1.87	2.62	0.32	0.10	2.84	99.34	0.02	0.49
DHC-86.7m	68.17	13.29	4.08	0.03	1.43	0.98	1.53	2.68	0.68	0.10	7.08	100.03	0.16	0.54
DHC-89.9m	80.59	9.74	1.44	0.02	0.25	1.20	2.16	2.83	0.32	0.06	1.50	100.10	0.01	0.38

Appendix 14. Whole-rock geochemistry of drill-core samples from the Bayinwula deposit. Major elements (in %), organic carbon (Corg, in %) and total sulphur (Stot, in %).

Sample ID	SiO ₂	Al ₂ O ₃	Fe ₂ O ₃	MnO	MgO	CaO	Na ₂ O	K ₂ O	TiO ₂	P ₂ O ₅	PF	Total	Corg	Stot
DH1-111.6m	74.14	12.07	1.77	0.02	0.53	0.35	1.65	2.82	0.66	0.04	5.94	99.97	0.52	0.23
DH1-120.8m	85.80	7.54	0.34	0.00	0.05	0.14	1.37	3.85	0.07	<LOD	0.94	100.10	0.01	0.13
DH1-122.4m	82.39	8.85	0.89	0.01	0.13	0.23	1.66	4.05	0.18	<LOD	1.76	100.16	0.08	0.13
DH1-128.3m	82.96	8.55	0.50	0.00	0.04	0.26	1.87	3.86	0.07	<LOD	0.89	99.01	0.00	0.00
DH1-133.3m	81.94	9.25	0.68	0.00	0.08	0.18	1.99	4.25	0.09	<LOD	1.21	99.68	0.00	0.00
DH1-139.8m	79.22	10.78	0.63	0.01	0.11	0.41	2.46	4.20	0.17	0.03	1.58	99.59	0.01	0.00
DH1-142.5m	73.64	9.92	3.68	0.01	0.30	0.60	2.02	3.37	0.22	0.08	6.29	100.12	1.48	0.05
DH1-144.8m	70.95	13.14	2.06	0.02	0.59	0.39	1.76	2.99	0.67	0.04	6.50	99.09	0.44	0.40
DH1-146.3m	70.51	14.15	2.23	0.02	0.70	0.43	1.76	3.04	0.76	0.04	6.65	100.28	0.57	0.29
DH1-147.3m	68.93	14.21	3.13	0.02	0.77	0.40	1.53	3.02	0.74	0.04	7.02	99.80	0.13	0.04
DH2-111.8m	75.93	11.61	1.81	0.02	0.34	0.35	1.93	3.26	0.69	0.03	4.25	100.22	0.25	0.49
DH2-121.3m	83.04	9.05	0.65	0.01	0.11	0.25	1.86	3.85	0.14	0.03	1.20	100.19	0.00	0.24
DH2-123.6m	81.16	9.97	0.51	0.00	0.10	0.35	2.14	4.19	0.13	0.03	1.19	99.75	0.01	0.18
DH2-128.0m	83.00	9.01	0.61	0.01	0.09	0.25	1.84	4.04	0.12	<LOD	1.13	100.09	0.02	0.06
DH2-134.5m	81.33	9.66	0.57	0.00	0.10	0.25	2.01	4.34	0.14	0.03	1.11	99.53	0.00	0.02
DH2-135.4m	81.51	9.44	0.75	0.01	0.12	0.23	1.79	4.39	0.16	0.03	1.38	99.80	0.02	0.32
DH2-139.5m	84.45	8.29	0.55	0.02	0.08	0.19	1.70	3.79	0.10	<LOD	0.96	100.12	0.00	0.02
DH2-146.2m	70.40	12.95	2.31	0.02	0.44	0.52	2.33	3.37	0.55	0.04	6.55	99.47	1.11	0.89
DH2-152.6m	68.57	14.22	3.50	0.02	0.78	0.48	2.00	2.75	0.68	0.05	7.98	101.02	0.58	1.00
DH2-156.0m	82.26	9.41	0.58	0.01	0.08	0.28	2.45	3.59	0.12	0.03	0.95	99.76	0.00	0.26
DH3-117.0m	82.27	8.92	0.55	0.00	0.08	0.26	1.73	4.17	0.09	0.03	1.38	99.46	0.01	0.25
DH3-125.0m	72.11	12.63	2.47	0.02	0.51	0.39	2.00	3.05	0.60	0.03	5.96	99.76	0.28	0.72
DH3-128.9m	70.59	12.45	3.52	0.02	0.49	0.42	2.05	3.06	0.63	0.03	6.49	99.75	0.47	1.50
DH3-132.8m	79.84	9.10	1.11	0.01	0.09	0.25	1.94	3.98	0.27	<LOD	2.37	98.94	0.17	0.60
DH3-135.6m	78.54	9.03	1.46	0.01	0.12	0.29	1.83	3.83	0.14	0.03	4.81	100.08	1.36	0.88
DH3-138.4m	79.26	10.35	1.03	0.01	0.11	0.32	2.83	3.48	0.15	0.03	2.21	99.78	0.13	0.53
DH3-140.0m	77.11	11.12	1.45	0.01	0.21	0.37	2.82	3.33	0.26	0.03	3.61	100.31	0.33	0.64
DH3-142.0m	72.34	12.46	2.21	0.01	0.31	0.50	3.24	3.22	0.35	0.04	5.39	100.08	1.20	1.11

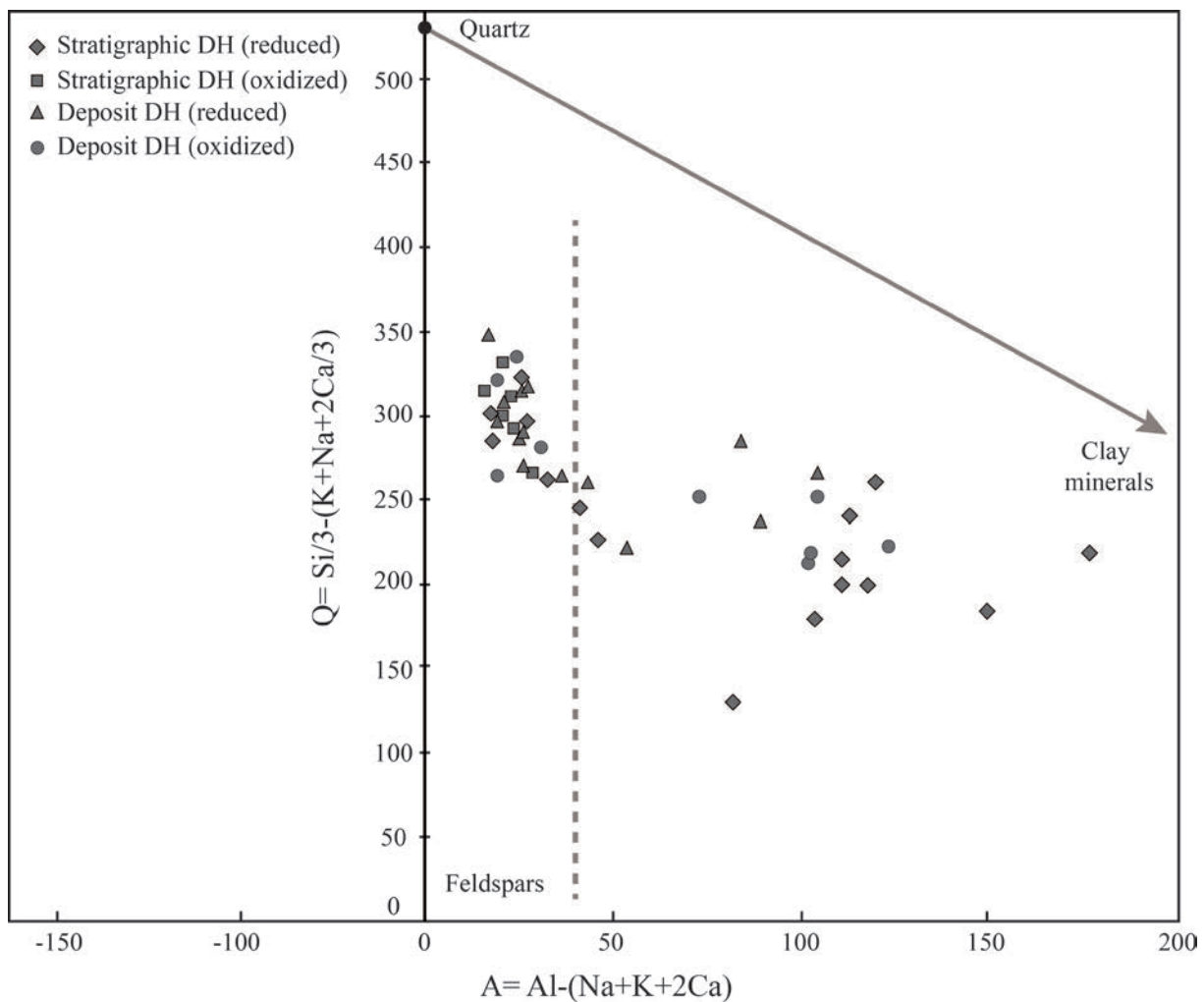
Appendix 15. Whole-rock geochemistry of stratigraphic drill-core samples from the Bayinwula area. Trace elements (in ppm).

Sample ID	As	Ni	Co	Cu	Zn	La	Ce	Nd	Mo	V	U	Th	Zr
DHA-114.7m	10.07	<LOD	1.67	<LOD	14.10	16.23	37.12	14.74	0.66	12.91	4.55	5.57	101.00
DHA-120.8m	2.22	6.43	3.18	<LOD	31.08	34.90	74.80	30.00	0.51	29.77	10.52	18.11	376.20
DHA-127.5m	1.87	<LOD	2.95	<LOD	15.38	21.30	58.93	19.16	<LOD	7.67	25.55	4.69	67.86
DHA-141.5m	8.37	<LOD	1.78	<LOD	21.40	24.18	56.39	21.38	0.51	15.96	31.95	7.36	123.70
DHA-156.0m	6.92	<LOD	2.33	<LOD	14.02	18.07	42.34	17.05	3.46	9.40	39.90	6.90	92.45
DHA-169.5m	2.26	<LOD	2.72	<LOD	16.70	27.89	63.83	24.23	0.51	13.09	13.77	8.89	124.10
DHA-175.8m	7.36	19.32	10.35	20.20	241.10	33.29	72.10	36.56	5.92	62.39	820.70	14.36	287.10
DHA-183.6m	8.92	<LOD	3.06	<LOD	20.47	30.75	74.69	31.88	3.82	13.11	79.64	8.85	136.10
DHA-186.8m	50.71	12.23	7.01	<LOD	155.80	21.59	53.29	23.53	50.73	28.18	1058.00	7.79	270.10
DHB-35.3m	8.03	14.26	5.34	9.32	68.17	29.04	48.73	27.07	1.20	74.12	4.49	8.45	149.80
DHB-48.4m	8.02	8.17	3.93	6.32	33.04	17.65	31.94	16.07	<LOD	41.85	1.96	4.77	84.87
DHB-54.7m	8.73	10.54	4.65	20.02	64.14	22.37	35.14	20.57	0.65	38.37	6.07	4.79	98.30
DHB-63.8m	57.48	27.74	15.08	15.03	81.15	19.43	35.82	22.59	3.81	73.76	14.80	7.18	99.52
DHB-64.2m	14.26	82.03	46.72	34.51	219.10	65.57	138.00	73.55	4.47	107.60	244.80	12.94	162.80
DHB-64.5m	42.24	45.19	21.33	39.70	92.32	97.71	182.20	92.21	9.06	102.40	472.40	14.18	149.30
DHB-65.6m	7.85	13.44	8.29	8.73	67.48	36.44	59.98	33.00	0.89	53.58	18.70	6.35	136.90
DHB-71.1m	32.64	40.39	20.12	33.07	171.50	166.10	274.30	153.60	11.90	84.14	65.63	13.39	114.50
DHB-74.8m	8.12	24.19	14.10	10.90	153.90	56.93	105.70	58.79	1.57	61.30	24.81	8.01	128.20
DHB-91.8m	2.78	13.99	8.19	9.05	41.24	19.73	38.90	18.48	0.56	64.96	3.22	6.91	172.70
DHB-99.0m	3.79	13.75	8.27	7.61	40.61	22.28	41.45	19.98	0.83	50.24	2.44	5.81	127.50
DHB-100.8m	5.75	25.85	14.64	15.13	306.20	45.64	85.66	44.57	4.11	80.60	6.65	8.50	153.30
DHC-61.2m	3.98	55.31	26.30	30.45	87.01	38.25	73.39	33.03	0.91	105.40	1.96	7.89	161.40
DHC-70.4m	2.53	7.32	4.72	<LOD	17.24	22.32	41.98	17.44	0.54	27.48	1.42	4.62	121.40
DHC-80.3m	11.87	15.22	9.40	6.75	22.50	18.13	34.98	14.78	2.52	27.05	3.06	3.84	91.78
DHC-83.2m	10.57	18.77	12.07	36.83	27.80	18.09	37.82	17.02	1.53	36.42	7.84	4.21	101.20
DHC-86.7m	4.45	24.14	13.57	17.32	76.03	33.50	64.47	27.89	1.39	71.77	31.36	7.84	171.90
DHC-89.9m	3.46	10.29	8.21	17.29	23.18	17.70	34.30	14.31	0.74	21.60	10.45	3.27	131.60

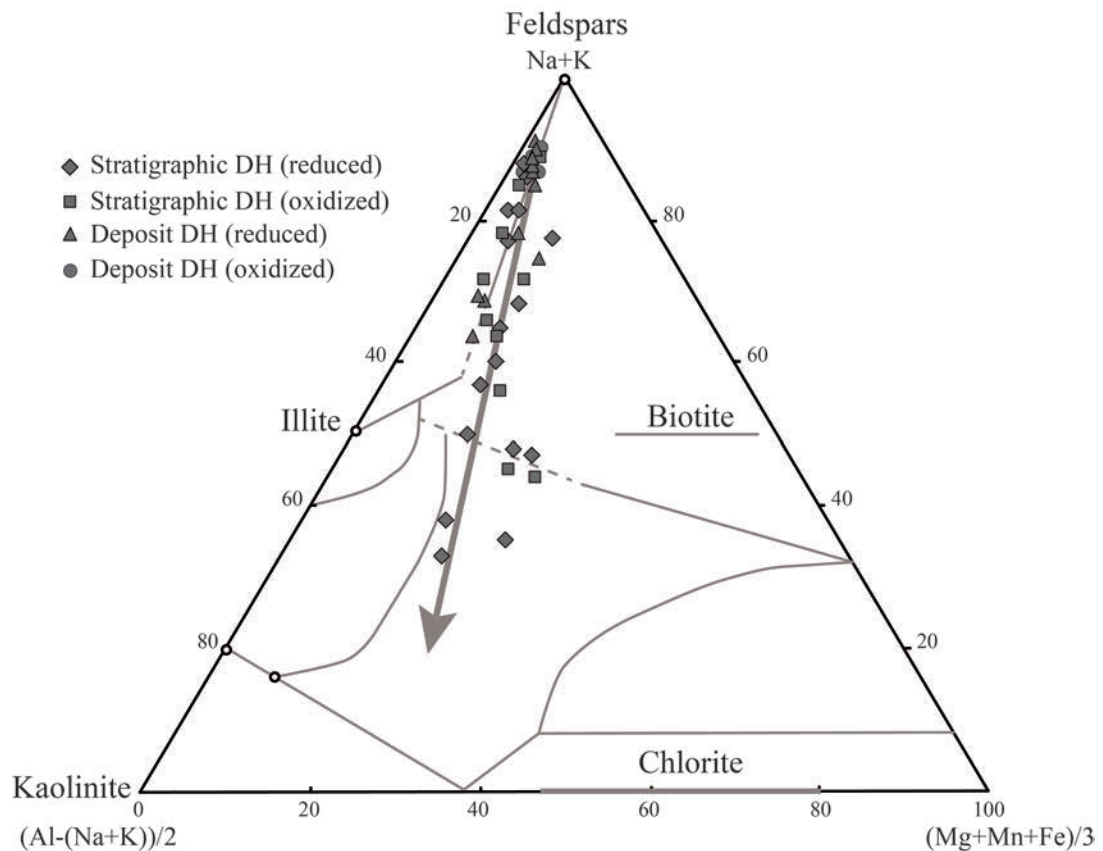
Appendix 16. Whole-rock geochemistry of drill-core samples from the Bayinwula deposit. Trace elements (in ppm).

Sample ID	As	Ni	Co	Cu	Zn	La	Ce	Nd	Mo	V	U	Th	Zr
DH1-111.6m	21.30	9.16	7.15	10.77	49.73	28.64	61.31	25.93	120.50	40.41	698.00	13.91	358.30
DH1-120.8m	3.26	<LOD	1.55	<LOD	11.66	13.70	33.78	12.07	0.91	5.10	19.00	4.30	73.34
DH1-122.4m	6.51	8.65	4.37	6.34	21.05	17.57	43.12	17.38	2.61	11.67	16.78	6.50	118.30
DH1-128.3m	8.44	<LOD	1.50	<LOD	<LOD	13.55	30.68	12.07	2.51	6.04	4.65	3.61	30.35
DH1-133.3m	11.06	<LOD	2.08	<LOD	12.88	14.71	32.70	12.86	2.51	7.35	5.51	4.69	88.72
DH1-139.8m	9.61	<LOD	2.26	5.64	12.47	20.54	48.50	18.82	4.84	9.65	8.00	5.67	90.31
DH1-142.5m	37.79	47.79	26.62	18.90	161.50	100.60	256.30	95.89	21.02	45.22	147.70	8.39	337.90
DH1-144.8m	12.06	19.86	12.74	12.92	60.70	37.46	76.74	33.38	11.22	45.30	111.90	14.65	344.30
DH1-146.3m	8.83	30.46	14.85	26.01	77.47	39.42	79.61	34.13	15.20	53.13	92.34	15.63	393.00
DH1-147.3m	7.94	17.50	4.67	18.38	62.13	40.35	79.53	35.40	4.69	50.55	17.89	14.08	342.00
DH2-111.8m	19.42	6.39	4.12	11.80	38.85	39.41	84.04	34.15	4.27	33.78	70.31	20.98	643.90
DH2-121.3m	8.63	5.17	2.67	6.58	12.24	18.65	42.18	16.54	3.91	9.38	37.26	6.48	108.80
DH2-123.6m	7.18	6.93	5.22	<LOD	13.36	15.84	37.84	14.32	6.57	8.99	45.97	4.42	93.54
DH2-128.0m	4.03	5.96	2.82	7.24	13.34	16.54	35.32	14.12	2.74	8.44	10.94	5.62	106.00
DH2-134.5m	3.05	<LOD	1.69	5.55	<LOD	20.29	42.69	17.35	1.96	8.83	10.40	6.14	131.10
DH2-135.4m	11.99	5.21	3.89	<LOD	11.08	20.35	42.82	17.83	17.45	10.79	55.81	6.66	117.20
DH2-139.5m	7.24	5.43	1.65	5.02	11.36	12.19	29.43	11.94	2.46	6.33	6.52	3.96	75.80
DH2-146.2m	14.90	11.27	5.94	9.47	110.60	39.22	86.24	39.22	18.28	34.24	120.20	19.22	471.70
DH2-152.6m	13.48	19.40	10.43	19.07	53.37	29.71	65.83	30.99	34.58	53.22	65.47	11.93	308.20
DH2-156.0m	7.28	6.11	1.95	<LOD	<LOD	12.09	27.24	12.71	25.51	7.85	30.55	4.57	110.80
DH3-117.0m	7.67	7.42	4.39	<LOD	14.27	15.56	39.61	15.77	4.86	10.64	25.42	4.14	63.67
DH3-125.0m	30.48	14.86	5.85	11.38	46.71	28.53	62.01	28.06	22.87	31.66	46.26	11.75	355.60
DH3-128.9m	56.14	10.49	6.40	10.72	43.82	41.18	85.52	36.27	41.56	37.63	44.75	16.61	534.00
DH3-132.8m	28.33	<LOD	2.36	<LOD	25.28	17.93	39.01	15.64	65.01	11.22	60.86	7.30	141.70
DH3-135.6m	22.41	6.22	2.88	<LOD	94.36	15.55	38.10	16.25	46.54	36.96	62.96	4.54	132.30
DH3-138.4m	17.58	6.37	3.96	<LOD	21.41	14.05	32.46	15.20	38.30	13.23	40.96	5.02	122.30
DH3-140.0m	18.18	6.27	3.48	<LOD	28.12	16.31	38.17	17.42	31.01	20.75	60.86	5.37	175.10
DH3-142.0m	20.04	13.08	4.40	<LOD	102.30	21.39	50.25	23.94	53.72	34.02	117.20	7.17	307.90

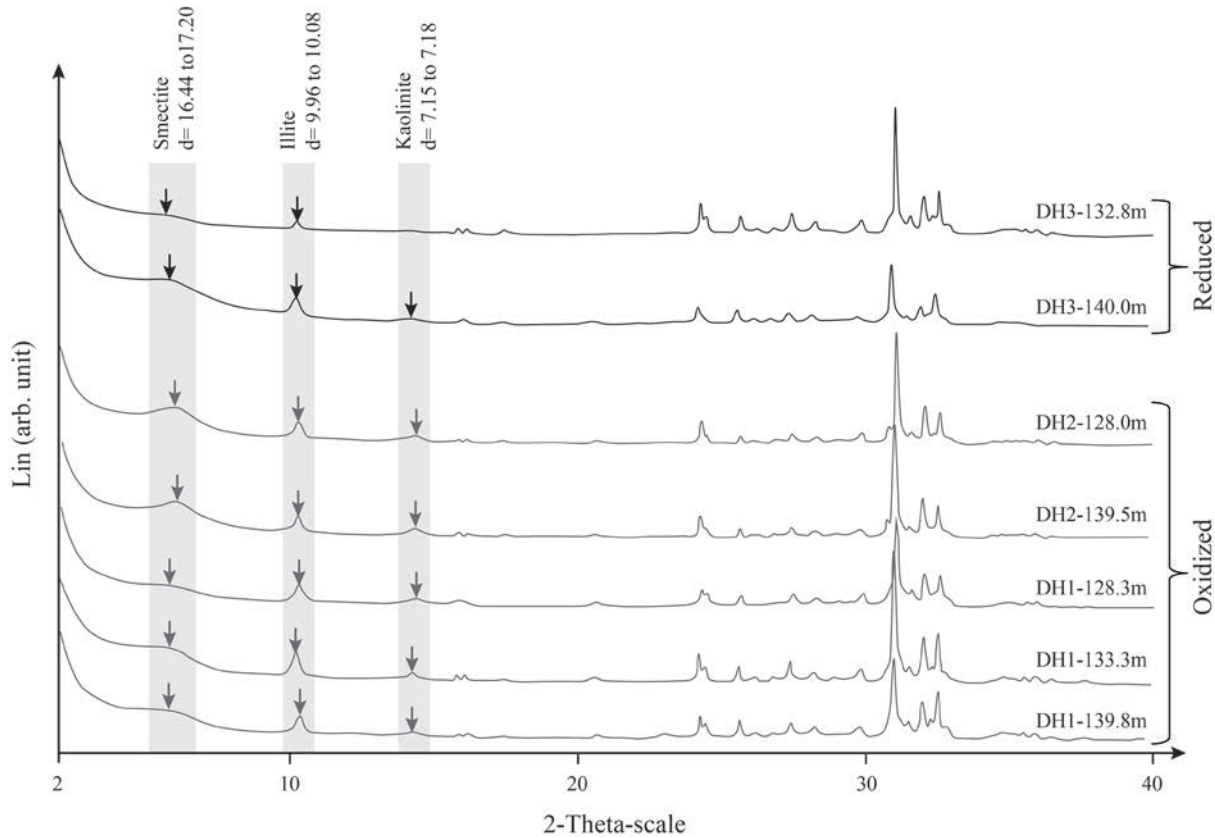
Appendix 17. Q-A diagram showing the relative abundance between quartz, feldspar and clay minerals in sandstone of the Saihan Formation.



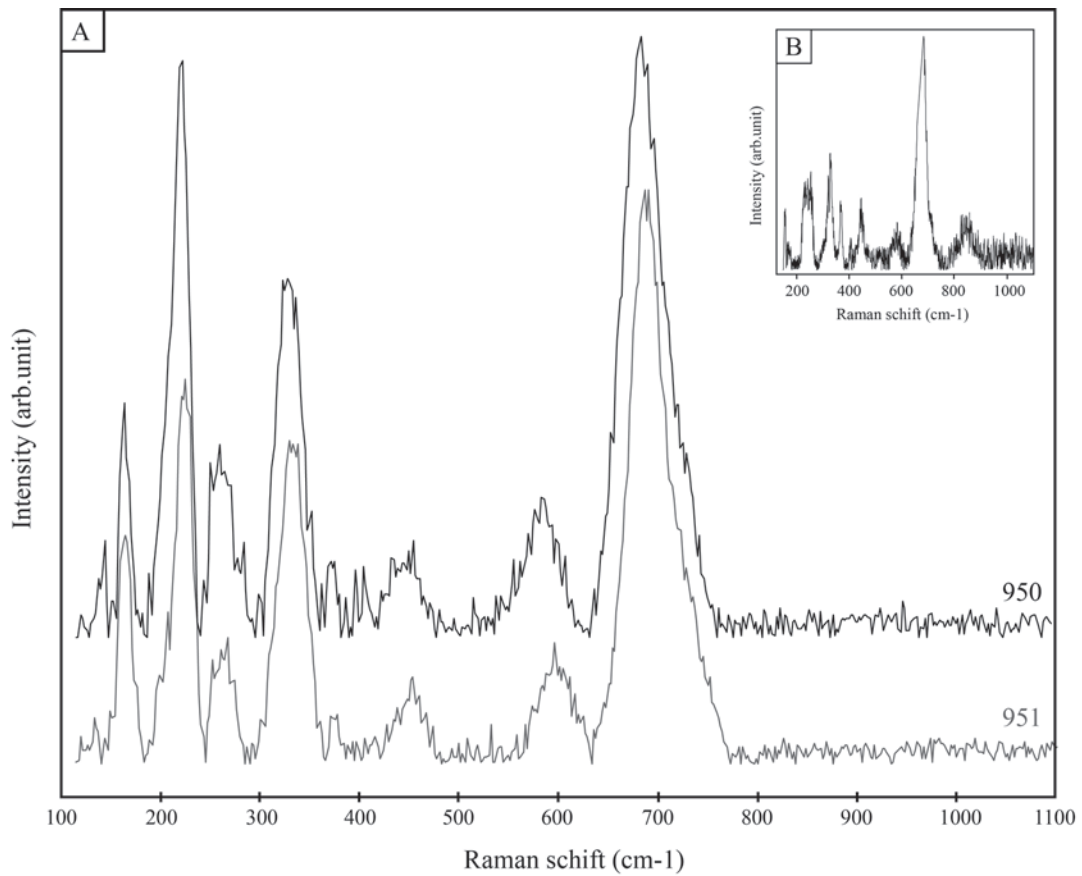
Appendix 18. Na+K / Al-(Na+K))/2 / (Mg+Mn+Fe)/3 diagram showing the typology of clay minerals occurring in sandstone of the Saihan Formation.



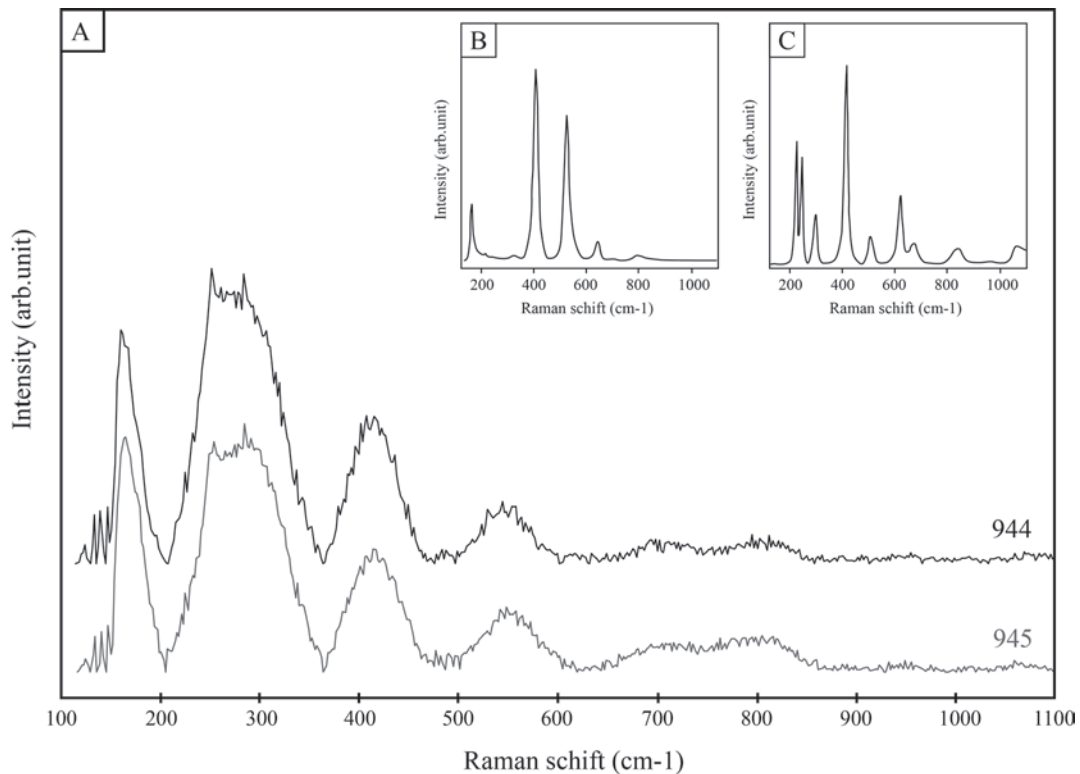
Appendix 19. X-ray diffractograms of sandstone hosting the Bayinwula deposit from the oxidized to the reduced zone.



Appendix 20 .A= representative Raman spectra from relatively preserved Fe-Ti oxides. B= Reference spectrum of ilmenite from RRUFF database.



Appendix 21. A= representative Raman spectra from altered Fe-Ti oxides. B= Reference spectrum of anatase from RRUFF database. C= reference spectrum of hematite from RRUFF database.



CONCLUSIONES GENERALES



Le bassin d’Erlian est un bassin sédimentaire intracontinental du Nord-Est de la Chine (Mongolie intérieure) formé au cours de l’extension continentale qui se développe au Mésozoïque en Asie de l’Est (Chapitre 1). A l’instar de nombreux autres bassins de la province métallogénique centre asiatique qui s’étend depuis le Kazakhstan au Sud de la Sibérie et au Nord de la Chine, il contient des minéralisations uranifères de type roll front qui représentent aujourd’hui une des ressources en uranium les plus économiques.

Sur l’exemple du bassin d’Erlian, dans le cadre de ce travail de thèse nous avons tenté d’appréhender l’intégralité du cycle de l’uranium à l’échelle régionale, depuis son extraction du manteau lithosphérique jusqu’à son dépôt sous la forme de minéralisation de type synsédimentaire-diagénétique et épigénétique de type roll front.

Le socle sur lequel repose le bassin d’Erlian correspond à la partie Sud-Est de la ceinture orogénique d’Asie centrale (COCA). Il s’est formé principalement au Paléozoïque par subductions et accrétions successives de micro-continents, d’arcs magmatiques et de prismes d’accretion sédimentaire qui se sont assemblés entre le craton sibérien et le craton de Chine du Nord. Les données géochronologiques U/Pb sur zircons et U-Th-Pb sur monazites appartenant aux granites et aux roches volcaniques du socle environnant le bassin d’Erlian nous ont permis de dater ces roches de la fin du Paléozoïque (Carbonifère-Permien; 312.4 ± 4.8 Ma et 291.3 ± 4.8 Ma) et du Trias (236.8 ± 5.8 Ma). De plus, les âges obtenus sur les monazites détritiques appartenant aux grès des unités sédimentaires du bassin ont donné une gamme d’âges, plus large allant du Paléozoïque au Crétacé: avec des âges hercyniens (322.2 ± 8.8 Ma), indosiniens (238.0 ± 39.0 Ma), yanshanien (160.3 ± 7.6 Ma) et crétacé (103.6 ± 6.3 Ma). Ainsi, le socle sur lequel repose le bassin d’Erlian est composé de roches formées à l’Hercynien, au moment de l’accretion du COCA, mais également au cours des différentes orogenèses plus jeunes, indosiniennes et yanshanienne, qui se sont succédées jusqu’à l’extension majeure de la fin du Mésozoïque. Cela signifie également que l’ensemble de ces roches a contribué au remplissage du bassin en tant que sources des sédiments et probablement de l’uranium piégé de manière synsédimentaire. Les analyses Sm-Nd réalisées sur les granites et les roches volcaniques hercyniennes et indosiniennes ont montré des valeurs très faibles du rapport $^{143}\text{Nd}/^{144}\text{Nd}_i$ ($0.512241 < ^{143}\text{Nd}/^{144}\text{Nd}_i < 0.512523$) qui indiquent que ces roches sont probablement dérivées de la fusion partielle d’un manteau enrichi. Les valeurs $\epsilon\text{Nd}_{(t)}$ ($-2.0 < \epsilon\text{Nd}_{(t)} < 5.3$) confirment cette source mantellique mais suggèrent également un mélange avec du matériel crustal ($\epsilon\text{Nd}_{(t)} < -1.0$) pour les granites indosiniens (Chapitre 4). Les granites hercyniens et indosiniens correspondent principalement à des granites métalumineux qui se caractérisent respectivement par des séries magmatiques calco-alcalines peu potassiques et

calco-alcalines fortement potassiques. Les environnements géodynamiques de mise en place de ces granites correspondent à: (i) un contexte de subduction océanique à la fin de l’Hercynien (Lin et al., 2008) synchrone de la formation des granites calco-alcalin peu potassiques, mais pendant lequel des sédiments ont pu être injectés dans le manteau et ainsi contribuer à son enrichissement en éléments incompatibles tel que l’uranium sans pour autant avoir été mis à contribution pour la genèse du magmatisme à ce stade; (ii) un contexte de fin de subduction pendant lequel du matériel continental à pu être subducté avec une enrichment supplémentaire du manteau en éléments incompatibles et associé à l'accrétion finale des blocs continentaux à l’Indosinien (Lin et al., 2008). Les granites indosiniens calco-alcalins fortement potassiques qui sont alors formés montrent un enrichissement important non seulement en K mais également en U et Th. Par cristallisation fractionnée des roches très différencierées fortement enrichies en U (jusqu’à 21 ppm U) sont formées. Elles présentent une paragenèse minérale à biotite, amphibole, titanite, allanite, U-thorite, zircon et apatite caractéristique de ce type de magmatisme. Ici, l’U-thorite (moy.= 1.00 wt.% U) et l’allanite (moy.= 0.09 wt.% U) représentent les principaux minéraux porteurs d’U et sont tous deux métamictes, indiquant que leur concentration en uranium a pu être libérée en grande partie de la structure cristalline et relâchée dans la roche et dans les fluides qui ont pu y percoler. Les valeurs des rapports Th/U élevés (jusqu’à 19) dans les échantillons les plus superficiels suggèrent qu’une majeure partie de l’uranium contenu dans ceux-ci a été lessivée. Un bilan de masse calculé pour les granites indosiniens indique qu’ils ont pu libérer au minimum 6000t U/km³ (Chapitre 4). Par conséquent, les granites Indosiniens constituent des sources primaires privilégiées pour les minéralisations encaissées dans le bassin. Enfin, les âges modèles (T_{DM}) calculés pour ces roches indiquent un âge maximum d’extraction de l’uranium du manteau au Néoprotérozoïque (< 893 Ma) qui correspondrait à un épisode de rifting majeur dans cette région, responsable de la fragmentation du super continent Rodinia (Li et al., 2003). De ce fait, la province métallogénique d’Asie centrale serait une province jeune comparée aux autres provinces majeures du Canada, d’Australie et d’Afrique qui sont en rapport avec des socles Archéens à Paléoprotérozoïque.

Le bassin d’Erlian s’est développé au cours de trois épisodes tectono-sédimentaires majeurs, de la fin du Jurassique à la fin du Crétacé : (i) une phase pré-rift exprimée par la production de roches volcaniques principalement intermédiaires à acides, (ii) une phase syn-rift caractérisée par le dépôt des sédiments fluvio-lacustres des formations d’Arshan et de Tengge’er et (iii) une phase post-rift caractérisée par le dépôt de sédiments principalement fluviatiles des formations de Saihan et Erlian.

Les analyses U/Pb sur zircons réalisées sur les roches volcaniques situées à la base du bassin ont permis de dater l'ouverture de celui-ci à la fin du Jurassique-début du Crétacé (146 Ma±0). L'étude des faciès sédimentaires de la formation d'Erlian a permis d'identifier des facies sableux de chenaux fluviatiles et des faciès à dominante argileuse de plaine d'inondation (marais, lobe de débordement...). L'association de ces faciès et leur succession dans la colonne stratigraphique caractérisent un environnement de dépôt de plaine alluviale au sein duquel s'est développé un système fluviatile de type tresse (Chapitre 2). L'évolution stratigraphique de ces dépôts post-rifts montre clairement une alternance entre des unités sableuses dominées par des faciès de chenaux fluviatiles et des unités plutôt argileuses dominées par des faciès de plaine d'inondation, latéralement plus ou moins continues. Cette alternance traduit les pics de l'activité tectonique régionale qui s'exprime par une chute du niveau de base (niveau des lacs en domaine intracontinental) et la dominance des dépôts sableux de chenaux fluviatiles lors des phases de surrection, ainsi que par une hausse du niveau de base et la dominance des faciès argileux de plaine d'inondation lors des calmes tectoniques. Ainsi, la phase post-rift du bassin d'Erlian et des bassins environnants semblent correspondre à un contexte tectono-sédimentaire favorable pour la formation des réservoirs gréseux perméables et confinés qui correspondent aux pièges de la minéralisation uranifère. Les assemblages palynologiques déterminés pour la formation de Saihan et la formation d'Erlian (Chapitre 2) indiquent respectivement un âge Aptien-Albien (*Asteropollis asteroides* discriminant) et un âge de la fin du Campanien (*Ulmipollenites* ou *Ulmoideipites*, *Cranwellia*, *Buttinia* et *Momipites*). Le relai entre la phase syn-rift et la phase post-rift qui tend vers la fermeture du bassin, s'exprime par une discordance majeure au toit de la formation de Tengge'er et à la base de la formation de Saihan. Enfin, l'ensemble des unités du bassin a subit un raccourcissement NO-SE qui se caractérise par l'inversion des structures, la formation de plis antiformes et le basculement des unités sédimentaires. Cette inversion post-crétacée semble être à l'origine de la mise en drainage des réservoirs gréseux et donc de l'initiation du système roll front dans le bassin dont les minéralisations ont été datées au Tertiaire (44±5 Ma; Nie, 2008).

L'étude du gisement de Nuheting (10 000t U @ 0.03-0.1%; Dahlkamp, 2009) encaissé dans les faciès de plaine d'inondation (niveaux silto-argileux) de la formation d'Erlian a permis d'identifier des pré-concentrations syn-sédimentaires d'uranium et de caractériser l'évolution de ces concentrations au cours de la diagenèse (Chapitre 6). Les observations pétrographiques ainsi que les données minéralogiques et géochimiques sur roche totale ont montré trois phases de concentration de l'uranium distinctes:

- (i) Une phase de pré-concentration syn-sédimentaire où l'uranium est principalement adsorbé aux minéraux argileux ou associé à la matière organique (MO) détritique. L'uranium est dans ce cas concentré directement dans les environnements de dépôt sédimentaire de type marais ou de lacs peu profonds, présentant des conditions anoxiques dominantes.
- (ii) Une phase de minéralisation diagénétique où l'uranium a précipité sous forme de coffinite et pechblende en épigénie de la pyrite ou de la matière organique pyritisée. La pyrolyse rock-eval ainsi que les données géochimiques et les observations pétrographiques réalisées sur la matière organique ont permis de caractériser un kérogène de type IV (type III dégradé ou dérivé d'une MO pauvre en H). Les sédiments hôte de la minéralisation contiennent une MO présentant une faible maturité thermique et ne contiennent pas d'hydrocarbures migrés. Les pyrites se présentent sous forme de cristaux sub-automorphes, de ciment ou en épigénie de la matière organique. La signature en éléments traces de ces différentes pyrite indiquent des fortes concentrations en Se, Mo et As ce qui tente à démontrer une cristallisation commune au cours de la diagenèse précoce des sédiments de la formation d'Erlian. L'intégration des éléments tels que Mo et Se dans la pyrite caractérise un environnement réducteur favorable à la précipitation de l'uranium. Ainsi, au cours de l'évolution diagénétique de ces sédiments (compaction, recristallisation des argiles...) l'uranium va être en grande partie désorbé des minéraux argileux puis il va précipiter quasi *in situ* sous la forme de coffinite et pechblende. La faible perméabilité des faciès hôtes ne permet pas une redistribution majeure de l'uranium mais favorise plutôt sa reconcentration *in situ*.
- (iii) Une phase épigénétique qui se caractérise par la cimentation en sulfate et carbonate de la minéralisation uranifère. Cette cimentation tardive met en évidence la circulation d'un fluide oxydant qui pourrait avoir remobilisé une partie de la minéralisation. Cependant, les observations de cette cimentation sont très localisées et compte tenu de la faible perméabilité de la roche encaissante, une éventuelle remobilisation de l'uranium serait très limitée.

L'étude du gisement de Nuheting a donc permis de mettre en évidence de fortes pré-concentrations syn-sédimentaires dans le bassin d'Erlian, mais cette étude a surtout démontré que ces concentrations pouvaient être redistribuées et s'exprimer sous forme de phases minérales distinctes au cours de l'évolution diagénétique des sédiments et éventuellement être remobilisées de manière mineure par des épisodes épigénétiques de circulations fluides.

L'étude du gisement de Bayinwula localisé dans le sous-bassin de Manite a permis d'aborder les conditions physico-chimiques de formation d'une minéralisation de type roll front et de proposer un modèle génétique (Chapitre 7).

Le gisement de Bayinwula est encaissé dans les réservoirs gréseux perméables et réduits de la formation de Saihan. Des données géochimiques sur roche totale ont montré des concentrations élevées en U dans les parties réduites de ces grès à l'échelle du sous-bassin (2.44 à 70,31 ppm U; moy.= 30,36 ppm U). L'étude minéralogique détaillée des grès a permis d'identifier des oxydes de fer et titane détritiques (initialement de type ilménite pour une grande majorité et titano-magnétite) comme phases majeures porteuses des concentrations en U (38 % de l'U de la roche totale est porté par ces oxydes). Le reste des concentrations étant potentiellement porté par la matière organique. Les oxydes de Fe-Ti altérés présentent des concentrations élevées en uranium (1000-5000 ppm U) associées à une perte en fer importante (15-20 wt.% FeO après altération). Cette concentration en U peut-être en partie héritée des réactions d'altération qui se sont produites au sein de la roche source mais elle est plus probablement, issue en majeure partie de la redistribution de concentrations syn-sédimentaires au cours de l'évolution diagénétique des sédiments de la formation de Saihan. Les réservoirs gréseux réduits à l'échelle régionale présentent des pyrites diagénétiques sub-automorphe très peu enrichies en éléments traces avec une signature isotopique $\delta^{34}\text{S}$ légèrement négative (-6.09 à -3.77 ‰). Ces grès contiennent également de la matière organique d'origine continentale abondante qui se caractérise par un kérogène de type IV et une faible maturité thermique. Ils ne contiennent pas d'hydrocarbures migrés.

La phase minéralisatrice du gisement de Bayinwula se déroule en deux étapes majeures:

(i) En aval du front, dans la zone dite « à pyrite », des bactéries sulfato-réductrices dégradent la MO et réduisent les sulfates des eaux phéatiques infiltrées en sulfures de fer principalement. Trois populations de pyrite/marcassite ont été observées. Ces sulfures de fer présentent successivement des morphologies framboïdales, collomorphes et sub-automorphes caractérisées par des concentrations élevées en éléments traces tels que As (de 121 à 1531 ppm), Ni (de 70 à 320 ppm) et Co (de 41 à 288 ppm). Concentrations progressivement décroissantes des phases framboïdales aux phases sub-automorphes. La morphologie des disulfures de fer, les signatures isotopiques $\delta^{34}\text{S}$ clairement négatives (-30.54 à -7.47 ‰) des phases framboïdales et collomorphes, ainsi que les teneurs élevées en phosphore des phases uranifères précipitées mettent en évidence l'activité bactérienne. Les valeurs $\delta^{34}\text{S}$ légèrement négatives à très positives (-6.93 à +18.77 ‰) des pyrites sub-automorphes et la diminution de leur teneurs en éléments en trace marquerait l'arrêt des

processus biogéniques et le relai vers des processus chimiques. Dans la zone à pyrite, les oxydes de fer et titane et la matière organique sont progressivement remplacés par la pyrite. Le H₂S produit par les bactéries contribue à augmenter la solubilité des oxydes qui sont progressivement dissous au profit et remplacés par de la pyrite. Au cours de cette dissolution, l'uranium est reconcentré au sein des petits grains d'oxyde de titane résiduels qui montrent alors des teneurs en U pouvant atteindre plusieurs pourcents. L'essentiel de l'uranium piégé dans les oxydes de Fe-Ti et la matière organique est libéré et devient ainsi disponible au lessivage lors de l'arrivée de la solution oxydante qui circule dans le réservoir gréseux.

- (ii) Dans la zone oxydée, l'uranium est présent en solution sous forme U (VI) dans les eaux phréatiques oxydantes qui s'infiltrent dans les niveaux de grès perméables. Les gammes de pH mesurées dans les eaux d'aquifère de la zone de Bayinwula (pH= 6.35-8.48; Nie, 2010) seraient favorables au transport de l'U sous la forme dominante du complexe $\text{UO}_2(\text{HPO}_4)_2^{2-}$. Au front rédox, l'ion uranyl est réduit en U (IV) et précipite sous forme de coffinite riche en phosphore et de ningyoite en épigénie de la pyrite ou de la MO. Le H₂S produit par les bactéries sulfato-réductrices contribue à former une barrière réductrice efficace qui favorise la réduction et donc le dépôt de l'uranium.

Ainsi, les travaux réalisés sur le gisement de Bayinwula ont permis de proposer un modèle de minéralisation d'origine essentiellement biogénique, où le rôle des oxydes de fer et titane en tant que minéral hôte d'une grande partie des préconcentrations d'uranium syn-sédimentaires/diagénétiques et le rôle des bactéries sulfato-réductrices sont majeurs. Ici, le rôle des bactéries est multiple: (i) elles permettent de rendre l'U porté par les oxydes de fer et titane et la matière organique plus disponible au lessivage par les solutions oxydantes, (ii) elles sont à l'origine de la cristallisation en grande quantité de pyrite qui constitue le principal minéral support de la minéralisation et (iii) elles produisent une grande quantité de H₂S qui permet de créer une barrière réductrice favorisant la précipitation de l'uranium, (iv) elles mobilisent le phosphore qui entre dans la constitution des minéraux uranifères et contribuent à l'enrichissement en métaux sensibles au rédox des sulfures néoformés.

En Chine du Nord, de nombreux bassins sédimentaires intracontinentaux formés au cours de l’extension Mésozoïque (Jurassique-Crétacé) renferment des gisements d’uranium encaissés dans des formations sédimentaires gréseuses, de type roll front ou tabulaires. Les gisements de Wuyier, Wuyiyi, Wuyisan et Shihongtan dans le bassin de Yilli (Min et al., 2005a; 2005b), les gisements de la zone de Dongsheng dans le bassin d’Ordos (Cai et al., 2007a; 2007b), et enfin des minéralisation dans le bassin du Kailu (Cai and Li, 2008). Les formations pièges sont constitués de différents types de faciès sédimentaires: (i) les sables de chenaux fluviatiles, (ii) les sables de chenaux deltaïques ou de front de deltas lacustres et (iii) les faciès silto-argileux de plaine d’inondation (pour les minéralisations stratiformes). Par conséquent, ces faciès sédimentaires, déposés entre la fin du Jurassique et le Crétacé selon les bassins, correspondent à des cibles à privilégier pour l’exploration. Cependant, les faciès de chenaux fluviatiles de type tresse, largement représentés au sein des sédiments post-rifts, représentent les réservoirs les plus favorables. L’ensemble des minéralisations connues dans ces bassins sont d’âge Tertiaire avec des remobilisations d’âge plus récent. Des modèles biogéniques pour les gisements encaissés dans les bassins de Yilli et d’Ordos ont également été proposés par les auteurs qui les ont étudiés (Min et al., 2005a; 2005b; Cai et al., 2007a; 2007b). Ainsi, ce modèle de minéralisation semble être commun dans cette région. Il est donc possible que ce type de modèle génétique puisse prévaloir pour la plupart des gisements d’uranium localisés dans des formations gréseuses de la province métallogénique d’Asie centrale. Ici, l’abondance relative en matière organique détritique contenue dans les réservoirs gréseux de ces différents bassins pourrait constituer un facteur limitant majeur de la sulfato-réduction bactérienne.

REFERENCES

BIBLIOGRAPHIQUES

A

- Abdelouas, A., Lu, Y.M., Lutze, W., Nuttall, H.E., 1998. Reduction of U(VI) to U(IV) by indigenous bacteria in contaminated ground water. *Journal of Contaminant Hydrology* 35, 217-233.
- Adams, S.S., Smith, R.B., 1981. Geology and recognition criteria for sandstone uranium deposits in mixed fluvial shallow marine sedimentary sequences, South Texas – final report. U.S. Department of Energy, Grand Junction Office, Colorado, Bendix Field Engineering Corporation, GJBX-4 (81), 146 pp.
- Allen, M.B., McDonald, D.I.M., Xun, Z., Vincent, S.J., Brouet-Menzies, C., 1998. Transtensional deformation in the evolution of the Bohai Basin, northern China. In: Holdsworth, R.E., Strachan, R.A., Dewey, J.F. (eds), *Continental transpressional and transtensional tectonics*. Geological Society, London, Special Publications 135, 215-229.
- Amrhein, C., Mosher, P.A., Brown, A.D., 1993. The effects of redox on Mo, U, B, V and As solubility in evaporation pond soil. *Soil Science* 155-4.
- An, M.J., Shi, Y.L., 2006. Lithospheric thickness of the Chinese continent. *Physical Earth Planetary Interiors* 159, 257-266.

B

- Baag, C., Baag, C. E., 1994. Aeromagnetic interpretation of the Southern and Western offshore Korea. *Korean Journal of Petroleum Geology* 2, 51-57.
- Bachma, F.S., Merkel, B.J., 2010. Sorption and desorption of uranium (VI) on clay minerals. In: Clay in natural & engineered barriers for radioactive waste confinement, 4th international meeting, March 2010, Nantes, France, 391-392.
- Badarch, G., Cunningham, W.D., Windley, B.F., 2002. A new terrane subdivision for Mongolia: implications for the Phanerozoic crustal growth of Central Asia. *Journal of Asian Earth Sciences* 21, 87-110.
- Bai, J., 1996. Precambrian crustal evolution of China. Geological Publishing House, Beijing.
- Bai, J., Dai, F.Y., 1996. The early Precambrian crustal evolution of China. *Journal of Southeast Asian Earth Sciences* 13, 205-214.
- Bai, J., Dai, F.Y., 1998. Archaean crust of China. In: Ma, X.Y., Bai, J., (Eds), *Precambrian crustal evolution of China*. Geological Publishing House, Beijing, 15-86.

- Bartolini, A., Larson, R.L., 2001. Pacific microplate and the Pangea supercontinent in the Early to Middle Jurassic. *Geology* 29, 735-738.
- BBGMR, 1991. Regional geology of the Beijing Municipality. Geological Memoirs of Ministry of Geology and Mineral Resources 27, Geological Publishing House, Beijing, p. 598.
- Bekker, A., Holland, H.D., Wang, P.L., Rumble, D., Stein, H.J., Hannah, J.L., Coetzee, L.L., Beukes, N.J., 2004. Dating the rise of atmospheric oxygen. *Nature* 427, 117–120.
- Belyi, V.M., Vinogradov, V.I., and Lisitsin, A.K., 1972. Sulfur isotope composition of uranium roll ore bodies and its genetic significance: *Litologiya i Poleznye Iskopaemye* 6, 42-53. (English translation, New York, Consultants Bureau, Div. Plenum Pub. Corp.)
- Bennett, P.C., Siegel, D.I., 1987. Increased solubility of quartz in H₂O due to complexing by organic compounds. *Nature* 326, 684-686.
- Berkey, C.P., Morris, F.K., 1927. Natural History of Central Asia, Volume II. Geology of Mongolia. The American Museum of Natural History, New York, 475 pp.
- Bird, P., 1979. Initiation of intracontinental subduction in the Himalaya. *Journal of Geophysical Research* 83, 4975-4987.
- Bo, H.Z., Kuan, Q.M., 2006. High resolution sequence stratigraphic character and sandstone type uranium ore formation: A case from Saihan Formation in Bayinwula area, Erlian Basin. *World Nuclear Geoscience* 23-4, 194-198.
- Bonnetti, C., Malartre, F., Huault, V., Cuney, M., Bourlange, S., Liu, X., Peng, Y., accepted manuscript. Sedimentology, stratigraphy and palynological record of the late Cretaceous Erlian Formation, Erlian Basin, Inner Mongolia, People's Republic of China. Accepted manuscript in *Cretaceous Research Journal*.
- Boyle, D.R., 1982. The formation of basal-type uranium deposits in South Central British Columbia. *Econ. Geol.* 77, 1176-1209.
- Brett-Surman, M.K., 1979. Phylogeny and palaeobiogeography of hadrosaurian dinosaurs. *Nature* 277, 560-562.
- Brookins, D.G., 1976. Position of uraninite and/or coffinite accumulation to the hematite pyrite interface in sandstone-type deposits. *Economic Geology* 71, 944–948.
- Brown, K., Cohen, A.D., 1995. Stratigraphic and micropetrographic occurrences of pyrite in sediments at the confluence of carbonate and peat-forming depositional systems, southern Florida, U.S.A. *Org. Geochem.* 22, 105-126.
- Brun, J.P., Sokoutis, D., Van Den Driessche, J., 1994. Analogue modeling of detachment faultsystems and core complexes. *Geology* 22, 319-322.

Buck, W.R., 1991. Modes of continental lithospheric extension. *Journal of Geophysical Research* 96 (B12), 161-178. doi: 10.1029/91JB01485.

Bustin, R.M., Cameron, A.R., Grieve, D.A., Kalkreuth, W.D., 1989. Coal petrology. Its principles, methods and applications. Geological Association of Canada, Short Course Notes 3, 1-230.

Byerlee, J., 1978. Friction of rocks. *Pure and Applied Geophysics* 116, 615-626.

Chappell, B., W., White, A., J., R., 1974. Two contrasting granite types: 25 years later. *Australian Journal of Earth Sciences* 48, 489-499.

C

Cabrera, L., Cabrera, M., Gorchs, R., de las Heras, F.X.C., 2002. Lacustrine basin dynamics and organo-sulphur compound origin in a carbonate-rich lacustrine system (Late Oligocene Mequinenza Formation, SE Ebro Basin, NE Spain). *Sedimentary Geology* 148, 289-317.

Cai, Y.Q., Li, S.X., 2008. Sedimentary environment analysis of Yaojia formation-the ore-hosting stratum of Qianjiadian uranium deposit. *China National Knowledge Infrastructure, Uranium Geology* 2, 66-72.

Cai, C., Li, H., Qin, M., Luo, X., Wang, F., Ou, G., 2007. Biogenic and petroleum-related ore-forming processes in Dongsheng uranium deposit, NW China. *Ore Geology Reviews* 32, 262-274.

Cai, Z.G., Li, H.R., Tang, S.C., 1990. Cretaceous in Erlian Basin, in : Wang, S.E., (Eds.), *Stratigraphy of China 11. The Cretaceous System of China*. Geological Publishing House, Beijing, pp. 146-184. (in Chinese).

Canfield, D.E., and Farquhar, J., 2012. The global sulfur cycle, in: Knoll, A.H., Canfield, D.E., Konhauser, K.O. (Eds.), *Fundamentals of geobiology*. Wiley-Blackwell, pp. 49-64.

Caroll, A.R., Graham, S.A., Smith, M.E., 2010. Walled sedimentary basins of China. *Basin Research* 22, 17-32.

Casagrande, D.J., 1987. Sulphur in peat and coal, in: Scott, A.C. (Eds.), *Coal and coal bearing strata: recent advances*. Geological Society of London, Special Publication 32, pp. 87-105.

Charles, N., 2010. Mécanismes de l'extension continentale au Mésozoïque en Asie de l'Est. Doctorat de l'université d'Orléans, Chapitre 2.

- Charles, N., Augier, R., Gumiaux, C., Monié, P., Chen, Y., Faure, M., Zhu, R., 2013. Timing, duration and role of magmatism in wide rift systems: Insights from the Jiaodong Peninsula (China, East Asia). *Gondwana Research* 24, 412-428.
- Charles, N., Faure, M., Chen, Y., 2009. The Montagne Noire migmatitic dome emplacement (French Massif Central): new insights from petrofabric and AMS studies. *Journal of Structural Geology* 31, 1423-1440.
- Charles, N., Gumiaux, C., Augier, R., Chen, Y., Lin, W., Zhu, R., 2010. Metamorphic Core Complex vs. Synkinematic pluton in continental extension setting: Insights from key structures (Shandong Province, eastern China). *Journal of Asian Earth Sciences*, doi:10.1016/j.jseaes.2010.07.006 (in press).
- Chen, L., 2009. Lithospheric structure variations between the eastern and central North China Craton from S- and P-receiver function migration. *Physics of the Earth and Planetary Interiors* 173, 216–227.
- Chen, L., 2010. Concordant structural variations from the surface to the base of the uppermantle in the North China Craton and its tectonic implications. *Lithos*, doi:10.1016/j.lithos.2009.12.007.
- Chen, Y., Chen, W., 1997. Mesozoic volcanic rocks: chronology, geochemistry and tectonicbackground. Seismology Press, Beijing, p. 279.
- Chen, L., Cheng, C., Wei, Z., 2009. Seismic evidence for significant lateral variations inlithospheric thickness beneath the central and western North China Craton. *Earth and Planetary Science Letters* 286, 216-227.
- Chen, P.J., Jin, F., 1999. Jehol Biota. *Palaeoworld*, Special Issue 11, University of Science and Technology of China Press, Hefei, 342 pp. (in Chinese, English abstract).
- Chen, G.Y., Song, Z.H., An, C.Q., Cheng, L.H., Zhuang, Z., Fu, Z.W., Lu, Z.L., Hu, J.F., 1991. Three dimensional crust and upper mantle structure of the North China region. *Acta Geophysica Sinica* 34, 172-181.
- Chen, L., Tao, W., Zhao, L., Zheng, T., 2008. Distinct lateral variation of lithospheric thickness in the Northeastern North China Craton. *Earth and Planetary Science Letters* 267, 56–68.
- Chen, G., Wang, T., Li, L., Li, S., Li, J., 2010. Characteristics of a sublacustrine fan in a half graben rift lake basin and its petroleum prospects: Case study on the second member of the Tenggeer Formation, Saihantala Sag, Erlian Basin. *PETROL. EXPLOR. DEVELOP.*, 37(1): 63–69.

- Chi, J., Lu, F., Zhao, L., Zhao, C., Zheng, J., Deng, F., 1992. A study of primary diamonddeposits North China platform-genesis and prospects. China University of Geosciences, Beijing.
- Choi, S.G., Kwon, S.T., Ree, J.H., So, C.S., Pak, S.J., 2005. Origin of Mesozoic Goldmineralization in South Korea. *The Island Arc* 14, 102-114.
- Chough, S.K., Kwon, S.T., Ree, J.H., Choi, D.K., 2000. Tectonic and sedimentary evolutionof the Korean Peninsula: a review and new view. *Earth Science Reviews* 52, 175-235.
- Cocherie, A., Albarede, F., 2001. An improved U-Th-Pb age calculation for electron microprobe dating of monazite. *Geochemica et Cosmochimica Acta* 65-24, 4509-4522.
- Compston, W., Williams, I.S., Meyer, C.E., 1984. U/Pb geochronology of zircons from lunar breccias 73217 using a sensitive high mass resolution ion microprobe, in: Proc. 14th Lunar and Planetary Science Conference, Part 2, *Geophysical research* 89B, 525-534.
- Cong, 2009. Nuclear Industry in China.
- Cox. K.G., Beu, J.D., Pankhurst, R.J., 1979. The interpretation of igneous rocks. George, Allen and Unwin, London.
- Cuney, M., 2009. The extreme diversity of uranium deposits. *Mineral Dep.*, 44, 3–9.
- Cuney, M., 2010. Evolution of Uranium Fractionation Processes through Time: Driving the Secular Variation of Uranium Deposit Types. *Economic Geology* 105, 553–569.
- Cuney, M., Friedrich, M., 1987. Physicochemical and crystal-chemical controls on accessory mineral paragenesis in granitoids: implications for uranium metallogenesis. *Bulletin de Mineralogie* 110, 235-247.
- Cuney, M., Kyser, K., 2008. Recent and not-so-recent developments in uranium deposits and implications for exploration. *Mineralogical Association of Canada* 39, 257 pp.
- Currie, P.J., Eberth, D.A., 1993. Palaeontology, sedimentology and palaeoecology of the Iren Dabasu Formation (Upper Cretaceous), Inner Mongolia, People's Republic of China. *Cretaceous Research* 14, 127-144.

D

- Dahlkamp, F.J., 2009. Uranium Deposits of the world: Asia. Springer Ed., 493 pp.
- Daoudene, Y., Gapais, D., Ledru, P., Cocherie, A., Hocquet, S., Donskaya, T.V., 2009. TheEreendavaa Range (north-eastern Mongolia): an additional argument for Mesozoicextension throughout eastern Asia. *International of Earth Sciences (Geol Rundsch)*, doi: 10.1007/s00531-008-0412-2.

- Darby, B.J., Davis, G.A., Zhang, X., Wu, F., Wilde, S., Yang, J., 2004. The newly discovered Waziyu metamorphic core complex, Yiwulüshan, western Liaoning province, Northwest China. *Earth Science Frontiers* 11, 145-155.
- Davidson, S.C., 2005. Sedimentation history and provenance analysis of a late Mesozoic rifting event at Tavan Har, East Gobi, Mongolia. *Frontiers: The Interdisciplinary Journal of Study Abroad* 12, 91-126.
- Davis, G.A., Darby, B. J., Zheng, Y., Spell, T.L., 2002. Geometric and temporal evolution of an extensional detachment fault, Hohhot metamorphic core complex, Inner Mongolia, China. *Geology* 30, 1003-1006.
- Davis, G.H., Coney, P.J., 1979. Geologic development of the Cordilleran metamorphic core complexes. *Geology* 7, 120-124.
- Davis, G.A., Qian, X., Zheng, Y., Yu, H., Wang, C., Mao, T.H., Gehrels, G.E., Muhammad S., Fryxell, J.E., 1996. Mesozoic deformation and plutonism in the Yunmeng Shan: A Chinese metamorphic core complex north of Beijing, China. In: A. Yin & T.A. Harrison, Eds., *The tectonic evolution of Asia*. Cambridge University Press, New York, 253-280.
- Davis, G.A., Zheng, Y., Wang, C., Darby, B.J., Zhang, C. and Gehrels, G., 2001. Mesozoic tectonic evolution of the Yanshan fold and thrust belt, with emphasis on Hebei and Liaoning provinces, northern China. *Geological Society of America Memoir* 194, 171-197.
- De Paolo, D.J., 1988. Neodymium isotope geochemistry: An introduction. Springer Verlag, New York.
- Debon, F., Lefort, P., 1983. A chemical-mineralogical classification of common plutonic rocks and associations. *Trans. R. Soc. Edinburgh: Earth Sci.* 73, 135-149.
- Debon, F., Lefort, P., 1988. A cationic classification of common plutonic rocks and their magmatic associations: principles, method, applications. *Bulletin de Minéralogie* 111, 493-510.
- Demaison, G.J., Hoick, A.J.J., Jones, R.W., Moore, G.T., 1983. Predictive source bed stratigraphy; a guide to regional petroleum occurrence: Proceedings of the 11th World Petroleum Congress, London, v. 2, p. 17-29.
- Devoto, R.H., 1978. Uranium in Phanerozoic sandstone and volcanic rocks. Short course in uranium deposits; their mineralogy and origin. Mineralogical Association of Canada, Short Course Handbook 3, 293-305.
- Diessel, C.F.K., 1992. Coal-bearing depositional systems. Springer Ed., 721 pp.

- Dill, H.G., Altangerel, S., Bulgamaa, J., Hongor, O., Khishigsuren, S., Majiguren, Y., Myagmarsuren, S., Heunisch, C., 2004. The Baganuur coal deposit, Mongolia: depositional environments and paleoecology of a Lower Cretaceous coal-bearing intermontane basin in Eastern Asia. International Journal of Coal Geology 60, 197-236.
- Ding, T., Bai, R., Li, Y., Wan, D., Zou, X., Zhang, Q., Determination of the absolute 32S/34S ratio of IAEA-S-1 reference material and V-CDT sulphur isotope standard. Science in China Series D: Earth Sciences 42-1, 45-51.
- Donskaya, T.V., Windley, B.F., Mazukabzov, A.M., Kröner, A., Sklyarov, E.V., Gladkochub, D.P., Ponomarchuk, V.A., Badarch, G., Reichow, M.K., Hegner, E., 2008. Age and evolution of late Mesozoic metamorphic core complexes in southern Siberia and northern Mongolia. Journal of Geological Society of London 165, 405-421.
- Dou, L., 1997. Lower Cretaceous petroleum system of NE China. Journal of Petroleum Geology 20, 474-488.
- Dou, L., Chang, L., 2003. Fault linkage patterns and their control on the formation of the petroleum systems of the Erlian Basin, Eastern China. Marine and Petroleum Geology 20, 1213-1224.
- Dou, L., Zhu, Y., Yang, T., Xu, S., Ping, X., 1998. Origins of heavy oils in the Erlian Basin\ NE China. Elsevier; Marine and Petroleum Geology 15, p. 658_670.
- Durand, B., 1980. Kerogen: Insoluble Organic Matter from Sedimentary Rocks. Technip Ed., 519 pp.
- Duhamel, I., Cuney, M., Van Lichtervelde, M., 2009. First characterization of uraninite in an Archean peraluminous granitic pegmatite at Tanco (Manitoba, Canada). Inference for uraninite placer deposits. Geological Association of Canada, Mineralogical Association of Canada Conference, Québec, Canada.

E

- Eide, E.A., McWilliams, M.O., Liou, J.G., 1994. 40Ar/39Ar geochronology and exhumation of high-pressure to ultrahigh. Geology 22, 601-604.
- Elsasser, W.M., 1971. Sea-floor spreading as thermal convection. Journal of Geophysical Research 76, 1101-1112.
- Enkin, R.J., Yang, Z., Chen, Y., Courtillot, V., 1992. Paleomagnetic constraints on the geodynamic history of the major blocks of China from the Permian to the Present. Journal of Geophysical Research 97, 13953-13989.

- Erdenetsogt, B.O., Lee, I., Bat-Erdene, D., Jargal, L., 2009. Mongolian coal-bearing basin Geological settings, coal characteristics, distribution, and resources. International Journal of Coal Geology 80, 87-104.
- Espitalie, J., Deroo, G., Marquis, F., 1985. Rock-Eval Pyrolysis and Its Applications. Oil and Gas Science and Technology, IFP rev., 72 pp.
- Ethridge, F.G., Wood, L.J., Schumm, S.A., 1998. Cyclic variables controlling fluvial sequence development: problems and perspectives, in: Shanley, K.W., MacCabe, P.J. (Eds), Relative role of eustasy, climate and tectonism in continental rocks. SEPM, Special Publication 59, 17-29.
- Everhart, D.L., 1985. Tectonic setting of the world's sandstone-type uranium deposits. In: Geological environments of sandstone-type uranium deposits, TEDOC-328, IAEA, Vienna, 21-46.

F

- Faccenna, C., Di Giuseppe, E., Funiciello, F., Lallemand, S., van Hunen, J., 2009. Control of sea floor aging on the migration of the Izu-Bonin-Mariana trench. Earth and Planetary Science Letters 288, 386-398.
- Fan, W.M., Guo, F., Wang, Y.J., Lin, G., 2003. Late Mesozoic calc-alkaline volcanism of post-orogenic extension in the northern Da Hinggan Mountains, northeastern China. Journal of Volcanology and Geothermal Research 121, 115-135.
- Fan, X., Nie, F., Chen, Y., Wang, W., 2008. Discussion on age and paleo geographical environment of ore bearing strata for sandstone-type uranium deposits in Bayanwula area, Erlian Basin. Uranium Geology 24-3, 151-154. (in Chinese, English abstract).
- Fan, W., Zhang, H.F., Baker, J., Jarvis, K.E., Mason, P.R.D., Menzies, M.A., 2000. On and off the North China Craton: where is the Archaean keel? Journal of Petrology 41, 933-950.
- Farquhar, J., Wing, B.A., 2003. Multiple sulfur isotopes and the evolution of the atmosphere. Earth and Planetary Science Letters 213, 1-13.
- Faure, M., Lin, W., Chen, Y., 2012. Is the Jurassic (Yanshanian) intraplate tectonics of North China due to westward indentation of the North China Block ? Terra Nova, accepted manuscript.
- Faure, M., Lin, W., Shu, L., Sun, Y., Schärer, U., 1999. Tectonics of the Dabieshan (E. China) and possible exhumation mechanism of ultra high-pressure rocks. Terra Nova 11, 251-258.

- Faure, M., Sun, Y., Shu, L., Monié, P., Charvet, J., 1996. Extensional tectonics within a subduction-type orogen. The case study of the Wugongshan dome (Jiangxi Province, SE China). *Tectonophysics* 263, 77-108.
- Faure, M., Trap, P., Lin, W., Monié, P., Bruguier, O., 2007. The formation of the North China Craton by two Palaeoproterozoic continental collisions in Lüliang-Hengshan-Wutaishan-Fuping massifs. *Episodes* 30, 1-12.
- Finch, W.I., 1996. Uranium provinces of North America – Their definition, distribution, and models. *U.S. Geol. Surv. Bull.* 2141, 1-18.
- Finch, W.I., Davis, J.F. 1985. Sandstone-type uranium deposits – An introduction. In: Geological environments of sandstone-type uranium deposits, TEDOC-328, IAEA, Vienna, 11-20.
- Fu, M., Hu, S., Wang, J., 2005. Thermal regime transition in eastern North China and its tectonic implication. *Science in China Series D* 48, 840-848.

G

- Gao, S., Rudnick, R.L., Carlson, R.W., McDonough, W.F., Liu, Y.S., 2002. Re-Os evidence for replacement of ancient mantle lithosphere beneath the North China Craton. *Earth and Planetary Science Letters* 198, 307-322.
- Gächter, R., Meyer, J.S., 1993. The role of microorganisms in mobilization and fixation of phosphorus in sediments. *Hydrobiologia* 253, 103–121.
- Ge, W., C., Wu, F., Zhou, C., Zhang, J., 2007. Porphyry Cu-Mo deposits in the eastern Xing'an-Mongolian Orogenic Belt: Mineralization ages and their geodynamic implications. *Chinese Science Bulletin* 52-24, 3416-3427.
- Girdler, R.W., 1961. The measurement and computation of anisotropy of magnetic susceptibility of rocks. *Geophys. J. R. Astr. Soc.* 5, 34-44.
- Goldhaber, M.B., Reynolds, R.L., Rye, R.O., 1978. Origin of a South Texas Roll-Type Uranium Deposit: II. Sulfide Petrology and Sulfur Isotope Studies. *Economic Geology* 73, 1690-1705.
- Gou, Y.X., Wang, Z.Z., Yang, J.D., 1986. Cretaceous Ostracoda from Eren Basin of Nei Mongol along with sedimentary environments, in: Nanjing Institute of Geology and Palaeontology, Academia Sinica, the First Exploration Company, North China Oil Field, Ministry of Oil Industry (Eds.), *Cenozoic-Mesozoic Palaeontology and Stratigraphy of East China, Series 2. Cretaceous Ostracod and Sporo-Pollen Fossils of*

- Eren Basin. Anhui Science and Technology Publishing House, Hefei, 104 pp. (in Chinese, English abstract).
- Grabau, A.W., 1923. Cretaceous Mollusca from north China. Bulletin of the Geological Survey of China 5, 183-198.
- Graham, S.A., Hendrix, M.S., Johnson, C.L., Badamgarav, D., Badarch, G., Amory, J., Porte, M., Barsbold, R., Webb, L.E., Hacker, B.R., 2001. Sedimentary record and tectonic implications of Mesozoic rifting in southern Mongolia. Geological Society of America Bulletin 113, 1560-1579.
- Granger, W., Berkey, C.P., 1922. Discovery of Cretaceous and older Tertiary strata in Mongolia. American Museum Novitates 42, 1-7.
- Granger H.C., Warren, C.G., 1969. Unstable sulfur compounds and the origin of the roll-type uranium deposits. Economic Geology 64, 160-171.
- Griffin, W.L., Andi, Z., O'Reilly, S.Y., Ryan, C.G., 1998. Phanerozoic evolution of the lithosphere beneath the Sino-Korean craton. In: Flower, M., Ching, S.L., Lo, C.H., Lee, T.Y. (Eds), Mantle dynamics and plate interactions in East Asia. AGU Geodynamics Series 27, 107-126.
- Griffin, W.L., Fisher, N.I., Friedman, J., Ryan, C.G., O'Reilly, S.Y., 1999. Cr-pyrope garnets in the lithospheric mantle I Compositional systematics and relations to tectonic setting. Journal of Petrology 40, 679-704.
- Griffin, W.L., O'Reilly, S.Y., Ryan, C.G., 1992. Composition and thermal structure of the lithosphere beneath South Africa, Siberia and China: proton microprobe studies. International Symposium on Cenozoic volcanic rocks and deep-seated xenoliths of China and its environs, Beijing, vol. 20.
- Gu, Z.W., Huang, B.Y., Chen, C.Z., 1976. Fossil Lamellibranchiata of China. Science Press, Beijing, 522 pp. (in Chinese).
- Gu, Z.W., Li, Z.S., Yu, X.H., 1997. Lower Cretaceous Bivalves from the Eastern Heilongjiang Province of China. Science Press, Beijing, 301 pp.
- Guo, C.L., Wu, F.Y., Yang, J.H., Lin, J.Q., Sun, D.Y., 2004. The extensional setting of the Early Cretaceous magmatism in eastern China: example from the Yinmawanshan pluton in southern Liaodong Peninsula. Acta Petrologica Sinica 20, 1193-1204 (in Chinese with English abstract).

H

- Hacker, B.R., Ratschbacher, L., Webb, L., Ireland, T., Walker, D., Dong, S., 1998. U/Pbzircon ages constrain the architecture of the ultrahigh-pressure Qinling-Dabie orogen, China. *Earth Planetary Science Letters* 161, 215-230.
- Harshman, E.N., 1972. Geology and uranium deposits Shirley basin area, Wyoming. US Geological Survey, Prof. Pap. 745, p.82.
- He, G.Z., 1987. Mantle xenoliths from kimberlites in China. In: Nixon, P.N. (Ed), *Mantlexenoliths*. Wiley & Sons, Chichester, 182-185.
- Hedlund, R.W., Norris, G., 1968. Spores and pollen grains from Fredericksburgian (Albian) strata, Marshall County, Oklahoma: Pollen et Spores 10-1, 129-159.
- Herbin J.P., Deroo G., (1979). Etude sédimentologique de la matière organique dans les argiles noires crétacées de l'Atlantique sud. *Docum. Lab. Géol. Fac. Sci. Lyon* 75, 71-87.
- Hicks, J. F., Brinkman, D.L., Nichols D.J., Watabe M., 1999. Paleomagnetic and palynologic analyses of Albian to Santonian strata at Bayan Shireh, Burkhan, and Khuren Dukh, eastern Gobi Desert, Mongolia. *Cretaceous Research* 20, 829-850.
- Hofmann, A.W., 1988. Chemical differentiation of the Earth: the relationship between mantle, continental crust, and oceanic crust. *Earth and Planetary Science Letters* 90, 297–314.
- Holland, H.D., 2002. Volcanic gases, black smokers, and the great oxidation event. *Geochimica et Cosmochimica Acta* 66, 3811-3826.
- Houseman, G. A., D. P. McKenzie, and P. Molnar (1981). Convective instability of a thickened boundary layer and its relevance for the thermal evolution of continental convergent belts. *J. Geophys. Res.*, 86, 6115-6132.
- Howard, J.H., 1977. Geochemistry of selenium: formation of ferroselite and selenium behavior in the vicinity of oxidizing sulfide and uranium deposits. *Geochimica and Cosmochimica Acta* 41-11, 1665-1678.
- Hua, B., Xu, H., Terry, J., Deng, B., 2006. Kinetics of uranium (VI) reduction by hydrogen sulfide in anoxic aqueous systems. *Environmental Science and Technology* 40, 4666-4671.
- Huang, J., Zhao, D., 2006. High-resolution mantle tomography of China and surrounding regions. *Journal of Geophysical Research* 111, doi: 10.1029/2005JB004066.

Hutchens, E., Valsami-Jones, E., Harouiya, N., Chairat, C., Oelkers, EH., McEldoney, S. 2006. An Experimental Investigation of the Effect of *Bacillus megaterium* on Apatite Dissolution. *Geomicrobiol Journal* 19, 343–367.

I

ICS, International commission on stratigraphy, 2006. International stratigraphic chart.

Ichinnorov, N., 2003a. Discovery of Early Cretaceous pollen and spores from the Shaazan Govi area, Southeastern Mongolia. *Mongolian Geoscientist* 18, 2-7.

Ichinnorov, N., 2003b. Palynocomplex of the Lower Cretaceous sediments of the eastern Mongolia. *Mongolian Geoscientist* 22, 12-16.

Ishihara, S., 2007. Origin of the Cenozoic-Mesozoic magnetite-series and ilmenite-series granitoids in East Asia. *Gondwana Research* 11, 247-260.

J

Jahn, B.M., Auvray, B., Cornichet, J., Bai, Y.L., Shen, Q.L., Liu, D.Y., 1987. 3.5 Ga old amphibolites from eastern Hebei province, China: field occurrence, petrography, Sm-Nd isochron age and REE geochemistry. *Precambrian Research* 34, 311-346.

Jahn, B.M., Ernst, W.G., 1990. Late Archaean Sm-Nd isochron age for Sino-Korean Craton, China. *Precambrian Research* 46, 295-306.

Jayananda, M., Martin, H., Peucat, J.-J., Mahabaleswar, B., 1995. Late Archaean crust–mantle interactions: geochemistry of LREE—enriched mantle derived magmas. Example of the Closepet batholith, southern India. *Contribution to Mineralogy and Petrology* 119, 314-329.

Jensen, M.L., 1958. Sulfur isotopes and the origin of sandstone-type uranium ore deposits. *Economic Geology* 53, 598–616.

Jerzykiewicz, T., Russel, D.A., 1991. Late Mezosoic stratigraphy and vertebrates of the Gobi Basin. *Cretaceous Research* 12, 121-144.

Ji, Q., Chen, W., Wang, W.L., Jin, X.C., Zhang, J.P., Liu, Y.X., Zhang, H., Yao, P.Y., Ji, S.A., Yuan, C.X., Zhang, Y., You, H.L., 2004. Mesozoic Jehol Biota of Western Liaoning. Geological Publishing House, Beijing, 375 pp. (in Chinese).

Jin, J., Meng, Q.R., Zhang, Y., Xu, D., 2000. Jurassic-Cretaceous evolution of the Yingenbasin and its petroleum potential. *Acta Petrologica Sinica* 21, 13-19.

Johnson, C.L., 2004. Polyphase evolution of the East Gobi basin: sedimentary and structural records of Mesozoic-Cenozoic intraplate deformation in Mongolia. *Basin Research* 16, 79-99.

K

Keen, C., and Dehler, S., A., 1993. Stretching and Sudsidence: rifting of conjugate margins in the North Atlantic region. *AAPG Bulletin*, v.12, p. 1219-1229.

Kimura, G., Tasaki, T., Kono, M., 1990. Mesozoic collision-extrusion tectonics in eastern Asia. *Tectonophysics* 181, p.15– 23.

Khand, Y., Badagarav, D., Ariunchimeg, Y., Barsbold, R., 2000. Cretaceous System in Mongolia and its Depositional Environment. In: Okada, H., Mateer, N.J. (Eds.), *Cretaceous Environments of Asia*. Elsevier, Amsterdam, 49-79.

Kim, S.W., Oh, C.W., Choi, S.G., Ryu, I.C., Itaya, T., 2005. Ridge subduction-related Jurassic plutonism in and around the Okcheon metamorphic belt, South Korea, and implications for northeast Asian tectonics. *International Geological Review* 47, 248-269.

Kim, C.B., Turek, A., 1996. Advances in U/Pb zircon geochronology of Mesozoic plutonism in the southwestern part of Ryongnam massif. *Korean Geochemical Journal* 30, 323-338.

Kirillova, G.L., 2003. Late Mesozoic–Cenozoic sedimentary basins of active continental margin of Southeast Russia: paleogeography, tectonics, and coal-oil-gas presence. *Marine and Petroleum Geology* 20, 385-397.

Kusky, T., Windley, B.F., Zhai, M.G., 2007. Tectonic evolution of the North China Block: from orogen to craton to orogen. In: Zhai, M.G., Windley, B.F., Kusky, T., Meng, Q.R. (Eds), *Mesozoic sub-continental lithospheric thinning under eastern Asia*. Geological Society of London, Special Publications 280, 1-34.

L

Lach, P., Mercadier, J., Dubessy, J., Boiron, M.C., Cuney, M., 2013. In situ quantitative measurement of rare earth elements in uranium oxides by laser ablation-inductively coupled plasma-mass spectrometry. *Geostandards and Geoanalytical Research*, 1-20.

Lallemand, S., Jolivet, L., 1986. Japan Sea: A pull-apart basin. *Earth and Planetary Science Letters* 76, 375-389.

Landais, P., 1996. Organic geochemistry of sedimentary uranium ore deposits. *Ore Geology Reviews* 11, 33-51.

- Langmuir, D., 1978. Uranium solution-mineral equilibria at low temperature with applications to sedimentary ore deposits. *Geochemica et Cosmochimica Acta* 42-6, 457-569.
- Lee, D.W., 1999. Strike-slip fault tectonics and basin formation during the Cretaceous in the Korean Peninsula. *The Island Arc* 8, 218-231.
- Lee, S.R., Walker, R.J., 2006. Re-Os isotope systematics of mantle xenoliths from South Korea: evidence for complex growth and loss of lithospheric mantle beneath East Asia. *Chemical Geology* 231, 90-101.
- Leisen, M., 2011. Analyse chimique des inclusions fluides par ablation-laser couplée à l'ICPMS et applications géochimiques. Unpublished PhD. Dissertation, Université de Lorraine, France, 308 pp.
- Lepvrier, C., Maluski, H., 2008. The Triassic Indosinian orogeny in East Asia. *Comptes Rendus Geoscience* 340, 75-82.
- Li, X.H., 2000. Cretaceous magmatism and lithospheric extension in southeast China. *Journal of Asian Earth Science* 18, 293-305.
- Li, J., Batten, D.J., Zhang, Y., 2011. Palynological record from a composite core through Late Cretaceous-early Paleocene deposits in the Songliao Basin, Northeast China and its biostratigraphic implications. *Cretaceous Research* 32, 1-12.
- Li, Z.X., LI, X.H., Kinny, P.D., Wang, J., Zhang, S., Zhou, H., Geochronology of Neoproterozoic syn-rift magmatism in the Yangtze Craton, South China and correlations with other continents: evidence for a mantle superplume that broke Rodinia. *Precambrian Research* 122, 85-109.
- Li, S.L., Mooney, W.D., 1998. Crustal structure of China from deep seismic sounding profiles. *Tectonophysics* 288, 105-113.
- Li, X., Wu, J., Liao, J., Zhang, D., Yang, J., Feng, Y., Zeng, J., Wen, W., Yang, Y., Tang, J., Liu, N., 2013. Adsorption and desorption of uranium (VI) in aerated zone soil. *Journal of Environmental Radioactivity* 115, 143-150.
- Lin, C., Eriksson, K., Sitian, L., Yongxian, W., Jianye, R., and Yanmei, Z., 2001. Sequence architecture, depositional systems, and controls on development of lacustrine basin fills in part of the Erlian basin, northeast China. *American Association of Petroleum Geologists* 85-11, 2017-2043.
- Lin, W., Faure, M., Monié, P., Schärer, U., Panis, D., 2008. Mesozoic extensional tectonics in Eastern Asia: The South Liaodong Peninsula Metamorphic Core Complex (NEChina). *Journal of Geology* 116, 134-154.

- Lin, W., Faure, M., Monié, P., Wang, Q.C., 2007. Polyphase Mesozoic tectonics in the eastern part of the North China Blocks: insights from the Liaoning Peninsula massif (NE China). In: Zhai, M.-G., Windley, B.F., Kusky, T.M. & Meng, Q.R. (eds), 2007. Mesozoic sub-continental lithospheric thinning under eastern Asia. Geological Society, London, Special Publications 280, 153-170.
- Lin, W., Faure, M., Nomade, S., Shang, Q., Renne, P.R., 2008. Permian-Triassic amalgamation of Asia : Insights from Northeast China sutures and their place in the final collision of North China and Siberia. Comptes Rendus Geoscience 340, 190-201.
- Lin, Q., Ge, W.C., Sun, D.Y., Wu, F.Y., Chong, K.W., Kyung, D.M., Myung, S.J., Moon, W., Chi, S.K., Sung, H.Y., 1998. Tectonic significance of Mesozoic volcanic rocks in northeastern China. Scientia Geologica Sinica 33, 129-138 (in Chinese with English abstract).
- Lin, W., Wang, Q., 2006. Late Mesozoic extensional tectonics in the North China Block: crustal response to subcontinental mantle removal? Bulletin de la Société Géologique de France 177, 287-294.
- Liu, D.Y., 1992. Seismic tomography in China. International Geological Congress, Tokyo 3,668.
- Liu, H.F., 1986. Geodynamic scenario and structural styles of Mesozoic and Cenozoic basins in China. Am. Assoc. Pet. Geol. Bulletin 70, 377-395.
- Liu, Y.K., 1998. Constraints on crustal evolution and gold metallogeny in the Northwestern Jiaodong Peninsula, China, from SHRIMP U-Pb zircon studies of granitoids. Ore Geology Reviews 13, 275-291.
- Liu, J., Davis, G., Lin, Z., Wu, F., 2005. The Liaonian metamorphic core complex, southeastern Liaoning Province, North China: A likely contributor to Cretaceous rotation of eastern Liaoning, Korea and contiguous areas. Tectonophysics 407, 65-80.
- Liu, Y., Gao, S., Yuan, H., Zhou, L., Liu, X., Wang, X., Hu, Z., Wang, L., 2004. U-Pb zircon ages and Nd, Sr and Pb isotopes of lower crustal xenoliths from North China Craton: insights on evolution of lower continental crust. Chemical Geology 211, 87-109.
- Liu, D.Y., Nutman, A.P., Compston, W., Wu, J.S., Shen, Q.H., 1992. Remnants of >3800 Ma crust in the Chinese part of the Sino-Korean craton. Geology 20, 339-342.
- Lizitsyn A.K., Kuznetsova, E.C., 1967. Role of microorganisms in development of geochemical reduction barriers where limonitization bedded zones wedge out: Akad.

Nauk SSSR Izv. Ser. Geol. 1, 31-44. (English translation, Internat. Geology Rev. 9, 1180-1191).

Logatchev, N.A., Zorin, Y.A., 1987. Evidence and causes for the two-stage development of the Baikal rift. Tectonophysics 143, 225-234.

Lonergan, L., White, N., 1997. Origin of the Betic-Rif mountain belt. Tectonics 16, 504-522.

Lu, F., Huan, Z., Zheng, J., Ren, Y., 1991. Characteristics of Palaeozoic mantle lithosphere in Fuxian, Liaoning Province. Geological Science and Technology Information 10, 1-20. China University of Geosciences, Beijing.

Luo, Q., Liu, G., Wang, B., 1992. The research of metamorphic core complex of Hongzhen-Anqing area, Lower Yangtze. J. Nanjing University (Natural Sciences) 4, 14-25 (In Chinese with English abstract).

M

Ma, Q., 1994. Nonmarine Cretaceous bivalve assemblages in China. Cretaceous Research 15, 271-284.

Ma, X.Y., 1989. Lithospheric dynamics map of China and adjacent seas (1/4 000 000) and explanatory notes. Geological Publishing House, Beijing, China.

Ma, Y., Cui, S., Wu, G., Wu, H., Zhu, D., Li, X., Feng, X., 1999. The structural feature of metamorphic core complex in Yiwulüshan Mountains, West Liaoning. Acta Geoscientia Sinica 20, 385-391.

Ma, X., Wu, D., 1987. Cenozoic extensional tectonics in China. Tectonophysics 133, 243-255.

Machel, H.G., 2001. Bacterial and thermochemical sulphate reduction in diagenetic settings – old and new insights. Sedimentary Geology 140, 143-175.

Marriott, S.B., 1999. The use of models in the interpretation of the effects of base-level change on alluvial architecture, in: Smith N.D., Rogers J. (Eds), Fluvial sedimentology VI, International Association of Sedimentologists, Special Publication 28, pp. 271-281.

Maruyama, S., Isozaki, Y., Kimura, G., Terabayashi, M., 1997. Paleogeographic maps of the Japanese Islands: Plate tectonic synthesis from 750 Ma to present. The Island Arc 6, 121-142.

Massmann, G., Tichomirowa, M., Merz, C., Pekdeger, A., 2003. Sulfide oxidation and sulphate reduction in a shallow groundwater system (Oderbruch Aquifer, Germany). Journal of hydrology 2787, 231-243.

- Mattauer, M., Matte, P., Malavieille, J., Tapponnier, P., Maluski, H., Xu, Z., Lu, Y., Tang, Y., 1985. Tectonics of Qinling belt: Build-up and evolution of eastern Asia. *Nature* 317, 496-500.
- Mazukabzov, A.M., Donskaya, T.V., Gladkochub, D.P., Sklyarov, E.V., Ponomarchuk, V.A., Sal'nikova, E.B., 2006. Structure and age of the metamorphic core complex of the Burgutui ridge (Southwestern Transbaikal region). *Dokl Earth Sci* 407, 179-183.
- Meisel, T., Walker, R.J., Irving, A.J., Lorand, J.P., 2001. Osmium isotopic compositions of mantle xenoliths: a global perspective. *Geochimica and Cosmochimica Acta* 65, 1311–1323.
- Meng, Q-R., 2003. What drove late Mesozoic extension of the northern China-Mongolia tract? *Tectonophysics* 369, p.155-174.
- Meng, Q., Hu, J-M., Jin, J-Q., Zhang, Y., Xu, D-F., 2003. Tectonics of the late Mesozoic wide extensional basin system in the China-Mongolia border region. *Basin Research* 15, 397–415.
- Menzies, M.A., Fan, W.M., Zhang, M., 1993. Palaeozoic and Cenozoic lithoproses and the loss of >120 km of Archean lithosphere, Sino-Korean Craton, China, in: Prichard, H.M., Alabaster, T., Harris, N.B.W., Neary, C.R. (eds), *Magmatic processes and plate tectonics*. Geological Society, London, Special Publications 76, 71-81.
- Menzies, M.A., Xu, Y., 1998. Geodynamics of the North China Craton. In: Flower, M., Chung, S.L., Lo, C.H., Lee, T.Y. (Eds), *Mantle dynamics and plate interactions in East Asia*. AGU 27, 155-165.
- Menzies, M.A., Xu, Y., Zhang, H., Fan, W., 2007. Integration of geology, geophysics and geochemistry: a key to understanding the North China Craton. *Lithos* 96, 1-21.
- Menzies, M.A., Xu, Y.G., 1998. Geodynamics of the North China Craton, in: Flower, M.F.J., Chung, S.L., Lo, C.H., Lee, T.Y. (eds), *Mantle dynamics and plate interaction in East Asia*, American Geophysical Union, Washington D.C., Geodynamic series 100, 107-126.
- Miall, A.D., 1996. *The Geology of Fluvial Deposits*. Springer Ed., 582 pp.
- Miall, A.D., 2010. Alluvial deposits, in: James, N.P., Dalrymple, R.W. (Eds), *Facies Models 4*, Queen's University, Kingston, Canada, pp. 105-138.
- Miao, L., Luo, Z., Guan, K., Huang, J., 1998. The implication of the SHRIMP U-Pb age in zircon to the petrogenesis of the Linglong granite, East Shandong Province. *Acta Petrologica Sinica* 14, 198-206 (in Chinese with English abstract).

- Michard, A., Gurriet, P., Soudant, M., Albarede, F., 1985. Nd isotopes in French phanerozoic shales : external vs internal aspects of crustal evolution. *Geochim. Cosmochim. Acta* 49, 601-610.
- Min, M.Z., Chen, J., Wang, J.P., Wei, G.H., Fayek, M., 2005a. Mineral paragenesis and textures associated with sandstone-hosted roll-front uranium deposits, NW China. *Ore Geology Reviews* 26, 51–69.
- Min, M.Z., Xu, M.H., Chen, J., Fayek, M., 2005b. Evidence of uranium biomineralization in sandstone-hosted roll-front uranium deposits, northwestern China. *Ore Geology Reviews* 26, 198–206.
- Mossman, D.J., Gauthier-Lafaye, F., Nagy, B., Rigali, M.J., 1998. Chemistry of organic-rich black shales overlying the natural nuclear fission reactors of Oklo, republic of Gabon. *Energy Sources* 20, 521-539.
- Mueller, A., Halbach, P., 1983. The Anderson Mine (Arizona) – An Early Diagenetic Uranium Deposit in Miocene Lake Sediments. *Economic Geology* 78, 275-292.
- Munara, A., 2012. Formation des gisements d'uranium de type roll: approche minéralogique et géochimique du gisement uranifère de Muyunkum (Bassin de Chu-Sarysu, Kazakhstan). Thèse de doctorat de l'Université de Lorraine.
- Munier-Lamy, C., Adrian, P., Berthelin, J., Rouiller, J., 1986. Comparison of binding abilities of fluvic and humic acids extracted from recent marine sediments with UO₂²⁺. *Organic Geochemistry* 9, 285-292.
- Mustin, C., de Donato, P., Berthelin, J., Marion, P., 1993. Surface sulphur as promoting agent of pyrite leaching by *Thiobacillus ferrooxidans*. *FEMS Microbiology Reviews* 11, 71-77.

N

- Nakashima, S., 1992. Kinetics and thermodynamics of U reduction by natural and simple organic matter. *Organic Geochemistry* 19, 4-6, 421-430.
- Nie, F., 2008. Uranium mineralization of the Bayawula deposit, Erlian Basin, northeast China. IAEA Technical Meeting “Uranium exploration and mining methods”, Jordan, Amman, 17-21 November 2008.
- Nie, F., Chen, A., Hu, Q., Shen, K., Qin, M., Li, M., Jiang, M., 2007. Discussion on the early Cretaceous sandstone-type uranium deposits, Erlian Basin, Inner Mongolia. *Journal of Stratigraphy* 31-3, 272-279. (in Chinese, English abstract).

- Niu, Y.L., 2005. Generation and evolution of basaltic magmas: some basic concepts and anew view on the origin of Mesozoic-Cenozoic basaltic volcanism in eastern China. Geological Journal of Chinese University 11, 9-46.
- Niu, L., Huang, S., Yang, G., 1995. The characteristics of uranium mineralization and genesis of Nuheting uranium deposit in Erlian Basin, Inner Mongolia. China Nuclear Science and Technology Report 1995-00 (in Chinese, English abstract).
- Nichols, D.J., 2003. Biodiversity changes in Cretaceous palynofloras of eastern Asia and western North America. Journal of Asian Earth Sciences 21, 823-833.
- Nichols, D.J., Matsukawa, M., Ito, M., 2006. Palynology and age of some Cretaceous nonmarine deposits in Mongolia and China. Cretaceous Research 27, 241-251.
- Nichols, D.J., Watabe, M., Ichinnorov, N., Ya, A., 2001. Preliminary report on the palynology of the Cretaceous of the Gobi Desert, Mongolia. IX Palynological Congress.
- Northrup, C.J., Royden, L.H., Burchfiel, B.C., 1995. Motion of the Pacific Plate relative to Eurasia and its potential relation to Cenozoic extension along the eastern margin of Eurasia. Geology 23, 719-722.

O

- OECD-NEA/IAEA, 2004. Recent developments in uranium resources and production with emphasis on in situ leach mining.
- OECD-NEA/IAEA, 2005. Developments in uranium resources, production, demand and the environment.
- OECD/NEA/IAEA, 2008. Uranium 2007: Resources, production and Demand, 2007 Red Book. OECD, Paris, France.
- OECD-NEA/IAEA, 2010. Uranium 2009: Resources, Production and Demand, 2009 Red Book. OECD, Paris France.
- OECD/NEA/IAEA, 2012. Uranium 2011: Resources, production and Demand, 2011 Red Book. OECD, Paris, France.
- Oh, C.W., Kusky, T., 2007. Review of the late Permian to Triassic Hongseong-Odesancollision belt in South Korea and its tectonic correlation with Korea, China and Japan. International Geology Reviews, Special Liu volume 49.
- Okada, H., 1999. Plume-related sedimentary basins in East Asia during the Cretaceous. Palaeogeography Palaeoclimatology Palaeoecology 150, 1-11.
- Olivier, N., Hantzpergue, P., Gaillard, C., Pittet, B., Leinfelder, R., Shmid, D., Werner, W., 2003. Microbialite morphology, structure and growth: a model of the Upper Jurassic

reefs of the Chay Peninsula (Western France). Palaeogeography, Palaeoclimatology, Palaeoecology 193, 383-404.

Otton, J.K., 1984. Surficial uranium deposits: summary and conclusions. In: Surficial uranium deposits, IAEA, Vienna, IAEA-TEDOC-322, 252 pp.

Owen, D.E., Otton, J.K. 1995. Mountain wetlands: efficient uranium filters-potential impacts. Ecological Engineering 5, 77-93.

P

Pagel, M., Cavellec, S., Forbes, P., Gerbaut, O., Vergely, P., Wagani, I., and Mathieu, R., 2005. Uranium deposits in the Arlit area (Niger): SGA Meeting, Meeting the Global Challenge, 8th, Beijing, China, Proceedings, 303–305.

Payne, T.E., 1999. Uranium (VI) interaction with mineral surfaces: controlling factors and surface complexation modelling. PhD dissertation of the University of New South Wales, 390 pp.

Pearce, J.A., Harris, N.W., Tindle, A.G., 1984. Trace element discrimination diagrams for the tectonic interpretation of granitic rocks. Journal of Petrology 25, 956-983.

Pei, F.P., Xu, W.I., Yang, D.B., Ji, W.Q., Yu, Y., Zhang, X.Z., 2008. Mesozoic volcanicrocks in the southern Songliao basin: zircon U/Pb ages and their constraints on thenature of basin basement. Earth Science (Journal of China University of Geosciences) 32, 603-617 (in Chinese with English abstract).

Posamentier, H.W., Allen G.P., 1999. Siliciclastic sequence stratigraphy: concepts and applications. SEPM, Concepts in Sedimentology and Paleontology 7, 210 pp.

R

Rackley, R.I., 1972. Environment of Wyoming Tertiary uranium deposits. American Association of Petroleum Geologists 56, 755-774.

Ratschbacher, L., Hacker, B.R., Calvert, A., Webb, L.E., Grimmer, J.C., McWilliams, M.O., Ireland, T., Dong, S., Hu, J., 2003. Tectonics of the Qinling (Central China): tectonostratigraphy, geochronology, and deformation history. Tectonophysics 366, 1-53.

Ratschbacher, L., Hacker, B.R., Webb, L.E., McWilliams, M., Ireland, T., Dong, S., Calvert, A., Chateigner, D., Wenk, H.R., 2000. Exhumation of the ultrahigh-pressurecontinental crust in east central China: Cretaceous and Cenozoic unroofing and the Tan-Lu fault. Journal of the Geophysical Research 105, 13303-13338.

- Reinhardt, J., and Sigeo, W.R., 1988. Paleosols and weathering through geologic time. The Geological Society of America, Special Publication 213, 181 pp.
- Ren, J., Chen, Y., Niu, B., Liu, Z. and Liu, F., 1990. Tectonic Evolution and Deposits of Continental Lithosphere of East China and Adjacent Areas (in Chinese). Science Press, Beijing.
- Ren, J., Li, S., Jiao, G., 1998. Extensional tectonic system of the Erlian fault basin group and its deep background. Journal of China University of Geosciences 23, 567-572.
- Ren, J., Tamaki, K., Li, S. & Zhang, J., 2002. Late Mesozoic and Cenozoic rifting and its dynamic setting in Eastern China and adjacent areas. Tectonophysics 344, p.175-205.
- Retallack, G.J., 1997. A colour guide to paleosols. Wiley Ed., 175 pp.
- Reynolds, R. L., Goldhaber, M. B., 1978, Origin of a south Texas roll-type uranium deposit: I. Alteration of iron-titanium oxide minerals. Economic Geology 73, 1677-1689.
- Reynolds, R.L., Goldhaber, M.B., 1982. Biogenic and nonbiogenic ore-forming processes in the South Texas uranium district: evidence from the Panna Maria deposit. Economic Geology 77, 541-556.
- Reynolds, R.L., Goldhaber, M.B., 1983. Iron Disulfide Minerals and the Genesis of Roll-Type Uranium Deposit. Economic Geology 78, 105-120.
- Robb, L. J. and Meyer, F.M., M., 1990. The nature of the Witwatersrand hinterland: conjectures on the source area problem. Economic Geology 85, 511-536.
- Robb, L. J., Meyer, F.M., Ferraz, M.F., Drennan, G.K., 1990. The distribution of radioelements in Archaean granites of the Kaapvaal Craton, with implications for the source of uranium in the Witwatersrand Basin. South African Journal of Geology 93, 5-40.
- Rollinson, H., 1993. Using geochemical data: evaluation, presentation, interpretation. Pearson Ed. Edinburgh, 352 pp.
- Rozhdestvensky, A.K., 1966. New iguanodonts from Central Asia: phylogenetic and taxonomic relationships between late Iguanodontidae and early Hadrosauridae. Paleontologicheskii Zhurnal, 103-116.
- Rozhdestvensky, A.K., 1977. The study of dinosaurs in Asia. Journal of the Palaeontological Society of India 20, 102-119.
- RTMCFEH (Research Team on the Mesozoic Coal-Bearing Formations in Eastern Heilongjiang), 1986. A Study on the Longzhaogou Group in Eastern Heilongjiang Province and its Correlation with the Jixi Group. Heilongjiang Science and Technology Publishing House, Harbin, 172 pp. (in Chinese, English abstract).

Ru, K., Pigott, J.D., 1986. Episodic rifting and subsidence in the South China Sea. *Pet. Geol. Bulletin* 70, 1136-1155.

Rudnick, R.L., Gao, S., Ling, W.L., Liu, Y.S., McDonough, W., 2004. Petrology and geochemistry of spinel peridotite xenoliths from Hannuoba and Qixia, North China Craton. *Lithos* 77, 609-637. Rutherford, E., 1906. Radioactive transformations. Scribners, New York.

S

Sagong, H., Kwon, S.T., 2005. Mesozoic episodic magmatism in South Korea and its tectonic implication. *Tectonics* 24 (2004TC001720).

Sarangi, A. K., Singh A.S., 2006. Vein type uranium in the Jagunda uranium deposits, Singhbhum, India. Abstract, 12th IAGOD Symposium, Moscow, Russia.

Saunders, A.D., Norry, M.J., Tarney, J., 1988. Origin of MORB and chemically depleted mantle reservoirs: trace element constraints. *Journal of Petrology, Special Lithosphere Issue*, 415-445.

Schellart, W.P., 2005. Influence of the subducting plate velocity on the geometry of the slab and migration of the subduction hinge. *Earth and Planetary Science Letters* 231, 197-19.

Schellart, W.P., Jessel, M.W., Lister, G.S., 2003. Asymmetric deformation in the back-arc region of the Kuril arc, northwest Pacific: new insights from analogue modeling. *Tectonics* 22, 1047.

Schulz, B., Bombach, K., Pawlig, S., Braetz, H., 2004. Neoproterozoic to early Palaeozoic magmatic evolution in the Gondwana-derived Austroalpine basement to the south of the Tauern Window, Eastern Alps. *International Journal of Earth Sciences* 93, 824-843.

Schumm, S.A., 1977. The fluvial system. Blackburn Press Ed., 338 pp.

Schumm, S.A., 2006. River variability and complexity. Cambridge University Press, Cambridge, 220 pp.

Schumm, S.A., Dumont J.F., Holbrook J.M., 2000. Active tectonics and alluvial rivers. Cambridge University Press, Cambridge, 276 pp.

Scott, R.W., Wan, X., Wang, C., Huang, Q., 2012. Late Cretaceous chronostratigraphy (Turonian – Maastrichtian): SK1 core Songliao Basin, China. *Geoscience Frontiers*, 1-11.

Sengör, A.M., Burke, K., 1978. Relative timing of rifting and volcanism on Earth and its tectonic implications. *Geophysical Research Letters* 5, 419-421.

- Sha, J., 2007. Cretaceous stratigraphy of northeast China: non-marine and marine correlation. *Cretaceous Research* 28, 146-170.
- Shanley, K.W., McCabe, P.J., 1994. Perspectives on the sequence stratigraphy of continental strata. *American Association of Petroleum Geologists* 78, 544-568.
- Shaw, D., Sturchio, N., 1992. Boron-Lithium Relationships in Rhyolites and Associated Thermal Waters. *Geochim. Cosmochim. Acta* 56, 3723-3731.
- Shuvalov, V.F., 2000. The Cretaceous stratigraphy and palaeobiogeography of Mongolia, in: Benton, M.J., Shishkin, M.A., Unwin, D.M., Kurochkin, E.N. (Eds), *The Age of Dinosaurs in Russia and Mongolia*. Cambridge University Press, Cambridge, 256-278.
- SIGMR (Shenyang Institute of Geology and Mineral Resources), 1980. *Palaeontogical Atlas of Northeast China 2. Mesozoic and Cenozoic Volume*. Geological Publishing House, Beijing, 403 pp. (in Chinese).
- Skelton, P., 2006. *The Cretaceous world*. The Open University, Cambridge University Press, Cambridge, 360 pp.
- SMJGRT (Soviet-Mongolia Joint Geoscience's Research Team), 1980. *Fundamental GeologicProblems of Mongolia*. Geological Publishing House, Beijing, 169 p.
- Snow, J.E., Reisberg, L., 1995. Os isotopic systematics of the MORB mantle: results fromaltered abyssal peridotites. *Earth and Planetary Science Letters* 133, 411-421.
- Song, Z.C., Liu, G.W., Li, W.B., 1986. Early Cretaceous Palynological Assemblages from Eren Basin of Nei Mongol, in: Nanjing Institute of Geology and Palaeontology, Academia Sinica, the First Exploration Company, North China Oil Field, Ministry of Oil Industry (Eds.), *Cenozoic-Mesozoic Palaeontology and Stratigraphy of East China, Series 2. Cretaceous Ostracod and Sporo-pollen Fossils of Eren Basin*. Anhui Science and Technology Publishing House, Hefei, pp. 105-335. (in Chinese, English abstract).
- Stepashko, A.A., 2006. The Cretaceous Dynamics of the Pacific Plate and Stages of Magmatic Activity in Northeastern Asia. *Geotectonics* 40, 225-235.
- Su, S., Niu, Y., Deng, J., Liu, C., Zhao, G., Zhao, X., 2007. Petrology and geochronology of Xuejiashiliang igneous complex and their genetic link to the lithospheric thinning during Yanshanian orogenesis in eastern China. *Lithos* 96, 90-107.
- Sun, G., Zheng, S.L., Dilcher, D.L., 2001. Early Angiosperms and their Associated Plants from Western Liaoning, China. Scientific and Technological Education Publishing House, Shanghai, 227 pp. (in Chinese and English).
- Sun, G., Ji Q., Dilcher, D.L., Zheng, Q., Nixon, K.C., Wang, X., 2002. Archaefructaceae, a new basal angiosperm family. *Science* 296, 899-904.

T

- Tallarico, F.H.B., Figueiredo, B.R., Groves, D.I., Kositcin, N., McNaughton, N.J., Fletcher, I.R., and Rego, J.L., 2005. Geology and SHRIMP U-Pb geochronology of the Igaraپ Bahia deposit, Carajás copper-gold belt, Brazil: An Archean (2.57 Ga) example of iron-oxide Cu-Au-(U-REE) mineralization. *Economic Geology*, 100, p. 7–28.
- Tatsumi, Y., Maruyama, S., Nohda, S., 1990. Mechanism of back arc opening in the Japan Sea: role of asthenospheric injection. *Tectonophysics* 181, 299-306.
- Traynor, J.J., Sladen, C., 1995. Tectonic and stratigraphy evolution of the Mongolian People's Republic and its influence on hydrocarbon geology and potential. *Marine and Petroleum Geology* 12, 35- 52.
- Taylor, T.N., Taylor, E.L., Krings, M., 2009. Paleobotany. The biology and evolution of fossil plants. Academic Press, Elsevier Ed., 1230 pp.
- Tian, Z.Y., Han, P., Xu, K.D., 1992. The Mesozoic-Cenozoic East China rift system. *Tectonophysics* 208, 341-363.
- Teclu, D., Tivchev, G., Laing, M., Wallis, M., 2008. Bioremoval of arsenic species from contaminated waters by sulphate-reducing bacteria. *Water Research* 42, 4885-4893.
- Thode, H.G., Kleerboper, H., McElcheran, D., 1951. Isotopic fractionation in the bacterial reduction of sulphate. *London Research* 4, 581-582.
- Tirel, C., Brun, J.P., Burov, E., 2008. Dynamics and structural development of metamorphic core complexes. *Tectonics* 113. doi:10.1029/2005JB003694.
- Trap, P., 2007. Style tectonique et contexte géodynamique au Paléoprotérozoïque. Exemple du Craton de Chine du Nord. Thèse doctorale de l'Université d'Orléans.
- Trap, P., Faure, M., Lin, W., Bruguier, O., Monié, P., 2008. Contrasted tectonic styles for the Paleoproterozoic evolution of the North China Craton. Evidence for a not, vert, similar~2.1 Ga thermal and tectonic event in the Fuping Massif. *Journal of Structural Geology* 30, 1109-1125.
- Treese, K.L., Wilkinson, B.H., 1982. Peat-marl deposition in a Holocene paludal-lacustrine basin, Sucker Lake, Michigan. *Sedimentology* 29, 375-390.
- Turek, A., Kim, C.B., 1995. U/Pb zircon ages of Mesozoic plutons in the Damyang-Geochang area, Ryongnam massif. *Korean Geochemical Journal* 29, 243-258.

V

- Vakhrameev, V.A., 1991. Jurassic and Cretaceous Floras and Climates of the Earth. Cambridge University Press, Cambridge, 318 pp.
- Van Itterbeeck, J., Horne, D.J., Bultynck, P., Vandenberghe, N., 2005. Stratigraphy and Palaeoenvironment of the dinosaur-bearing Upper Cretaceous Iren Dabasu Formation, Inner Mongolia, People's Republic of China. *Cretaceous Research* 26, 699-725.
- Van Itterbeeck, J., Missiaen, P., Folie, A., Markevick, V.S., Van Damme, D., Dian-Yong, G., Smith, T., 2007. Woodland in a fluvio-lacustrine environment on the dry Mongolian Plateau during the late Paleocene: Evidence from the mammal bearing Subeng section (Inner Mongolia, P.R. China). *Palaeogeography, Palaeoclimatology, Palaeoecology* 243, 55-78.

W

- Wan, X., Zhao, J., Scott, R.W., Wang, P., Feng, Z., Huang, Q., Xi, D., 2012. Late Cretaceous stratigraphy, Songliao Basin, NE China: SK1 cores. *Palaeogeography, Palaeoclimatology, Palaeoecology*, in press.
- Wang, H.S., 1929. The geology and mineral resources of Mishan and Muleng, Kirin. *Bulletin of the Geological Survey of China* 13, 27-31.
- Wang, D., Aller, R., Sanudo-Wilhelmy, S.A., 2011. Redox speciation and early diagenetic behaviour of dissolved molybdenum in sulfidic muds. *Marine Chemistry* 125, 101-107.
- Wang, P., Du, X., Wang, J., Wang, D., 1995a. The chronostratigraphy and stratigraphic classification of the Cretaceous of the Songliao basin. *Acta Geologica Sinica* 69, 372-381.
- Wang, P.J., Liu, Z.J., Wang, S.X., Song, W.H., 2002. $^{40}\text{Ar}/^{39}\text{Ar}$ and K/Ar dating of volcanic rocks in the Songliao basin, NE China: constraints on stratigraphy and basin dynamics. *International Journal of Earth Sciences* 91, 331-340.
- Wang, L.G., Qiu, Y.M., McNaughton, N.J., Groves, D.I., Luo, Z.K., Huang, J.Z., Miao, L.C., Liu, Y.K., 1998. Constraints on crustal evolution and gold metallogeny in the Northwestern Jiaodong Peninsula, China, from SHRIMP U-Pb zircon studies of granitoids. *Ore Geology Reviews* 13, 275-291.
- Wang, F., Zhou X.-H., Zhang, L.-C., Ying, J.-F., Zhang, Y.-T., Wu, F.-Y., Zhu, R.-X., 2006. Late Mesozoic volcanism in the Great Xing'an Range (NE China): Timing and implications for the dynamic setting of NE Asia. *Earth and Planetary Science Letters* 251, 179-198.

- Watson, M.P., Hayward, A.B., Parkinson, D.N., Zhang, Z.M., 1987. Plate tectonic history, basin development and petroleum source rock deposition onshore China. *Marine Petroleum Geology* 4, 205-225.
- Weaver, B.L., 1991. The origin of ocean island basalt end-member compositions: trace element and isotopic constraints. *Earth Planetary Science Letter* 104, 381-397.
- Webb, L.E., Graham, S.A., Johnson, C.L., Badarch, G., Hendrix, S., 1999. Occurrence, age, and implications of the Yagan-Onch Hayrhan metamorphic core complex, southern Mongolia. *Geology* 27, 143-146.
- Wei, S., Qin, M., Li, Y., He, Z., Chen, A., Shen, K., (2005). Late Mesozoic-Cenozoic tectono sedimentary evolution and sandstone-hosted uranium mineralization of the Erlian basin. *Mineral Deposit Research: Meeting the Global Challenge, 8th Biennial SGA Meeting Beijing, metallogeny and exploration, Chapter 3-27, p. 320-322.*
- Weishampel, D.B., Horner, J.R., 1986. The hadrosaurid dinosaurs of the Iren Dabasu Formation (People's Republic of China, Late Cretaceous). *Journal of Vertebrate Paleontology* 6, 38-45.
- Wernicke, B.P., Axen, G.J., Snow, J.K., 1988. Basin and Range extensional tectonics in the latitude of Las Vegas, Nevada. *The Geological Society of America* 100, 1738-1757.
- Wiedenbeck, K., Allé, P., Corfu, F., Griffi, W.L. Meier, M., Oberli, I., Von Quadt, A., Roddick, J.C., Spiegel, W., 1995. Three natural standards for U-Th-Pb, Lu-Hf, trace element and REE analyses, *Geostandard Newsletter* 19-1, 1.23.
- Wilde, S.A., Zhou, X.H., Nemchin, A.A., Sun, M., 2003. Mesozoic crust-mantle interaction beneath North China craton: a consequence of the dispersal of Gondwana land and accretion of Asia. *Geology* 31, 817-820.
- Wilson, S.A., Ridley, W.I., Koenig, A.E., 2002. Development of sulphide calibration standards for the laser ablation inductively-coupled plasma mass spectrometry technique. *J. Anal At. Spectrom* 17, 406-409.
- Wong, J., Sun, M., Xing, G., Li, X.H., Zhao, G., Wong, K., Yuan, C., Xia, W., Li , L., Wu, F.Y., 2009. Geochemical and zircon U-Pb and Hf isotopic study of the Baijuhuajian metaluminous A-type granite: Extension at 125-100 Ma and its tectonic significance for South China. *Lithos* 112, 289-305.
- Wu, Z., Cui, S., Zhu, D., Feng, X., Ma, Y., 2000a. Thermal evolution of plutons and uplift process of the Yanshan orogenic belt. *Acta Geologica Sinica* 74, 7-13.

- Wu, J., Hu, W., Jiao, J., 1998. Mesozoic pollen assemblages of Ejin Qi depression, Yingenbasin, Inner Mongolia. *Journal of Changchun University Sciences and Technology* 28, 247-253.
- Wu, F.Y., Han, R.H., Yang, J.H., Wilde, S.A., Zhai, M.G., Park, S.C., 2007. Initial constraints on the timing of granitic magmatism in North Korea using U-Pb zircon geochronology. *Chemical Geology* 238, 232-248.
- Wu, F.Y., Jahn, B.M., Wilde, S., Sun, D.Y., 2000b. Phanerozoic crustal growth: U-Pb and Sr-Nd isotopic evidence from the granites in northeastern China. *Tectonophysics* 328, 89-113.
- Wu, F.Y., Lin, J.Q., Wilde, S.A., Sun, D.Y., Yang, J.H., 2005a. Nature and significance of the Early Cretaceous giant igneous event in eastern China. *Earth Planetary Science Letters* 233, 103-119.
- Wu, J., Liu, D., Geng, Y., Song, B., Li, Z., 1992. Archaean granitic rocks around Anshan, Liaoning, China. *International Geological Congress* 50.
- Wu, L., Qi, J., Wang, T., Zhang, X., Xu, Y., 1982. Mesozoic volcanic rocks in the eastern part of China. *Acta Geologica Sinica* 64, 221-234.
- Wu, G., Sun, F., Zhao, C., Li, Z., Zhao, A., Pang, Q., Li, G., 2005b. Discovery of the Early Paleozoic post-collisional granites in northern margin of the Erguna massif and its geological significance. *Chinese Science Bulletin*, 50, 2733-2743.
- Wu, F.Y., Sun, D.Y., Li, H., Jahn, B.M., Wilde, S., 2002. A-type granites in northeastern China: age and geochemical constraints on their petrogenesis. *Chemical Geology* 187, 143-173.
- Wu, F.Y., Walker, R., Ren, X.W., Sun, D.Y., Zhou, X.H., 2003. Osmium isotopic constraints on the age of lithospheric mantle beneath northeastern China. *Chemical Geology* 196, 107-129.
- Wu, F.Y., Yang, J.H., Wilde, S.A., Zhang, X.O., 2005c. Geochronology, petrogenesis and tectonic implications of Jurassic granites in the Liaodong Peninsula, NE China. *Chemical geology* 221, 127-156.

X

- Xiao, W., Windley, B.F., Hao, J., Zhai, M., 2003. Accretion leading to collision and the Permian Solonker suture, Inner Mongolia, China: Termination of the Central Asian orogenic belt. *Tectonics* 22, 1069.

Xingzhong, L., Weixun, Z., 1990. Uranium Provinces in China and their Distribution pattern.

- Xu, X.S., O'Reilly, S.Y., Griffin, W.L., Zhou, X.M., 1998. The nature of the Cenozoic lithosphere at Hushan, central eastern China. In: Flower, M., Chung, S.L., Lo, C.H., Lee, T.Y. (Eds), Mantle dynamics and plate interactions in East Asia. AGU 27, 167-196.
- Xu, Y.G., 2001. Thermo-tectonic destruction of the Archaean lithospheric keel beneath the Sino-Korean craton in China: evidence, timing and mechanism. Physics and Chemistry of the Earth 26, 747-757.
- Xu, Y.G., 2007. Diachronous lithospheric thinning of the North China Craton and formation of the Daxin'anling-Taihangshan gravity lineament. Lithos 96, 281-298.
- Xu, X., Tan, Q., Wang, J., Zhao, X., Tan, L., 2007. A gigantic bird-like dinosaur from the Late Cretaceous of China. Nature 447, 844-847.

Y

- Yan, Y., An, W., Xu, X., 2010. Study on rocks feature in ore target layers of Nuheting mudstone-type uranium deposit. China Academic Journal Publishing House, 4, 44-46.
- Yang, J.H., Wu, F.Y., Wilde, S.A., Xie, L.W., Yang, Y.H., Liu, X.M., 2007. Tracing magma mixing in granite genesis: in situ U-Pb dating and Hf-isotope analysis of zircons. Contributions to Mineralogy and Petrology 153, 177-190.
- Yano, T., Wu, G.Y., 1997. Late Mesozoic geodynamics relating Circum-Pacific mobile belt and Darwin Rise. J. Geol. Soc. Philipp. 52 (3-4), 235-271.
- Yarmolyuk, V.V., Kovalenko, V.I., 2001. The Mesozoic-Cenozoic of Mongolia. In: Dergunov, A.B. (Ed), Tectonics, Magmatism and Metallogeny of Mongolia. Taylor & Francis Group, London, 203-244.
- Ye, H., Zhang, B., Mao, F., 1987. The Cenozoic tectonic evolution of the Great North China: two types of rifting and crustal necking in the Great North China and their tectonic implications. Tectonophysics 133, 217-227.
- Ye, D.Q., Zhong, X.C., Zhao, C.B., 1990. Cretaceous subdivision and correlation of oil-and gas-bearing areas of northern China, in: Ye, D.Q., Zhong, X.C. (Eds.), Cretaceous in Oil and Gas-bearing Areas of Northern China. Series on stratigraphy and palaeontology of oil and gas bearing areas in China. Petroleum Industry Press, Beijing, pp. 1-44. (in Chinese).
- Yi, Z.J., Tan, K.X., Tan, A.L., Yu, Z.X., Wang, S.Q., 2007. Influence of environmental factors on reductive bioprecipitation of uranium by sulphate reducing bacteria. International Biodeterioration and Biodegradation 60, 258-266.

- Yin, A., Nie, S., 1996. A Phanerozoic palinspastic reconstruction of China and its neighboring regions. In: Yin, A., and Harrison, T. A. (Eds). *The tectonic evolution of Asia*. New York, Cambridge University Press, 442–485.
- Ying, J.F., Zhou, X.H., Zhang, L.C., Wang, F., 2010a. Geochronological framework of Mesozoic volcanic rocks in the Great Xing'an Range, NE China, and their geodynamic implications. *Journal of Asian Earth Sciences*, doi:10.1016/j.jseaes.2010.04.035.
- Ying, J.F., Zhou, X.H., Zhang, L.C., Wang, F., Zhang, Y.T., 2010b. Geochronological and geochemical investigation of the Late Mesozoic volcanic rocks from the northern Great Xing'an Range and their tectonic implications. *International Journal of Earth Sciences* 99, 357-378.
- Yu, X.H., Wang, W.L., Liu, X.T., et al., 1987. *Mesozoic Stratigraphy and Palaeontology of Western Liaoning*. Geological Publication House, Beijing, 385 pp. (in Chinese, English abstract).
- Yuan, X.C., (chief compiler), 1996. *Atlas of geophysics in China*. Publication of the International Lithosphere Program 201.

Z

- Zhai, M.G., Liu, W.J., 2003. Paleoproterozoic tectonic history of the North China Craton: a review. *Precambrian Research* 122, 183-199.
- Zhai, M.G., Windley, B.F., Kusky, T.M., Meng, Q.R. (eds), 2007. *Mesozoic sub-continental lithospheric thinning under eastern Asia*. Geological Society, London, Special Publications 280.
- Zhang, S., 2009. *Geological formation names of China*. Springer Ed., 2 volumes, 1537 pp.
- Zhang, R., Ding, W., 1996. Discussion on geological characteristics of Nuheting type uranium deposit and the relation between oil and gas-bearing water and uranium metallogenesis. In: *Galaxy of research achievements of uranium geology of China*, Bureau of Geology, China National Nuclear Corporation, Beijing, 205-214.
- Zhang, Y.Q., Dong, S.W., Zhao, Y., 2008b. Jurassic tectonics of North China: A synthetic view. *Acta Geological Sinica* 82, 310-326.
- Zhang, F.Q., Chen, H.L., Yu, X., Dong, C.W., Yang, S.F., Pang, Y.M., Batt, G.E., 2010a. Early Cretaceous volcanism in the northern Songliao basin, NE China, and its geodynamic implication. *Gondwana Research*, doi:10.1016/j.gr.2010.03.011.
- Zhang, J.H., Gao, S., Ge, W.C., Wu, F.Y., Yang, J.H., Wilde, S.A., Li, M., 2010b. Geochronology of the Mesozoic volcanic rocks in the Great Xing'an Range,

- northeastern China: Implications for subduction-induced delamination. *Chemical Geology*, doi:10.1016/j.chemgeo.2010.05.013.
- Zhang, J.H., Ge, W.C., Wu, F.Y., Wilde, S.A., Yang, J.H., Liu, X.M., 2008a. Large-scale Early Cretaceous volcanic events in the northern Great Xing'an Range, Northeastern China. *Lithos* 102, 138-157.
- Zhang, H.Y., Hou, Q.L., Cao, D.Y., 2007. Tectono-chronologic constraints on a Mesozoic slip and thrust belt in the eastern Jiaodong Peninsula. *Science in China Series D* 50, 25-32.
- Zhang, P., Hu, S., Wan, G., 1989. A review of the geology of some kimberlites in China. *Geological Society of Australia Special Publication* 14, 392-400.
- Zhang, Y., Lim, A., Zhou, W., Zhang, W., Wang, Z., Chen, F., Hao, J., 2008. The study on uranium ore-forming predication of Saihangaozi-Bayinwula area. *Journal of East China Institute of Technology* 31-4, 319-323.
- Zhang, C.Y., Nie, F., Liu, Q., Fan, X., 2010. Discussion on electrical logging response of target layer for sandstone-type uranium deposits of Bayanwula area, Erlian Basin. *Uranium Geology* 26-2, 101-107.
- Zhang, A., Xu, D., Xie, X., Guo, L., Zhou, J., Wang, W., 1991. The status and future of diamond exploration in China. *CPRM Special Publication* 92, 10-11.
- Zhao, D., 1998. Diamonds and mantle xenoliths in kimberlites from the North China Craton and the Canadian Northwest Territories. Unpublished doctoral thesis, University of Michigan, 220 p.
- Zhao, W., Fang, J., 2007. Hydrocarbon migration characteristics of the Lower Cretaceous in the Erlian Basin. *Chinese Journal of Geochemistry* 26-1, 1-7.
- Zhao, G.C., Wilde, S.A., Cawood, P.A., Lu, L.Z., 1998. Thermal evolution of basement rocks from the eastern part of the North China Craton and its bearing on tectonic setting. *International Geology Reviews* 40, 706-721.
- Zhao, G.C., Wilde, S.A., Cawood, P.A., Lu, L.Z., 1999. Tectonothermal history of the basement rocks in the western zone of the North China Craton and its tectonic implications. *Tectonophysics* 310, 37-53.
- Zhao, L., Zheng, T.Y., Chen, L., Tang, Q.S., 2007. Shear wave splitting in eastern and Central China: implications for upper mantle deformation beneath continental margin. *Physics of the Earth and Planetary Interiors* 162, 73-84.

- Zheng, J., Griffin, W.L., O'Reilly, S.Y., Lu, F., Wang, C., Zhang, F., Li, H., 2004. 3.6 Galower crust in central China: new evidence on the assembly of the North China Craton. *Geology* 32, 229-233.
- Zhi, X., Peng, Z., Chen, D., Yu, C., Sun, W., Reisberg, L., 2001. The longevity of subcontinental lithospheric mantle beneath Jiansu-Anhui region. *Science in China Series D* 44, 1110-1118.
- Zhou, Z., Barrett, P.M., Hilton, J., 2003. An exceptionally preserved Lower Cretaceous ecosystem. *Nature* 421, 807-814.
- Zhou, W., Guan, T., Chen, Z., Li, J., Fan, L., Li, W., 2002. ISL-amenable sandstone-type uranium deposit: Global aspects and recent developments in China. In: Recent developments in uranium resources and production with emphasis on in situ leach mining, IAEA-TECDOC-1396, 2004.
- Zhou, T., Li, G., 2000. Tectonics, granitoids and Mesozoic gold deposits in East Shandong, China. *Ore Geology Reviews* 16, 71-90.
- Zhou, X.M., Li, W.X., 2000. Origin of Late Mesozoic igneous rocks in southeastern China: implications for lithospheric subduction and underplating of mafic magmas. *Tectonophysics* 326, 269-287.
- Zhou, X., Sun, T., Shen, W., Shu, L., Niu, Y., 2006. Petrogenesis of Mesozoic granitoids and volcanic rocks in South China: a response to tectonic evolution. *Episodes* 29, 26 33.
- Zhou, J.B., Wilde, S.A., Zhang, X.Z., Ren, S.M., Zheng, C.Q., 2010. Early Paleozoic metamorphic rocks of the Erguna block in the Great Xing'an Range, NE China: evidence for the timing of magmatic and metamorphic events and their tectonic implications. *Tectonophysics* 12, 50-78.
- Zhou, J.B., Wilde, S.A., Zhang, X.Z., Ren, S.M., Zheng, C.Q., 2010. Early Paleozoic metamorphic rocks of the Erguna block in the Great Xing'an Range, NE China: evidence for the timing of magmatic and metamorphic events and their tectonic implications. *Tectonophysics* 12, 50-78.
- Zorin, Y.A., 1999. Geodynamics of the western part of the Mongol-Okhotsk collisional belt, Trans-Baikal region (Russia) and Mongolia. *Tectonophysics* 306, 33-56.

Le bassin d'Erlian localisé au NE de la Chine s'est développé au cours de l'extension continentale de la fin du Mésozoïque en Asie de l'Est. Le socle sur lequel il repose correspond à la partie orientale de la ceinture orogénique centre asiatique. Les granites indosiniens (236.8 ± 5.8 Ma) étudiés, proviennent d'une série magmatique calco-alcaline fortement potassique dérivée de la fusion partielle d'un manteau enrichi ($^{143}\text{Nd}/^{144}\text{Nd}_i$ faible; $\epsilon\text{Nd}_{(t)}$ négatif) et correspondent à des sources majeures d'U. Les systèmes fluviatiles en tresse qui dominent au cours de l'épisode post-rift du bassin, sont des environnements favorables au dépôt des sables réduits qui constituent les pièges pour les minéralisations U. Les sédiments post-rifts contiennent des concentrations syn-sédimentaires significatives en U, principalement adsorbé aux minéraux argileux. Celles-ci sont ensuite redistribuées quasi *in situ* au cours de l'évolution diagénétique des sédiments, s'exprimant sous forme de coffinite et de pechblende (e.g. Nuheting). La MO contenue dans ces sédiments est d'origine continentale et correspond à un kérogène de type IV immature. Enfin, le gisement roll front de Bayinwula se caractérise par un modèle biogénique. Dans la zone à pyrite, la MO est dégradée par des bactéries sulfato-réductrices. La production de H_2S contribue à la dissolution des oxydes de fer/titane qui sont progressivement remplacés par la pyrite (de même que la MO), caractérisée par une signature $\delta^{34}\text{S}$ très négative. L'U porté par ces oxydes et la MO est libéré et peut alors être lessivé par les fluides oxydants. Le H_2S produit favorise la réduction de l'U qui précipite au front sous forme de coffinite et de ningyoite.

The Erlian Basin located in NE China developed during the late Mesozoic continental extension in eastern Asia. This basin lies on a basement corresponding to the eastern part of the Central Asia Orogenic Belt. Indosinian magmatism (236.8 ± 5.8 Ma) is widely represented by high-K calcalkaline granites derived from an enriched mantle (low $^{143}\text{Nd}/^{144}\text{Nd}_i$; negative $\epsilon\text{Nd}_{(t)}$) and correspond to major U sources. Braided fluvial systems of post-rift sediments of the Erlian Basin correspond to favorable sedimentary conditions for the genesis of permeable and reduced sandstones. Post-rift sediments contain significant synsedimentary U concentrations, mainly adsorbed on clay minerals. These pre-concentrations are redistributed *in situ*, during the diagenetic evolution, and mineralized as coffinite and pitchblende replacing pyrite or pyritized OM (e.g. Nuheting). The OM occurring within these sediments is mainly terrigenous and corresponds to kerogens of type IV, thermally immature. Finally, the roll front-type Bayinwula deposit is characterized by a biogenic model involving reactions between OM, U-rich Fe/Ti oxides and sulfate-reducing bacteria. In the pyrite zone, the OM is degraded by bacteria and replaced by pyrite. H_2S production contributes in the dissolution of Fe/Ti oxides that are progressively epigenized into pyrite, characterized by strongly negative values of $\delta^{34}\text{S}$. U concentrations from Fe/Ti oxides and OM are liberated and can be leached by oxygenated groundwater. H_2S creates a reducing barrier contributing in the reduction of uranium that precipitates at the redox front as coffinite and ningyoite.

Mots clés:

uranium, bassin d'Erlian, Nuheting, tabulaire, Bayinwula, roll front, modèle biogénique